Compact Adaptive Planar Antenna Arrays for Robust Satellite Navigation Systems

Doctoral thesis
for attaining the academic degree of

Doctor of Engineering (Dr. -Ing.)

presented to the Faculty of Electrical Engineering and Information Technology
Technische Universität Ilmenau

by M.Sc. Safwat Irteza Butt
(30. April 1983)

1. Reviewer: Univ.-Prof. Dr. rer. nat. habil. Matthias A. Hein
2. Reviewer: Prof. Dr.-Ing. habil. Reiner S. Thomä
3. Reviewer: Dr.-Ing. Achim Dreher

Submitted on: 07.07.2015
Defended on: 13.10.2016

urn:nbn:de:gbv:ilm1-2016000659

Abstract

Over the past two decades, humankind's reliance on global navigation satellite systems for precise positioning, navigation and timing services has grown remarkably. Such advanced applications vary from highly accurate surveying to intelligent transport systems, and from mobile network timing synchronisation to weather and climate monitoring. This envisages new and higher standards of robustness, accuracy, coverage and integrity in modern navigation receivers. Recently, this has been accomplished with the incorporation of the multi-element navigation antenna receiver. However, the industrialisation of this approach is limited due to the large antenna array size, hindered by the inter-element separation of half of the free-space wavelength, i.e. $\approx 10\ \mathrm{cm}$ at L band ($1 - 2\ \mathrm{GHz}$). In this thesis, compact navigation antenna arrays with smaller inter-element separations are proposed for the miniaturisation of the overall size. However, these arrays become afflicted with the adverse effects of mutual coupling. Therefore, various figures-of-merit for the analysis and design of a compact planar navigation antenna array, such as performance diversity degrees-of-freedom, directional finding capabilities, and polarisation purity, including mutual coupling effects, have been presented. This provides a general framework for the selection and configuration of the optimum compact navigation antenna array. In order to mitigate the mutual coupling, integration of the decoupling and matching network into customised compact navigation antenna array designs is performed. This is fostered by the correlated noise characterisation of the complete receiver. Furthermore, an analytical model of the equivalent carrier-to-interference-plus-noise ratio is derived to investigate the navigation performance in interference scenarios. In the end, this is complemented by the implementation of the complete navigation receiver for verification and robustness validation of the derived compact antenna array concepts in indoor and outdoor interference scenarios.

Zusammenfassung

In den zurückliegenden zwei Jahrzehnten ist die Abhängigkeit der Industriegesellschaft von satellitengestützten Ortungssystemen, Navigationsdiensten und Zeitsignalen dramatisch gewachsen. Darauf aufbauende moderne Anwendungen reichen von hochgenauen Ortungsgeräten bis zu intelligenten Transportsystemen und von der Synchronisation mobiler Netzwerke zu Wetter- und Klimabeobachtung. Dies setzt neue höhere Standards in der Robustheit, Genauigkeit, Verfügbarkeit und Verlässlichkeit moderner Navigationsempfänger voraus. Möglich werden diese Verbesserungen aktuell mit der Einführung von Multiantennensystemen in den Navigationsgeräten. Jedoch wird die Nutzung dieses Ansatzes durch die größeren Abmessungen der Antennenarrays erschwert, weil standardmäßig der Elementabstand zu einer halben Freiraumwellenlänge gewählt wird, was im L Band

ca.$10\ \mathrm{cm}$ bedeutet.

In dieser Arbeit werden kompakte Antennenarrays für Navigationsempfänger mit geringerem Elementabstand vorgeschlagen, die eine Miniaturisierung der Empfängerabmessungen erlauben. Diese kompakten Arrays werden in ihrer Leistungsfähigkeit jedoch durch die negativen Effekte der Verkopplung zwischen den Einzelelementen beeinträchtigt. Für die Beurteilung der Empfängerleistungsfähigkeit existieren verschiedene Qualitätsparameter für Analyse und Entwurf der planaren Arrays. Damit werden z. B. Diversity Freiheitsgrade, Qualität der Richtungsschätzung, Polarisationsreinheit und die wechselseitigen Kopplungen gemessen und eine Entwurfsumgebung wird vorgestellt, in der das optimale kompakte Antennenarray für den jeweiligen Einsatzzweck ausgewählt und konfiguriert werden kann. Dieser Prozess wird durch eine Analyse des Rauschens und seiner Korrelationseigenschaften für den gesamten Empfänger begleitet. Darüber hinaus wird ein analytisches Modell des effektiven carrier-to-interference-plus-noise ratio abgeleitet, um die Leistungsfähigkeit der Navigationsempfänger in Szenarien mit Störsignalen zu untersuchen. Schließlich werden diese Betrachtungen durch den Aufbau eines kompletten Satellitennavigationsempfängers ergänzt, um mit ihm den Nachweis der Funktionsfähigkeit und der stabilen Funktion des entworfenen Systems mit kompaktem Array unter Störereinfluss bei Laborbedingungen und im realen Außeneinsatz zu erbringen.

Theses of the Dissertation

– To meet the modern standards for **safety-of-life** critical applications like autonomous driving and intelligent transport systems, future **global navigation satellite systems** can benefit from compact antenna arrays to achieve **miniaturisation** and **robustness**.

– For any N-port antenna array, such that $N > 1$, the radiation process is defined by the superposition of N **orthogonal modes of radiation** or the diversity degrees-of-freedom. However, **compact** electrical size or inter-element separation less than half of free-space wavelength give rise to increased **mutual coupling** which degrades the **efficiency** of these degrees-of-freedom.

– **Eigen-decomposition** of the antenna array **spatial covariance matrix**, calculated using the scattering parameters or the far-field patterns, delivers the assessment of the fundamental modes of radiation or the **eigenmodes**.

– The **minimum eigenvalue** or the eigenvector with least efficiency dominates the overall radiation or reception performance of the compact antenna arrays. Primarily, this **figure-of-merit** can serve as a parameter for the selection and configuration of the **optimal** compact antenna array in the design process.

– Compact **planar** antenna array configurations provide flexibility of **geometrical** optimisation for efficient degrees-of-freedom and achieving improved **direction-finding** capabilities.

– The **polarisation purity** of the compact antenna array eigenmodes is worsened by mutual coupling, particularly for the **higher-order modes** and must be taken into account in the design process for optimum performance.

– An optimum **trade-off** between miniaturisation and absolute radiation efficiencies is vital for application of these arrays in robust navigation receivers because the efficiency **enhancement** provided by realistic **decoupling and matching** is limited.

– The decoupling and matching network **integration** with the antenna array demands miniaturisation of the network, and careful implementation for **minimum ohmic losses**. The decoupling and matching generally comes before the low-noise amplifier, and any additional losses, i.e. **noise contribution**, will adversely affect the system's performance.

– The **noise characterisation** of the **complete** navigation antenna array receiver, including the network losses, yields the **equivalent carrier-to-interference-plus-**

noise ratio by applying the conventional deterministic beamformer with null-constraints. This **framework** allows for performance measure predictions in respect of the navigation receiver.

– The **impact** of the polarisation impurity in the higher-order modes on the receiver's **vulnerability** to the **arbitrary-polarised interferer** is characterised in the equivalent carrier-to-interference-plus-noise ratio. This is useful in analysing compact antenna array robustness in worst **interference scenarios** before its integration with the receiver.

– **Low-cost**, miniaturised, compact navigation antenna arrays, using **off-the-shelf** ceramic patch antennas and quadrature couplers are possible. This is helpful for **mass-production**.

– The developed compact navigation antenna array receiver incorporating decoupling and matching network integration allows for **realistic measurements** in real-world scenarios to **verify** its navigation robustness.

– The **practical applicability** of decoupling and matching for compact antenna arrays becomes **crucial** and prominent in the **interference-limited scenarios**; therefore, its implementation is necessary for **robust** compact navigation antenna array receivers.

Preface

This work is a compilation of the research carried out at the RF and Microwave Research Laboratory of the Technische Universität Ilmenau. The research has been part of the project "Compact adaptive terminal antenna for robust satellite navigation" (KOMPASSION) and the on-going project "Compact satellite receiver systems for robust navigation applications" (KOSERNA). These projects and thus this work at the laboratory have been funded by the German Aerospace Center (grant no. 50NA1007 and 50NA1405) on behalf of the German Federal Ministry of Economics and Technology, for which I am highly obliged.

I am grateful to the head of laboratory, Univ.-Prof. Dr. rer. nat. habil. Prof. Matthias Hein for his valuable support and guidance. The successful completion of this work has been stimulated by his visionary ideas and suggestions.

I would also like to thank Prof. Dr.-Ing. habil. Reiner S. Thomä and Dr.-Ing. Achim Dreher for reviewing this work.

I am thankful to Dr.-Ing. Ralf Stephan for his precious discussions, and providing valuable support into the practical aspects. I am humbly obliged to the friendly yet aspiring environment provided by my colleagues Dipl.-Ing. Hendrik Bayer, Dipl.-Ing. Alexander Krauss, Dipl.-Ing. Stephanie Kühn, M.Sc. Saqib Kaleem and Dipl.-Ing. Frank Wollenschläger. I am thankful to the technical assistance provided by Mr. Michael Huhn and Mr. Matthias Zocher.

I am thankful to the colleagues in the project consortium. These include: M.Sc. Matteo Sgammini, Dr.-Ing. Achim Hornbostel, and M.Sc. Lothar Kürz for their valuable support in conducting joint research collaborations. I am deeply grateful to M.Sc. Eric Schäfer for his technical investigations and his support in writings of several joint publications.

I am thankful to be blessed with the emotional support of my lovely wife Maryiam. Her insights and driving force made the completion of this work easier and colourful. I am thankful to my brother, Anse Irteza, for his ever presence and support.

Finally, I am thankful to my parents for their motivational support. This work is a tribute to their hardships and efforts.

Safwat Irteza Butt
Ilmenau, 7th July 2015

Contents

Chapter 1

Introduction

In the era of miniaturised sophisticated *navigation receivers*, space restrictions are far more severe on the antenna [1], [96], [128], [129]. This conventionally leads to the simple and practical choice of a single-element microstrip antenna, due to its low-profile, light weight and small size [1, Chapter 2],[2]. However, with the urbanisation of human dwelling, it becomes difficult for the fixed radiation pattern antenna to maintain the *availability*, *integrity* and *accuracy* of the received data, which may jeopardise the performance of the whole system [88], [18]–[21], [97], [98]. Hence, a compact, cost-effective and low-profile solution for receiver controlled radiation pattern antennas is vital to ensure robustness in receivers against interference, multipath signals, spoofing and shadowing. Generally, *antenna arrays* replenish the use of beamforming and interference suppression to achieve accuracy, robustness, availability and reliability [89], [22], [99]–[101]. These multi-element antennas can take different configurations ranging from linear to three-dimensional forms. Nevertheless, the limiting factor for the overall dimensions, to minimise *mutual coupling* and maximise directivity, is inter-element separation. The optimal separation for minimal coupling is *half* of the free-space wavelength. This is quite bulky for L-band applications, which have operating frequency between $1 - 2$ GHz such as *global navigation satellite systems* (GNSS), where the *free-space wavelength* is up to 25 cm. Therefore, in modern navigation receivers, the application of antenna arrays are unattractive, which are restricted in space requirements.

It is intrinsic to the antennas; a nearby antenna will receive the backscattered energy from its neighbour. This is not just directly influenced by the immediately adjacent antenna but also indirectly from the other receiving antenna array elements. These coupled field wave may add constructively or destructively to the direct incident wave. This is a manifestation known as mutual coupling between the antenna array elements [3], [23], [24]. However, mutual coupling, causing a finite mutual impedance between the radiating elements, depends on the proximity of the antenna elements. This increases proportionally with decreasing inter-element separation $d < \lambda/2$, and the number of elements and

their separation will determine its ramification. Mutual coupling has adverse effects on the radiative performance of the antenna array, especially the higher-order *diversity degrees-of-freedom* or super-directive modes[25]–[27], [102], [103]. The integration of such compact antenna arrays in any application necessitates mitigation of the coupling; concerning this, several approaches have been put forward in recent years [90], [28], [29]. One of the innovative techniques is via orthogonal excitations and individual port matching. These orthogonal excitations may acquire the eigenmodes of the antenna array ensuing to the decoupled ports, and ideally achieve 100% radiation efficiency, which is not possible due to the ohmic losses with in the network and post matching networks are required to maximize the radiation efficiency. The practical realisation of *decoupling and matching networks* (DMN) involves the use of discrete lumped components, quasi-lumped components or directional couplers. The employment of DMN has been suggested to maximise the receiver of signal-to-noise ratio (SNR) [30]–[33]. The SNR is a crucial parameter for detecting and tracking the received data. The lower SNR indicates a longer transient and integration time, which is undesirable. In all these analyses the DMN is considered to be lossless, which presents only one half of the truth. In reality, these DMNs are dissipative, and may delimit their usage in noise limited receivers such as GNSS, where received signals are weak and below the noise level. The DMN losses between antenna and the first stage low-noise amplifier may degrade severely the noise figure of the receiver. Therefore, the *noise characterisation* of the DMN in terms of equivalent SNR post beamforming is necessary to identify the true benefit of DMN in the case of coupled arrays.

Some of the key questions investigated in this thesis are as follows:

– What are the challenges and limitations of the advanced robust GNSS receivers?

– What are the benefits of a multi-element GNSS antenna and its implications in the practical implementation of the modern navigation receivers?

– What are the evaluation methodologies for the compact antenna arrays inherited with the mutual coupling effects?

– What is the optimal miniaturised configuration for the compact planar antenna arrays?

– What is the influence of the number of elements, inter-element separation, and geometrical arrangement on the direction-finding capability of the planar antenna arrays?

– What are the available different techniques for mitigating mutual coupling and their fundamental limitations?

– What is the equivalent carrier-to-interference-plus-noise ratio (CINR) including the ohmic losses of the DMN for the navigation multi-element antenna receiver?

– Is it beneficial to deploy a realistic(lossy) DMN for complete compact navigation antenna array receiver?

These are addressed in different chapters as:

Chapter 2; Robustness of GNSS: This chapter describes the targeted application and provides the motivation of this work. The basic principle of the GNSS with emphasis on state-of-the-art civilian receivers is described. Moreover, the fundamental features and requirements of the antennas used in the modern navigation receivers are discussed. This is followed by discussions of the challenges and remedies of these receivers for public use to meet the demands of advanced safety-of-life (SoL) critical applications.

Chapter 3; Evaluation methodologies of compact planar antenna arrays: The different figures-of-merit for the analysis of the compact planar antenna arrays are presented. These provide a framework to find an optimal compact antenna array configuration for implementation in the robust navigation receivers. This optimisation parameters involve the minimum eigenvalue and the direction-finding capability of the compact antenna arrays.

Chapter 4; Compact robust GNSS antenna array receivers: This focuses on the practical implementations of compact four-element antenna arrays integrated with DMN. These antenna arrays are evaluated for the derived equivalent CINRs for navigation signals in the interference-limited scenarios. This provides insight into the merits and demerits of the DMN for compact antenna arrays.

Chapter 5; Adaptive compact navigation receiver demonstrator: In the end, a complete navigation receiver with conventional adaptive beamforming and interference suppression algorithms is developed to investigate the carrier-to-noise ratio (CNR) of the tracked navigation signals. These include both indoor and outdoor measurement campaigns for satellite signals with and without interference. Furthermore, the results of the equivalent CINR with and without DMN obtained in the previous chapters are verified.

Chapter 2

Robustness of Global Navigation Satellite Systems

Man's curiosity about his origins has persisted throughout human history, with landmarks serving as historical points of reference and, more recently, satellites serving the same function but with exponentially higher accuracy [4]. With advancements in digital maps, satellite navigation has become a major source of travel guidance and an efficient device for travel assistance. Therefore, in addition to its military applications, the public has benefited from daily use of mobile and personal hand-held devices equipped with satellite navigation functionality. A recent market survey determined that there are nearly four billion navigation devices operated worldwide [130]. This increased dependence on satellite navigation devices has precipitated several constraints on the system as a whole. These include better availability of the satellite signals globally, better navigation solution accuracy, integrity and continuity of system robustness. In SoL critical applications, robustness against jamming, interference and multipath become inevitable. These conditions and their effects will be discussed later in this chapter in section 2.4.

At the beginning of this chapter, the navigation system and its basic principles are introduced. The user segment is subsequently described in order to understand the main features of its various components, more specifically the features of the navigation antennas. In the last part of this chapter the challenges to the robustness of navigation receivers are presented. Finally, solutions proposed in the last two decades, are formulated to meet these challenges at the receiver end, which underpin the motivation for this research.

2.1 Basic principle of GNSS

Satellites that provide precise positioning and timing data are called GNSS [5]. The term *global* refers to the global coverage or accessibility of these signals anywhere on the planet.

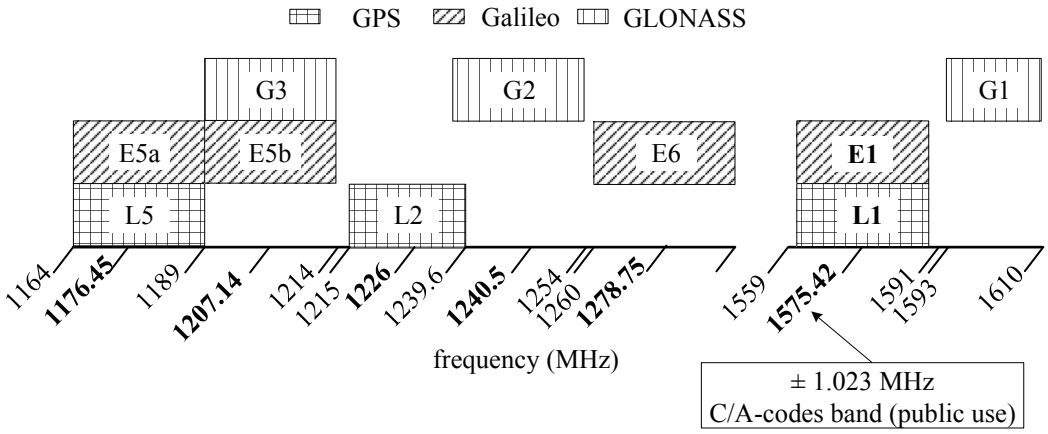

Figure 2.1: The L-band allocation of frequency spectrum for the operating carrier frequencies and bandwidths of various GNSS signals.

The complete global coverage is achieved by a minimum of 24 medium orbit satellites travelling around the earth in several orbital planes. Generally, the GNSS is classified into three segments: space, control, and user. The space includes the satellites, the control is responsible for maintaining the health and error-corrections of the satellites, and the user includes the receivers to determine position, velocity and time (PVT) information[4, Chapter 3].

In the near future, GNSS will consist of four independent satellite navigation systems. The first and most popular complete system operated by the United States is known as the Global Position System (GPS), which started full operation in the early 90s. It maintains the availability of at least 24 satellites spread across six orbital planes to ensure availability above 95% of the time with each satellite orbiting the Earth twice a day [4, p. 358]. Simultaneously, the then-Soviet Union developed a global orbiting navigation satellite system (GLONASS), but its full orbital constellation of 24 satellites was only just deployed in 2011 [131]. In 2002, the European Union initiated the development of its fully inter-operable worldwide satellite navigation system comprising high-precision hydrogen master clocks, advanced rescue and SoL features as part of its global navigation satellite system called Galileo, which currently has eight satellites in space; it is supposed to be fully operational by 2020 [128]. The fourth-generation system is an upgrade to its regional navigation satellite system (RNSS) developed by China, called Compass (Beidou), into a fully-fledged GNSS system for global coverage[5, Section 12.1.2]. All these systems occupy the frequency spectrum of the L-band, i.e. $1000 - 2000$ MHz, ranging from 1164 MHz to 1610 MHz, which are presented in Fig. 2.1.

2.1.1 Characteristics of the satellite signal

The GPS satellite signals employ the code division multiple access technique (CDMA), which is a spread spectrum technique that allows each satellite to use the same frequency but different codes without mutual interference. Each satellite is assigned a pseudo random noise (PRN) code and navigation message, which is modulated over carrier frequency. At L1, i.e. 1575.42 MHz, there are two different types of PRN ranging codes that are transmitted from each satellite: a coarse acquisition (C/A) and precision (P) code [132, p. 4]. The C/A-codes, available for civilian use, are short length codes with a duration of one millisecond and repeat constantly. The P-code has a duration of seven days and repeats after approximately every Saturday at midnight. However, these P-codes are encrypted to Y-codes restricting use to the military, which provides anti-spoofing capabilities. The intentional degradation of C/A code known as selection availability has been inactive since 2001, which increases the stand-alone receiver positioning accuracy within a radius of six meters 95% of the time. With the planned modernisation of the satellites, three additional signals were incorporated at L2C, i.e. 1227.60 MHz, to correct for the ionospheric corrections, at L5, i.e. 1176.45 MHz for SoL applications, and at L1C, i.e. 1575.42 MHz, with a new modulation scheme presenting a zero gain at the carrier frequency or the split power spectrum [133], [134]. These are intended to improve the accuracy and provide robustness to civilian users with standards similar to those of military users.

The European Galileo and Compass satellites operate on similar signal bands to GPS based on the principle of the CDMA technique. However, Galileo incorporates a search and rescue feature, which enables the use of its satellites as transponders. This provides a feedback loop between the user and the space segment offering services in critical or disaster situations [5, Section 11.3]. The GLONASS operates across different carrier frequency bands for the transmission of its data. The primary difference between the characteristics of the aforementioned satellite systems is that in GLONASS each satellite has the same code but different frequencies, which uses frequency division multiple access (FDMA). This work highlights the C/A-codes of GPS and Galileo at the L1 and E1 bands, respectively, only.

For the GPS system, the received signal, $y_k(t)$, at the output of the antenna from the satellite k can be expressed at time instant t as:

$$y_k(t) = \underbrace{A}_{1}\,\underbrace{x_{\mathrm{m}}(t)}_{2}\,\underbrace{\sin(\omega_c t + \phi_k)}_{3} + \underbrace{n(t)}_{4}\,. \tag{2.1}$$

Here,

1. A is the amplitude of the transmitted signal;
2. This is the exclusive-or of the navigation message $x_{\mathrm{n}}(t)$ and $x_{\mathrm{c}}(t)$, the non-return to zero (NRZ) PRN sequence of the k satellite. The navigation message has a one-bit

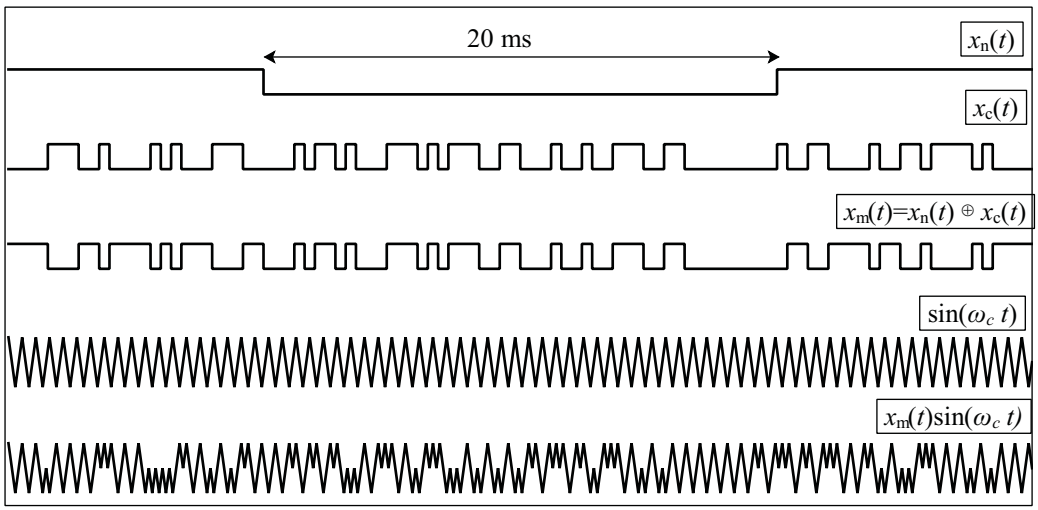

Figure 2.2: The satellite signal waveforms of GPS L1 navigation message ($x_{\mathrm{n}}(t)$), C/A-code ($x_{\mathrm{c}}(t)$), and BPSK direct spread sequence.

length of $20\ \mathrm{ms}$, which represents 20 replicas of the PRN-codes, each with a duration of one millisecond;

3. This represents the nominal carrier, which for GPS L1 C/A is $1575.42\ \mathrm{MHz}$ and is modulated with $x_{\mathrm{m}}(t)$; The phase ϕ_k contains the Doppler-induced variations due to the movement of the satellite and receiver, ionospheric and tropospheric effects, and phase noise of the satellite local oscillator;

4. The thermal noise and the background noise, which may be assumed as additive white Gaussian noise in the simplest model;

The different wave forms associated with the navigation signal are shown in Fig. 2.2.

2.1.2 Positioning

A navigation system like any communication system consists of a transmitter *satellite* and a *receiver*, typically a mobile device. The principal operation of determining the receiver's position requires direct line-of-sight to the satellites, because the satellite signal is unable to penetrate water, soils or other obstacles. In metropolitan areas, these signals can be blocked by buildings or nearby mountains, which lead to the blockage of positioning information.

The receiver requires information from at least four satellites to localise itself accurately enough. The decoded satellite signal reveals the transmitted navigation message.

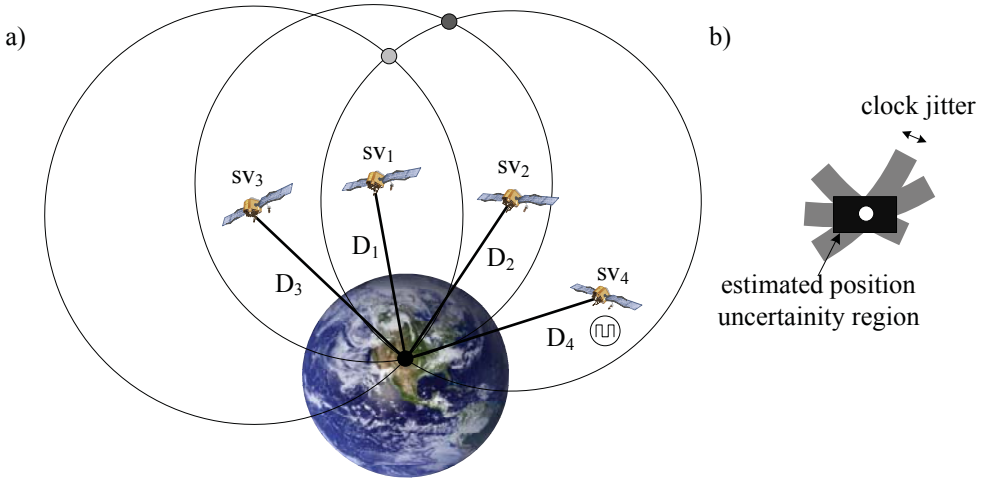

Figure 2.3: (a) The ranging circles with radii D_1, D_2, D_3, and D_4 for estimation of the position on Earth with each of the four satellites, respectively, grey dot indicates one of the first and second satellite intersection points, black dot appears due to the intersection with the third satellite, which is discarded. (b) The zoomed version of the intersecting circles, where the local oscillator clock jitter and uncertainty in the position estimation is depicted as the black rectangular region.

This mainly contains the data frames of information comprising the precise location of the transmitting satellite and the time of transmission. There is other auxiliary information that can assist the receiver in correcting the errors that degrade the range measurements. Typically, these navigation messages are monitored and corrected by the control stations to improve performance over time. But, how do these four satellite navigation messages help in determining the receiver's position? This can be explained with the aid of Fig. 2.3. The receiver determines the travel time, i.e. the duration of the transmission of the code from satellite to the receiver. This time is gathered from each satellite, and converted into the respective distances by multiplying by the travelling speed of the wave, which is assumed here to be the speed of light in vacuum. Three satellites are sufficient for trilateration, though due to receiver clock offsets, acquisition of the fourth satellite is necessary because this permits the use of inexpensive quartz crystal in the receiver electronics. Therefore, at any given point the receiver should be able to maintain direct line-of-sight with four satellites at minimum to ascertain its position.

On the other hand, the distance from a satellite can also be determined using the carrier frequency phase estimation, which has a resolution up to $19\ \mathrm{cm}$. But, the carrier phase ambiguity resolution is challenging to achieve, as it demands special data like known receiver information to resolve, which is difficult and expensive to implement for commercial purposes at every location on earth. Regardless of the range measurement techniques, there are several other sources of position errors inherent in atmospheric effects, receiver noise,

and satellite data. The approximate typical estimates of these errors are listed in [4, Table 7.4]. These can reduce the overall positioning accuracy up to $10\ \mathrm{m}$.

2.1.3 Performance standards of GNSS

The performance standards of the GNSS service depend on the user needs. These services vary from the basic PVT to the advanced SoL, and search and rescue. The services provided by the GNSS are affected by the location of the user, time of the measurement, and the surrounding outdoor environment, i.e. rural or urban.

Accuracy: This is referred to as the difference between the retrieved position using GNSS and the true or absolute PVT information. In statistics, it is the uncertainty radius of the PVT information at a given time period around the true PVT. In 2014, modern navigation standalone receivers using the standard positioning service available for civilian use have a horizontal positioning error of $3.5\ \mathrm{m}$, whereas the vertical positioning error increases to $5\ \mathrm{m}$ according to the survey report published by the Federal Aviation Authority [135, Fig. 5.2, p. 22].

Availability: This is referred to as the visibility or acquisition of the minimum number of satellites required to determine the PVT solution. It is given as the percentage of time adhering to certain criteria of the PVT solution error.

Integrity: The confidence measure of the PVT solution with ability to monitor anomalies in the PVT solution. The system should have the capacity to provide additional information on the reliability of the signals. This is a crucial service required in SoL applications e.g. aviation.

Continuity: This defines the ability of the navigation system to provide the PVT solution to the user without interruption.

Robustness: The ability of the system to determine the authenticity of the received signals. This is to protect the system against spoofing, jamming and multipath.

Interoperability: With the beginning of the complete GNSS operated by different countries, the interoperability of these systems is of utmost importance. This will allow for a combined PVT solution that delivers better availability, accuracies, integrity, continuity and robustness. In addition, this may be foreseen as avoidance of inter-system interference.

2.2 Receiver architecture

The user segment of the GNSS consists of a hardware called a receiver and a software to map the receiver position output on a graphical user interface. Like any typical communication receiver, the navigation receiver can be divided into three main categories: antenna, front-end (FE), and the baseband processing unit. The antenna plays a pivotal role in receiver performance, and, therefore, it will be discussed in the next section separately.

2.2.1 Front-end

Here, the FE refers to two main blocks of the receiver: one is the analogue and the other is digital. The analogue FE is normally designed using homodyne or zero-IF and heterodyne or low-IF architecture, i.e. $2 - 150$ MHz. Here, the term "IF" refers to the intermediate frequency, which is obtained after the down-conversion of the received carrier at radio frequency (RF). In case of zero-IF FE, the signal is centred around 0 Hz. This architecture relaxes the complexities of devices because of the absence of imaging of the signal. However, as most of C/A code energy is centred at DC, it is highly sensitive to DC-offsets and flicker noise. In comparison, low-IF architecture is insensitive to the aforementioned problems. But, it has the drawback of restricted image rejection, which can be cured using a careful frequency plan and filtering. In practice, due to aforementioned reasons the zero-IF architecture is not applied in navigation receivers. Therefore, further receiver discussions and implementations will be limited to the low-IF architecture .

The received power from a satellite at L1/E1 band is approximately -157 dBW with an ideal isotropic right-hand circularly polarised (RHCP) antenna [4, Table 10.2]. Considering the 2.046 MHz C/A-code bandwidth, the thermal noise power is equal to -141 dBW. This indicates that the received signal strength is below the thermal noise floor. This means that any additional noise due to the analogue FE can adversely affect the positioning accuracy. Therefore, the analogue FE architecture and the properties of components demand careful consideration. On the other hand, the digital FE includes the analog-to-digital converter, its role and impact on the performance of the receiver is been discussed in [4] for further reference.

2.2.2 Baseband processing

In the digital domain, the core processing units of the L1/E1 baseband receiver are the (1) acquisition and the (2) tracking algorithm. After the tracking algorithms, the navigation message is retrieved, which is used to evaluate the PVT estimates for the receiver.

Signal Acquisition As the PRN-codes for the C/A-codes are known, the receiver must generate the replicas of these codes. Principally, these codes are individually phase-shifted per chip and then multiplied by the incoming signal, after removal of the carrier frequency. This process is called *code correlation*. There is a maximum correlation if the code is matched and exactly aligned with the received satellite signal. The carrier frequency wipe-off is basically the multiplication of the incoming signal by a replicated carrier plus Doppler in the receiver. Therefore, it is important to determine the Doppler frequency offset due to the movement of the satellite and the frequency offset in the receiver's reference oscillator compared to its specified frequency. This is a complete two-dimensional search to determine which satellites are present in the visible space. Over the years, several acquisition techniques have been developed in both the time and frequency domain, though

these are not the focus of this thesis [6, Chapter 7]. However, the frequency domain using the fast-Fourier transform reduces the number of operations and time in which to calculate the solution. Perhaps this is the reason it is being widely employed in commercial receivers and also in this work.

Signal Tracking After the search of the visible satellites by the acquisition algorithm is finished, the next step is to track the satellite until it disappears from the visible space or the signal-to-noise ratio (SNR) drops below a threshold, and is referred to as *tracking* [6, Chapter 8]. The tracking is repeatedly performed, for both the frequency and code domains, in order to maintain the replica carrier-frequency and the code-phase aligned with changes occurring over time. Therefore, the core of the tracking algorithms is the code-tracking loop (DLL) and the carrier-frequency tracking loop (PLL). At first, the PLL adjusts the error in the carrier-frequency according to the received signal and the previous iteration replica of the carrier-frequency. The new replica is multiplied by the incoming signal to wipe off the carrier frequency. The code-phase error is adjusted by applying three-way parallel multiplication using the early, prompt and late codes. In the last step, the baseband signals multiplied by prompt codes are integrated and dumped to calculate the navigation message, which has a duration of $20\ \mathrm{ms}$.

2.2.3 State-of-the-art GNSS receivers

Before discussing the GNSS antennas and its related properties and requirements, a review of the current state-of-the-art receivers is necessary to analyse the miniaturisation of the GNSS devices. In the literature, the very first integrated chipset of the GPS FE was introduced in the early $90\mathrm{s}$ [96]. This was based on the gallium arsenide technology. However, this was replaced by low-cost and popular complementary metal oxide semiconductor (CMOS) technology suitable for the L-band. Sometimes in the literature, silicon germanium has been proposed, which provides lower noise compared to the CMOS technology, but it is also more expensive. A brief list of the GNSS receiver architectures for different technologies and their performance limitations are given in [7, p. 20].

Nowadays, many semiconductor companies provide complete GNSS receiver chipset solutions. For information on the two oldest chipset solutions with independent FE and baseband signal processing modules, please see [7, p. 21-22]. In order to get an idea of the size of modern receivers and technology, five modern highly miniaturised available complete GNSS chipset solutions are presented in Table 2.1. These are integrated designs for the FE module and the baseband signal processing module. Generally, the input of the receiver is directly connect to the passive or active antenna output, whereas the output of the receiver is the decoded GPS navigation message output. The ublox M8030 is the smallest of all with a footprint of $3\ \mathrm{mm} \times 3\ \mathrm{mm}$ and has the highest receiver sensitivity. All are compatible with the available GNSS constellations except Buffalo and Furano, which are limited to GPS and GLONASS. Note, the mentioned chipsets operate only within the

Table 2.1: State-of-the-art available commercial GNSS L1 receiver integrated chipsets.

receiver chipset	**size** mm × mm	**GNSS support**	**receiver sensitivity** (dBm)
Mediatek [136] MT3333	6×6	GPS, Galileo, GLONASS and Beidou	-165
ublox[129] M8030	3×3	GPS, Galileo, GLONASS and Beidou	-167
Buffalo [137] B1919	19×19	GPS and GLONASS	-157
Furuno [138] ePV7010B	7×7	GPS, Galileo and GLONASS	-161
ST8090FG [139]	6×6	GPS, Galileo, GLONASS and Beidou	-162

L1 frequency and do not yet take advantage of the available multi-band signals for better accuracy and robustness. The incorporation of compatibility with these signals is planned in the near future when the modernisation of the satellites is completed.

2.3 Types and features of antennas

An antenna is the eye and ear of any receiver, which provides electromagnetic vision and a hearing interface to the outer world. Thus, a well-designed GNSS antenna is critical to a reliable and low-noise receiver. However, the design of the antenna is of secondary importance to the GNSS system, creating the necessity for a simpler, cheaper and smaller antenna design. Nonetheless, due to notoriously weak satellite signals arriving from all directions and coverage at the L-band, i.e. free-space wavelength up to $25\ \mathrm{cm}$, the antenna design process becomes complex and challenging to meet the demands of reduced costs, fabrication simplicity and small form factors. In order to interpret the antenna specifications for GNSS applications, the fundamentals are introduced in terms of crucial parameter parameters like impedance bandwidth, polarisation, and radiation. In consideration of the needs of more precise and accurate positioning, additional requirements of phase-centre stability and multipath/interference suppression are also presented.

2.3.1 Antenna gain

The total radiated power P_{rad} is found by integrating the flow of the Poynting vector through a closed surface. With the surface of integration defined as a sphere of radius r, which is large enough to hold the far-field approximation to be valid, then the P_{rad} is given by [3, Equation 2.13]:

$$P_{\text{rad}} = \frac{1}{2\eta_{\text{o}}} \int_0^{2\pi} \int_0^{\pi} |\vec{E}(r,\theta,\phi)|^2 \cos\theta \mathrm{d}\phi \mathrm{d}\theta. \tag{2.2}$$

The η_o is the intrinsic free-space wave impedance, which is approximately equal to $377\ \Omega s$. $\theta \in [-\pi/2, \pi/2]$ where zenith refers to $\theta = \pi/2$ called "elevation". In the far-field electric field, $\vec{E}$ is transformed into

$$\vec{E_{\text{o}}}(\theta,\phi) = r \cdot \vec{E}(r,\theta,\phi) e^{jkr}. \tag{2.3}$$

The far-field electric field consists of two orthogonal components given by E_θ^o and E_ϕ^o, where the radial component is zero in the far-field zone. Therefore,

$$|\vec{E_{\text{o}}}(\theta,\phi)|^2 = |E_\theta^{\text{o}}(\theta,\phi)|^2 + |E_\phi^{\text{o}}(\theta,\phi)|^2 \tag{2.4}$$

Now, if the normalised far-field pattern is introduced, then the normalised far-field electric field is donated by $\vec{F}(\theta,\phi)$, which is given by [26, Equation 4]:

$$|\vec{F}(\theta,\phi)|^2 = \frac{4\pi}{2\eta_{\mathrm{o}}}|\vec{E}_{\mathrm{o}}(\theta,\phi)|^2. \tag{2.5}$$

This $\vec{F}(\theta,\phi)$ refers to the *complex amplitude realised gain of the antenna with respect to an ideal isotropic radiator*. This includes the ohmic as well as the mismatching losses. Now, the radiated power (2.2) using (2.5) becomes,

$$P_{\mathrm{rad}} = \frac{1}{4\pi}\int_0^{2\pi}\int_0^{\pi}|\vec{F}(\theta,\phi)|^2\cos\theta \mathrm{d}\phi\mathrm{d}\theta. \tag{2.6}$$

In the case of navigation receivers, the desired signal is RHCP. Therefore, the amplitude realised gain of the RHCP component in far-field is $F_{\mathrm{RHCP}}(\theta,\phi)$. An ideal RHCP isotropic radiator would have $\vec{F}(\theta,\phi) = [F_{\mathrm{RHCP}}(\theta,\phi) \quad F_{\mathrm{LHCP}}(\theta,\phi)] = [1 \quad 0]$.

The accepted power P_{acc} of the antenna is related to the input power P_{in} and the reflected power P_{re} according to

$$P_{\mathrm{acc}} = P_{\mathrm{in}} - P_{\mathrm{re}}. \tag{2.7}$$

If the incident and the reflected power waves on the antenna input terminals are defined by complex vectors $\vec{b}$ and $\vec{a}$ respectively, such that $P_{\mathrm{re}} = \vec{b}^*\vec{b} = |\vec{b}|^2$ and $P_{\mathrm{in}} = \vec{a}^*\vec{a} = |\vec{a}|^2$ for the single antenna. Therefore, (2.7) becomes

$$P_{\mathrm{acc}} = |\vec{a}|^2 - |\vec{b}|^2, \tag{2.8}$$

With $\vec{b} = \vec{\Gamma}\vec{a}$, where $\vec{\Gamma}$ is the complex reflection coefficient of the antenna. Also, assuming the normalised incident power wave, i.e. $|\vec{a}|^2 = 1$. Putting this into (2.8) it becomes,

$$P_{\mathrm{acc}} = 1 - |\Gamma|^2. \tag{2.9}$$

The relationship between the total radiated power and the accepted power can be expressed as:

$$P_{\mathrm{rad}} = P_{\mathrm{acc}} - P_{\mathrm{loss}}, \tag{2.10}$$

here, P_{loss} represents the ohmic losses within the antenna. Therefore, P_{rad} includes the complete parameters of the antenna and shall be used for the performance analysis of the antenna. In the case of a lossless antenna, $P_{\mathrm{rad}} = P_{\mathrm{acc}}$. It is worth mentioning that the derivations above are valid for both the transmitting and the receiving cases due to the reciprocity of the antennas. In the ideal receive case, the P_{rad} notation is replaced by P_{rec}.

The characterisation and performance of the fixed pattern navigation antenna are determined by several parameters mentioned above, but of these gain and beamwidth are the most important factors. The GNSS receiver antennas need to have RHCP. If an isotropic

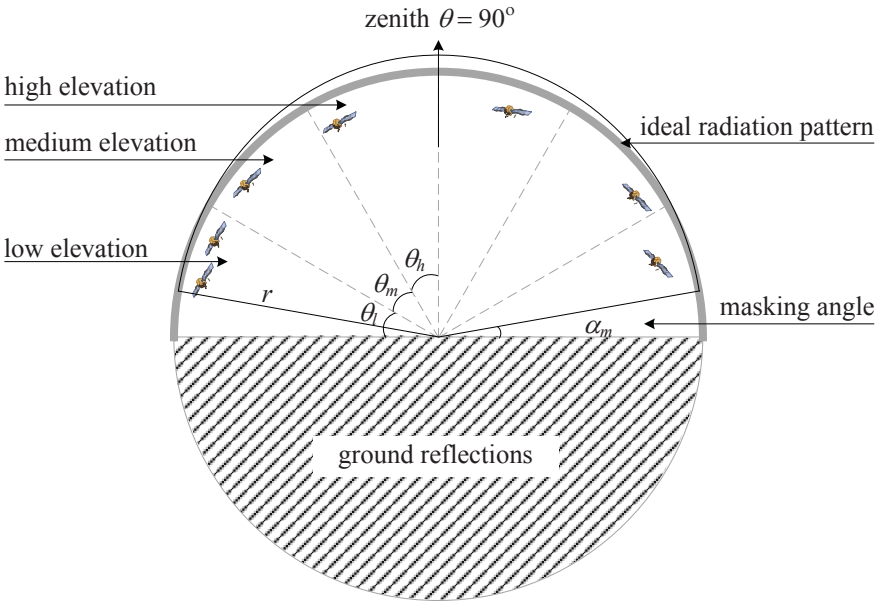

Figure 2.4: Radiation pattern contour (solid grey line) requirements for a GNSS antenna with a sharp masking angle to suppress ground reflections.

lossless RHCP antenna is assumed, then the maximum $|F_{\text{RHCP}}|^2 = 1$ or 0 dBic. If the area of reception is reduced to the upper hemisphere with a restricted elevation minimum masking angle. Because, it is expected that reception below this angle will make the receiver vulnerable to multipath, and ground-reflections. Keeping this, and masking angle $\alpha_{\text{m}} = 0$, the lossless antenna can achieve the maximum realised gain $|F_{\text{RHCP}}|^2 = 3$ dBi. A masking angle restriction increases the maximum possible value of the realised gain by a factor of $(1 - \sin \alpha_m)$, which at $\alpha_{\text{m}} = 5^{\text{o}}$ is increased to approximately 3.4 dBi. Obviously, increasing the masking angle will proportionally increase the realised gain or directivity of the antenna because of the required radiation area due to the decreased beamwidth requirements. However, this will reduce the number of received satellites. The reduction of the available satellites directly influences the positioning capability and accuracy of the receiver.

Effect of radiation pattern on positioning accuracy: The effects of the various error sources between the receiver and the satellite are collectively denoted as user range error (URE). However, the standard deviation of the overall solution is a multiple of URE and the geometric dilution-of-precision (GDOP) of the acquired or visible satellite geometric. The GDOP is the uncertainty of all the estimated ranging parameters including latitude, longitude, height, and the clock offset. The GDOP defines the confidence value in the estimated position. The GDOP can be calculated using the geometric location of the satellites, and is described by the following matrix [34, Chapter 11]:

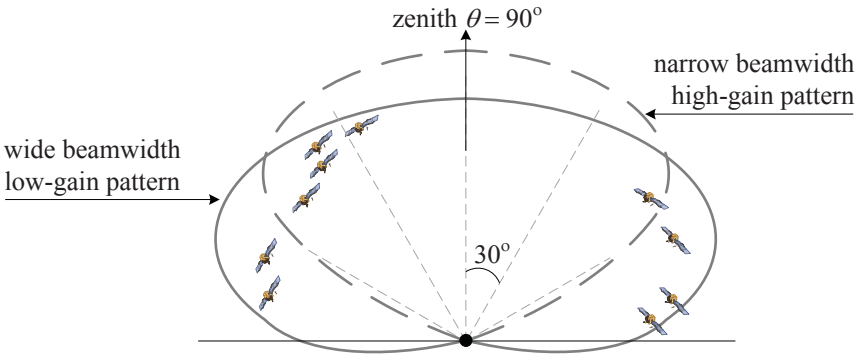

Figure 2.5: Radiation pattern influence of a low- (solid line) and high-gain (dotted line) antenna types, such as a rectangular Patch and Horn antenna [3].

Table 2.2: Visible satellites constellation and their respective angular positions recorded in Ilmenau, Germany.

sv number	elevation (degree)	azimuth (degree)	sv number	elevation (degree)	azimuth (degree)
11	66	282	27	26	158
32	54	213	28	24	306
4	53	284	20	11	233
1	45	285	24	3	26
14	39	89	18	1	55

$$\bar{\Upsilon} = \begin{bmatrix} dp_1 & dq_1 & dr_1 & 1 \\ . & . & . & . \\ dp_k & dq_k & dr_k & 1 \end{bmatrix}, \tag{2.11}$$

where, $dp_k = \cos\theta_k \cdot \sin\phi_k$, $dq_k = \cos\theta_k \cdot \cos\phi_k$, and $dr_k = \sin\theta_k$. The $k = 4$, that is the number of satellites used for the calculation of the receiver's position. Now, the scalar GDOP is given by:

$$GDOP = \sqrt{\mathrm{tr}\{[\bar{\Upsilon}^{\mathrm{T}}\bar{\Upsilon}]^{-1}\}}. \tag{2.12}$$

Example: The visible satellite constellation recorded in Ilmenau, Germany at $03:30\,\mathrm{pm}$, on 23^{rd} October, 2014 is shown in Fig. 2.4. The satellite vehicle (SV) values along with their respective positions in elevation and azimuth are given in Table 2.2. First, assuming an antenna with narrow beamwidth, high-gain, and maximum radiation in zenith directions with masking angle of 30^o. The corresponding gain pattern of the antenna

is depicted in Fig. 2.5. Following these specifications, the antenna is capable of acquiring only five high- and medium-elevation satellites. Considering four of these satellites, high elevation, i.e. sv number 11, 32, 4, 1 for the positioning calculations. Then, the $GDOP$ using (2.12) is 107, which is significant. But, if all the lowest-elevation satellites are considered, then the $GDOP$ decreases to 18. On the other hand, if the antenna is designed with a wide beamwidth antenna and low-gain sufficient enough to acquire the satellites. This is depicted by the solid line in Fig. 2.5. This type of antenna is able to acquire all the visible satellites. For this type of antenna, the minimum possible $GDOP$ is reduced to 3.5 by choosing one satellite close to zenith and the remaining three from the lowest elevation. In fact, Parkinson in [34] has shown that with four satellites, one at the elevation angle 90^{o} and azimuth 0^{o}, and three at elevation angle of 5^{o} with equally spaced azimuth angles result in the minimum $GDOP$ of 1.73. This is the lowest limit, though, in general the $GDOP$ equals approximately 3.5, which is considered acceptable. One can conclude that the beam pattern or beamwidth of the antenna does affect the positioning accuracy, and it becomes preferable to have wider beamwidth in order to acquire both low- and high-elevation satellites to achieve the low $GDOP$. This also signifies the influence of the low-elevation satellites in the positioning accuracy.

Carrier-to-noise density ratio: The capability of the receiver to acquire and track the satellites depends on the CNR $\chi_o(\text{dB-Hz})$. This includes the noise contribution from the environment, antenna and the first-stage amplification. In the theoretical models developed in this work, the noise contribution of the receiver components after the first amplification stage FE are assumed to be negligible. The available carrier power depends on the realised gain of the antenna in the given direction and is interpreted as

$$C(\theta,\phi) = P_{\text{sat}}|F_{\text{RHCP}}(\theta,\phi)|^2 \qquad (\text{dBW}), \tag{2.13}$$

P_{sat}, which is the reference received satellite signal carrier power using an ideal isotropic RHCP radiator. The available received power from Galileo and GPS satellites on earth can be found in [4, p. 565]. The noise power spectral density ratio, referred to as the input of the first stage amplifier, typically a low-noise amplifier (LNA), can be derived using the system noise temperature T_{sys}, and is given by:

$$N_{\text{o}}^{\text{dB}} = 10\log(k_{\text{B}}T_{\text{sys}}) \qquad (\text{dBW/Hz}), \tag{2.14}$$

$$\text{where, } T_{\text{sys}} = T_{\text{A}} + T_{\text{LNA}} \qquad (\text{K}). \tag{2.15}$$

k_{B} is the Boltzmann constant, which is equal to 1.38×10^{-23} J/K. The antenna effective noise temperature T_{A}, in Kelvins (K), includes the contribution of the captured sky-noise and the ohmic and mismatching losses. This can be calculated using the radiated (2.6) and accepted power (2.9), which normalised to the P_{in} convert into the respective efficiencies, therefore

$$T_{\text{A}} = T_{\text{env}}\eta_{\text{rad}} + T_{\text{amb}}(\eta_{\text{acc}} - \eta_{\text{rad}}) \qquad (\text{K}). \tag{2.16}$$

Here, $\eta_{\text{rad}} = P_{\text{rad}}/P_{\text{in}}$ as $P_{\text{in}} = 1$ W. Above T_{env} represents the environmental temperature, which is a scalar quantity denoting the integration of the angular temperature function in the upper-hemisphere space. For simplification, it is assumed equal to 100 K with uniform distribution in the upper hemisphere. Following the assumption that the antenna and the analogue receiver are perfectly matched given $P_{\text{acc}} = P_{\text{in}}$ and $|\vec{\Gamma}|^2 = 0$. This leads to $\eta_{\text{acc}} = 1$ in (2.16).

Normally, the noise figure (NF) of the LNA can be obtained from the specification parameters of the amplifier. Therefore, the temperature of the LNA at the system reference temperature which is considered here to be the ambient temperature, and is given by:

$$T_{\text{LNA}} = (\text{NF} - 1)T_{\text{amb}}. \qquad (\text{K}) \tag{2.17}$$

The received χ_o of the satellite from a given direction can be obtained using (2.13) and (2.14)

$$\chi_o(\theta, \phi) = (C(\theta, \phi)/N_{\text{o}})^{\text{dB}}. \qquad (\text{dB-Hz}) \tag{2.18}$$

Therefore, higher the antenna gain and lower the system noise temperature better the CNR of the receiver. The higher CNR will ensure early acquisition of the satellite but maintaining higher gain in all upper-hemisphere is difficult to achieve as discussed in the last section, therefore a trade-off between CNR and maximum number of satellites acquisition is considered in the antenna design.

2.3.2 Polarisation

The transmitted GNSS satellite signals are RHCP because the circular polarisation is unaffected by the polarisation change in the ionosphere layer due to the Earth's magnetic field. Therefore, the receiving antenna needs to be designed and optimised for maximum reception in the RHCP. In reality, the RHCP antenna will always possess the content of left-hand circularly polarised (LHCP), the cross-polarisation. Nevertheless, the antenna design can be further optimised for minimum LHCP reception. It is important to minimise this in all directions, particularly above the masking angle in order to reject multipath reflections.

A figure-of-merit determining the purity of the RHCP is defined as the axial ratio. It can be expressed as

$$AR(\theta, \phi) = \frac{|F_{\text{RHCP}}(\theta, \phi)| + |F_{\text{LHCP}}(\theta, \phi)|}{|F_{\text{RHCP}}(\theta, \phi)| - |F_{\text{LHCP}}(\theta, \phi)|}. \tag{2.19}$$

In the case of a pure RHCP antenna with no LHCP, i.e. $F_{LHCP} = 0$, the $AR = 1$ or 0 dB. The discussion is limited to navigation receiver antennas only such that $AR = 0$ dB defines the best case, and $AR = \infty$ dB is the worst case.

Table 2.3: Minimum RHCP gain and maximum axial ratio standard for GNSS airborne antennas at L1 band [1].

elevation angle (degree)	minimum RHCP gain (dBi)	maximum axial ratio (dB)
>45	-2	3
15-45		6
10-15	-3	8
5-9*	-4.5	

* At horizon maximum allowed antenna RHCP gain is -2 dBi.

Sometimes, a term called cross-polarisation discrimination (XPD) is also used to define the circular-polarised antennas. This is defined by

$$XPD(\theta,\phi) = \frac{|F_{\text{RHCP}}(\theta,\phi)|}{|F_{\text{LHCP}}(\theta,\phi)|}. \tag{2.20}$$

Using (2.19) and ((2.20)), the axial ratio can also be expressed in terms of XPD,

$$AR(\theta,\phi) = \frac{XPD(\theta,\phi)+1}{XPD(\theta,\phi)-1}. \tag{2.21}$$

Generally, the navigation antenna polarisation performance is indicated by the axial ratio. This term will be applied to define the performance of the antenna. Based on the transmitting satellite and receiver antenna axial ratio, there is a polarisation mismatch loss according to [8]

$$L_{\text{PM}} = -10\log_{10}\left[\frac{1}{2}\left(1+\frac{4AR_{\text{s}}AR_{\text{r}}+(AR_{\text{s}}^2-1)(AR_{\text{s}}^2-1)\cos 2\Delta\theta}{(AR_{\text{s}}^2+1)(AR_{\text{s}}^2+1)}\right)\right]. \quad (\text{dB}) \tag{2.22}$$

The minimum requirements for a satellite antenna axial ratio $AR_{\text{s}} = 1.8$ dB [132, p. 19]. If the receiver antenna axial ratio is $AR_{\text{r}} = 3$ dB, and with relative tilt angle between the major axes of the polarisation ellipses of the satellite and the receiver antenna $\Delta\theta = 0^{\text{o}}$, the polarisation mismatch loss using (2.22) is 0.02 dB, whereas for $AR_{\text{r}} = 6$ dB it increases to 0.2 dB. The minimum loss occurs when the $AR_{\text{r}} = AR_{\text{s}}$. In case of the perfect linear polarised receiver antenna, $AR_{\text{r}} = \infty$. Therefore, if the satellite antenna is perfectly RHCP, then one can expect a polarisation mismatch loss of at least 3 dB, which is not acceptable. This may also occur for RHCP patch antennas when the satellite signal impinges on the low elevation, and the received polarisation becomes linear because of the diminished horizontal component of the radiated field due to the presence of the perfect conducting ground-plane.

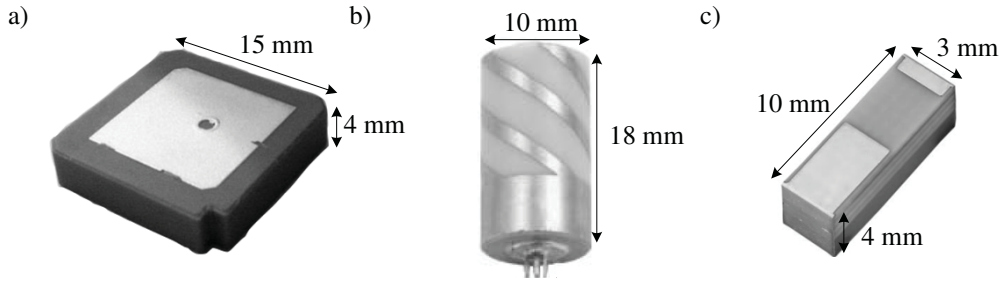

Figure 2.6: Different single-element GNSS antenna types used in commercial navigation devices [1]. (a) High permittivity truncated square patch antenna. (b) Dielectric loaded quadrafilar helix antenna. (c) Surface mount microstrip technology based loop antenna.

2.3.3 Phase centre

The phase centre in terms of the IEEE standards is defined for an antenna as the location of the point with respect to the antenna, which, taken as the centre of a radiation sphere, provides a constant phase either over the entire surface or at least over the portion of the surface with significant radiation [140]. However, in reality the measured phase over the radiating surface will have variations called phase centre variations. These variations may occur over a range of angles and frequencies. Similarly, the phase centre where all the wanted signal is collected may not collide with the actual antenna reference point, for example the physical centre of the antenna, but may depend on the type or design of the antenna as well. This offset of the phase centre from the antenna reference point is called the phase centre offset. This parameter is typically mentioned in the data-sheets or manuals of the commercial antennas to improve receiver positioning accuracy calculation. In this work, it is assumed that the absolute phase centre of the radiation is the physical centre of the antenna array. Further descriptions and effects of phase centre variations on the GPS measurements can be found in [35], [104].

2.3.4 Commercial GNSS antennas

The requirements of the RHCP antenna types for the receiver and satellite are different. The satellite antennas need to be high-gain directional antennas. The receiver antennas, depending on the user requirements, vary from fixed-radiation pattern antennas (FRPA) to control-radiation pattern antennas (CRPA). In the case of the FRPA, its ideal orientation is omni-directional in the upper-hemisphere with a sharp masking angle in order to cover maximum satellite reception. The limitation of this angle varies depending on the type of application. The antennas comprising both acceptable gain in the upper-hemisphere and lower axial ratio are generally difficult to design along with large ground-plane structures.

Microstrip antenna The most popular and widely used antenna in GNSS receivers is

the microstrip antenna, typically the *patch antenna*. The patch antennas are superior because of their low profile, compact size, light weight, ability to conform to their shape and low manufacturing cost. The integration of these antennas with the circuitry of the receiver is easy. The amount of radiation can be reduced significantly using ceramic substrates that offer high dielectric constants, i.e. greater than 40, with high-quality factors.

Typical values associated with these antennas are 60^{o} 3–dB beamwidth, which makes them excellent candidates for use as receivers. The impedance matching bandwidth is normally 2–4%. This can be enhanced by increasing the height of the substrate, which has a high dielectric constant. However, increased thickness leads to the propagation of surface waves that need to be considered to optimise the antenna properties. This may lead to reduced gain at high elevation instead of higher gain at low elevation.

Quadrifilar helix antenna (QHA) This is designed using an array of four helically shaped antennas wrapped around a cylinder. This produces a broad 3–dB beamwidth, i.e. 120^{o}, for the upper-hemisphere with low axial ratio. The cylinder can be made of dielectric material to reduce the size and cost of the antenna. This type of antenna is especially suitable for use in mobile devices. It is also a narrow-band antenna, but is not affected by the common mode noise in the ground-plane. In addition, the axial ratio is not altered by the ground-plane dimensions in the main-lobe direction, in contrast to patch antennas.

Loop antenna Hand-held devices like mobiles, personal digital assistants, etc. have stringent space and cost requirements. Also, the antenna pattern needs to accommodate different orientations of the device. This leads to inexpensive wire antenna designs that are currently employed in commercial devices, e.g. loop antenna. These antennas are linearly polarised, which precipitates a loss of at least 3 dB for the incoming satellite signals. However, it has been shown that in urban environments with dominant multipath, a linearly polarised antenna performs equally well as compared to a RHCP antenna [105]. The mounting on the edge of the device printed circuit board with surrounded ground-plane from three sides gives better flexibility. The antenna efficiency is 40–50% with a linear polarised realised gain up to 2 dBi. This type is not suitable, due to the high reception level of multipath, for the advanced robust navigation receivers where major concern is high positioning accuracy and integrity.

2.4 Robustness requirements and challenging environments

In conjunction with precision and accuracy of the navigation receivers, it is also desirable to provide robustness and reliability in challenging or harsh environments. These environments may be limited by interference, multipath, and atmospheric effects.

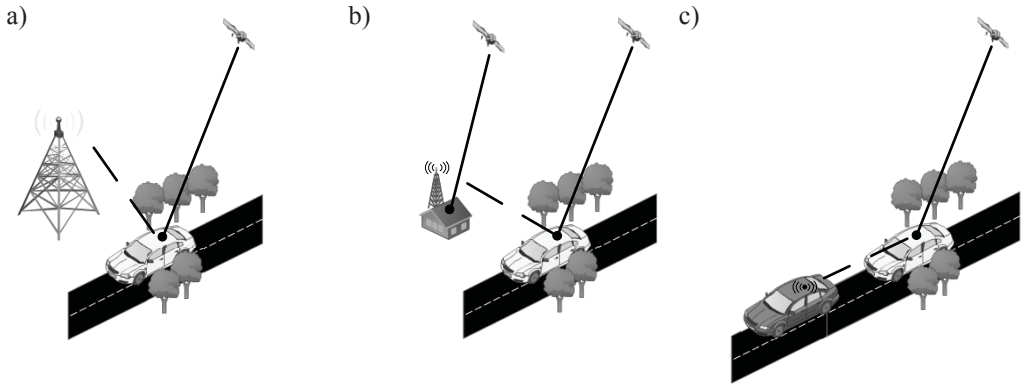

Figure 2.7: Interference scenarios for the GNSS antenna mounted on the roof-top of a car. (a) Intra communication system out-of-band interference, (b) GNSS repeater spoofing, and (c) in-car jammers or PPDs.

2.4.1 Interference

The first type of impairment that can degrade GNSS performance is the *interference*. This may result in degraded navigation accuracy or sometimes complete loss of positioning estimation. Any undesired radio frequency source that is received by the GNSS receiver is classified as interference. These can be divided into two main types: in-band, and out-of-band interference. Normally, out-of-band interference is categorised as unintentional, e.g. radio emissions from the licensed RF systems in the vicinity of the GNSS spectrum like GSM-1800. This type of interference is typically suppressed through selective filtering in the receiver analogue front end, which in modern receiver architectures, is prevalent [97].

On the contrary, in-band interference is mostly considered intentional with an aim to disrupt the GNSS receiver and completely block the positioning information, or to produce false position. The two classes of such types of interference are *jamming* and *spoofing*. By jamming, high-power radio frequencies are transmitted to block the weak GNSS signals. In spoofing, an artificial satellite signal resembling the set of normal GNSS signals is broadcast to deceive the receiver with false position.

The theoretical framework for the effect of interference on the receiver estimation of the CNR for GPS acquisition and tracking algorithm is thoroughly presented in [106], [107]. This work is extended for the estimation of the CNR for the Galileo signals in the doctoral dissertation of Balei [91]. In summary, the estimations of the CNR after the correlation stages are more accurate and reliable, since the spectral shape of the interference inside the bandwidth of the front end has no effect. Galileo E1 signal is more robust to CW interferers at the centre frequency, whereas GPS delivers better robustness against CW interferers that are away from the centre frequency. For a single antenna element, the effective directional CNR influenced by the carrier tracking, demodulation and acquisition

can be expressed according to [106, Equation 5] as:

$$\chi(\theta,\phi) = \frac{C(\theta,\phi)h_s}{N_o h_s + C_{\mathrm{J}}(\theta_J,\phi_J)h_c}$$
$$\text{where} \quad h_s = \int_{-B_s/2}^{B_s/2} H_s(f)\mathrm{d}f, \qquad h_c = \int_{-B_s/2}^{B_s/2} H_s(f)H_J(f)\mathrm{d}f. \tag{2.23}$$

H_s is defined as the power spectral density normalised to unit area over infinite limits, and $C(\theta,\phi)$ is given according to (2.13). It is assumed that FE bandwidth is wide enough to contain all signal power, which leads to $h_s = 1$. h_c is the spectral correlation coefficient. The received jammer signal is $C_{\mathrm{J}}(\theta_J,\phi_J) = P_{\mathrm{J}} \cdot |F(\theta_J,\phi_J)|^2$, where P_{J} is the jammer power, in dBW, received by an ideal isotropic antenna. Consider the case of a narrow band jammer at the centre of the signal band with bandwidth much smaller than signal bandwidth such as $B_J << B_s$. Therefore, the signal is constant over the jammer band, which means h_c is a constant depending on the function of the $H_s(f)$ or the power spectral density function of the signal, with interferer band directly centred at the signal band $h_c = H_s(0)$. For GPS signals having a conventional binary phase shift keying (BPSK) modulation with code period of t_c, power spectral density function is given by:

$$\begin{aligned} & H_s(f) = t_c \operatorname{sinc}^2(\pi f t_c), \\ \text{with} \quad & H_s(0) = t_c. \end{aligned} \tag{2.24}$$

Example: Consider a C/A-code GPS receiver with thermal noise power spectral density $N_{\mathrm{o}} = -204\ \mathrm{dBW/Hz}$ and received satellite signal power of $C_{\mathrm{sat}} = -161\ \mathrm{dBW}$ with antenna realised gain in the direction of the signal $3\ \mathrm{dBi}$. Therefore, the carrier-to-noise density ratio $\chi_{\mathrm{o}} = 46\ \mathrm{dB\text{-}Hz}$ without interference while ignoring the implementation losses within the receiver. The receiver bandwidth is considered to be $4\ \mathrm{MHz}$. The interferer signal impinges on the low elevation with antenna-realised gain of $-3\ \mathrm{dBi}$ in its direction and bandwidth of $4\ \mathrm{kHz}$. The numerically estimated effective CNR is shown in Fig. 2.8, which gives an insight into the CNR degradation due to a single jammer. The CNR drops to $38\ \mathrm{dB\text{-}Hz}$ with jammer-to-signal ratio (JSR) of $20\ \mathrm{dB}$. In comparison to the C/A-codes, P-codes used by military exhibit $10\ \mathrm{dB}$ better robustness in the case of the narrow band interferer.

The signal characteristics of civil GPS jammers have been described in [108]. These jammers range from high-power continuous wave (CW) signals to chirp signals where the CW frequency is incorporated within the signal bandwidth over time. Previously, the jamming was employed by the military only, but recent advancement of the cheap, though illegal, personal privacy devices (PPD) have posed a serious jamming threat to the public

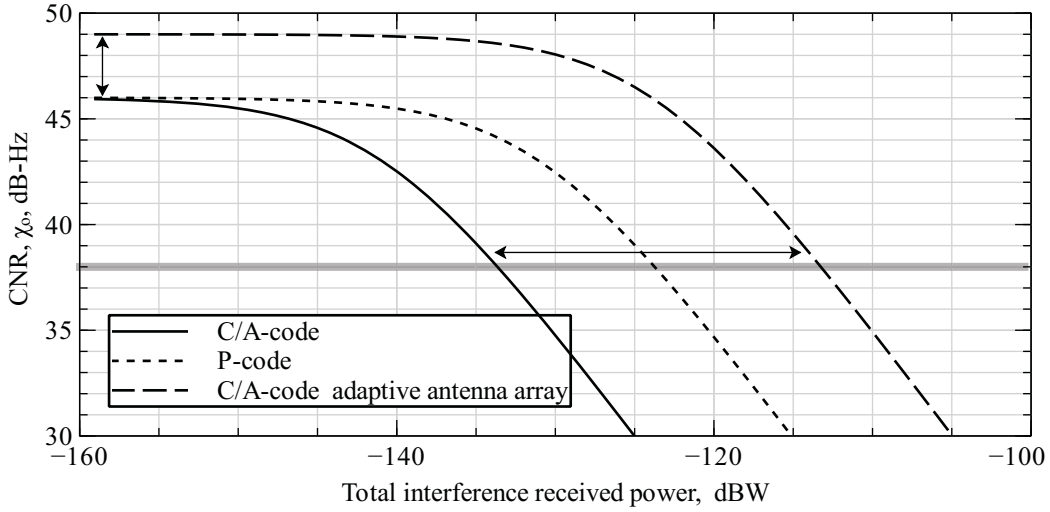

Figure 2.8: Numerical effective CNR for single narrow band interferer with wide FE bandwidth, i.e. 4 MHz. The grey line indicates, $\chi_o = 38$ dB-Hz, the typical threshold of the navigation receiver to acquire the satellite signal without integration [7].

use of GNSS systems [109]. The potential threats of these jammers have been discussed in [21]. An experimental survey of the commercially available GNSS receiver operation in the presence of these PPDs has been carried out in [98]. The result shows that with a JSR of 25 dB only, the PVT solution is lost for more than 90% of the time, and in the case of a solution, the positioning error accuracy is increased by 100–200 m in range, clearly sabotaging the SoL applications.

2.4.2 Multipath

As mentioned earlier, the GNSS signals can be reflected by buildings, walls, vehicles, and the ground. Therefore, the reflected signals will combine constructively or destructively with the received direct line-of-sight signal. This phenomenon is called *multipath*. A typical scenario for multipath is shown in Fig. 2.9. This has a detrimental effect on the code correlation peak estimation, which results in false satellite code phase estimations. In this case, the constructive reflection phase leads to positive ranging estimates, while negative ranging estimates for the destructive reflection. The strength and path delay of the reflections determine the magnitude of the code tracking or phase error. The maximum pseudo-range error due to multipath can be up to half of the code chip, i.e. 150 m for C/A-codes [20]. In the case of the non-line-of-sight criteria with no visible sky, like in urban areas with tall skyscrapers, the presence of multipath signals have a severe effect on the positioning and tracking algorithms. The multipath signal is mostly LHCP or ar-

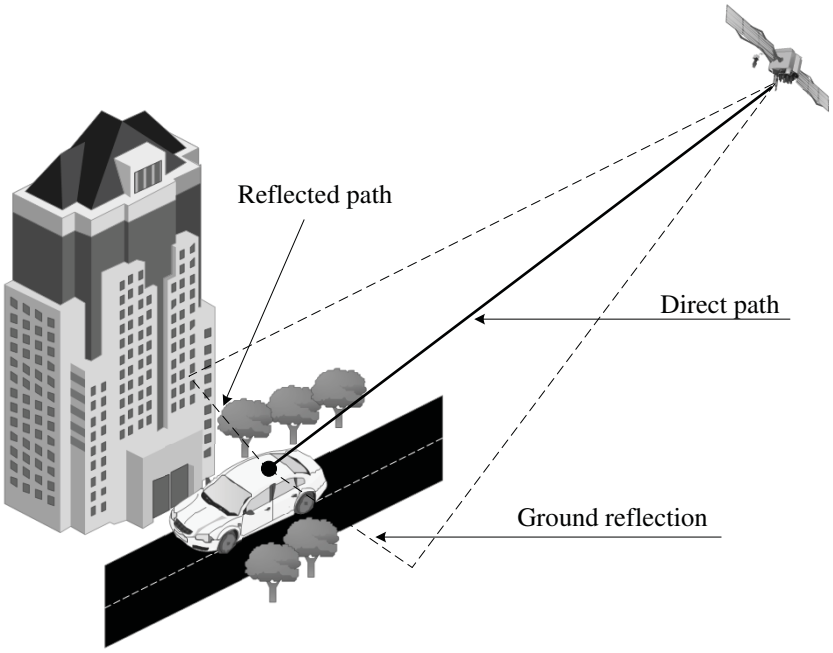

Figure 2.9: Multipath scenario for a satellite signal in an urban environment.

bitrarily polarised. On the contrary, the realistic GNSS receiver antenna is purely RHCP in the high-elevation angles, whereas at low elevation the RHCP and LHCP receptions are comparable. Therefore, the multipath impinging from high elevation angles does not affect much the code-tracking algorithms. However, the low-elevation multipath from the ground or sea may undermine the receiver performance and need to be mitigated by masking using antenna design [141] or digitally by choosing only medium- and high-elevation satellites for positioning calculations.

2.4.3 Atmospheric effects

The GNSS signal traverses and interacts with Earth's atmosphere during propagation before being captured by the receiver. In terms of GNSS applications, the Earth's atmosphere can be divided into two major portions: troposphere and ionosphere. The troposphere region is the closest of the two ranging from 0 to $20\ \mathrm{km}$ in the direction of space. It consists of all the meteorological phenomena like clouds and precipitation. The ionosphere is ionised by the incident solar radiation, which creates a small fraction of positively charged ions and free electrons. The density of the free electrons fluctuates with the distance from Earth and the time of day. Further details about the variations of the ionospheric layer can be found in [36].

The primary influence of the atmospheric layers on the electromagnetic signal propa-

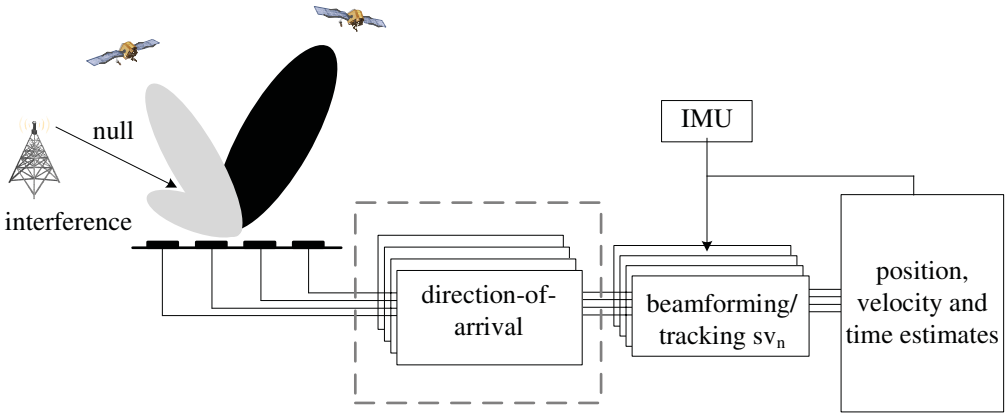

Figure 2.10: Multi-antenna receiver architecture with independent adaptive beamforming, and DOA estimation for each satellite while suppressing the interference. IMU stands for the inertial measurement unit, which may provide the attitude estimations.

gation is the atmospheric refraction. This propagation also affects the amplitude and the phase of the signal depending on its frequency. In case of the GNSS signal, this is applicable and for the troposphere can be from 2 to 10 meters, while in the ionosphere it is more severe, ranging from $10\ \mathrm{m}$ up to complete loss of the signal. Over the years, several techniques using dual-band receivers have been used to nullify the atmospheric effects in critical applications, e.g. surveying, mining, and mobile robots.

In October, 2003 the electromagnetic storm in the Earth's atmosphere during the 23^{rd} solar cycle severely disturbed the ionospheric region causing a large-scale navigation signal blackout in Sweden [37]. Even in the case of the dual-band receiver errors up to few centimetres were reported, causing severe disruption to crucial applications mentioned earlier.

2.5 Multiple-antenna based GNSS receivers

Recently, multiple-antenna based navigation receivers have received significant attention in the research community. A multiple element receiver can be classified into FRPA or a CRPA. FRPA in this case mainly serves as the high-directional antenna, it's easy to implement and integrate into the existing receiver but has limited benefits against the degradation of the signal due to the multipath, interference and atmospheric effects. However, the CRPA provides the adaptation capability to align the maximum antenna radiation in the desired direction of the satellite or the signal-of-interest while minimising the radiation in the unwanted signal direction. This provides the capability for monitoring, investigating and counteracting the malefactors due to the earlier mentioned challenges to the navigation receivers. A block diagram of the multi-antenna adaptive navigation receiver architecture

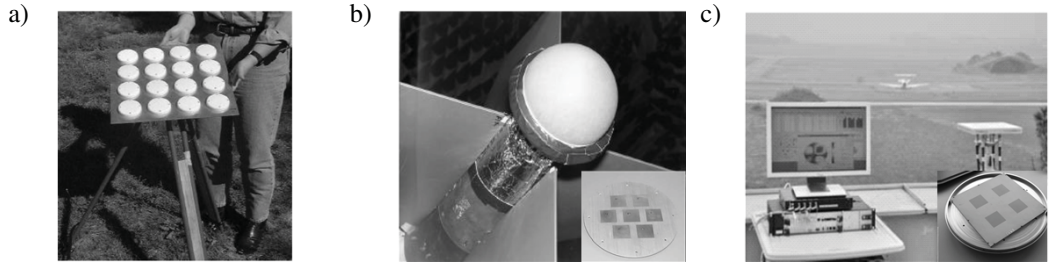

Figure 2.11: Different multiple-antenna based GNSS systems. NavSYS HAGR GNSS sydtem using (a) 16-element antenna array, (b) seven-element antenna array, (c) DLR GALANT four-element GNSS system.

is sketched in Fig. 2.10. This allows for the maximum gain in the direction of the satellite and a buffer for the interference to increase the CINR ratio.

In 1999, NAVSYS presented test results using multiple-antenna with digital beamsteering for GPS receivers. The digital beamforming is performed adaptively, and in parallel, for each visible satellite. The complete system is called a high-gain advanced GPS receiver [110]–[112]. In the beginning, these antenna arrays consisted of 7-, 16- and 100-element antenna arrays. It is shown that the use of antenna arrays provided a gain from 10 to 20 dB in the direction of desired satellites, which is responsible for improving the CNR and position measurement accuracy. In [113], [114], similar arrays are used to investigate and mitigate the effect of multipath on the receiver. The 7-element antenna array had a footprint of 18 cm with an inter-element separation of $d = \lambda/2$, where λ is the free-space wavelength, which is for the L1-band approximately 10 cm. The main motivation behind the construction of such receivers at that time was to support the anti-jamming capability of the receivers employed by military aircrafts and vehicles. Therefore, the size of the antenna array was not restricted.

The institute of communication and navigation centre at German aerospace centre (DLR/IKN) in [22], [100], [38] presented a GNSS multi-element receiver targeting the SoL public applications including surveying, aviation, maritime, and civilian users. It provides the capability of direction-of-arrival (DOA) estimation, giving altitude information, beamforming with interference and multipath mitigation. This is a robust solution against the challenges encountered by the integrity and accuracy of the GNSS receiver. The antenna array consisted of four elements in a square arrangement with a footprint of approximately 30 cm.

Several dissertations have been written on the adaptive array processing of the multiple-antenna GNSS receiver in the past decade. In [89] software-based implementation techniques of adaptive array receivers for interference rejection are presented. [92]along with array-processing techniques has discussed several calibration techniques to improve the performance of such receivers. Also, work regarding the array processing

algorithm implementation for multipath mitigation has been discussed in [88].

The entire antenna arrays employed in the above-mentioned work, which are related to the development of a multi-element GNSS receiver, included the inter-element separation of half of the free-space wavelength. The major merit of this is obviously the minimum mutual coupling between the elements. In the L-band, this separation is significantly large, e.g. at L1 is $10\ \mathrm{cm}$. This dimension is large as compared to previously mentioned single element base navigation receivers currently used in the market. In contrast to the military, the public communication devices integrated with navigation receivers have strong restrictions on the size requirements, which make use of multi-element antenna-based navigation receivers an unattractive solution. Therefore, it is important to reduce the inter-element separation in order to decrease the overall dimensions of the antenna array generating the possibility of its integration into the modern commercial navigation receivers. This will surely provide the robustness, integrity, and accuracy of measurements that are critical to modern SoL applications.

Compact antenna arrays have recently received significant attention in the literature [102], [103], [39]–[43]. This offers the reduced inter-element separation solution and miniaturisation of the antenna array size. However, it experiences inherent mutual coupling, which degrades the radiation performance of the antenna array considerably. Several approaches have been investigated and implemented to mitigate the effects of mutual coupling [28], [29], [44]–[46]. This is somewhat similar to restoration of the radiation properties of the compact antenna arrays, though it is not possible to achieve miniaturisation and performance equivalent to a conventional antenna array having $d = \lambda/2$. Most of these compact antenna arrays have been designed and targeted for mobile communication applications. Therefore, it is important to characterise and devise a general strategy to optimise and design a compact *navigation* antenna array. This will be the focus of the following chapters.

2.6 Summary

The review of the basic principles of the GNSS technology is presented for a better understanding of its applications, which is primarily positioning. Moreover, the characteristics of the satellite signals are discussed, particularly C/A-codes.

The main GNSS receiver components include antenna, FE and the baseband signal processing. The antenna is the pivotal block in the receiver chain and its properties greatly influence the performance of the receiver. A low-gain antenna with minimum requirement of $-2\ \mathrm{dBi}$ along with $3\ \mathrm{dB}$ beamwidth requirement of greater than 120^{o} and sharp cut-off for a masking angle of 5^{o} are typical for GNSS receiver antennas. These gain requirements along with low masking angle designed to suppress the ground reflections are difficult to achieve. The most common type of antenna fulfilling these criterion is the microstrip

patch antenna. This provides moderate gain in the upper hemisphere with low masking angle. However, it does suffer from high cross-polarisation content in the lower elevation, which makes the receiver vulnerable against multipath. On the other hand, the quadrafilar helix antenna provides low cross-polarisation, but doesn't provide masking angle at the horizon for suppressing ground reflections and also has a non-planar structure, which may not be attractive for certain commercial communication devices. Therefore, it is critical to consider the intended receiver implementation while designing and choosing the type of antenna.

The challenges and vulnerabilities to existing GNSS receivers include multipath, atmospheric effects, and interference. The multipath and atmospheric effects degrade the accuracy and integrity of the positioning, but these challenges have been thoroughly addressed in the last decade by upgrading the satellite and receiver with new signals that need to be considered at the receiver as well, an example of which is dual-band standalone GNSS receivers with L1 and L2C capability to correct for the ionospheric effects, which improve the accuracy to the level of centimetres. The interference can be intentional such as jamming and spoofing or unintentional, which is generally referred to as transmissions in the vicinity of the GNSS bands by other communication system. The in-Car or PPD jammers have emerged as greater threats to the SoL applications like aviation and maritime. Moreover, the malicious blocking of GNSS for strategic and privacy reasons is ever present. With the advancement of autonomous transport systems, spoofing, which confuses the GNSS receiver with fake satellites and false position solutions, become inevitable and needs to be addressed by modern receivers.

The multi-element antenna GNSS receivers, with the aid of advanced adaptive beamforming and nulling, provide an advanced solution to the challenges mentioned above, though conventional inter-element spacing of half of the free-space wavelength, is unsuitable for miniaturised communication devices. This inter-element spacing is favoured because it gives minimal mutual coupling, which degrades the radiation performance of the antenna array. This hinders the miniaturisation of the overall GNSS receiver and presents challenging tasks for reducing the inter-element separation while mitigating the mutual coupling effects. Therefore, it is important to characterise the mutual coupling effects on the performance of the GNSS antenna array. The design parameters for evaluating the compact antenna arrays with requirements of the GNSS need to be investigated, which is the motivation of the next chapter.

Chapter 3

Evaluation Methodologies of Compact Planar Antenna Arrays

Antenna arrays have become viable components of communication systems because of their capability to meet modern standards of robustness, integrity, quality and reliability for public use. This integration has been further facilitated by advancements in the digital signal processing techniques, which are simpler to implement and at the same time provide faster computations. Moreover, miniaturisation of analogue integrated circuitry has made it possible to integrate such systems into space-limited communication devices. One commercial success story is the implementation of the multiple-input-multiple-output (MIMO) in mobile communication systems such as long-term evolution (LTE) [47].

However, overall antenna array size in these modern miniaturised receivers has been mostly limited to the separation between neighbouring elements equal to $d = \lambda/2$, thus limiting the overall compactness of the system [48]. In the case of the L-band in particular where $\lambda \approx 20$ cm, this significant separation among elements becomes a limiting factor for designing a compact array. A widespread application in L-band is the GNSS, where multi-element antenna arrays are becoming attractive for accurate and robust reception of the navigation signal in the presence of interferers. As a result, in addition to compactness, this application demands efficient arrays with maximal diversity capability or all degrees-of-freedom to be equally efficient and low-noise receivers.

Compact arrays with an inter-element separation $d < \lambda/2$ suffer from mutual coupling [24], [25] and, hence, degrade overall system performance. Digital beamforming at the baseband could mitigate the effects of coupling for a compact array to some extent, though at the expense of reduced dynamic range or radiative diversity degrees-of-freedom [27], [102]. Recently, techniques for reducing coupling have been reported, using DMN [90] involving eigenmode excitation, or defected ground structures (DGS) as an electromagnetic band-gap (EBG) configuration in printed antennas [115]. In conjunction with addressing coupling reduction between elements, it is necessary to optimise the array design with re-

spect to its diversity degrees-of-freedom. Several methods involving, e.g. an analysis of the super-directivity sensitivity factor, mutual impedance, or active reflection coefficient have been identified [3], [9], [49], but lack complete scalable performance characterisation. In [43], [90], an approach is introduced that utilises eigenmode radiation efficiencies to analyse the performance of a compact array

In order to evaluate an antenna array, the first step is to model and analyse the parameters that encompass the effects of power dissipated, i.e. lost within the antenna, and reflected due to impedance mismatch, along with power radiated in the presence of coupling between neighbouring elements. Power dissipation within the antenna is mainly due to the losses in the dielectric substrate materials and to the finite conductivity of metal surfaces. Therefore, their practical characterisation in performance analysis is necessary, especially in the case of printed antennas. Compact arrays inherit a finite real part of mutual impedance Z_{ij}, which results in feed impedance for individual radiators different from their self-impedance for beamforming, giving rise to reflection losses. All of these effects negatively affect the total efficiency of the antenna.

This chapter begins with the basic introduction of the mutual coupling in the compact planar antenna arrays. This is followed by the eigen-analysis of the computed covariance matrix, using measured realised gain amplitude embedded patterns, to obtain a figure-of-merit for general compact antenna array optimisation. Next, the relationship and effects of the eigenvalues on the diversity degrees-of-freedom in terms of diversity gain and loss are presented. Then, the different compact planar antenna arrays of the ceramic truncated square patch are simulated and fabricated to identify an optimum configuration for the construction of the compact navigation receiver in later chapters. In the end, insight into the polarisation impurity and the direction-finding capabilities of the compact antenna arrays are investigated.

3.1 Mutual coupling

The electromagnetic interaction and energy interchange between antenna elements in the antenna array is a phenomenon called *mutual coupling*. In the case of compact antenna arrays, the disparity in size between the smaller inter-element separation compared to half of the free-space wavelength is significant. Before going into the quantitative analysis of the mutual coupling, an intuitive explanation or examination is discussed to understand mutual coupling. In Fig. 3.1, the transmit and receive cases for a typical two-element antenna array are shown.

Mutual coupling in transmit case is depicted in Fig 3.1a with antennas 1 and 2 connected with generators. If the generator for antenna 1 is turned on, a forward wave a_1 will travel in the direction of the antenna. A portion of it will be reflected in the originating backward wave b_1. In the case of the complex conjugate match between the antenna and

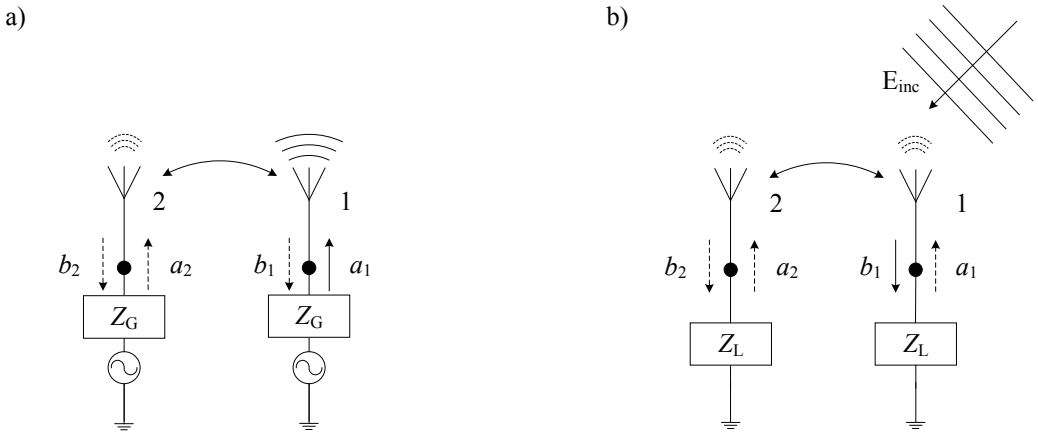

Figure 3.1: Mutual coupling electromagnetic wave path flow (a) from antenna "1" to antenna "2" when in transmitting mode and (b) from antenna "1" to antenna "2" when in receiving mode at reference terminating impedance Z_{L}.

the generator, maximum power travels to the antenna and is eventually radiated. However, due to the presence of mutual coupling, some of the radiating energy is coupled into the nearby antenna element, causing a current flow in the antenna, some of which is re-radiated; the rest flows towards the generator b_2, which is reflected depending on the impedance of the generator and its excitation. This re-scattered energy is again re-radiated into free space and some is coupled again to antenna 1 and so forth. The re-scattered waves will alter the amplitude and phase of the outward waves from the generators. Therefore, the resultant radiated energy is a superposition of the radiated and re-scattered fields. This means the far-field pattern of the transmitting coupled antenna array is not only dependent on individual excitations of the elements, but also on the coupled parasitic excitations that originate due to mutual coupling. The amount of mutual coupling in this case depends on the following:

1. Excitation of the antenna elements;
2. Input impedance of the generators;
3. Radiation characteristics of the individual antenna elements;
4. Geometrical configuration of the antenna array;
5. Inter-element separation d in terms of wavelengths.

Mutual coupling in receive case is depicted in Fig. 3.1b with antennas 1 and 2 connected to the termination loads Z_{L}. The incident plane wave from the far zone $\mathrm{E_{inc}}$ is received by antenna 1, given as b_1. Some of it is reflected depending on the mismatch

a_1 that is radiated into the free space. Some of the radiated energy is coupled into the nearby antenna element 2, which appears as b_2. This incoming wave may be reflected, and if so, it is then re-radiated and coupled again, and so forth. The energy received by the individual antenna element is the superposition of the incident or direct wave, and the re-scattered waves coupled parasitically from the neighbouring elements. The amount of mutual coupling in this case depends on the following:

1. Direction of the incident plane wave.
2. Termination impedance or load impedance Z_{L}.
3. Receiving properties of the individual antennas.
4. Geometrical configuration of the antenna array.
5. Inter-element separation d.

3.1.1 Mutual impedance

The mutual coupling effect in its simplest and fundamental form can be characterised quantitatively using the mutual impedance originating between the elements of the antenna array. As the voltage and current relationship of the N element antenna array, the circuit according to [25], [3, Chapter 8] can be written as follows:

$$\vec{v}_{\mathrm{a}} = \bar{Z}\vec{i}_{\mathrm{a}} \tag{3.1}$$

Here, $\vec{v}_{\mathrm{a}} = [v_1, v_2, ..., v_N]^T$ and $\vec{i}_{\mathrm{a}} = [i_1, i_2, ..., i_N]$ represent the excited voltage sources and the terminal currents on the antenna elements, respectively. The $\bar{Z}$ is the impedance matrix of the antenna array describing the self and mutual impedance

$$\bar{Z} = \begin{bmatrix} Z_{11} & Z_{12} & . & . & Z_{1N} \\ Z_{21} & Z_{22} & . & . & . \\ . & . & . & . & . \\ . & . & . & . & . \\ Z_{N1} & . & . & . & Z_{NN} \end{bmatrix}.$$

The diagonal elements Z_{nn} of the $\bar{Z}$ donate the self-impedance of the n^{th} antenna element, whereas the non-diagonal elements Z_{nk}, are the mutual impedance between the n^{th} and the k^{th} element of the antenna array.

In the absence of mutual coupling, the non-diagonal elements of the antenna array matrix are zero. Therefore, the *driving point or feed impedance* of the individual antenna element is equal to the self-impedance of each element. The driving point impedance of the n^{th} antenna element is defined by the following:

$$Z_{nd} = \frac{v_n}{i_n} = Z_{nn} + \sum_{k=1 \mid k \neq n}^{N} Z_{nk} \frac{i_k}{i_n}. \tag{3.2}$$

The presence of mutual coupling leads to a finite value of the mutual impedance. The measurement of this mutual impedance for the planar antenna arrays is given by [116]. By definition, the conventional mutual impedance is the ratio of the induced open-circuit voltage of one antenna to the exciting terminal current of the other antenna as described above. However, Hui et. al [50], [51] have shown that this conventional definition of mutual impedance cannot accurately measure the mutual coupling effect, due to its deficiency to take into account the direction information of the receiving signals, because of the requirement one of the antenna elements in the transmitting mode whereas in a receiving array, all antenna elements are in the receiving mode, being illuminated by external source(s). Hui in [23] also introduced a new method for the measurement of the improved mutual impedance which is difficult and not easily scalable for larger arrays to measure because it involves the measurement of scattering parameters of the antenna array with and without(removed) neighbouring elements. This inadequacy in the measurements of mutual impedance matrix inhibits its generalisation as the figure-of-merit for compact antenna arrays.

3.1.2 Consequence of the mutual coupling

The effect of the strength of mutual coupling on the performance of the antenna array depends mainly on (1) the design of the single antenna elements, (2) the relative distance and placement of the elements, and (3) the required beam scan volume and the number of beams. The mutual coupling distorts the antenna array far-field pattern and introduces impedance variations [24], [25]. The mutual coupling also has detrimental effects on the polarisation properties of the individual array elements as well, which will be discussed in the latter part of this chapter.

Another demerit of mutual coupling is due to the feed impedance variation for different excitations known as the *active reflection coefficients*. This makes it practically impossible to match the antenna array elements independently for the entire range of excitations or incident wave direction of arrivals. For the transmitter, this may lead to the modification of transmission transfer characteristics.

3.1.3 Surface waves in planar antennas

In addition to the radiated free space wave coupling, the microstrip antennas have the inherent capacity for excitation or launch of the surface wave modes as illustrated in Fig. 3.2. The power trapped in the surface waves is eventually lost or result in energy storage, in

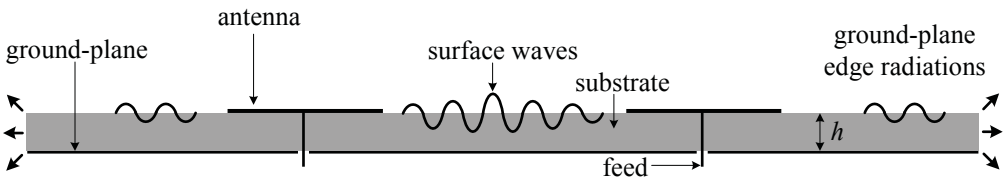

Figure 3.2: Illustration of the surface waves and the unwanted ground-plane edge radiations in planar antenna arrays.

the case of infinite substrate, and therefore degrades the radiation efficiency and bandwidth of the antenna [52]. In reality, infinite substrates normally have finite size, which in turn causes the diffraction of the surface waves at the edges of the ground-plane. These diffractions distort the radiation pattern of the antenna and do not contribute to the desired direction. In other ways, these propagations from the ground-plane edges are uncontrollable from the perspective of the feed point excitation characteristics. These radiations may help in the acquisition of low-orbit navigation satellites, but at the same time the vulnerability of the antenna towards multipath and ground reflections is higher. Furthermore, these surface waves will enhance the mutual coupling between antenna array elements, since the surface wave fields decay more slowly with radial distance than the free space wave fields. Due to these reasons, the surface waves are undesirable, and require special consideration in the design to minimise and diminish their effects. For the antenna arrays, the launch of the surface waves will make the beamforming of the antenna radiation difficult and result in distorted patterns, which negatively impinge on the operation of such antenna types.

There are two types of surface waves in microstrip antennas: (1) the transverse magnetic (TM) mode and (2) the transverse electric (TE) modes [2, Section 4.2]. The TE modes launch surface waves with electric fields parallel to the surface, whereas the magnetic field loops extend vertically out of the surface of the substrate, and vice versa for the TM mode [53]. The launch of these unwanted surface modes depends on the relative permittivity ϵ_{r}, the relative permeability μ_{r} and the thickness h of the dielectric substrate. The cut-off frequencies for the different surface wave modes are [54, Equation 4.2]

$$f_{\mathrm{sur}}^{c} = \frac{mc}{4h\sqrt{\epsilon_{\mathrm{r}}\mu_{\mathrm{r}} - 1}}, \tag{3.3}$$

where $m = 1, 3, 5, ...$ for the TE modes, and $m = 0, 2, 4, ...$ for the TM modes. This means that the surface waves will occur on all microstrip antennas because the lowest surface wave mode TM_0 has a cut-off frequency equal to DC.

In order to minimize the power launched into the surface wave modes the thickness and the ϵ_{r} can be decreased, assuming that the $\mu_{\mathrm{r}} = 1$. However, this will result in reduced the radiation efficiency and the matching bandwidth of the antenna array. If a microstip

patch antenna is designed for the L1/E1 band frequencies, using a dielectric substrate with $\epsilon_{\mathrm{r}} = 45$ then $h \leq 7\ \mathrm{mm}$ in order to minimise the energy being coupled into the surface waves.

3.2 Antenna array spatial covariance matrix

The covariance matrix depicts the information regarding the radiation or reception and exchange of the power individually and in-between respectively of the antenna array elements. This serves as a crucial parameter in determining the performance of the antenna array characteristics like CNR, eigenvectors and eigenvalues, diversity, etc.

3.2.1 Generalisation to multi-port antennas

An extension of the reflection coefficient of single-port antennas discussed in the last chapter of the multi-port antenna is *scattering parameters.* Generally, these parameters play a significant role in the characterisation of microwave circuits. For further details regarding scattering parameters, the reader should consult [10]. If the antenna array incident power waves or the excitation vectors are given by a complex column vector $\vec{a} = [a_1, ...a_{n-1}, a_n]^{\mathrm{T}}$, where n denotes the element or the port of the antenna array, then the

$$P_{\mathrm{in}} = \vec{a}^{\mathrm{H}}\vec{a} = \sum_{n=1}^{N} |a_n|^2 = 1. \tag{3.4}$$

The N represents the total number of radiating elements in the antenna array. In similar ways, the reflected waves can be represented by the column vector $\vec{b} = [b_1, ...b_{n-1}, b_n]^{\mathrm{T}}$ which are expressed in terms of the reflected power:

$$P_{\mathrm{re}} = \vec{b}^{\mathrm{H}}\vec{b} = \sum_{n=1}^{N} |b_n|^2 \leq 1. \tag{3.5}$$

The available power to the antenna array P_{acc}, in relationship to the incident and the reflected power is expressed by (2.7). The expansion in terms of the power waves and scattering parameters, $\vec{b} = \bar{S}\vec{a}$, yields

$$\begin{aligned} P_{\mathrm{acc}} &= \vec{a}^{\mathrm{H}}\vec{a} - \vec{b}^{\mathrm{H}}\vec{b}, \\ &= \vec{a}^{\mathrm{H}}(\bar{I} - \bar{S}^{\mathrm{H}}\bar{S})\vec{a}. \end{aligned} \tag{3.6}$$

Assuming a lossless antenna array, the covariance matrix using the accepted power (3.6) and (3.4) is then expressed as follows:

$$\bar{R} = \bar{R}_{\mathrm{acc}} = \bar{I} - \bar{S}^{\mathrm{H}}\bar{S}. \tag{3.7}$$

However, (3.7) does not take into account the ohmic losses of the antenna. Thus, another expression of the covariance matrix using embedded far-field realised gain patterns is derived. In the previous chapter, the complex realised total amplitude gain of the single antenna is given by $\vec{F}(\theta, \phi)$. For n^{th} element of the antenna array, this is $\vec{F}_n(\theta, \phi)$. Similar to the excitation vectors, n represents the element of the antenna array at which the radiation pattern is measured, and it ranges from 1 to N. Generally, the antenna array individual element patterns are measured with other elements terminated with a reference impedance Z_o. These patterns are called the *embedded* or the *active* patterns in contrast to the isolated patterns. And for conventional antenna arrays, with $d = \lambda/2$ and assuming minimal mutual coupling, the embedded patterns completely suffice the radiation performance of the antenna array.

Now extending (2.6) for the multiple antennas

$$P_{\text{rad}}(\vec{a}) = \frac{1}{4\pi} \int_0^{2\pi} \int_0^{\pi} |\sum_{n=1}^{N} a_n \vec{F}_n(\theta, \phi)|^2 \cos\theta \mathrm{d}\phi \mathrm{d}\theta. \tag{3.8}$$

This can be expanded after rewriting and rearranging the integrand as:

$$P_{\text{rad}}(\vec{a}) = \frac{1}{4\pi} \sum_{n=1}^{N} \sum_{m=1}^{N} a_n^* a_m \int_0^{2\pi} \int_0^{\pi} \vec{F}_n^{\text{H}}(\theta, \phi) \vec{F}_m(\theta, \phi) \cos\theta \mathrm{d}\phi \mathrm{d}\theta. \tag{3.9}$$

Using (3.4), the covariance matrix of the antenna array including ohmic losses is given by

$$\begin{aligned} \bar{R} = \bar{R}_{\text{rad},nm} &= \frac{1}{4\pi} \int_0^{2\pi} \int_0^{\pi} \vec{F}_n^{\text{H}}(\theta, \phi) \vec{F}_m(\theta, \phi) \cos\theta \mathrm{d}\phi \mathrm{d}\theta, \\ &= \frac{1}{4\pi} \int_0^{2\pi} \int_0^{\pi} (F_{\theta n}^{\text{H}}(\theta, \phi) F_{\theta m}(\theta, \phi) \\ &\quad + F_{\phi n}^{\text{H}}(\theta, \phi) F_{\phi m}(\theta, \phi)) \cos\theta \mathrm{d}\phi \mathrm{d}\theta. \end{aligned} \tag{3.10}$$

Therefore, there are two ways to compute the spatial covariance matrix of the antenna array using the accepted power or the scattering parameters and the radiated power or the realised gain far-field patterns which includes losses of the antenna. Generally, the notation $\bar{R}$ will be used throughout this work to denote the antenna array spatial covariance matrix unless $\{\cdot\}_{\text{acc}}$ or $\{\cdot\}_{\text{rad}}$ is specified to highlight the use of the accepted or radiated power, respectively.

The diagonal elements of the $\bar{R}$ donate the auto-correlation or the power radiated by the embedded beam patterns of the individual array elements. On the other hand, the off-diagonal elements of the covariance matrix indicate the cross-correlation or the coupled power between the beam patterns of element n and m of the array. This can also be

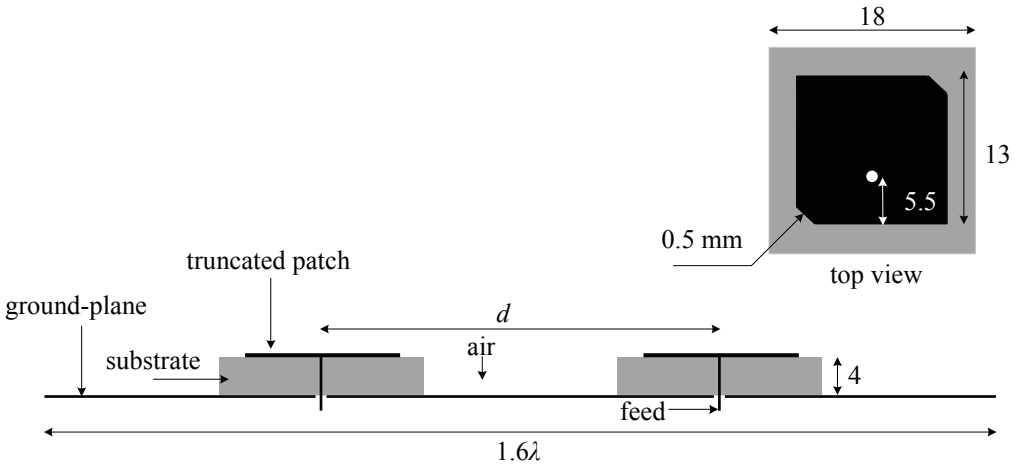

Figure 3.3: Design and geometrical dimensions of the simulated two-element GNSS L1/E1 band antenna array mounted on a common ground-plane; d is the inter-element separation in terms of wavelength. Here, all units are in mm.

referred to as the measure of beam superposition between the elements of the antenna array. An *ideal antenna array* that is lossless, reciprocal, and perfectly matched gives rise to the covariance matrix such that the diagonal elements of $\bar{R}$ are equal to 1, and off-diagonal are zero. Note that this representation is independent of the shape of embedded beam patterns.

3.2.2 Influence of the current excitation on the efficiency

As far as the efficiency of the antenna array elements is considered, it is straightforward without mutual coupling, i.e. off-diagonal elements of the covariance matrix are zero, and can be extracted from $\mathrm{tr}\{\bar{I} - \bar{R}\}$. In the case of the compact antenna arrays, the efficiency will depend on the excitation vectors or the impinging direction of the source. After the normalisation of incident power, which is equal to unity, the efficiency of the antenna array for excitation vector $\bar{a}$ is given by:

$$\lambda(\vec{a}) = \frac{\vec{a}^{\mathrm{H}}\bar{R}\vec{a}}{\vec{a}^{\mathrm{H}}\vec{a}} = \vec{a}^{\mathrm{H}}\bar{R}\vec{a}, \quad \text{with } \vec{a}^{\mathrm{H}}\vec{a} = 1. \tag{3.11}$$

As an example, a miniaturised lossless truncated ceramic patch antenna, using high dielectric permittivity substrate of $\epsilon_{\mathrm{r}} \approx 45$, is simulated, and optimised for the impedance matching and maximum RHCP realized-gain. The employed simulator is a 3D electromagnetic solver based on a finite-element method known as Ansoft HFSS version 14.0 [142]. The individual element properties i.e., the feeding point position and the geometry of the

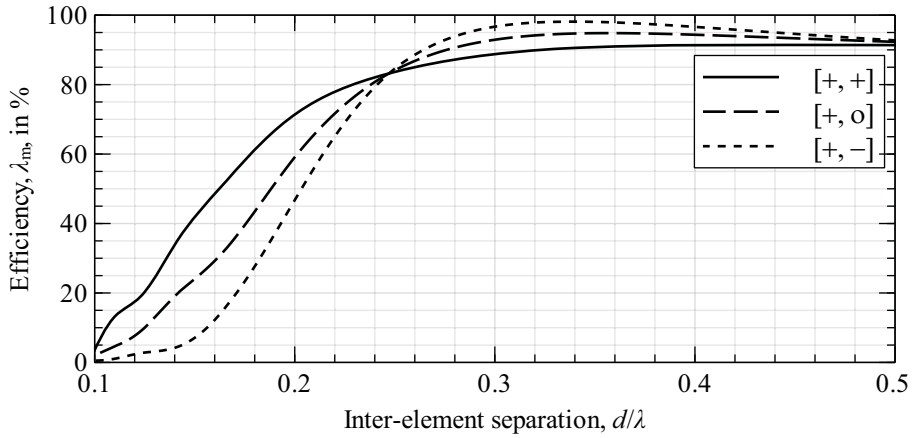

Figure 3.4: The analytically computed efficiency values for different excitation coefficients of the two-element antenna array with varying inter-element separation, d.

patch, are adjusted to achieve the reflection or matching coefficient, i.e. $S_{11} < -10$ dB at the L1/E1 band. The antenna radiation properties are tuned for the RHCP in the main-lobe direction mainly to achieve the desired $AR < 3$ dB. The final parameters for the optimised antenna are shown in Fig. 3.3. This design will be used in the simulated ceramic patch antenna arrays employed throughout this chapter.

Now, a similar element is placed in a linear array configuration at a separation distance of d. This d is varied from $\lambda/2$ to $\lambda/10$ in order to observe the effect of mutual coupling on the antenna covariance matrix and the corresponding efficiencies. As the antenna losses are ignored, the $\bar{S}$ matrix can be used to calculate the spatial covariance matrix using (3.7).

$$\bar{R}_{\text{acc}}^{\lambda/2} = \begin{bmatrix} 0.92 & 0.01\angle{-166^{\text{o}}} \\ 0.01\angle{166^{\text{o}}} & 0.92 \end{bmatrix}, \bar{R}_{\text{acc}}^{\lambda/6} = \begin{bmatrix} 0.33 & 0.18\angle{-5^{\text{o}}} \\ 0.18\angle{-5^{\text{o}}} & 0.33 \end{bmatrix}$$

represent the computed covariance matrices for $d = \lambda/2$ and $d = \lambda/6$, respectively. Clearly, these matrices are Hermitian matrices. The off-diagonal elements indicate the percentage of correlated power, which is higher in the case of $d = \lambda/6$ due to the presence of mutual coupling. It can also be observed that $d = \lambda/2$ is not zero but minimal.

The analytically computed efficiencies for different excitation coefficients of the two-element simulated lossless antenna array with various inter-element separations are shown in Fig. 3.4. If the antenna array with $d = \lambda/2$ is excited with $\vec{a} = [\frac{1}{\sqrt{2}}, \frac{1}{\sqrt{2}}]^{\text{T}}$, then the calculated efficiency is 91%. In comparison, if the excitation coefficients are $\vec{a} = [\frac{1}{\sqrt{2}}, -\frac{1}{\sqrt{2}}]^{\text{T}}$ then the efficiency is 93%. There is no difference between the two efficiencies, which means the resulting λ_{m} is not affected by the current excitation vectors. Moreover, the array exhibits minimal mutual coupling at this inter-element separation, and is the suitable choice for implementation in the conventional antenna arrays. In contrast, if the second

case, where $d = \lambda/6$, is considered, then the efficiencies for the excitation coefficients are 53% and 17%, respectively. This is a difference of approximately 5 dB, which is significant. Therefore, in the presence of mutual coupling, the efficiency of the antenna is dependent on the current excitation vector, and also signifies the importance of the covariance matrix calculation for the performance evaluation of the compact antenna arrays, which will be the focus in the next section.

3.2.3 Beam-pattern orthogonality and port coupling

The beam-pattern orthogonality means that the non-diagonal elements of the antenna array covariance matrix $\bar{R}$ are zero. This corresponds to the uncorrelated embedded antenna patterns. In comparison, port coupling is referred to as the non-diagonal elements of the scattering parameters of $\bar{S}$. Often in literature, the port coupling defines the mutual coupling properties of the antenna array, which is not completely true. Let's consider two practical examples of two-element microstrip ceramic patch antenna arrays discussed in the earlier section: inter-element separation of $d = \lambda/4$ and a circularly-polarised antenna element. The scattering parameters of this antenna array in are given as follows:

$$\bar{S}_{\lambda/4} = \begin{bmatrix} 0.1 & 0.4\angle 86^{\text{o}} \\ 0.4\angle 86^{\text{o}} & 0.1 \end{bmatrix}.$$

This suggests the port coupling or mutual coupling between the antenna elements is approximately 16%. However, in contrast, the antenna array covariance matrix is given as follows:

$$\bar{R}_{\lambda/4} = \begin{bmatrix} 0.83 & 0 \\ 0 & 0.83 \end{bmatrix},$$

which suggests no beam overlap showing that the antenna elements are uncorrelated. Even though the scattering parameters reveal moderate coupling between the elements, there is no beam overlap.

Another interesting example of multi-port antennas employed in GNSS applications is the dual-polarised patch antenna element for improved polarisation diversity. For the dual linearly polarised antennas, the generated TM_{10} and TM_{01} while considering a rectangular patch give rise to perfect port decoupling and no beam overlap. However, the dual circular polarised truncated square patch antenna, which involves a combination of the two diagonal TM modes, is required to generate the RHCP and LHCP each, respectively. The simulated scattering matrix for this lossless antenna is

$$\bar{S}_{\text{DCP}} = \begin{bmatrix} 0.3\angle 137^{\text{o}} & 0.7\angle 45^{\text{o}} \\ 0.7\angle 45^{\text{o}} & 0.3\angle 137^{\text{o}} \end{bmatrix}.$$

This shows the port coupling to be approximately 50%. But, the computation of the covariance matrix,

$$\bar{R}_{\text{DCP}} = \begin{bmatrix} 0.4 & 0 \\ 0 & 0.4 \end{bmatrix},$$

reveals no beam overlap. Principally, beam overlap implies port coupling, but the converse is not generally true and should be avoided in the characterisation and analyses of the coupled antenna arrays in particular. The phenomena of the mutual coupling as explained in the first section of this chapter predominantly occur in the free space and may not be exactly depicted at the port level. In contrast, the beam overlap using the antenna covariance matrix suggests a true depiction of the radiation process of the antenna array.

3.3 The fundamental modes of radiation

The following work builds upon the conceptual foundations laid by C. Volmer [90] in his doctoral dissertation for eigenmode formulation of the radiation process of arbitrary multi-port antennas. For a symmetric antenna array, the covariance matrix is a Hermitian, i.e. $\bar{R} = \bar{R}^{\text{H}}$ [11, Theorem 4.1.3]. This property allows for the investigation of the fundamental structure or characteristics of the covariance matrix. Mathematically, this is the evaluation of the maximum and minimum of the functions associated with these matrices. One such principal component analysis of the covariance matrix is known as the *eigen-decomposition* [11, Chapter 1]. This decomposes the matrix into associated *eigenvectors* and *eigenvalues*. The eigen-decomposition of the covariance matrix can be written as follows:

$$\bar{R} = \bar{Q}\bar{\Lambda}\bar{Q}^{\text{H}}. \tag{3.12}$$

The eigen-decomposition is based on finding the set of the values or the roots of the characteristic polynomial of the matrix $\bar{R}$, i.e. $\det(\bar{R} - \lambda\bar{I}) = 0$. The matrix $\bar{Q}$ consists of the column vectors, which diagonalise the covariance matrix with the condition that the $\bar{Q}\bar{Q}^{\text{H}} = \bar{I}$, where $\bar{I}$ is an identity matrix. $\bar{\Lambda}$ is a diagonal matrix with $\bar{\Lambda} = \text{diag}\{\lambda_1, ..., \lambda_n\}$, λ_n represent the corresponding eigenvalues of the eigenvectors. The eigenvectors are not unique, whereas the eigenvalues can be distinct. Therefore, for a $N \times N$ antenna array covariance matrix, there are at most N distinct or non-distinct possible eigenvalues.

Further investigating the radiation properties of the antenna array, consider the covariance matrix, $\bar{R}$, associated with the antenna array computed from its given set of n embedded antenna patterns $\vec{F}_n(\theta, \phi)$. Now, the new normalised fictive antenna patterns are $\vec{F}^n_{\text{ev}}(\theta, \phi)$ formed by applying the corresponding eigenvectors k of the computed $\bar{R}$. This new set of antenna patterns can be analytically accomplished with the linear superposition of the embedded antenna patterns as shown by [90, Equation 2.31]

$$\vec{F}_{\text{ev}}^{n}(\theta,\phi) = \frac{1}{\sqrt{\lambda_n}} \sum_{j=1}^{N} \bar{Q}_{jn} \vec{F}_j(\theta,\phi). \tag{3.13}$$

The new covariance matrix $\bar{R}_{\text{ev}}$ for these eigenmode antenna patterns is identified using (3.7), which can be condensed into the following:

$$\bar{R}_{\text{ev}} = \frac{1}{\sqrt{\lambda_i \lambda_j}} \bar{\Lambda}_{ij} = \begin{cases} 1 & \text{if } i = j, \\ 0 & \text{otherwise.} \end{cases} \tag{3.14}$$

This is also valid for the receiving case (see [90, Chapter 2]). The (3.14) outcome is similar to the findings in [26, Section XI] that the eigenmodes are mutually orthogonal. These modes form the orthonormal basis for the linear pattern space that can be spanned by the given antenna array and constitute the complete diversity degrees-of-freedom available in the array. The eigenvectors are responsible for the pattern shape, whereas the eigenvalues relate to the corresponding radiation efficiencies. In fact, these radiation modes are the fundamental representation of a given antenna array as observed in [90, Section 2.2.3]. However, it is generally impossible to achieve non-zero beam overlap for the eigenmode excitation due to the ohmic losses of the feed networks.

3.3.1 The minimum eigenvalue

In a compact manner, the eigenvalues, which represent the radiation efficiencies of the corresponding eigenmodes, can be evaluated as

$$\lambda_m = \frac{\vec{q}_m^{\,\text{H}} \bar{R} \vec{q}_m}{\vec{q}_m^{\,\text{H}} \vec{q}_m}, \tag{3.15}$$

where m donates the number of column vectors of $\bar{Q}$.

Now, the maximum possible radiation efficiency or the best case for the antenna array is given by $\lambda_{\text{max}} = \max\{\lambda_m\}$ where $m = 1, 2, ..N$. Similarly, the minimum eigenefficiency is given by $\lambda_{\text{min}} = \min\{\lambda_m\}$, and defines the worst-case radiation efficiency possible from the antenna array. The nominal case or the mean eigenefficiency is given as follows:

$$\lambda_{\text{avg}} = \frac{1}{N} \sum_{m=1}^{N} \lambda_m = \frac{1}{N} \operatorname{tr}\{\bar{R}\}, \tag{3.16}$$

which is also given by the normalised trace of the covariance matrix $\bar{R}$ [55, Equation. 17].

The analytically computed eigenvalues for the simulated lossless four- and six-element antenna arrays are indicated in Table 3.1. For all the different configurations the maximum

Table 3.1: Modal eigenvalues for the simulated lossless four- and six-element ceramic patch antenna arrays in square-shaped and hexagonal-shaped configuration, respectively. λ_{min}, λ_{avg}, and λ_{max} are the corresponding minimum, average, and maximum eigenvalues. The single-element antenna design is similar to the one shown in Fig. 3.3.

	4-element		**6-element**	
modes	$d = \lambda/2^1$	$d = \lambda/4$	$d = \lambda/4$	$d = \lambda/5^2$
1	0.96	0.83	0.90	0.89
2	0.94	0.68	0.88	0.61
3	0.90	0.48	0.85	0.61
4	0.85	0.30	0.33	0.19
5			0.28	0.15
6			0.20	0.08
λ_{min}	0.85	0.30	0.20	0.08
λ_{avg}	0.91	0.57	0.57	0.41
λ_{max}	0.96	0.83	0.90	0.89

[1,2] Same overall size of the antenna arrays.

and average eigenvalues are close and show no variation among each other. However, minimum eigenvalue, λ_{min}, is severely affected by the compactness and choice of number of elements of the antenna array. In fact, the minimum eigenvalue dictates the minimum performance of the antenna array, and can be considered a lower bound to the antenna array achievable efficiency. Therefore, if the minimum eigenvalue is maximised while designing the antenna array, the overall efficiency performance of the array will be enhanced. In addition, it becomes interesting to analyse the translation of the eigenvalue performance in terms of the antenna diversity, which follows in the next section.

3.4 Diversity reception

In any communication receiver, the received signal is a superposition of the multitude of the signals, which include the line-of-sight and multipath signal field strength. The multipath occurs due to the scattering of the signals from the nearby ground, mountains, buildings and objects larger than the wavelength of the signal. This superposition of the signals can be constructive and destructive depending on the length and the characteristics of the path. This may lead to the fading of the instantaneous SNR by a significant margin, such that the operation of the receiver is impeded.

To combat fading, modern receivers exploit independent or uncorrelated paths to improve reception diversity using multiple antennas. This technique is called *antenna diver-*

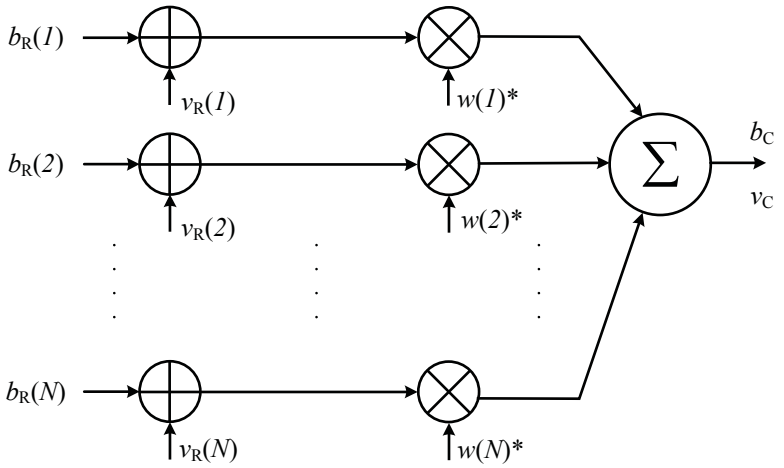

Figure 3.5: Signal flow graph of the linear diversity combiner receiver [56]. The complex received signal envelopes and the receiver noise are represented by $b_{\mathrm{R}}(n)$ and $\nu_{\mathrm{R}}(n)$, respectively. The respective receiver branches are combined with weights $w(n)^*$ and later summed. The weighted or equivalent combined received signal and noise are denoted by b_{C} and ν_{C}, respectively.

sity. The diversity degrees-of-freedom are proportional to the number of antenna elements, so the more antenna elements, the greater the exploits of multiple signal paths. However, it is necessary to place the antenna elements at half of free-space wavelength to achieve the uncorrelated and independent signal impingement conditions, in other words *full diversity*. But, if the antenna element separation is reduced, then the mutual coupling results in correlated paths, which diminishes or reduces these diversity degrees-of-freedom. Therefore, a N element compact array may deliver similar diversity performance as an $N-1$ or even lesser number of element conventional half free-space wavelength array, which undermines the miniaturisation due to decreased inter-element separation.

To establish the diversity performance of the antenna array based on its covariance matrix or the eigenvalues, a simplified diversity receiver is modelled (see Fig. 3.5). The instantaneous combined signal power is

$$P_{\mathrm{C}}^{\mathrm{sig}} = \vec{w}^{\mathrm{H}} \vec{b}_{\mathrm{R}} \vec{b}_{\mathrm{R}}^{\mathrm{H}} \vec{w}. \tag{3.17}$$

For simplicity, the noise contribution of the receiver components is modelled as the additive zero-mean Gaussian random process over each receiver branch. Furthermore, the noise contribution of each receiver chain is uncorrelated. Therefore, the additive combined and weighted noise power for the equivalent receiver or system noise temperature T_{sys} according to [12, Equation 2.2] is expressed as

$$P_{\mathrm{C}}^{\mathrm{noise}} = \vec{w}^{\mathrm{H}} k_{\mathrm{o}} T_{\mathrm{sys}} B \vec{w}. \tag{3.18}$$

The quality of the received signal expressed by the SNR for the combined signal, γ_{C}, as a function of the weights $\vec{w}$, is

$$\gamma_{\mathrm{C}}(\vec{w}) = \frac{P_{\mathrm{C}}^{\mathrm{sig}}}{P_{\mathrm{C}}^{\mathrm{noise}}} = \frac{\vec{w}^{\mathrm{H}}\vec{b}_{\mathrm{R}}\vec{b}_{\mathrm{R}}^{\mathrm{H}}\vec{w}}{k_{\mathrm{o}}T_{\mathrm{sys}}B}, \qquad \text{with } \vec{w}^{\mathrm{H}}\vec{w} = 1. \tag{3.19}$$

The relationship between the previously introduced CNR and SNR, γ , according to [4] is given by:

$$\chi_{\mathrm{o}} = 10\mathrm{log}[\gamma \cdot B]. \qquad (\mathrm{dB\text{-}Hz}) \tag{3.20}$$

Now, the two familiar diversity terms associated with performance of the antenna array are the diversity gain and diversity loss. For further derivations and discussion, the Rayleigh distribution of the signal amplitude is considered [13, p. 44]. The optimum weight vector that maximises the SNR in (3.19) has been introduced as the maximum ratio combiner [57], [58]

$$\vec{w}_{\mathrm{opt}} = \vec{b}_{\mathrm{R}}. \tag{3.21}$$

This is basically the eigenvector corresponding to the largest eigenvalue that maximises SNR in the received or radiated direction. This may suggest that the diversity, under these assumptions, is more of an optimistic value of the compact antenna array, because mutual coupling has no effect on the largest eigenvalue of the antenna array, under the assumption of a single source only. Therefore, it may not be an optimal figure of merit to analyse the robustness of the compact antenna array. But, it does provide the average of maximum achievable performance gain in all directions from the given antenna array, which is also useful, particularly for mobile communication applications.

3.4.1 Diversity gain

The diversity gain represents the improvement of the average combined maximum SNR γ_{max} normalised to the instantaneous single branch SNR γ_o for a given outage probability $p(\gamma)$ in all directions [14, Section 1.2.2]. More specifically, it minimises the probability of deep fades in the received SNR. The diversity gain is the equivalent insertion gain quantity to determine the benefits of the diversity. A closed-form formula for the diversity gain in terms of the signal covariance matrix and its corresponding eigenvalues has been derived in [59, Equation 29]. This allows instantaneous determination of the diversity performance of the antenna arrays (distinct eigenvalues) under the assumption mentioned above that the probability density function is given by Rayleigh distribution [60, Equation 30]

$$p(\gamma) = \sum_{n=1}^{N} \frac{e^{-\gamma/\lambda_n}}{\left(\prod_{k=1}^{N} \lambda_k\right) \prod_{\substack{m=1 \\ m\neq n}}^{N} \left(\frac{1}{\lambda_m} - \frac{1}{\lambda_n}\right)}, \qquad \text{for } \gamma > 0. \tag{3.22}$$

Mathematically, the diversity gain G_{D} definition as a function of the signal covariance matrix $\bar{R}$ and outage probability p is

$$G_{\mathrm{D}}(\bar{R}, p) = \frac{d_{\bar{R}}^{-1}(p)}{d_1^{-1}(p)}, \tag{3.23}$$

where $d_1^{-1}(\cdot)$ and $d_{\bar{R}}^{-1}(\cdot)$ donate the inverse functions for the cumulative distribution functions of the single antenna and of a diversity receiver described by $\bar{R}$, respectively. A simpler and faster approximation of this expression for N element array is given via the Maclaurin series expansion of $d_{\bar{R}}^{-1}(\cdot)$.

$$G_{\mathrm{D}}(\bar{R}, p) \approx \frac{q}{p}\left[1 + \frac{\mathrm{tr}\{\bar{R}^{-1}\}}{N(N+1)}q\right] = \frac{q}{p}\left[1 + \frac{\sum_{i=1}^{N} \lambda_i^{-1}}{N(N+1)}q\right], \tag{3.24}$$

and q can be obtained by

$$q = \sqrt[N]{N!\det\{\bar{R}\}p}, \tag{3.25}$$

or in terms of the eigenvalues $q = \sqrt[N]{N!p\prod_{i=1}^{N}\lambda_i}$. It may be noted that this is different than the array gain, which refers to the average increase in the SNR at the receiver, resulting at the combiner's output [14, Section 1.2.1]. This is the summation of the eigenvalues of the antenna array covariance matrix and is expressed as [11]

$$G_{\mathrm{A}}(\bar{R}) = 10\log[\mathrm{tr}\{\bar{R}\}] = 10\log\sum_{n=1}^{N}\lambda_n. \qquad (\mathrm{dB}) \tag{3.26}$$

The ideal single antenna will have an array gain of 0 dB. And for the ideal antenna arrays the array gain is equal to the number of elements N, as all the eigenvalues $\lambda_n = 1$. This insight is also similar to the general understanding that the percentage power captured by the antenna array is dictated by the efficiencies of the degrees-of-freedom.

3.4.2 Diversity loss

This is defined as the decrease in SNR of the compact N element antenna array as compared to the ideal N element antenna array. A simplified closed-form expression independent of the outage probability is derived in [59, Equation 25] and is given by

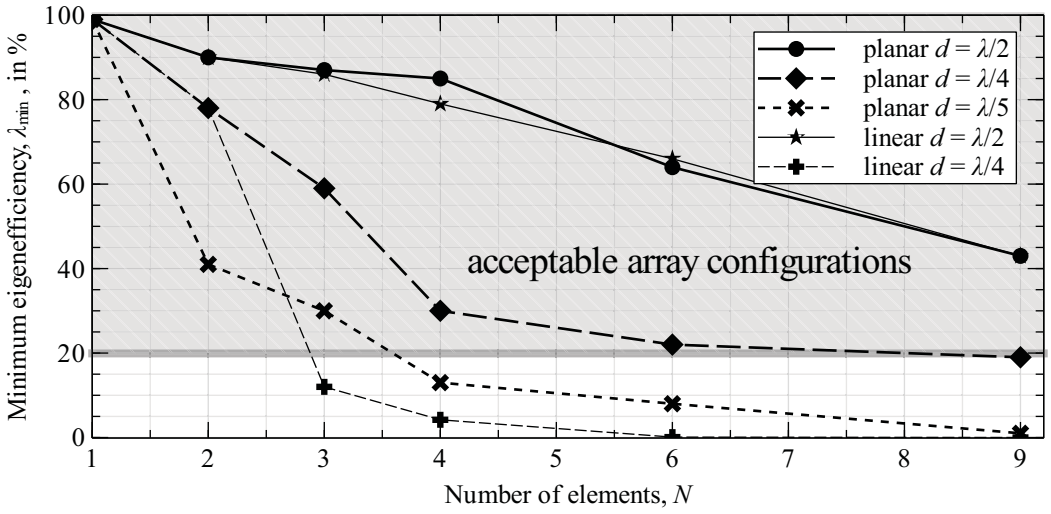

Figure 3.6: The minimum eigeefficiencies for simulated lossless arrays versus the number of radiating elements (N) for different inter-element separations (d) and different geometrical arrangements. The shaded region indicates the antenna array configurations with $\lambda_{\min} > 20\%$

.

$$L_{\mathrm{D}} \approx -\frac{10}{N}\log\left[\det\{\bar{R}\}\right] = -\frac{10}{N}\log\left[\prod_{i=1}^{N}\lambda_i\right]. \qquad (\mathrm{dB}) \qquad (3.27)$$

The dependence of the diversity loss on the product of the eigenvalues implies that the worst eigenvalue will increase the loss. Therefore, the least efficient mode of the antenna array will reduce the overall diversity performance severely. Also, according to (3.27), the diversity loss is inversely proportional to the number of elements; that is, more elements will decrease the influence of the individually degraded eigenefficiencies.

Note, the accuracy of the diversity loss expression mentioned above is limited to a four-element antenna array and is more precise for outage probability consideration of 1% [59]. On the other hand, if the coupling is strong such that $\lambda_{\max}/\lambda_{\min} > 10$, then the error as compared to the exact values becomes larger than $1\ \mathrm{dB}$. Over the frequency bandwidth, the accuracy characteristics of the diversity loss expression display narrow-band behaviour.

3.5 Compact ceramic patch antenna array configurations

The antenna array design engineers, while configuring the antenna parameters, target for the optimisation of higher gain, broad beamwidth and impedance matching bandwidth. These parameters are normally optimised according to the requirements of the applica-

tions in light of the possible scenarios or environments of operation. However, the inter-element separation is kept constant at half of the free-space wavelength to have minimum mutual coupling. But, in the presence of mutual coupling it becomes cumbersome to analyse and evaluate, and at the same time difficult to optimise the antenna array design for gain, beamwidth and impedance bandwidth values independent of the excitation coefficients. Therefore, as mentioned earlier, the eigenvectors define the entire vector space of the radiation. Therefore, eigenvectors along with the eigenvalues provide the complete information about the radiation process of the antenna array, and are the optimum tools for performance investigations of compact antenna array designs.

Now, the main focus of antenna array optimisation is to simplify and find an optimum array, without additional circuitry, with efficient degrees-of-freedom that are capable of delivering an acceptable CNR at the navigation receiver input. This value depends on the type of application and receiver characteristics. It is proposed that the maximisation of the minimum eigenvalue ensures the best radiation performance of the compact antenna arrays, which is further investigated with the simulation of different antenna array configurations. These involve adaptations of the following parameters:

1. Inter-element separation, d/λ.
2. Number of elements, N.
3. Geometrical arrangement of the elements.

In Fig. 3.6, the computed minimum eigenvalues of the $\bar{R}$, for various antenna arrays simulated, are displayed.

3.5.1 Optimal number of elements

According to (3.26), the antenna array gain is proportional to the total number of elements N. From the perspective of the receiver, this will ensure higher CNR in the desired source directions. Therefore, a straightforward choice is to fill the available space with the maximum number of elements. On the other hand, if robustness against interference is sought, the maximum number of nulls from a given antenna array with one degree of freedom fixed to the wanted signal direction are $N - 1$. However, the minimum eigenvalue for inter-element spacing $d = \lambda/2$ is reduced with increasing number of elements N as shown in Fig. 3.6, even though the maximum eigenvalue remains unchanged. This means that increasing number of elements in the array eventually degrade the diversity degrees-of-freedom, particularly the minimum eigenvalue. Therefore, it is not straightforward to achieve higher CNR and maximum nulls simply by increasing the number of elements. Basically, there is a trade-off between highest possible CNR and robustness of the receivers in the interference-limited scenario.

In the compact antenna array case, where the aperture area is already fixed and small, adding more elements will result in increased mutual coupling, which further degrades the eigenvalues of the higher-order modes, necessary for interference scenarios. Therefore, the number of elements should always be chosen such that for a fixed aperture area all degrees of freedom or eigenvalues, particularly minimum eigenvalue, are efficient enough to contribute equally towards the detection and acquisition of the desired signal.

3.5.2 Optimal inter-element separation

The mutual coupling increases with decreasing inter-element separation between the antenna array elements. This degrades the eigenefficiencies of the antenna array accordingly. Therefore, the antenna array diversity gain is inversely proportional to inter-element separation if the overall size remains fixed. Although smaller inter-element separation offers miniaturisation, which is a favourable attribute for modern receivers, it is challenged with greater mutual coupling. So, how much inter-element separation reduction is affordable without compromising significant loss of antenna array performance concerns most antenna array design engineers. Considering the same example for a two-element ceramic patch antenna array, the eigenefficiencies for $d = \lambda/4$ are $\lambda_1 = 0.85$ and $\lambda_2 = 0.84$. This is reduced to $\lambda_1 = 0.55$ and $\lambda_2 = 0.17$ for the $d = \lambda/6$ separation. Obviously, the better choice is the one that provides higher efficiency; that is, with larger separation. The minimum eigenvalue for compact inter-element separation is worsened further with increasing number of elements; see Fig. 3.6. One can say that it is a trade-off between miniaturisation and radiation performance of antenna arrays. Still, some radiation efficiency can be recovered by decreasing the mismatching losses of these higher-order modes (see discussions in Chapter 4).

For lossless compact antenna array configurations, according to Fig. 3.6, considering the minimum eigenvalue of 20% as a threshold, a designer's suitable choices are $N = 4$ with spacing of $d = \lambda/4$ or $N = 3$ with $d = \lambda/5$. The former configuration offers higher gain, more nulls but with a larger size as compared to the array mentioned later. Actually, it depends on the intended application and size constraints for the configuration of the array.

3.5.3 Optimal geometry

With inter-element separation $d = \lambda/2$ for similar number of elements N the minimum eigenvalue is least affected across different geometrical arrangements shown in Fig. 3.7, and is also similar for linear configurations. But if the inter-element separation is decreased, i.e. $d < \lambda/2$ the geometrical configuration variations have a significant impact on the minimum eigenvalue.

For the four-element antenna array, different geometrical configurations are feasible. The resulting eigenvalues are displayed in Table 3.2. It may be observed that at $d =$

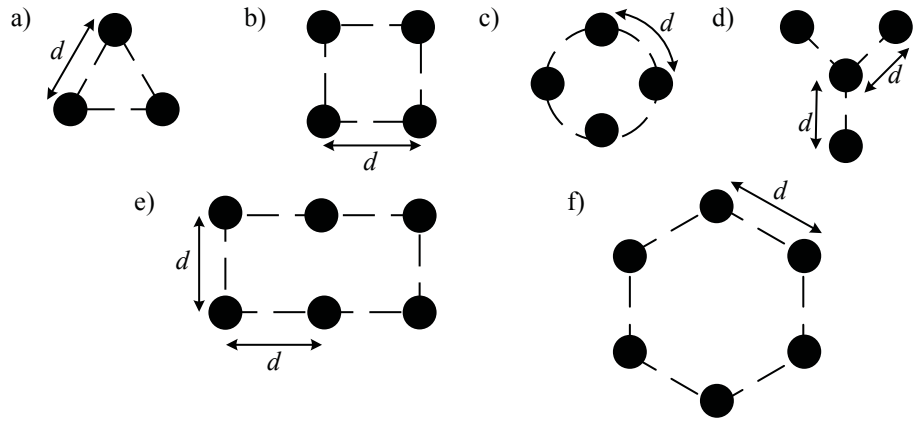

Figure 3.7: Geometrical arrangements for different designed antenna arrays (a) three elements triangular-shaped; four elements that are (b) square-shaped, (c) circular-shaped, (d) y-shaped; six elements that are (e) rectangular-shaped, (f) hexagonal-shaped.

Table 3.2: Eigenvalues for the simulated lossless four-element ceramic patch antenna arrays in different linear, square, and circular geometrical configurations with $d = \lambda/4$, and square geometry with $d = \lambda/5$. The computed diversity loss and gain for the respective arrays are also indicated.

modes	$d = \lambda/4$		$d = \lambda/5$	
	linear	square*	circular	square
1	0.88	0.83	0.83	0.71
2	0.81	0.68	0.78	0.40
3	0.66	0.48	0.39	0.30
4	0.02	0.30	0.09	0.14
$L_{\mathbf{D}}$ **(dB)**	5.02	2.76	4.02	4.81
$G_{\mathbf{D}}$ **(dB)**	15.39	16.34	15	14.31

Table 3.3: Minimum eigenvalues for the simulated six-element lossless ceramic patch antenna arrays in linear and planar geometrical configurations.

d	**linear**	**planar**	
		rectangular	hexagonal
$\lambda/2$	0.62	0.64	0.64
$\lambda/4$	0.02	0.06	0.21

$\lambda/4$ for the square shape antenna array the minimum eigenvalue is significantly larger than other geometrical configurations. Also, at $d = \lambda/5$ the minimum eigenvalue for

square shape is better than its counterpart geometries having $d = \lambda/4$. The diversity loss according to (3.27) is smallest for the square shape array as well. This is in agreement with the maximum diversity gain calculated at outage probability of 1% from (3.24). It may be concluded that the diversity figures-of-merit show similar behaviour as the minimum eigenvalue. In other words, the compact antenna array with largest minimum eigenvalue result in the maximum antenna diversity.

The extension to the six-element array reveals similar results for different geometrical configurations, shown in Table 3.3. Like the four-element case, the planar geometry gives minimum eigenvalues superior to the linear geometry. Furthermore, the hexagonal geometry provides better minimum eigenvalue as compared to the rectangular arrangement. Therefore, it can be generalised that the N–element compact array, where coupling is prominent, minimum eigenvalue is sensitive to the changes in the geometrical arrangement of the radiating elements, and can be optimised to achieve better diversity and robustness performance.

3.5.4 Examples: Fabricated four-element ceramic patch antenna arrays

In order to verify the results in the simulations, the four-element ceramic patch antenna array is fabricated using commercially available GPS antennas. These antennas are based on the ceramic substrates that offer high dielectric constants and low dielectric loss tangent. These antennas are optimised for RHCP in the main-lobe direction over a ground-plane of $70\ \mathrm{mm} \times 70\ \mathrm{mm}$ which is a standard size for the available off-the-shelf ceramic GPS patch antennas in the market.

Linear configuration: The antenna elements are mounted on the ground-plane of 1.6λ with an inter-element separation of $\lambda/4$ as shown in Fig. 3.8. The measured scattering parameters indicate the maximum coupling between any of the two elements is approximately $-7\ \mathrm{dB}$. Due to the presence of strong mutual coupling of the elements, the matching of the individual elements is also disrupted and shifted from the operating frequency. In the next step, the embedded far-field patterns of the antenna elements are measured, which are then applied to obtain the eigenvalues for all the diversity degrees-of-freedom of the antenna array. The eigenvalues are calculated by decomposing the integrated far-field realised gain patterns using (3.12) and are shown in Fig. 3.9. It can be observed that the maximum eigenvalue or the even mode has the highest efficiency, i.e. above 80% in the operating band, whereas the minimum eigenefficiency is below 5%, which is significantly low and useless in diversity receivers.

Planar configuration: Let's consider the case of four-element antenna array in a square geometry. The designed antenna array is shown in Fig. 3.10 The ground-plane size is identical to that of the linear antenna array. Similar to the linear array, the reflection coefficients at the operating frequency are disturbed due to the presence of mutual

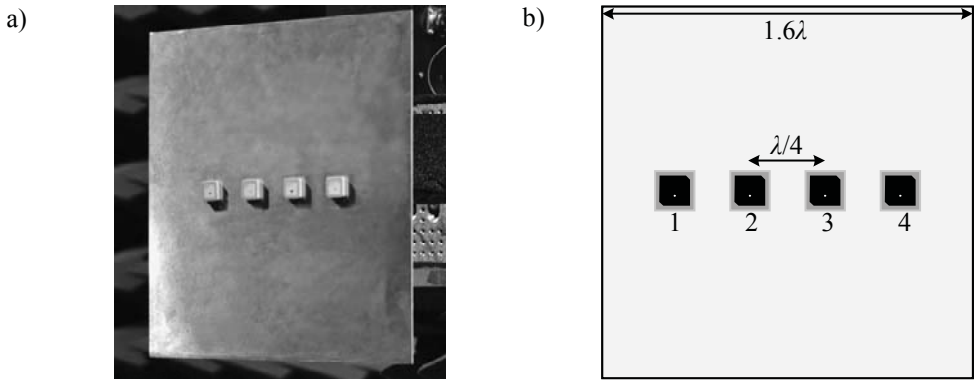

Figure 3.8: Linear four-element ceramic patch antenna array at L1/E1 bands with $d = \lambda/4$ and ground-plane size $1.6\lambda \times 1.6\lambda$. (a) The manufactured array. (b) Top-view sketch of the antenna array.

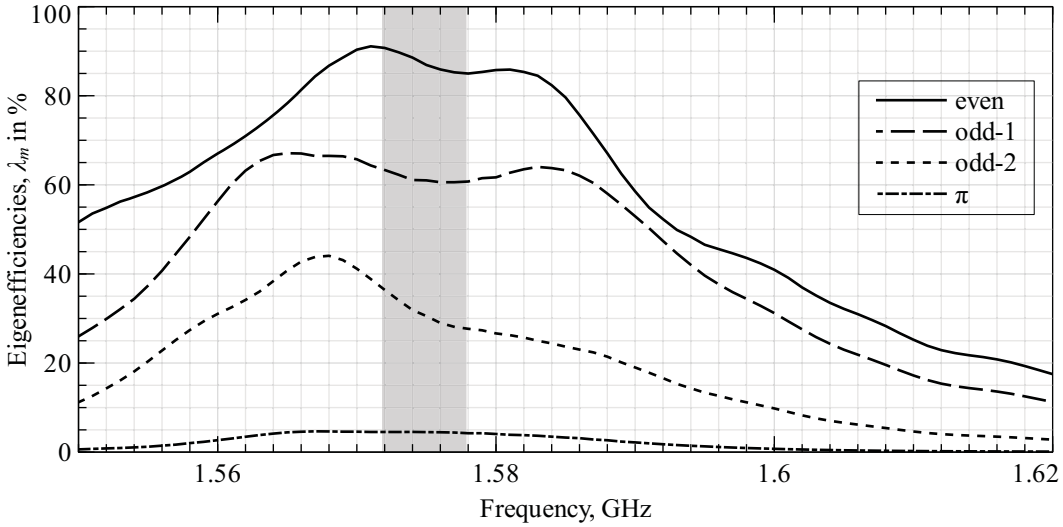

Figure 3.9: Computed eigenefficiencies, λ_m in %, for the fabricated four-element ceramic patch antenna array with $d = \lambda/4$. The highlighted grey portion indicates the operating L1/E1 band.

coupling, which has a maximum value of -8 dB. This is 1 dB less than the linear array. Now, the eigen-analysis, see Fig. 3.11, reveals that the maximum eigenvalue is still above 80%, whereas minimum eigenvalue increases to 20%, which is significantly greater than the linear array. This is in agreement with the results obtained for the optimal geometry analysis in simulations. The odd-1 and odd-2 mode eigenvalues are similar for both configurations. This suggests that the planar square geometry provides better minimum eigenvalues in comparison to the linear configuration. Note that the bandwidth of the odd-2 and π mode is considerably reduced as compared to the even and odd-1 mode for both

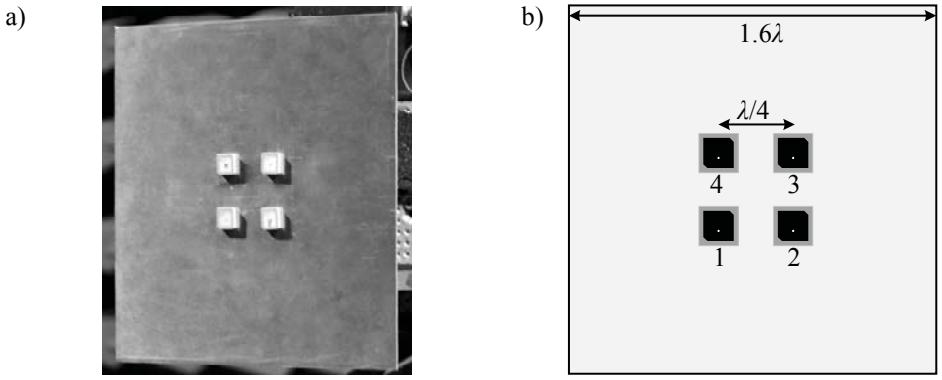

Figure 3.10: Planar square-shaped four-element ceramic patch antenna array at L1/E1 bands with $d = \lambda/4$ and ground-plane size $1.6\lambda \times 1.6\lambda$. (a) The manufactured antenna array. (b) Top-view sketch of the antenna array.

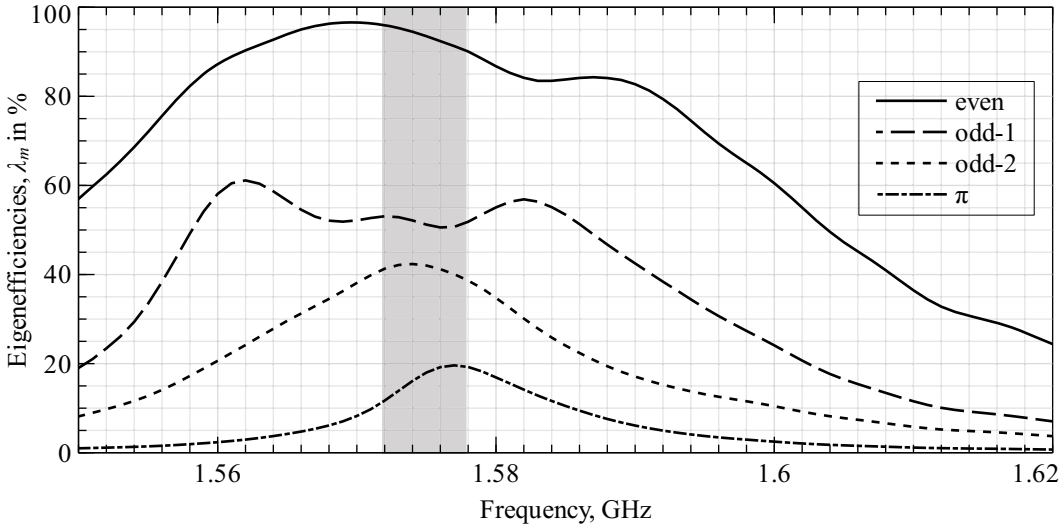

Figure 3.11: Computed eigenefficiencies, λ_m in %, for the fabricated four-element ceramic patch antenna array with $d = \lambda/4$. The highlighted grey portion indicate the operating L1/E1 band.

linear and planar configurations, which may be another limiting factor for certain types of GNSS signals. The bandwidth characteristics of the compact antenna arrays are discussed in the next chapter.

To visualise the difference in the radiation patterns of the individual antenna elements and the eigenmodes, the corresponding realised gain patterns are plotted. In Fig. 3.12 and Fig. 3.13, the measured embedded far-field RHCP and LHCP patterns for the elevation and azimuth cut are shown, respectively. It can be seen that the maximum RHCP and LHCP realised gain is approximately 0 dBi for all elements, and shape of the RHCP radiation patterns are quite similar to each other.

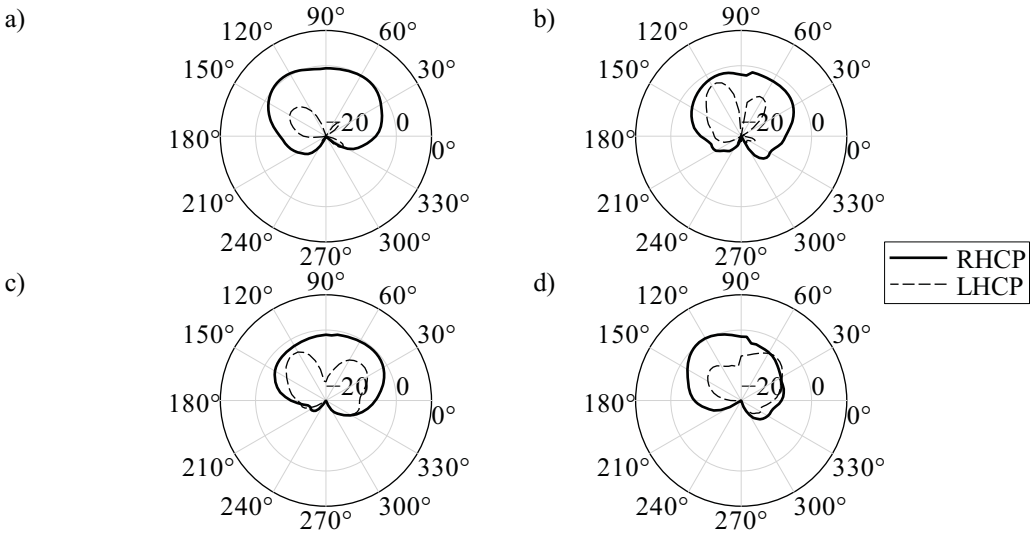

Figure 3.12: Measured embedded realised gain RHCP and LHCP in elevation with fixed azimuth $\phi = 0^{\text{o}}$, $|\vec{F}_{\text{RHCP}}(\theta, \phi)|^2$ (solid line) and $|\vec{F}_{\text{LHCP}}(\theta, \phi)|^2$ (dashed line) of the four-element square-shaped ceramic patch antenna array at the operating frequency $f_o = 1575.42$ MHz for element number (a) 1, (b) 2, (c) 3, and (d) 4, respectively.

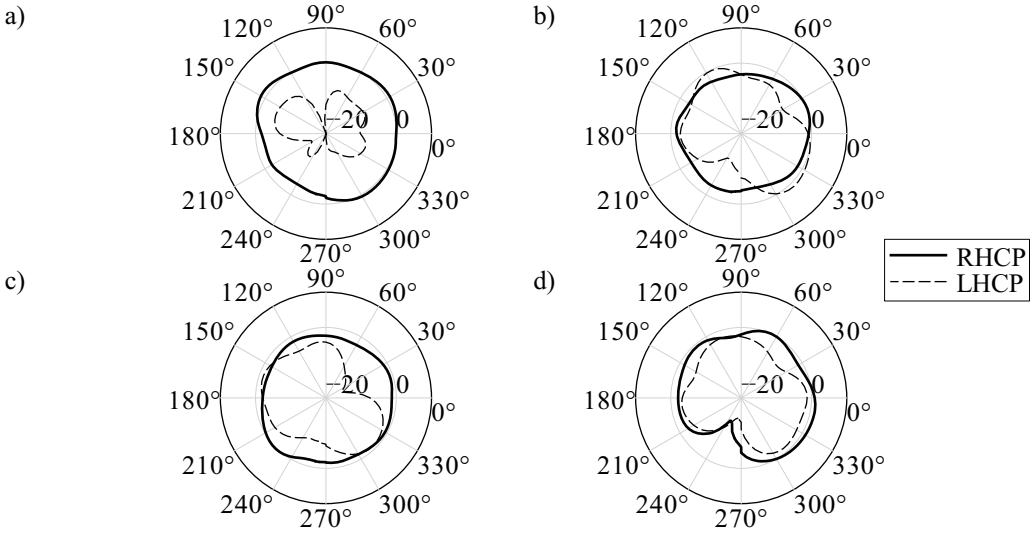

Figure 3.13: Measured embedded realised gain RHCP and LHCP in azimuth with fixed elevation $\theta = 30^{\text{o}}$, $|\vec{F}_{\text{RHCP}}(\theta, \phi)|^2$ (solid line) and $|\vec{F}_{\text{LHCP}}(\theta, \phi)|^2$ (dashed line) of the four-element square-shaped ceramic patch antenna array at the operating frequency $f_o = 1575.42$ MHz for element number (a) 1, (b) 2, (c) 3, and (d) 4, respectively.

Now, using (3.13), the eigenmode far-field patterns can be computed analytically. Again, the elevation cut with fixed azimuth, i.e. $\phi = 0^{\text{o}}$ is shown in the Fig. 3.14, whereas

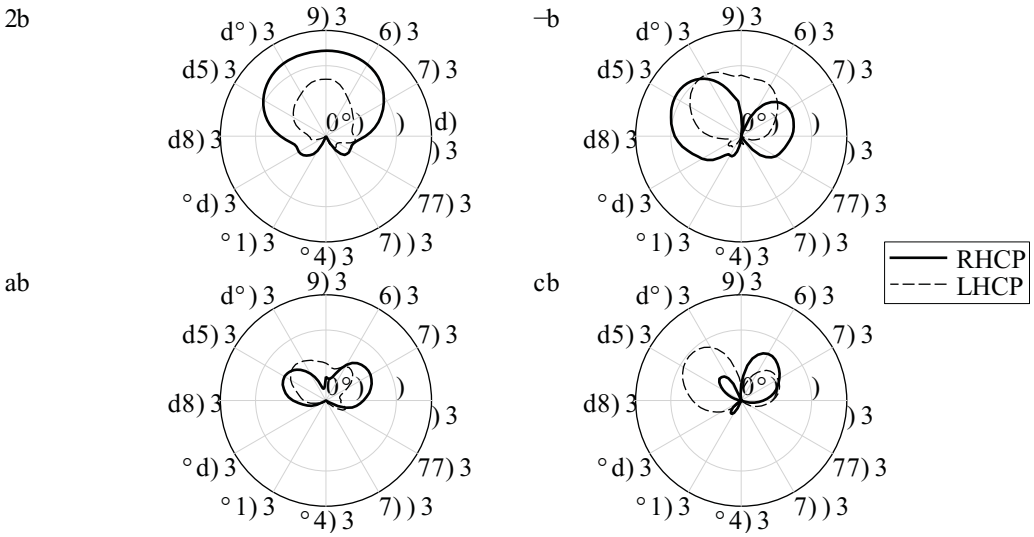

Figure 3.14: Analytically calculated eigenmode realised gain RHCP and LHCP in elevation with fixed azimuth $\phi = 0^{\text{o}}$, $|\vec{F}_{\text{m}}^{\text{RHCP}}(\theta,\phi)|^2$ (solid line) and $|\vec{F}_{\text{m}}^{\text{LHCP}}(\theta,\phi)|^2$ (dashed line) of the four-element square-shaped ceramic patch antenna array at the operating frequency $f_o = 1575.42\,\text{MHz}$ for (a) even, (b) odd-1, (c) odd-2, and (d) π mode, respectively.

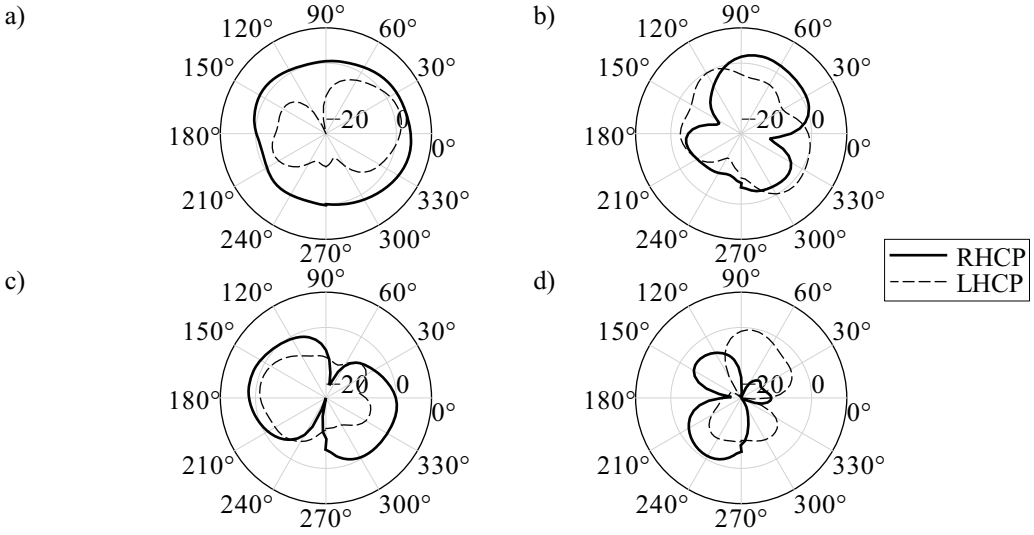

Figure 3.15: Analytically calculated eigenmode realised gain RHCP and LHCP in azimuth with fixed elevation $\theta = 30^{\text{o}}$, $|\vec{F}_{\text{m}}^{\text{RHCP}}(\theta,\phi)|^2$ (solid line) and $|\vec{F}_{\text{m}}^{\text{LHCP}}(\theta,\phi)|^2$ (dashed line) of the four-element square-shaped ceramic patch antenna array at the operating frequency $f_o = 1575.42\,\text{MHz}$ for (a) even, (b) odd-1, (c) odd-2, and (d) π mode, respectively.

the azimuth with fixed low-elevation, i.e. $\theta = 30^{\text{o}}$ is drawn in Fig 3.15. Altogether, these can be visualised as the radiation patterns of the eigenmodes or the orthogonal modes. The

even mode, that is, the in-phase excitation in this case, is responsible for radiation in the zenith. This mode gives the maximum realised gain for the RHCP, which is above 5 dBi in this case. The higher-order modes produce nulls in their patterns, which indicate the excitation of the out-of-phase excitation coefficients in the neighbouring elements. The π mode provides the maximum nulls, i.e. three for the four-element array, but minimum realised gain.

The cross-polarisation or LHCP gain for the even mode is high, which is not particularly desired for the main-lobe directions. With the higher modes, the cross-polarisation levels become comparable or even greater than the co-polarised gain values, which indicate increased sensitivity of the array to unwanted signals.

3.6 Polarisation purity

An ideal GNSS antenna array does not pose any content of the LHCP. However, in reality it is generally impossible to achieve. Typically, antenna designers quote the axial ratio of the antenna arrays in the main-lobe directions for the *combined* pattern case, that is, superposition of embedded patterns with equal phase and amplitudes [143]. For the symmetric antenna array, this combined mode represents the even mode with the largest eigenvalue of the antenna array. It can be observed for all four-element compact antenna designs mentioned in previous sections that the LHCP in the even mode is high in contrast to the individual antenna polarisation properties. The high LHCP in the even mode leads to susceptibility to multipath reflections, which can severely jeopardise the positioning accuracy and is unacceptable. Therefore, the antenna array must be optimised for the axial ratio in the even mode. On the other hand, insight into the higher modes of the compact array reveal significant values of LHCP sometimes even larger than the RHCP. These higher-order modes are crucial for acquisition of low-elevation satellites, beamforming and interference cancellation applications. With reception of an arbitrarily polarised interferer in both polarisations equally, the robustness of the receiver may be compromised, because of the requirement of multiple degrees-of-freedom to suppress such an interferer, which is discussed in detail in the next chapter.

With the discussion above and in combination with robustness requirements mentioned in the previous chatper, observation of antenna array polarisation purity in the even mode only is insufficient. Rather, it is vital to describe the polarisation performance of the higher-order modes as well, which is unfortunately overlooked or ignored in practice. In addition to the radiation efficiency of the antenna array, the eigen-analysis also provides the insight into the polarisation purity of the designed antenna arrays, which can be helpful for the optimisation of the antenna array for all conditions and scenarios, thus maximising the overall robustness.

In the previous section, a contributing factor for poor polarisation performance can be

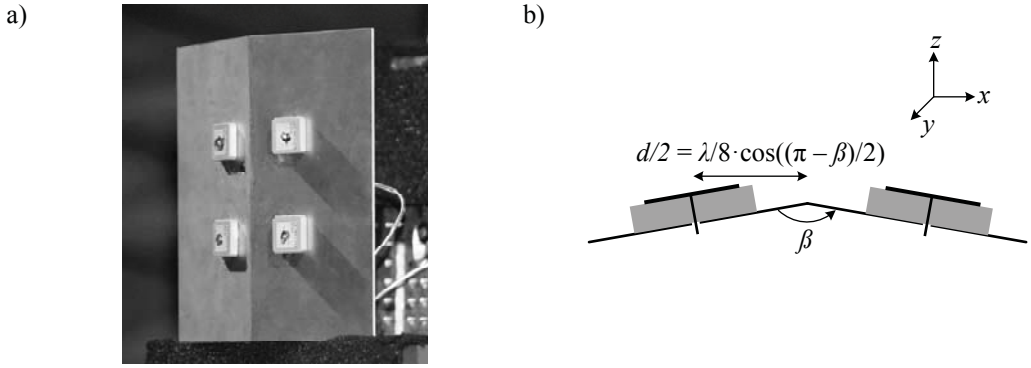

Figure 3.16: Elevation tilted, $\beta = 160^{\text{o}}$ or tilting angle of 10^{o} with respect to the horizon, four-element ceramic patch antenna array at L1/E1 bands with $d = \lambda/4$ and ground-plane size $0.80\lambda \times 0.80\lambda$.(a) The manufactured antenna array. (b) Side-view sketch of the tilted antenna array.

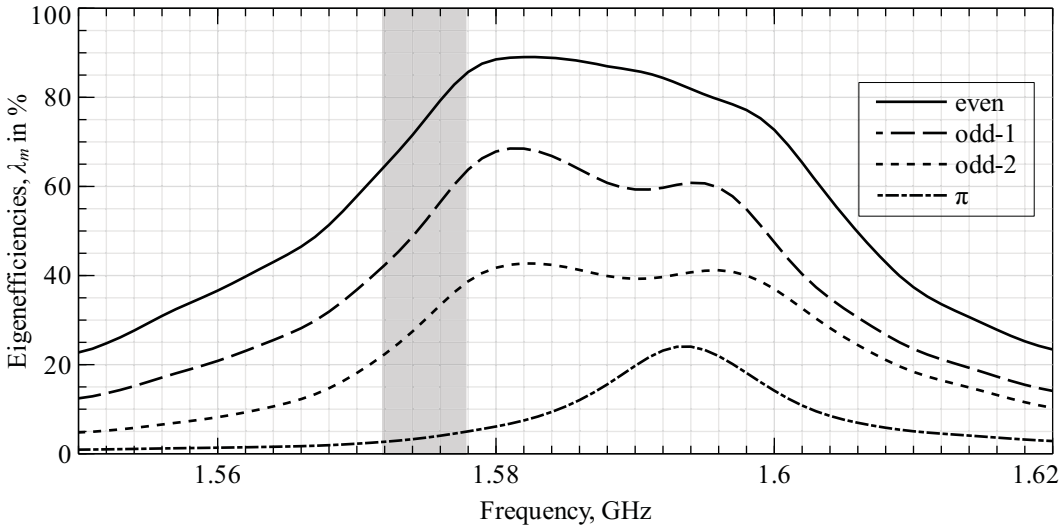

Figure 3.17: Computed eigenefficiencies, λ_m in %, for the tilted four-element ceramic patch antenna array with $d = \lambda/4$. The highlighted grey portion indicates the operating L1/E1 band.

the planar structure of the antenna arrays considered since the horizontal component of the electric field becomes zero at the surface of the ground-plane, where the antenna acts linearly polarised. Therefore, the axial ratio approaches infinity for an infinite ground-plane, assuming a state of linear polarisation. Much research has been undertaken to minimise the cross-polarisation with the ground-plane alterations such as choke ring and tilting [61]. On the other hand, the antenna designs such as those mentioned in Section 1.4 of quadrafilar helix type offer low cross-polarisation at low elevations as well. But complete eigenmode performance of such antenna type arrays along with small inter-element separations is non-existent in literature. Therefore, two examples of non-planar compact antenna arrays, i.e.

tilted ceramic patch antenna arrays and QHA arrays, are implemented to provide insight into the polarisation impurity in their respective eigenmode radiations. The former is an alteration of the structure of the planar antenna array, whereas the latter is the resilient polarisation antenna design.

3.6.1 Tilted ceramic patch antenna array

Intuitively, the antenna array can be optimised for the third dimension and evolve into a 3D antenna array by tilting. This tilting can be applied in xz, yz or both planes. The fabricated antenna array with tilting in xz plane is shown in Fig. 3.16 Here, the angle $\beta = 160^{\text{o}}$, which corresponds to a tilting of 10^{o}. The inter-element separation is $d = \lambda/4$. As observed in simulations, the measured scattering parameters show that the maximum coupling is similar to the planar case and is not decreased by tilting. Although the coupling coefficient in the tilting plane antenna elements is decreased by 1–$2\ \mathrm{dB}$. In simulations, different tilting angles up to 30^{o} are investigated and the mutual coupling is not significantly changed.

The eigen-analysis of the antenna array measured covariance matrix shows the maximum eigenvalues is comparable to the planar array, whereas the minimum eigenvalue improves to 25%. This improvement in the minimum eigenvalue can be attributed to the less disturbance of the reflections coefficients of the individual antenna elements because of the reduced coupling.

Now, in order to investigate the polarisation purity of the tilted antenna array, the measured realised gain patterns for the RHCP and LHCP at $f_o = 1575.42\ \mathrm{MHz}$ are plotted for elevation cut with fixed azimuth $\phi = 0^{\text{o}}$ in Fig. 3.18. For the even mode, the LHCP is higher than the planar antenna array. However, the LHCP is decreased in the higher-order modes and is below the RHCP gain in most directions. But it is still comparable. It may also be noted that the RHCP gain in the low elevation for the higher-order modes has become more symmetric around the zenith and is slightly improved, which is due to tilting. Similarly, the azimuth realised gain in RHCP and LHCP for fixed elevation $\theta = 30^{\text{o}}$ is plotted in the Fig. 3.19 The cross-polarisation is slightly suppressed like in elevation directions, but not completely removed or significantly decreased.

3.6.2 Quadrafilar helix antenna array

The compact antenna array using commercially available QHA has been fabricated [144]. For reader's interest, a customised printed QHA with reduce height four-element antenna array is presented in Appendix B. These antenna designs are types of wire antennas compared to patch antennas [3, Section 1.2.1]. The current distribution is in the $z-$direction, whereas for patch antennas it is present in the $xy-$ or the azimuth plane. It also possesses no surface wave propagation, which may help in the reduction of mutual coupling. Each element consists of four helix antennas with each excited relative quadrature phase to the

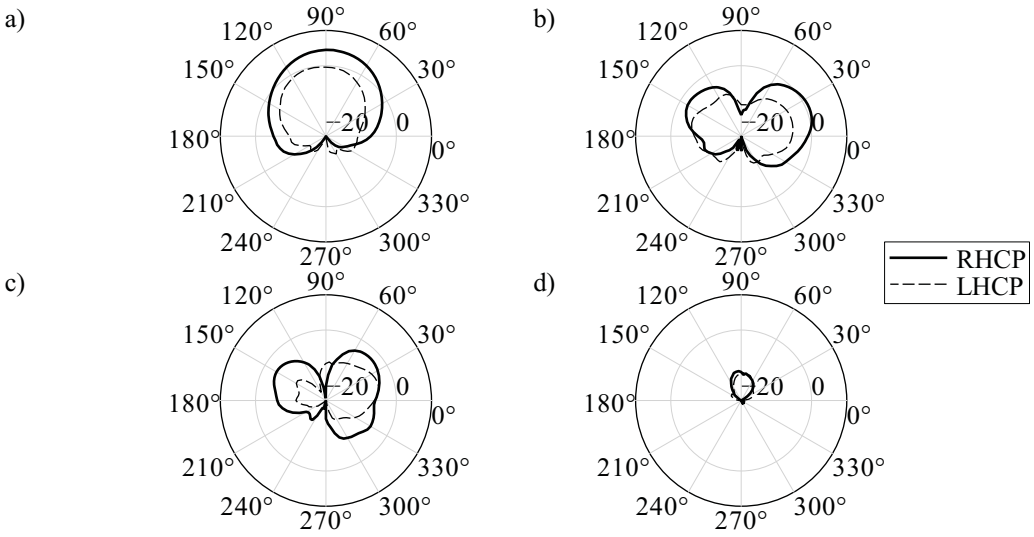

Figure 3.18: Measured eigenmode realised gain RHCP and LHCP in elevation with fixed azimuth $\phi = 30^{\text{o}}$, $|\vec{F}_{\text{m}}^{\text{RHCP}}(\theta, \phi)|^2$ (solid line) and $|\vec{F}_{\text{m}}^{\text{LHCP}}(\theta, \phi)|^2$ (dashed line), of the four-element tilted ceramic patch antenna array at the operating frequency $f_o = 1575.42$ MHz for (a) even, (b) odd-1, (c) odd-2, and (d) π mode respectively.

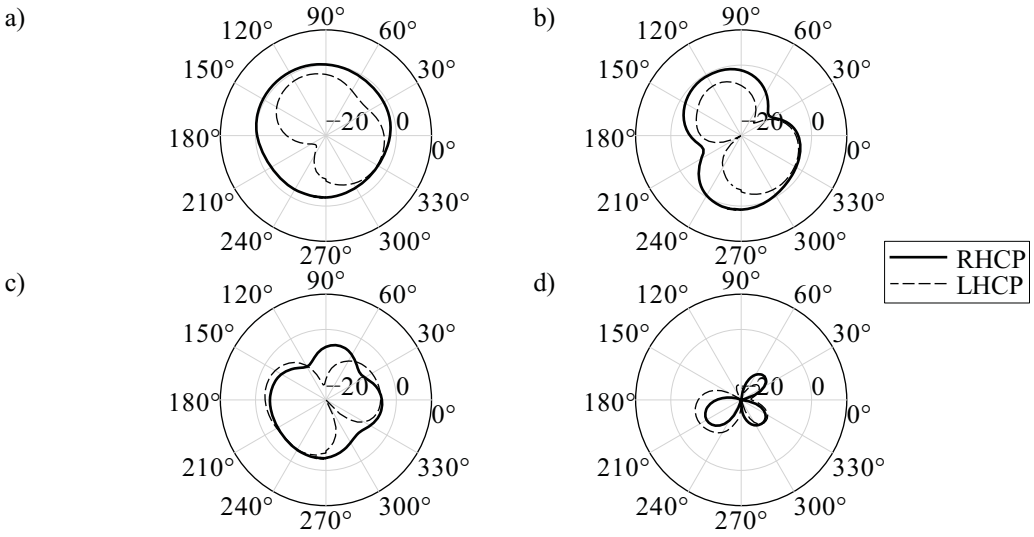

Figure 3.19: Measured eigenmode realised gain RHCP and LHCP in azimuth with fixed elevation $\theta = 30^{\text{o}}$, $|\vec{F}_{\text{m}}^{\text{RHCP}}(\theta, \phi)|^2$ (solid line) and $|\vec{F}_{\text{m}}^{\text{LHCP}}(\theta, \phi)|^2$ (dashed line), of the four-element tilted ceramic patch antenna array at the operating frequency $f_o = 1575.42$ MHz for (a) even, (b) odd-1, (c) odd-2, and (d) π mode respectively.

previous element responsible for the RHCP radiation in the zenith directions. This antenna array may not be interesting for the applications requiring planarity because of the height,

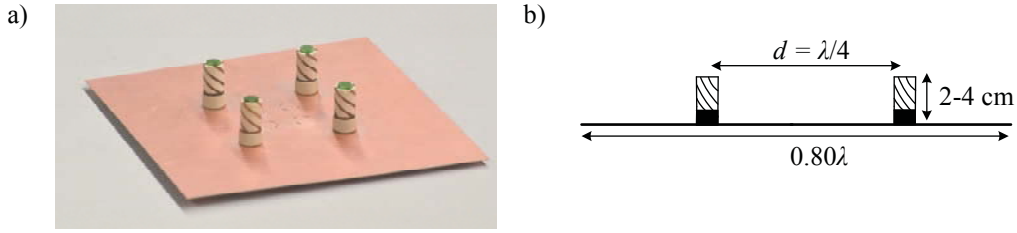

Figure 3.20: Square-shaped four-element quadrafilar helix GNSS antenna array at L1/E1 bands with $d = \lambda/4$ and ground-plane size $0.80\lambda \times 0.80\lambda$ (a) fabricated, (b) sketch, side view with dimensions.

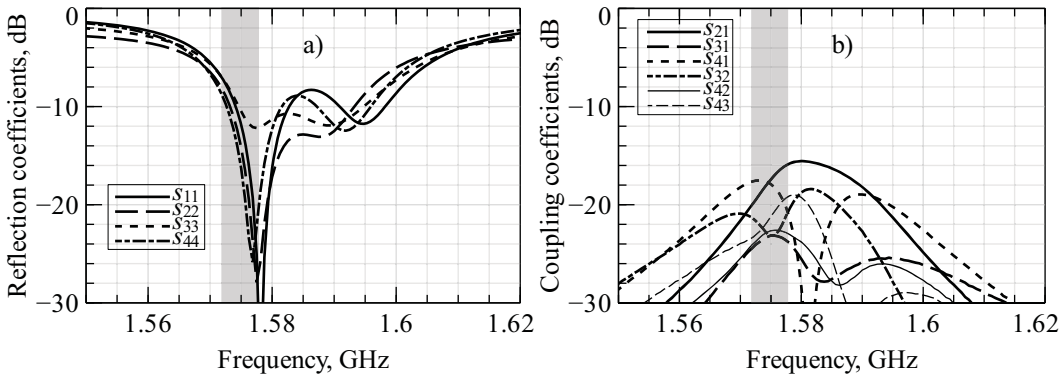

Figure 3.21: Measure scattering parameters of the quadrafilar helix antenna array, S_{ij}. (a) The reflection coefficients S_{ii} in dB, (b) The coupling coefficients S_{ij}, with $i \neq j$, in dB.

$h > 2$ cm, of the helix, though high permittivity dielectric loaded helix may be incorporated to reduce the height of these antennas. In this work, it is worth mentioning the radiation performance of another type of antenna, which independently offers more robust and accurate positioning in the GNSS receivers for safety-critical applications [1], as the compact antenna array design. The fabricated antenna array is shown in Fig. 3.20a. As mentioned previously, the elements are arranged in a square shape in the $xy-$plane. The chosen inter-element separation d is mentioned in Fig. 3.20b.

The measured scattering parameters are displayed in Fig. 3.21. The excellent matching performance of the antenna array at the desired operating band is manifestation of the fact that the maximum coupling is below -15 dB. However, the eigenvalues of the respective frequency shown in the Fig. 3.22 are quite poor. The even mode efficiency is below 50% whereas the π mode efficiency is below 1%. These low efficiencies can be attributed to the high loss-tangent of the dielectric and losses in the additional feeding network to excite circular polarisation mode of the individual elements. Therefore, the reduced coupling can be linked to the losses within the antenna element.

The realised gain RHCP and LHCP of the antenna array for all eigenmodes in the elevation and azimuth cuts for fixed azimuth $\phi = 0^{\text{o}}$ and $\theta = 0^{\text{o}}$ are plotted in Figs. 3.23 and

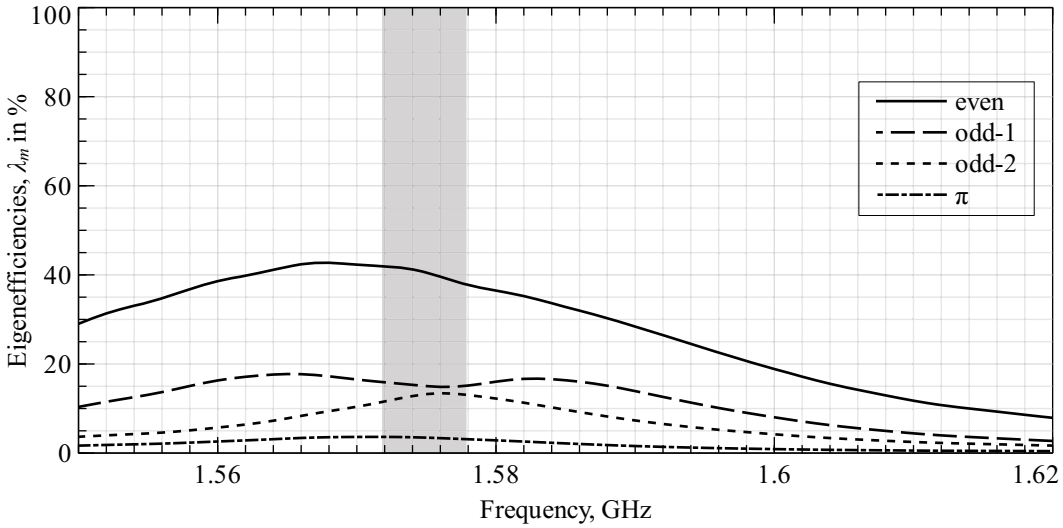

Figure 3.22: Computed eigenefficiencies, λ_m, for the four-elment quadrafilar helix antenna array with $d = \lambda/4$. The highlighted grey portion indicate the operating L1/E1 band.

3.24, respectively. The even mode maximum RHCP realised gain is $3\ \mathrm{dBi}$ approximately, whereas the LHCP is $-15\ \mathrm{dB}$ in almost all directions; this is the same in all azimuth directions as well. As stated earlier, this antenna array does offer higher gain at very low elevation angles close to the horizon. But, the higher-order modes suffer from low gain in the RHCP, and additionally the nulls are not well defined, which detract from the ability of the receiver to acquire the satellites in scenarios where these modes are active.

The axial ratio in the zenith direction plots for both QHA and tilted ceramic patch antenna array over the frequency are shown in Fig. 3.25. With $3\ \mathrm{dB}$ as cut-off criteria, the QHA array delivers wideband characteristics as compared to the tilted ceramic patch array. Nonetheless, for civilian L1/E1 GNSS, signal bandwidths are small, i.e. $2\ \mathrm{MHz}$, which is possible with tilted ceramic patch antennas as well. However, the axial ratio with tilted ceramic patch antenna is de-tuned and needs to be optimised. Therefore, the wideband characteristics of the QHA array offer better manufacturing tolerances which might be attractive for low-cost commercial applications.

3.7 Direction-of-Arrival estimation capabilities

Even though satellite position in terms of elevation and azimuth is provided in the ephemeris data, still the use of multiple-antenna receivers can facilitate the estimation of the DOA of the satellite signals independently. Collectively, this position information of the satellite—the attitude of the receiver—can be estimated, which provides crucial information for

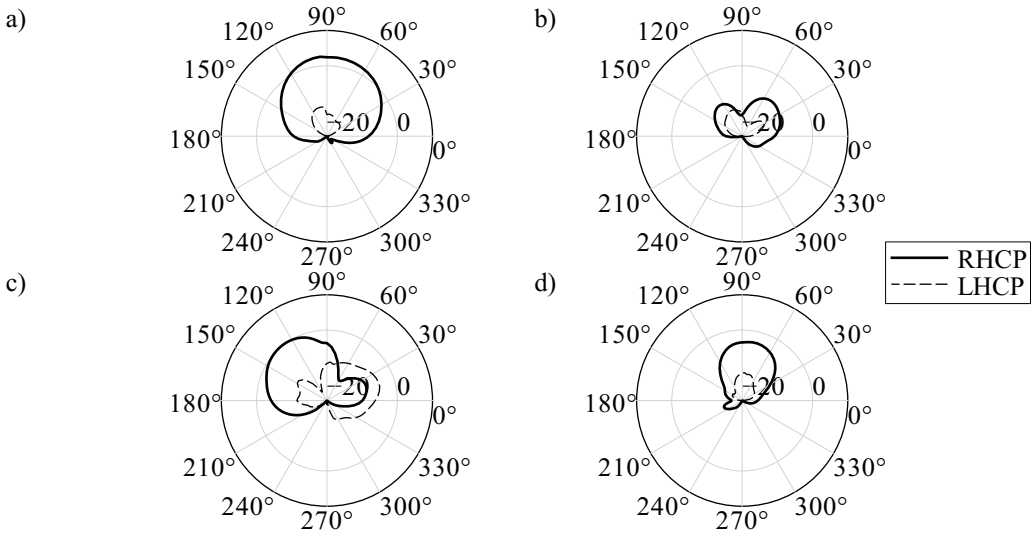

Figure 3.23: Measured eigenmode realised gain RHCP and LHCP in elevation with fixed azimuth $\phi = 30^{\text{o}}$, $|\vec{F}_{\text{m}}^{\text{RHCP}}(\theta, \phi)|^2$ (solid line) and $|\vec{F}_{\text{m}}^{\text{LHCP}}(\theta, \phi)|^2$ (dashed line) of the four-element square-shaped QHA array at the operating frequency $f_o = 1575.42$ MHz for (a) even, (b) odd-1, (c) odd-2, and (d) π mode respectively.

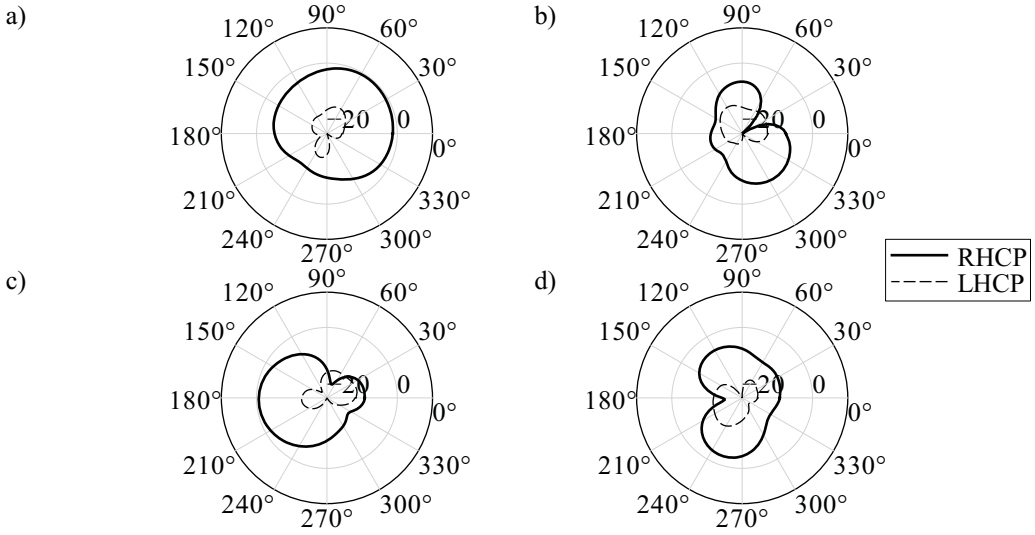

Figure 3.24: Measured eigenmode realised gain RHCP and LHCP in azimuth with fixed elevation $\theta = 30^{\text{o}}$, $|\vec{F}_{\text{m}}^{\text{RHCP}}(\theta, \phi)|^2$ (solid line) and $|\vec{F}_{\text{m}}^{\text{LHCP}}(\theta, \phi)|^2$ (dashed line) of the four-element square-shaped QHA array at the operating frequency $f_o = 1575.42$ MHz for (a) even, (b) odd-1, (c) odd-2, and (d) π mode respectively.

achieving more accurate and robust positioning. Primarily, the robustness of the receiver is enhanced against spoofing signals. Therefore, in addition to the eigen-analysis, the

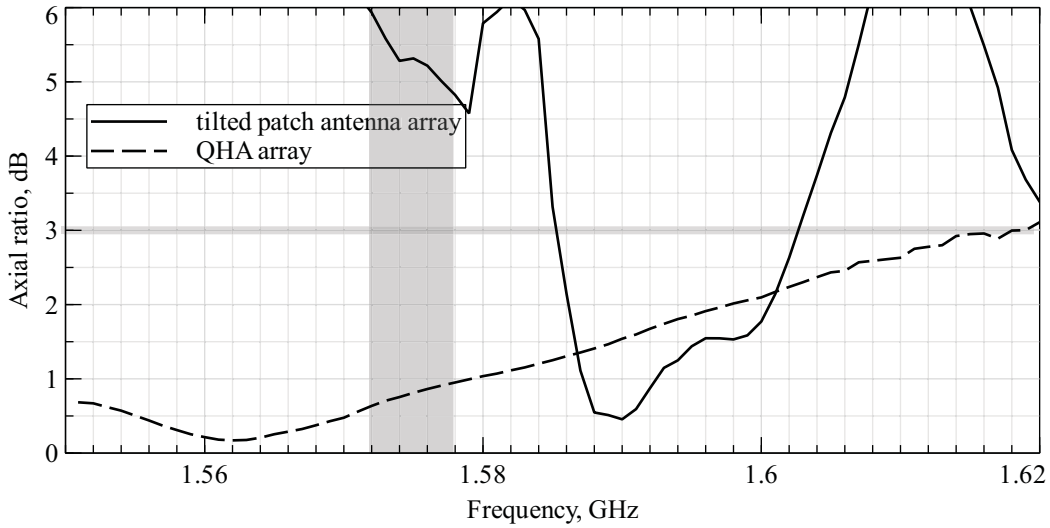

Figure 3.25: Measured axial ratio, in dB, of the even mode in the main-lobe directions, which is $\theta = 0^{\mathrm{o}}$, and $\phi = 0^{\mathrm{o}}$, for the fabricated tilted ceramic patch and QHA array.

direction-finding capabilities of the compact antenna array are investigated in this work. The Cramer-Rao lower bound (CRLB) provides the framework to evaluate the performance of any unbiased estimator; it provides the achievable minimum variance of the estimated variable [62]. In the case of DOA estimation of the elevation angle θ, where the estimate is defined by $\hat{\theta}$, the variance of the estimator satisfies the following condition:

$$CRLB_{\theta} \leq \mathrm{Var}\{\hat{\theta}\} \tag{3.28}$$

Consider the received signal with the assumption of white Gaussian noise with variance given by $\sigma^2 \bar{I}$. Then, the received signal for m^{th} sample from k^{th} source, with K being the total number of sources, is given by:

$$\vec{y}_k(m) = \vec{F}(\theta_k, \phi_k) x_{\mathrm{c}}(m) + \vec{n}(m). \tag{3.29}$$

Here, it is assumed that the number of samples M is much greater than the number of receiving antennas N. For the given model, the well-known asymptotic one-dimensional CRLB elevation, i.e. θ, in the deterministic case, which is sometimes called conditional model, is given by [62, Equation 4.1] (see also [63])

$$CRLB_{\theta} = \frac{\sigma^2}{2M} \left[\Re\{ \bar{\xi}^{\mathrm{H}} \bar{O}_{\perp}^{\mathrm{F}} \bar{\xi} \cdot \bar{R}_{\mathrm{xx}} \} \right]^{-1}. \tag{3.30}$$

$\bar{O}_{\perp}^{\mathrm{F}}$ is defined as the projection of the subspace orthogonal to the steering vector $\bar{F}_K = [\vec{F}(\theta_1, \phi_1), \vec{F}(\theta_k, \phi_k), ... \vec{F}(\theta_K, \phi_K)]$, which is a matrix of dimension $N \times K$, the noise

subspace. In case of the known interferer directions, the interference-free subspace projector $\bar{O}_{\perp}^{\text{int}}$ can be found using the $\bar{F}_{\text{int}}$, which is then multiplied by steering vectors in order to compute the CRLB. However, in this section, the discussion is limited to single source angular direction estimation with no interference for simplicity. And, $\bar{\xi}$ denotes the partial derivatives with respect to the unknown, which is θ_k in this case. Therefore,

$$\begin{aligned} \bar{O}_{\perp}^{\text{F}} &= [\bar{I}_N - \bar{F}_K(\bar{F}_K^{\text{H}}\bar{F}_K)^{-1}\bar{F}_K^{\text{H}}], \\ \bar{\xi} &= [\frac{\partial \vec{F}_1}{\partial \theta_1}, \frac{\partial \vec{F}_k}{\partial \theta_k} \cdots \frac{\partial \vec{F}_K}{\partial \theta_K}], \\ \text{and} \qquad \bar{R}_{\text{xx}} &= \frac{1}{M}\vec{x}^{\text{T}}\vec{x}. \end{aligned} \tag{3.31}$$

An extension to the CRLB for two dimensions case, that is the two unknowns θ and ϕ has been derived in following work [64, Equation 19-21]. The two-dimensional CRLB is

$$\bar{CRLB} = \begin{bmatrix} CRLB_{\theta\theta} & CRLB_{\theta\phi} \\ CRLB_{\phi\theta} & CRLB_{\phi\phi} \end{bmatrix} = \frac{\sigma^2}{2M}\left[\Re\{\bar{\xi}_{\theta\phi}^{\text{H}}\bar{O}_{\perp}^{\text{F}}\bar{\xi}_{\theta\phi} \cdot 1_{2,2}\bar{R}_{\text{xx}}\}\right]. \tag{3.32}$$

Now, the partial derivative matrix $\bar{\xi}_{\theta\phi}$ has a second dimension and is given by:

$$\bar{\xi}_{\theta\phi} = [\frac{\partial \vec{F}_1}{\partial \theta_1}, \frac{\partial \vec{F}_k}{\partial \theta_k} \cdots \frac{\partial \vec{F}_K}{\partial \theta_K}; \frac{\partial \vec{F}_1}{\partial \phi_1}, \frac{\partial \vec{F}_k}{\partial \phi_k} \cdots \frac{\partial \vec{F}_K}{\partial \phi_K}]. \tag{3.33}$$

In the case of limited angular resolution far-field pattern data, the partial derivative matrices can be interpolated by obtaining the effective aperture distribution function of the antenna array, which is thoroughly discussed in [117], and is not presented here. Now, two examples of GNSS antenna configurations for CRLB estimations are discussed. These include four- and six-element antenna arrays. The scenario consists of a single RHCP source spanning the upper hemisphere with $M = 100$ received signal samples, and a fixed SNR, i.e. $\gamma = -10$ dB, which is typical for the GNSS signals [4].

Effect of inter-element separation: The computed $CRLB_{\theta\theta}$ and $CRLB_{\phi\phi}$, in dB, for the four-element square-shaped array geometry with different inter-element separation d, for the upper hemisphere are shown in Fig. 3.26. Here, it may be pointed out that lower the variance bound, in dB, better is the direction-finding capability of antenna array. Therefore, best DOA performance or the minimum CRLB is asserted by the largest inter-element separation, $d = \lambda/2$, because of the larger aperture area. Reduced inter-element separation increase the CRLB by 6 dB and 10 dB for $d = \lambda/4$ and $d = \lambda/5$, respectively, particularly in the low-elevation directions. However, even for $d = \lambda/2$ at lower elevations at azimuth locations $\phi = 0^{\text{o}}, 90^{\text{o}}, 180^{\text{o}}$, and 270^{o}, the bound is higher, which is attributed to the geometrical placement of the antenna elements at the diagonals of the azimuth.

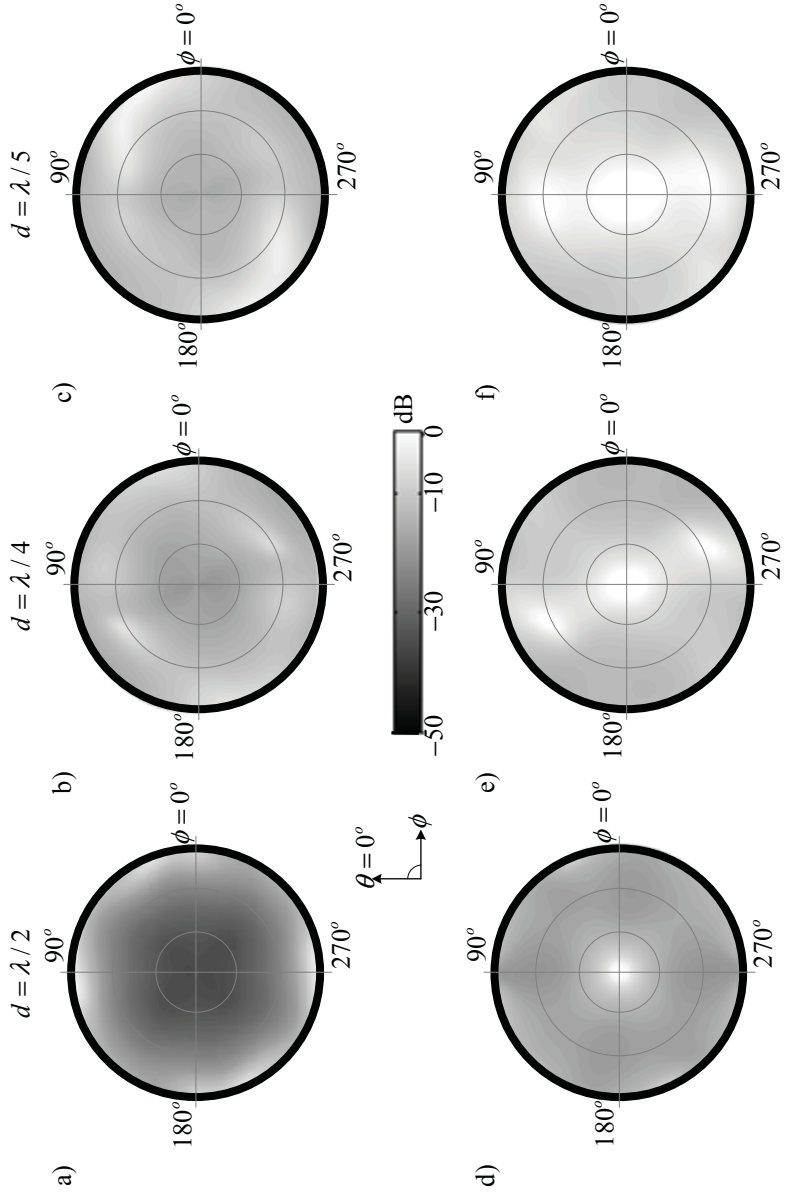

Figure 3.26: The estimated CRLB of the simulated four-element square-shaped lossless ceramic patch antenna arrays. Estimated $CRLB_{\theta\theta}$ for inter-element separation (a) $d = \lambda/2$, (b) $d = \lambda/4$, and (c) $d = \lambda/5$. Estimated $CRLB_{\phi\phi}$ for inter-element separation (d) $d = \lambda/2$, (e) $d = \lambda/4$, and (f) $d = \lambda/5$. Each column represents the same inter-element separation but different estimation angle.

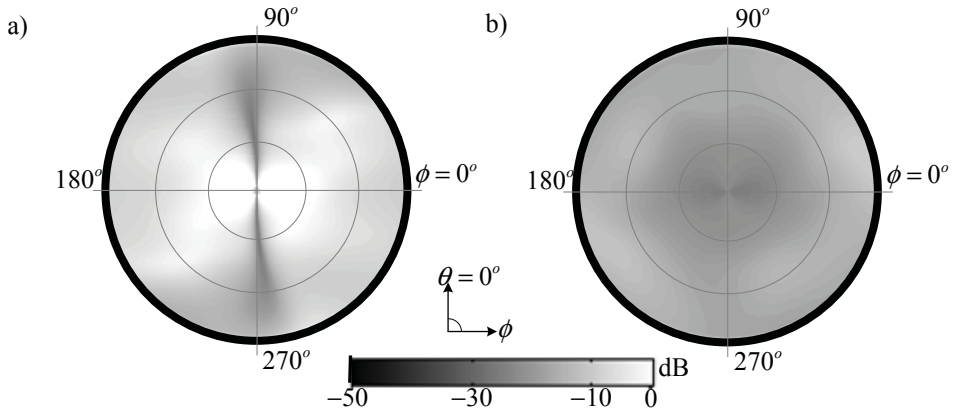

Figure 3.27: Estimated $CRLB_{\theta\theta}$ in the upper-hemisphere for the simulated four-element lossless square-shaped ceramic patch antenna array with inter-element separation $d = \lambda/4$ for (a) linear geometry oriented along $\phi = 0^{\text{o}}$ and (b) y-shaped geometry.

On the other hand, the $CRLB_{\phi\phi}$ is high on the zenith or high-elevation and is lower at lower elevation for the azimuth directions. This means that the DOA estimation is not spherically symmetric for elevation and azimuth. Furthermore, it also increases with decreasing inter-element separation. To simplify for the remaining section, the results are limited to the CRLB in elevation only.

Effect of geometry: In Fig. 3.27, $CRLB_{\theta\theta}$ is displayed for two different geometries of four-element antenna arrays with fixed inter-element separation, i.e. $d = \lambda/4$, which are linear and y-shaped (sketched in Fig. 3.7). The linear geometry is strongly impaired for DOA in the direction perpendicular to the orientation of the array (y-axis). This outcome is in accordance with the minimum eigenvalues in Table 3.2, which revealed that a linear configuration has the worst minimum eigenvalue. If the elements are distributed in a y-shaped geometry instead of the square shape, the CRLB is similar in high elevation but considerably improved for the low-elevation angles in all azimuth directions shown in Fig. 3.27b. Altogether, the mean DOA estimation is improved in comparison to the square geometry. However, it can be mentioned that the minimum eigenvalue for this y-shaped array is decreased by 20%. Therefore, this becomes a trade-off between better direction-finding capability and the robustness in the interference limited scenario. Nevertheless, it can be concluded that the antenna element arrangement even for the planar configuration can improve angular DOA estimation or achieving minimum CRLB.

Effect of number of elements: The six-element antenna array $CRLB_{\theta\theta}$ for hexagonal and rectangular geometry with $d = \lambda/4$ is shown in Fig. 3.28 The optimal CRLB is obtained for the hexagonal geometrical configuration. But, the rectangular geometry DOA performance is similar to the four-element square-shaped array, which may be attributed to the increased correlation among the embedded antenna patterns. Therefore, it is not

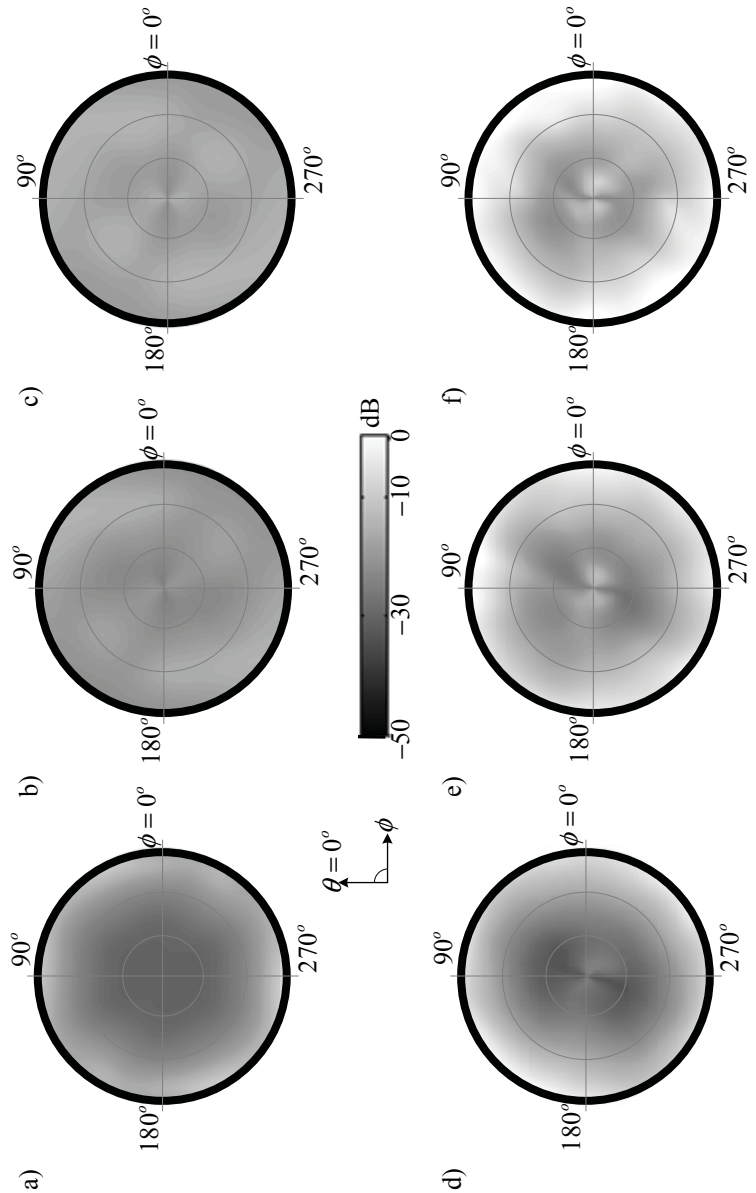

Figure 3.28: Estimated $CRLB_{\theta\theta}$ for the simulated six-element lossless ceramic patch antenna arrays. The hexagonal-shaped geometry with inter-element separation (a) $d = \lambda/2$, (b) $d = \lambda/4$, and (c) $d = \lambda/5$. The rectangular-shaped geometry with inter-element separation (d) $d = \lambda/2$, (e) $d = \lambda/4$, and (f) $d = \lambda/5$. Each column represents the same inter-element separation but different geometrical arrangement.

Table 3.4: Mean $CRLB_{\theta\theta}$, in dB, in the upper-hemisphere for the simulated four- and six-element lossless ceramic patch antenna arrays in the case of different geometrical and inter-element separation configurations.

	4-element			**6-element**		
geometry	$\lambda/2$	$\lambda/4$	$\lambda/5$	$\lambda/2$	$\lambda/4$	$\lambda/5$
square	-21	$-15(-12)$*	-12			
linear		$-4(-6)$*	-3			
y-shaped		-18				
hexagonal				-26	-20	-17
rectangular				-21	-16	-11

* The estimated values from the measured far-field patterns of the manufactured antenna arrays.

straightforward that increasing the number of elements minimises the CRLB; rather, it demands careful placement or geometrical configuration of the antenna elements to achieve optimal DOA performance.

The mean values for all directions in the upper hemisphere are presented in Table. 3.3. The CRLB for the implemented four-element arrays with $d = \lambda/4$ shown in Figs. 3.8 and 3.10 also verify the simulated antenna array CRLB and show similar behaviour.

3.8 Summary

In this chapter the phenomenon of mutual coupling is explained with the help of scattering waves interactions. In order to characterise the mutual coupling and its effect on the array radiation various figures-of-merit have been presented. Mutual impedance does offer a quick insight into the level of mutual coupling, however, its dependence on the illumination or excitation currents present difficulties of evaluating the array in wholesome. This problem is overcome by computing the array covariance matrix with either the available scattering parameters, which is only true for lossless antenna arrays, or the integration of the embedded realised amplitude gain of the antenna array in the sphere. Furthermore, the eigen-analysis or the eigen-decomposition of this covariance matrix provides basis function or eigenmodes of the array whose properties dictate the performance of the antenna array, in terms of the pattern shapes and the efficiencies, because in fact any scenario of illumination or excitation is a superposition of these basis functions. In general, all these diversity degrees-of-freedom need to be efficient and uniform, but the eigenvector corresponding to the minimum eigenvalue is proposed to be crucial for the diversity or the average SNR performance of the compact array in interference limited scenarios, and can

be solely optimised for improved quality of reception. Several lossless compact antenna arrays, using high dielectric permittivity truncated ceramic patch antennas, with different number of elements, inter-element separation and geometrical configurations are compared with respect to the minimum eigenvalue. This provides a platform for the choice of antenna array suitable for robust GNSS antenna arrays development in the coming chapters. It turns out, keeping the constraint of maximum three interferer scenario and minimum eigenvalue above 20%, suitable choices for the compact GNSS antenna arrays can be four elements with $d > \lambda/5$ in square arrangement or six elements with $d > \lambda/4$ in hexagonal shape geometry.

The polarisation purity of the compact antenna arrays is also specified by computing the eigenmode realised gain patterns for the respective polarisation analytically. The polarisation impurity of the even mode in the upper hemisphere can be optimised by altering the geometrical shape of the antenna elements, in presence of mutual coupling this is complex to achieve which sometimes require redesign and fabrication of the complete array. Therefore, it is necessary to tune the individual elements of the array, even mode polarisation characteristics, including the mutual coupling effects. This limits the practical use of readily available cheap ceramic antennas directly into the compact navigation receivers, where polarisation purity is intended.

This chapter provides the insight into direction-finding capabilities of the compact antenna arrays which determine the DOA performance of the receiver. For this purpose, the conventional CRLB is computed for simulated four and six element GNSS antenna arrays. Obviously, larger aperture area $d = \lambda/2$ results in the lower bound. The influence of geometry for the compact antenna array is quite significant. For example, the four-element antenna array with $d = \lambda/4$ in y-shaped geometry provides mean CRLB in upper hemisphere $3\ \mathrm{dB}$ (improved DOA estimations) less than the square geometry, even though it has the worse minimum eigenvalue relatively. Similarly, the six element antenna array for fixed inter-element separation hexagonal geometry provides $5\ \mathrm{dB}$ lower estimation variance than the rectangular. In a nutshell the geometry of the antenna array along with the aperture area does influence the direction-finding capabilities. Based on the observations, it may be concluded that usually, but not necessarily, the antenna array with higher minimum eigenvalue provides better DOA estimation.

Chapter 4

Compact Robust GNSS Antenna Array Receivers

In the previous chapter, insight into the degraded diversity degrees-of-freedom of the compact antenna arrays necessitates mitigation of the mutual coupling. This provides the possibility of restoring the power transfer between the antenna array and receiver disrupted due to mismatching or coupling. Theoretically, in the case of lossless implementation of such decoupling and matching full diversity can be achieved, but in reality this is not possible. Therefore, choice of the decoupling and matching technique and its implementation can greatly influence the performance of a receiver in particular, like its SNR.

As far as the decoupling of the antenna array is concerned, it can be performed either at the antenna level by introducing additional structures in between the antenna elements [46], [65]–[68] or by introducing decoupling networks, i.e. to excite orthogonal current distributions, eigenvectors, which result in the decoupling of the antenna ports [90], [28]. Generally, the available antenna-level decoupling techniques deliver narrow-band characteristics, whereas the network-based decoupling can be broadband but creates ohmic losses and requires additional space. Therefore, these designs need to be miniaturised and carefully optimised to achieve the desired purpose.

Customized miniaturized antenna arrays are developed and investigated for robust GNSS applications against narrow-band interference signals. In contrast to previous successful implementations, e.g. [100], the goal here is to provide the benefits of array processing on a smaller geometrical scale, where compactness is achieved by reducing both the size of the individual antenna elements as well as their inter-element separations. In order to achieve efficient radiative degrees-of-freedom, a DMN based on the eigenvector excitations explained in the previous section as proposed earlier, e.g. by Volmer [90] is integrated into the compact antenna arrays.

For receivers in general, and GNSS applications in particular, noise needs to be considered thoroughly since it limits overall system performance. DMNs are passive circuits;

they generate noise proportional to their ohmic losses. Since the DMN forms an integral part of the antenna, it must be connected directly to the feed ports of the array. Therefore, it must be placed in front of the first amplifier, resulting in a noise penalty that might outweigh the intended gain in diversity. So far, DMNs have been considered lossless [30]–[32], [69], [118]. To our knowledge, it has not yet been proven that real, i.e. dissipative, DMNs can be used beneficially for low-noise GNSS receivers.

Principally in this chapter, the influence of a real DMN on the system performance of the GNSS receiver chain is examined. The formulae for the CINR and the equivalent noise temperatures of the diversity receiver are derived from the antenna far-field patterns, the amplifier noise parameters, and their respective scattering parameters. Based on these equations, the performance of the whole receiver chain, with and without a dissipative DMN, is calculated and compared to the fabricated compact GNSS antenna arrays under different interference scenarios. Finally, a miniaturised compact GNSS array along with a DMN using cheap off-the-shelf components is developed for the purpose of industrial mass-production.

4.1 Techniques for antenna array decoupling

In the previous chapter, the mutual coupling of the compact antenna arrays was highlighted and discussed. For compact arrays there is a performance trade-off between the size and the number of elements of the antenna array. Obviously, the diversity performance of the antenna array with the same number of elements but smaller inter-element separations cannot be improved than larger inter-element separations. This may be enhanced by minimising the mismatch caused by the coupling. However, it is impossible to match the antenna array receiver elements for all possible direction of arrivals independently in the presence of strong coupling. Therefore, the compact antenna array poses a decoupling problem more than a matching one. Though, the ultimate goal is still matching of the antenna, which in fact follows the decoupling. Altogether, decoupling and matching is responsible for the overall improvement in antenna efficiency.

Perhaps due to the above mentioned reasons, decoupling techniques have received significant attention in the literature over the past decade. One such technique involves the reduction of the coupling between the antenna elements directly, e.g. defected ground structures, to ensure that the non-diagonal components of the scattering matrix are minimised, which may not be completely true for radiation decoupling as discussed in section 2.3 of the previous chapter. On the other hand, a decoupling network is designed to transform the antenna covariance matrix with the goal of making the cross-correlation coefficients zero.

4.1.1 Radiation element level decoupling

One way to perform the antenna decoupling is to directly reduce the mutual coupling between the elements. This is achieved by the introduction of additional structures in the ground-plane or the near-field to modify their current distributions. These techniques can be classified as follows:

1. Electromagnetic band-gap structures;
2. Parasitic structures;
3. Neutralisation lines.

EBG structures: EBG structures provide the pass- and stop-frequency band characteristics which, when inserted in between the antenna elements, stop and trap the coupled energy [70]. Typically, such structures take the form of DGS or frequency-selective surfaces. In case of microstrip antennas, these additionally help in suppressing surface waves.

The modification of the ground-plane for microstrip antenna arrays is not a suitable option for the receivers, where the circuitry is fabricated at the back of the antenna with the common ground-plane, for miniaturisation. Also, the size of structure is generally half of the free-space guide wavelength which is not attractive for compact antenna array designs. It is worth mentioning that most of the literature describing such implementations consider antenna element separations equal to $\lambda/2$, which brings about another uncertainty for implementation in compact antenna arrays. Normally, the smaller inter-element separations are avoided because of the larger size of the DGS unit cells. Furthermore, it becomes complex to deploy such structures in a planar antenna array with larger elements. Moreover, the backward radiation is increased for such designs, which is a drawback for GNSS receiving arrays.

There is another approach to implement EBG structures, i.e. the use of frequency-selective surfaces in between the ground-plane and the antenna layer [71]. This is expensive to implement because of the multi-layer technology. Besides the cost, it is narrowband and the frequency selectivity depends on the direction of illumination source, which is not suitable for GNSS applications where the useful satellites are present in the complete upper hemisphere.

The shorting-vias fence around the individual antenna elements is another approach to mitigate the mutual coupling. Maximum rejection is obtained when the fence is at quarter of a free-space wavelength distance from the elements. This hinders the miniaturisation of the inter-element separation between the antenna elements intended for the compact antenna array configurations.

Parasitic structures: This involves passive parasitic elements between the antenna elements. These new elements are terminated with reference load impedance, and absorb

the mutual coupling energy as described in [119]. This technique is especially used in wire antenna arrays, e.g. electronically-steerable parasitic array radiator antennas, even though here the main objective is to achieve higher directivity, but it still helps in mitigating mutual coupling effects. In the case of compact planar antenna arrays, it is not easy to place a replica parasitic element in between two radiating elements due to its two-dimensional structure and size. Apart from that, the parasitic elements have a resonant behaviour, and so the decoupling is narrow band.

Neutralisation line: A simple yet intuitive method of antenna-level decoupling is described in [68]. Here, a suspended transmission line is connected between the antenna array elements, and acts as a neutralisation line to counter the mutual coupling. Different configurations of the line provide either a high decoupling (isolation) over narrow frequency bandwidth or a moderate decoupling (isolation) over wide frequency bandwidth. Broadly speaking, this technique has only been investigated for two-element arrays because of its simplicity and the needed large lengths of line.

In general, decoupling techniques at the antenna-level are possible but the drawback of the additional structure size, narrow bandwidth and its placement around the antenna in particular makes them unsuitable for compact planar antenna arrays. Secondly, the properties of the decoupling structures at the antenna-level may depend on the array excitation current vectors which is undesirable for direction-finding arrays.

4.1.2 Network-based decoupling

Generally, in the recent past, two network-based techniques have been given considerable attention. The first is based on the current transformation network of an antenna array by applying a network consisting of lumped or discrete components. The second technique involves the exploitation of the symmetrical geometrical properties of the antenna array, which means that the eigenvectors required to decouple the antenna array are similar to the eigenvectors generated by the available $180^{\text{o}}-$*hybrid* and $90^{\text{o}}-$*directional* couplers.

Current transformation matrix based decoupling network: This involves using a transfer matrix to transform the antenna array scattering matrix into a new scattering matrix with the constraint $\bar{S}_{\text{A}} = \bar{0}$. The transformation matrix can take the form of the orthogonal vectors, such as eigenvectors, of the antenna array covariance matrix. In case of an N elements array to completely decouple the antenna array $N(2N-1)$, discrete components are required, whereas decoupling and matching together require $N(2N+1)$ discrete elements. Therefore, for the two-element compact antenna array, six elements are required to decouple the antenna array, which increases to 28 elements in the case of a four-element array. Surely, the complexity and the number of discrete elements increases with the number of radiating elements in the antenna array. The benefit of this technique is associated with the possibility of decoupling non-identical and non-symmetric antenna

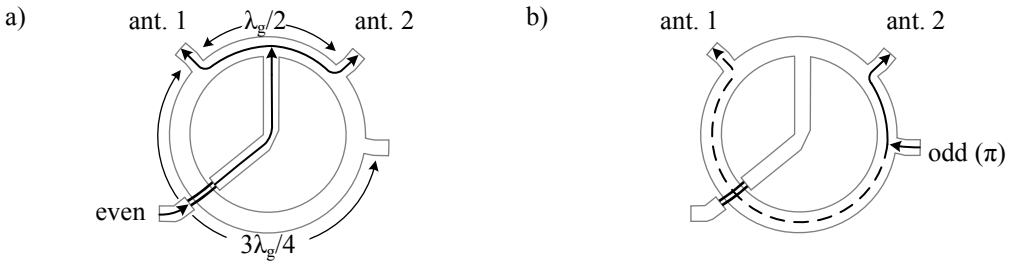

Figure 4.1: Signal flow of the single symmetric 180^{o}-hybrid coupler for the (a) even mode and (b) odd or π mode.

arrays. It also offers flexibility to receive from all possible arbitrary orthogonal basis vectors, depending on the type of the desired application, which may involve receiving from orthogonal sub-spaces of the hemisphere with a single main beam (single source) only.

The bandwidth and efficiency of the network depend on the losses or the quality of the individual components, in combination with the design of the network, due to possible raised number of cross-overs with the increasing number of elements. The drawback of this technique is the a priori knowledge of the antenna parameters, in particular the scattering parameters. The accuracy of these parameters measurements affect the overall performance of the network. This means that the network becomes specific to a particular antenna array and cannot be generalised for any other similar configuration antenna array.

Decoupling across symmetry planes: The simplest case of a two-element compact antenna array constitutes the foundation for decoupling larger symmetrical antenna arrays. The eigenvector matrix $\bar{Q}$ needed to decouple this antenna array is given by:

$$\bar{Q} = \frac{1}{\sqrt{2}} \begin{bmatrix} 1 & -1 \\ 1 & 1 \end{bmatrix} \tag{4.1}$$

The block matrices corresponding to the even and odd mode vectors are similar to the eigenvectors excited by the rat-race, $180^{\text{o}}-$hybrid [72], or branch-line couplers [73]. The first column vector of the $\bar{Q}$ matrix is the even mode of the coupler, whereas the second column is the odd, or the π, mode. In Fig. 4.1, the two modes of the $180^{\text{o}}-$hybrid coupler are illustrated. In this case, any type of directional coupler is suitable for the practical implementation of the decoupling network. For the symmetric case, the benefit of the decoupling network with directional couplers is that it does not require the scattering matrix of the antenna array to be known. For any $2N-$element antenna array the decoupling procedure is to partition the antenna array into its symmetric planes and then apply the two-port decoupling across each plane until all the elements and symmetries are exhausted. The necessary condition is that the array must possess at least one plane of symmetry, where

elements 1 to N are different, and are the same from $N+1$ to $2N$ elements. This antenna array symmetry is typically, but not necessarily, the result of geometrical symmetry. Therefore, for a symmetric antenna array, the scattering parameter in block notation can be written as

$$\bar{S} = \begin{bmatrix} \bar{S}_{11} & \bar{S}_{21} \\ \bar{S}_{21} & \bar{S}_{11} \end{bmatrix}. \tag{4.2}$$

A bank of symmetric $180^{\text{o}}-$hybrid couplers is applied to decouple the antenna array element across the single plane of symmetry. The individual decoupling of the two elements is not influenced or affected by the other decoupling. The new set of ports are further decoupled for the new symmetries until all the symmetries are exhausted. This type of decoupling procedure is valid for an array consisting of elements of the power two. However, as described in [90, Section 3.4.3] radiator merging arbitrary $N-$element arrays can also be decoupling using this strategy.

Let's consider the decoupling of the four-element square-shaped antenna array with hybrid couplers. First, the antenna array is decoupled by connecting two hybrid couplers across the vertical plane of symmetry. A single hybrid coupler is applied to decouple elements 1 and 2, and another one decouples elements 3 and 4. This creates an $even$ and an odd set of ports which are independent of each other. As a result of the additional horizontal symmetry plane, both sets are port-symmetric themselves and can therefore be decoupled with two hybrid couplers independently. The final decoupling network consists of four hybrid couplers as shown in Fig. 4.2. Note, the complete network is designed independently of any measurement data.

In Fig. 4.2a the $even$ mode signal flow inside the decoupling network is shown. The incoming signal is split into two equal amplitudes and phase signals. Subsequently, these two output signals excite the even modes of the next bank of hybrid couplers, which eventually excite all the antenna elements relative to each other with equal phase and amplitude. In Fig. 4.2b the odd mode of the first hybrid coupler is excited, which generates two equal amplitude but 180^{o} out-of-phase signals, which in turn again excite the even modes of the consequent hybrid couplers. Therefore, antennas 1 and 2 are excited with similar phases and antennas 3 and 4 are excited with similar phases to each other, but 180^{o} out-of-phase signals relative to the aforementioned antenna elements. This is denoted as the $odd-1$ mode. In Fig. 4.2c the $odd-2$ mode signal flow is illustrated. Now, antennas 2 and 3 are excited with similar phases, but 180^{o} out-of-phase with antennas 1 and 4. In the last scenario, shown in Fig. 4.2d, all the adjacent elements have equal amplitudes but 180^{o} out-of-phase excitation. From discussions in Chapter 3, this is the π mode, which has the least efficiency but maximum number of nulls. The complete excitation matrix is

a)

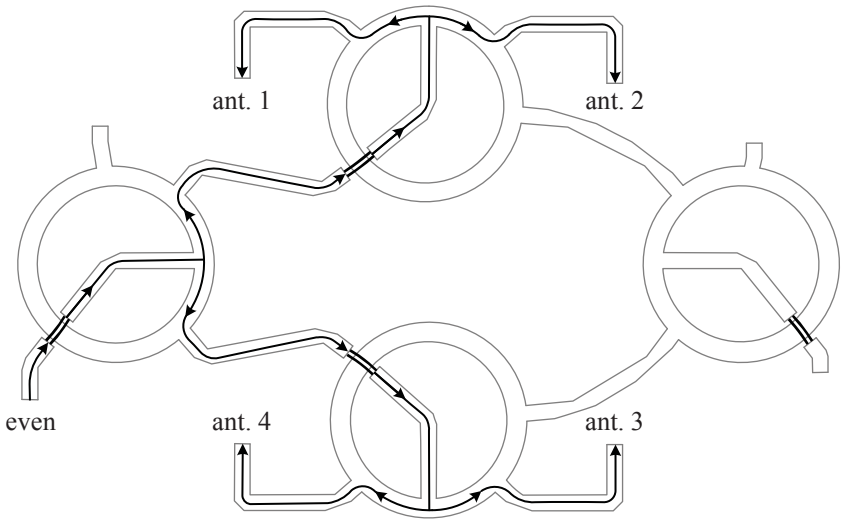
ant. 1
ant. 2
even
ant. 4
ant. 3
in-phase
out-of-phase
jumper

b)

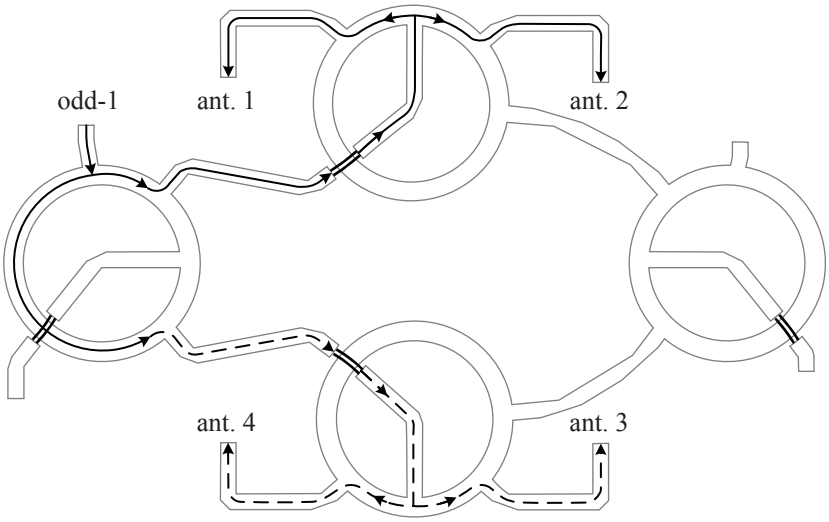
odd-1
ant. 1
ant. 2
ant. 4
ant. 3

c)

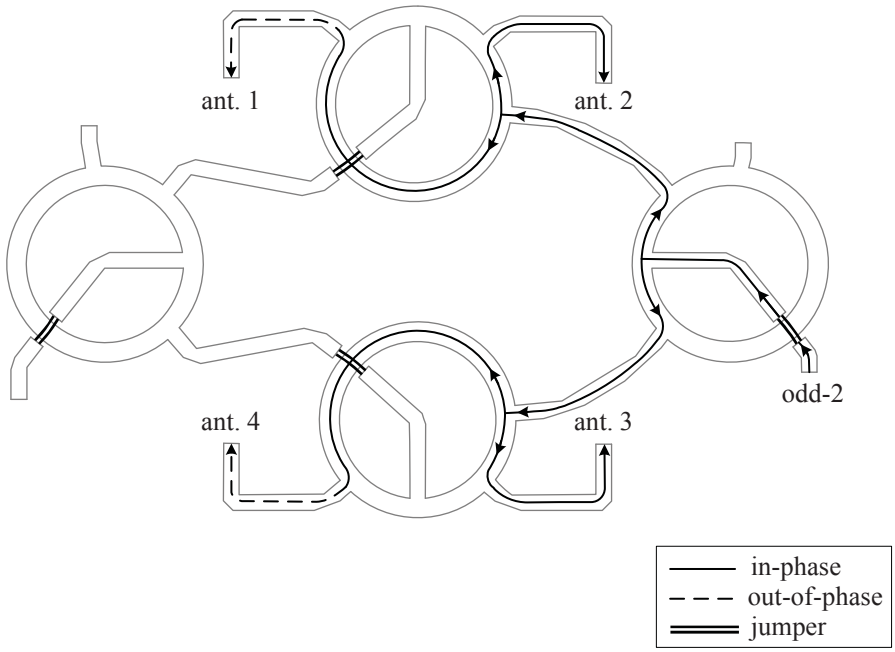

d)

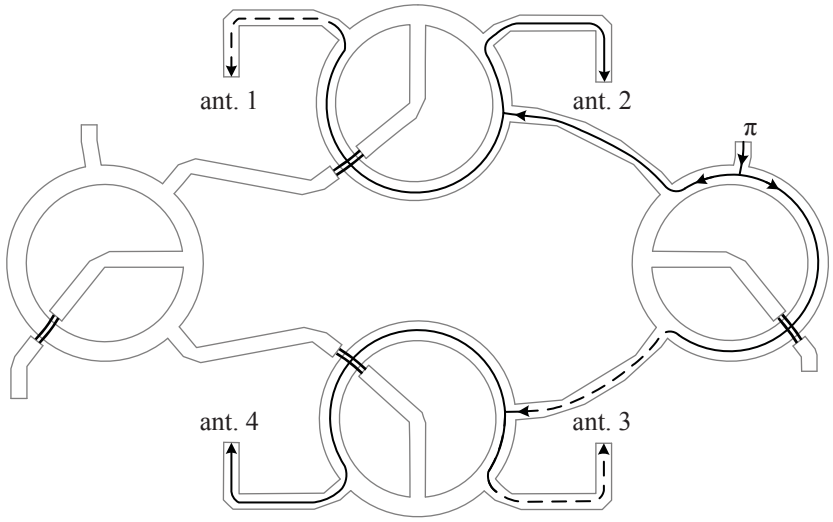

Figure 4.2: Decoupling network for the four-element antenna array using four 180^{o}-hybrid couplers. Additionally, illustration of the signal flow for the (a) even , (b) odd-1, (c) odd-2, and (d) π mode is sketched.

$$\bar{Q} = \frac{1}{2}\begin{bmatrix} 1 & 1 & -1 & -1 \\ 1 & 1 & 1 & 1 \\ 1 & -1 & 1 & -1 \\ 1 & -1 & -1 & 1 \end{bmatrix}. \tag{4.3}$$

This matrix also holds valid for the receive case because of the reciprocity.

4.2 Techniques for modal matching

Post decoupling, the antenna array scattering parameters become a diagonal matrix while the off-diagonal elements or the coupling coefficients become zero. Therefore, it is the individual ports impedance matching to a reference impedance $\bar{Z}_o$ that needs to be performed. For eigenmode antenna arrays, however, it is the impedance matching of the respective modes that needs to be carried out. As far as the reference impedance matching is concerned, complex conjugate matching of the input impedance denoted by $\bar{\Gamma}_{\mathrm{P}}$ of the LNA stage can be performed to achieve the maximum power transfer, sometimes called *power matching*. In the case of the receiver, it is useful to transform the impedance to $\bar{\Gamma}_{\mathrm{opt}}$ of the LNA, referring to the impedance value which provides the minimum NF instead of the maximum amplification gain; this strategy is known as *noise matching*. However, in one of the studies carried out in [157], it was observed that the modern designs of the LNA are optimised such that $\bar{\Gamma}_{\mathrm{P}}$ and $\bar{\Gamma}_{\mathrm{opt}}$ are close to each other, therefore, noise matching and power matching give similar CNR values.

Typically, the received signal comprises a fractional bandwidth, $B_{\mathrm{f}} = \Delta f / f_o$, around the carrier frequency, f_o, which, in the case of the L1/E1 C/A-code narrowband signal is approximately 0.1%. This increases to 1–2% for military P-codes. Therefore, for an antenna array the impedance matching fractional bandwidth is desired to be at least equal to or greater than the desired received signal bandwidth. This raises the question in the case of a compact antenna array which has a small aperture area, of how much of the impedance matching bandwidth of the modal antenna array is achievable. Hence, it is necessary to investigate the maximum impedance matching bandwidth limitations of the modal compact antenna array.

4.2.1 Fundamental bandwidth limitations

An antenna array with eigenmode excitation vectors can also be visualised as a multi-mode antenna which excites these fundamental modes from separate single feed ports. This approximate equivalence means that the reduction of the electrical size of the multi-mode antenna is similar to the miniaturisation of the inter-element separation of the antenna array.

Furthermore, the bandwidth limitation calculations of the multi-mode antenna can provide useful insight into the equivalently sized eigenmode antenna array bandwidth lower bounds, which will be employed in this section.

The far-field characteristics of the multi-mode antenna enclosed in a surface of radius, a, may be expressed in terms of the equivalent circuits of transverse electric, TE_{mn}, and transverse magnetic, TM_{mn}, modes, where m defines the order of the spherical Bessel function [15, Chapter 10], and n represents the azimuthal variation. Generally, the well-known Fano limit for the maximum achievable matching bandwidth of these modes is obtained using these equivalent circuits [74]. However, in the case of the higher-order modes, where $m > 1$, it is tedious to solve this with increasing circuit complexity and non-linearity of the Fano theory. Therefore, the resistance, inductance and capacitance based approximate equivalent circuits involving Q-factor, Q_{f}, valid for the above mentioned modes is described in [75, Section 2]. Here, Q_{f} represents the quality factor of the antenna radiation. It is commonly known that the achievable matching fractional bandwidth, B_{f}, is inversely proportional to Q. However, Gustaffson has derived an inequality for the lowest bound of the reflection coefficient, $|\Gamma|$, as a function of the antenna radiation quality factor and the fractional bandwidth, which is [75, Equation 25]

$$|\Gamma| \geq \exp\left(-\frac{\pi}{\kappa_{\text{m}}}(1 - B_{\text{f}}^2/4)\right), \qquad \text{where} \quad \kappa_{\text{m}} = Q_{\text{f}} B_{\text{f}}. \tag{4.4}$$

This follows that if the antenna quality factor for the given propagation mode is known then the achievable bandwidth for a given reflection coefficient can be estimated. The quality factor of the antenna is defined by the ratio of the stored reactive energy to the total radiated power. Furthermore, in this analysis it is assumed that the antennas are lossless, which follows

$$Q_{\text{f}} = \frac{4\pi f_o W}{P_{\text{rad}}}. \tag{4.5}$$

W is the maximum amount of stored electric and magnetic energy. In [76], Chu describes the quality factor closed form equation for the spherical modes, TM_{m0}, which possess a greater amount of stored electric energy in comparison to stored magnetic energy. Moreover, the quality factor is independent of the azimuthal mode index variations, therefore it is fixed to $n = 0$ [77, Section 2]. Also, relevant to our interest, the TM_{m0} are typical propagation modes in the case of a rectangular planar antenna [16, Section 4.2]. In the case of cylindrical modes, which are the superposition of TE and TM modes, the reader is referred to [77, Section 3]. For clarity and simplicity, here only the spherical modes are investigated. Now, the Q_{f} of the TM_{m0}, denoted as Q_m^{f}, is obtained by:

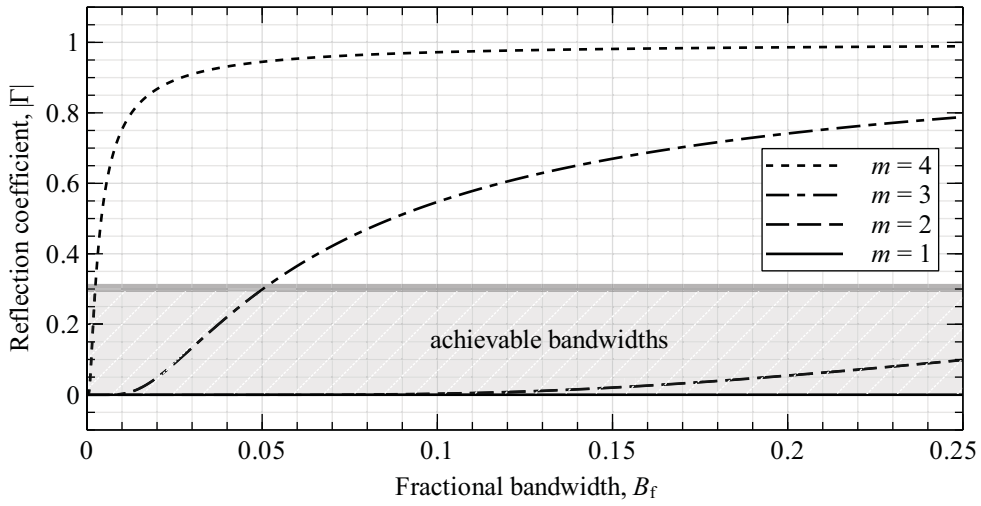

Figure 4.3: Numerically calculated fractional bandwidth limitations of the first four TM_{m0} modes of lossless antenna for a given reflection coefficient $|\Gamma|$ with electrical size fixed to $a = 0.25\lambda$. The grey line indicates the -10 dB criterion, and shaded region highlight the possible bandwidths for various modes.

$$
\begin{aligned}
Q_m^{\mathrm{f}} = ka[1 - \Bigg\{ \left(\frac{(ka)^2}{2} + m + 1 \right) \left(j_{s_m}^2(ka) + y_{s_m}^2(ka) \right) \Bigg\} \\
- \frac{ka}{2} \left(j_{s_{m+1}}^2(ka) + y_{s_{m+1}}^2(ka) \right) \\
+ ka \frac{(2n+3}{2} \left(j_{s_m}(ka) j_{s_{m+1}}(ka) + y_{s_{m+1}}(ka) y_{s_{m+1}}(ka) \right) \Bigg].
\end{aligned}
\tag{4.6}
$$

$j_{s_m}(ka)$ and $y_{s_m}(ka)$ represent the spherical Bessel functions of the first and second kind respectively, calculated for the m order at ka which is the electrical size of the antenna, and refers to a product of the wavenumber $k = 2\pi/\lambda$ and sphere with radius a enclosing the antenna. If the electrical size of the antenna is fixed such that $a = 0.25\lambda$, then the first four modes minimum bound for the reflection coefficient against the achievable fractional bandwidths is plotted in Fig. 4.3. This illustrates the fact that for a certain value of $|\Gamma|$, B_{f} decreases with increasing mode order. For example, if $|\Gamma| = 0.3$ and $B_{\mathrm{f}} = 5\%$, then only the first three modes meet this condition, and fourth mode is useless for this criteria. With a smaller electrical size, $ka \leq 1$, ultimately all modes of the antenna eventually become useless with increasing bandwidth.

In Fig. 4.4 for $m = 4$ with variable electrical size, a, the reflection coefficients along with maximum achievable fractional bandwidths B_{f} is shown. The increased antenna aper-

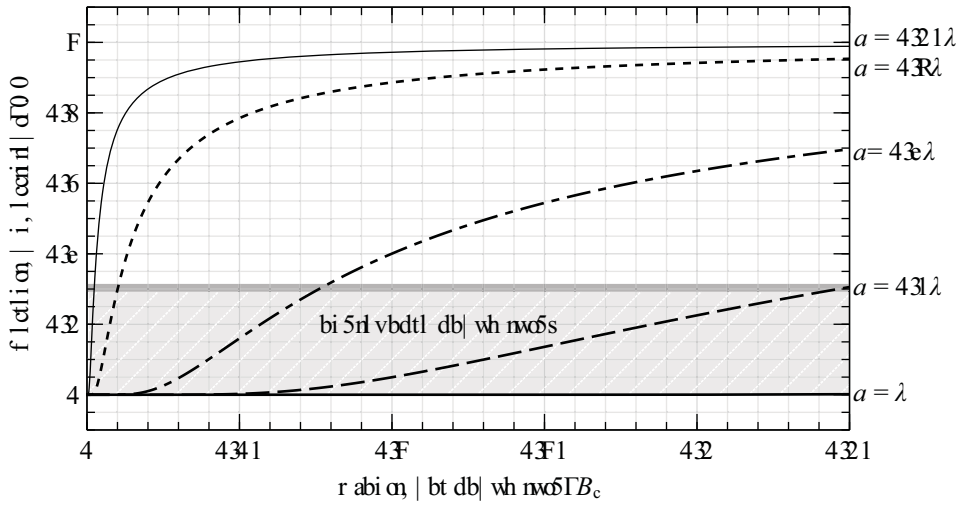

Figure 4.4: Numerically calculated fractional bandwidth limitations of the TM_{40} mode of lossless antenna for a given reflection coefficient $|\Gamma|$ with changing electrical size a. The grey line indicates the -10 dB criterion, and shaded region highlight the possible bandwidths for mode 4 in the case of different sizes a of the antenna.

ture offers larger bandwidth to achieve $|\Gamma| = 0.3$. Therefore, a trade-off for the larger size of the antenna is necessary to make all modes useful. Similarly, for higher modes, such curves can provide an insight into the limitations of fractional bandwidth for a given aperture size. Note, the antenna modal bandwidth constraints depend on the application and characteristics of the desired signal.

4.2.2 Practical implementations and implications

The matching network can be integrated after the decoupling to maximise the power transfer. Basically, this network constitutes passive lumped components. These lumped components can be designed via the quasi-lumped or off-the-shelf available discrete components. Therefore, the performance of the network is affected by the individual properties of these lumped components.

In case of the quasi-lumped strategy it is possible to achieve high quality -factor or high efficiencies for the individual components, which means better overall antenna array efficiency. However, this produces narrowband characteristics which make the network sensitive to the material and manufacturing tolerances, and it becomes difficult to tune and achieve the exact operating band. This demands the matching network to be either exposed and accessible for post-manufacturing tuning or re-configurable to match component design in order to cope with these tolerances. Furthermore, such modifications compromise

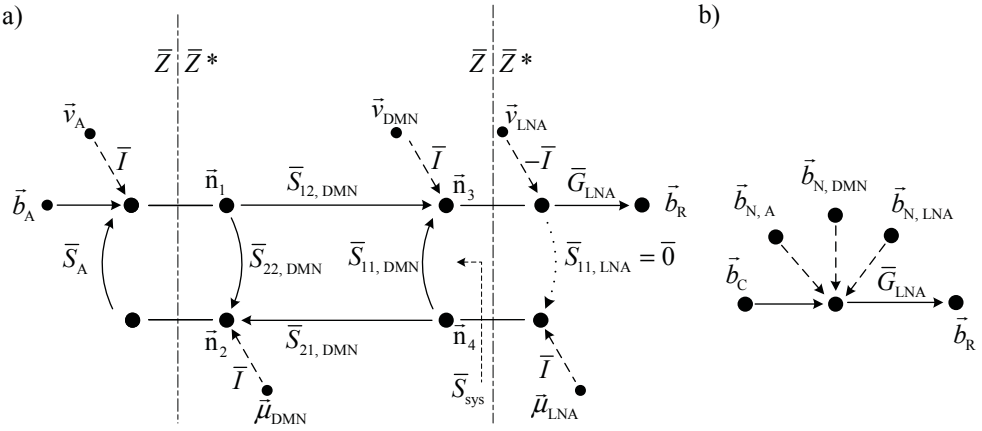

Figure 4.5: (a) Complete matrix signal flow diagram of the diversity receiver including the antenna array signal power waves $\vec{b}_A$ and the noise power waves $\vec{\nu}$ and $\vec{\mu}$ of the constituent receiver parts. (b) Collapsed signal flow graph of the received combined signal vector $\vec{b}_R$ involving the received noise power wave vectors $\vec{b}_{N,A}$, $\vec{b}_{N,DMN}$, and $\vec{b}_{N,LNA}$ along with signal power wave vector $\vec{b}_C$.

the overall miniaturisation and integration intended for compact antenna arrays.

The application of discrete off-the-shelf lumped components offer mounting and re-mounting flexibility in order to adjust for the manufacturing and material tolerances. In general, these lumped components have low quality-factor, with typical values ranging from 1–25 at the L-band[145], [146]. This results in greater bandwidth at the expense of losses of the network components, which will limit the maximum achievable CNR.

The material and design order of the matching network does affect the resulting bandwidth characteristics of the antenna array. This type of investigation is carried out in the work [90, Chapter 3], where different individual lumped designs and network topologies are implemented, especially for the bandwidth-limited compact antenna array higher-order modes. This reveals that the realised gain bandwidth product of the higher-order modes remain the same for all configurations, meaning that the increased bandwidth beyond the fundamental limit results in reduced realised gain, because of the ohmic losses within the network.

4.3 Noise characterisation of the robust receiver

Following the diversity model shown in Fig. 3.5, the matrix signal flow graph for the integrated receiver, including the antenna array, DMN and LNAs is depicted in Fig. 4.5. The edge weights in the graphs are matrices, which in general do not commute under multiplication. A Mason-like approach by Riegle and Lin [78] specifically developed for matrix signal flow graphs is applied to solve the noise matrices.

Now, the receiver noise covariance matrix, $\bar{R}_{\mathrm{n}}$, is defined as:

$$\bar{R}_{\mathrm{n}} = \mathrm{Var}\{\vec{b}_{\mathrm{n}}\} = k\bar{T}_{\mathrm{sys}}B. \tag{4.7}$$

To obtain this, firstly, the $\vec{\nu}$ and $\vec{\mu}$ forward and reverse travelling noise wave sources have been introduced. The simplified signal flow graph, according to Fig. 4.5b, the received noise covariance matrix is basically a superposition of the antenna array, DMN and the LNAs covariance matrices. Therefore,

$$\mathrm{Var}\{\vec{b}_{\mathrm{n}}\} = \mathrm{Var}\{\vec{b}_{\mathrm{N,\,A}}\} + \mathrm{Var}\{\vec{b}_{\mathrm{N,\,DMN}}\} + \mathrm{Var}\{\vec{b}_{\mathrm{N,\,LNA}}\}, \tag{4.8}$$

or in terms of the noise temperature matrices it leads to

$$\bar{T}_{\mathrm{sys}} = \bar{T}_{\mathrm{N,\,A}} + \bar{T}_{\mathrm{N,\,DMN}} + \bar{T}_{\mathrm{N,\,LNA}}. \tag{4.9}$$

Assuming uncorrelated noise sources, the respective noise temperature covariance matrices of receiver blocks can be calculated independently. All of these are derived at the reference plane definition at the input of the LNAs.

4.3.1 Antenna array noise

The noise temperature covariance matrix, $\bar{T}_{\mathrm{N,\,A}}$, of the antenna array depends on the received noise wave vector, $\vec{b}_{\mathrm{N,\,A}}$, which is given by the relationship:

$$\mathrm{Var}\{\vec{b}_{\mathrm{N,\,A}}\} = k\bar{T}_{\mathrm{N,\,A}}B. \tag{4.10}$$

Considering the noise-free DMN and LNA, the complete noise wave model is simplified, and the received noise wave vector at the input of the LNAs becomes

$$\vec{b}_{\mathrm{N,\,A}} = \bar{G}_{\mathrm{LNA}}\vec{\mathrm{n}}_3 \tag{4.11}$$

The complete set of equations for the respective node vectors are as follows:

$$\begin{aligned}
\vec{\mathrm{n}}_1 &= \vec{\nu}_{\mathrm{A}} + \bar{S}_{\mathrm{A}}\vec{\mathrm{n}}_2,\\
\vec{\mathrm{n}}_2 &= \bar{S}_{22,\,\mathrm{DMN}}\vec{\mathrm{n}}_1 + \bar{S}_{21,\,\mathrm{DMN}}\vec{\mathrm{n}}_4,\\
\vec{\mathrm{n}}_3 &= \bar{S}_{12,\,\mathrm{DMN}}\vec{\mathrm{n}}_1 + \bar{S}_{11,\,\mathrm{DMN}}\vec{\mathrm{n}}_4,\\
\vec{\mathrm{n}}_4 &= 0.
\end{aligned} \tag{4.12}$$

Now, manipulating (4.12) and solving for $\vec{\mathrm{n}}_3$,

$$\vec{\mathrm{n}}_3 = \bar{S}_{12,\,\mathrm{DMN}}(\bar{I} - \bar{S}_{\mathrm{A}}\bar{S}_{22,\,\mathrm{DMN}})^{-1}\vec{\nu}_{\mathrm{A}} \tag{4.13}$$

Here, the transfer gain matrix, $\bar{G}_{\text{DMN}}$, of the DMN can be defined as:

$$\bar{G}_{\text{DMN}} = \bar{S}_{12,\,\text{DMN}}(\bar{I} - \bar{S}_{\text{A}}\bar{S}_{22,\,\text{DMN}})^{-1}. \tag{4.14}$$

Therefore, the received antenna noise wave covariance matrix follows from:

$$\text{Var}\{\vec{b}_{\text{N, A}}\} = \bar{G}_{\text{LNA}}\bar{G}_{\text{DMN}}\bar{T}_{v_{\text{A}}}\bar{G}^{\text{H}}_{\text{DMN}}\bar{G}^{\text{H}}_{\text{LNA}}, \tag{4.15}$$

where $\text{Var}\{\vec{\nu}_{\text{A}}\} = k\bar{T}_{v_{\text{A}}}B$, basically, the noise contributions to the antenna are related to the environment noise captured by the antenna array and the ohmic losses within the antenna array.

The environment noise temperature captured by the antenna array can be obtained by the integration of the normalised realised gain patterns over the complete sphere along with the angular distribution function of the environment temperature. On other hand, the ohmic losses are associated with the ambient temperature $T_{\text{amb}} = 290\text{K}$. The ohmic losses within the antenna array can be calculated with the aid of the antenna array radiated and accepted power covariance matrix, as derived in the previous chapter. Therefore, the antenna noise wave vector covariance matrix is given by:

$$\begin{aligned}\bar{T}_{v_{\text{A}}} = \frac{1}{4\pi}\int_0^{2\pi}\int_0^{\pi} T_{\text{env}}(\theta,\phi)\cdot\vec{F}_n(\theta,\phi)\vec{F}^{\text{H}}_m(\theta,\phi)\text{cos}\theta\text{d}\phi\text{d}\theta \\ + T_{\text{amb}}(\bar{R}_{\text{acc}} - \bar{R}_{\text{rad}})^{\text{T}}\end{aligned} \tag{4.16}$$

However, if the environment temperature distribution is assumed to be uniform over the sphere then (4.16) is simplified to

$$\bar{T}_{v_{\text{A}}} = T_{\text{env}}\bar{R}_{\text{rad}} + T_{\text{amb}}(\bar{R}_{\text{acc}} - \bar{R}_{\text{rad}})^{\text{T}}. \tag{4.17}$$

Using (4.10) and the simplified form of (4.16), leads to the noise temperature covariance matrix of the antenna as

$$\bar{T}_{\text{N, A}} = \bar{G}_{\text{LNA}}\bar{G}_{\text{DMN}}(T_{\text{env}}\bar{R}^{\text{T}}_{\text{rad}} + T_{\text{amb}}(\bar{R}_{\text{acc}} - \bar{R}_{\text{rad}})^{\text{T}})\bar{G}^{\text{H}}_{\text{DMN}}\bar{G}^{\text{H}}_{\text{LNA}} \tag{4.18}$$

4.3.2 Decoupling and matching network noise

In previous studies, the DMN is considered to be lossless, which means that the noise contribution is zero. In other words, the lossless DMN will lead to $\bar{T}_{\text{N, DMN}} = 0$. But in reality the losses play a vital role in the characterisation of the receiver noise, as these appear before the first amplification stage and must be considered for complete performance analysis. Therefore, it is necessary to find the DMN covariance matrix and its contribution to the receiver noise.

The DMN noise covariance matrix is given by:

$$\text{Var}\{\vec{b}_{\text{N, DMN}}\} = k\bar{T}_{\text{N, DMN}}B \tag{4.19}$$

Now, the receiver signal flow diagram considers the forward and reverse travelling $\vec{\nu}_{\text{DMN}}$ and $\vec{\mu}_{\text{DMN}}$ respectively. Accordingly, the antenna and the LNA is assumed to be noise free. The received noise wave vector due to DMN noise using the matrix signal flow diagram can be written as:

$$\vec{b}_{\text{N, DMN}} = \bar{G}_{\text{LNA}}\vec{\text{n}}_3. \tag{4.20}$$

Similarly, the respective nodes shown in Fig. 4.5 can be equated as:

$$\begin{aligned}
\vec{\text{n}}_1 &= \bar{S}_{\text{A}}\vec{\text{n}}_2, \\
\vec{\text{n}}_2 &= \vec{\mu}_{\text{DMN}} + \bar{S}_{22,\,\text{DMN}}\vec{\text{n}}_1 + \bar{S}_{21,\,\text{DMN}}\vec{\text{n}}_4, \\
\vec{\text{n}}_3 &= \vec{\nu}_{\text{DMN}} + \bar{S}_{11,\,\text{DMN}}\vec{\text{n}}_4 + \bar{S}_{12,\,\text{DMN}}\vec{\text{n}}_1, \\
\vec{\text{n}}_4 &= 0.
\end{aligned} \tag{4.21}$$

Solving for $\vec{\text{n}}_3$ gives:

$$\vec{\text{n}}_3 = \vec{\nu}_{\text{DMN}} + \bar{G}_{\text{DMN}}\bar{S}_{\text{A}}\vec{\mu}_{\text{DMN}}. \tag{4.22}$$

Therefore, the DMN noise wave covariance matrix can also be written as:

$$\begin{aligned}
\text{Var}\{\vec{b}_{\text{N, DMN}}\} = \bar{G}_{\text{LNA}}(&\bar{T}_{v_{\text{DMN}}} + \bar{G}_{\text{DMN}}\bar{S}_{\text{A}}\bar{T}_{\mu_{\text{DMN}}}\bar{G}^{\text{H}}_{\text{DMN}}\bar{S}^{\text{H}}_{\text{A}} \\
&+ \bar{T}_{v\mu_{\text{DMN}}}\bar{G}^{\text{H}}_{\text{DMN}}\bar{S}^{\text{H}}_{\text{A}} + \bar{G}_{\text{DMN}}\bar{S}_{\text{A}}\bar{T}_{\mu v_{\text{DMN}}})\bar{G}^{\text{H}}_{\text{LNA}}.
\end{aligned} \tag{4.23}$$

In case of any two-port passive network, the noise waves covariance matrix can be found using the scattering parameters, and is given by:

$$\text{Var}\left\{\begin{pmatrix}\vec{\nu}_{\text{DMN}} \\ \vec{\mu}_{\text{DMN}})\end{pmatrix}\right\} = kB\begin{pmatrix}\bar{T}_{v_{\text{DMN}}} & \bar{T}_{v\mu_{\text{DMN}}} \\ \bar{T}_{\mu v_{\text{DMN}}} & \bar{T}_{\mu_{\text{DMN}}}\end{pmatrix} = kBT_{\text{amb}}(\bar{I} - \bar{S}_{\text{DMN}}\bar{S}^{\text{H}}_{\text{DMN}}) \tag{4.24}$$

or

$$\begin{aligned}
\bar{T}_{v_{\text{DMN}}} &= T_{\text{amb}}(\bar{I} - \bar{S}_{11,\,\text{DMN}}\bar{S}^{\text{H}}_{11,\,\text{DMN}} - \bar{S}_{21,\,\text{DMN}}\bar{S}^{\text{H}}_{12,\,\text{DMN}}), \\
\bar{T}_{\mu_{\text{DMN}}} &= T_{\text{amb}}(\bar{I} - \bar{S}_{12,\,\text{DMN}}\bar{S}^{\text{H}}_{21,\,\text{DMN}} - \bar{S}_{22,\,\text{DMN}}\bar{S}^{\text{H}}_{22,\,\text{DMN}}), \\
\bar{T}_{v\mu_{\text{DMN}}} &= T_{\text{amb}}(-\bar{S}_{11,\,\text{DMN}}\bar{S}^{\text{H}}_{21,\,\text{DMN}} - \bar{S}_{12,\,\text{DMN}}\bar{S}^{\text{H}}_{22,\,\text{DMN}}), \\
\text{and } \bar{T}_{\mu v_{\text{DMN}}} &= \bar{T}^{\text{H}}_{v\mu_{\text{DMN}}}.
\end{aligned} \tag{4.25}$$

Finally, the DMN noise temperature covariance matrix can be found using (4.20) and (4.24).

4.3.3 Low-noise amplifier noise

The LNA noise temperature is given by the covariance matrix of the received noise wave due to the forward and backward LNA noise waves, while considering the noise free antenna array and the DMN. According to Bosma's theorem for cascaded two-port devices at uniform temperature, T_{amb} (see Appendix A.2):

$$\text{Var}\{\vec{b}_{\text{N, LNA}}\} = k\bar{T}_{\text{N, LNA}}B(\bar{I} - \bar{S}_{\text{sys}}\bar{S}_{\text{sys}}^{\text{H}}). \tag{4.26}$$

The noise source waves for the LNA are modelled by $\vec{\nu}_{\text{LNA}}$ and $\vec{\mu}_{\text{LNA}}$ for the forward and backward waves, respectively. The received noise vector due to LNA noise sources is described by:

$$\vec{b}_{\text{N,LNA}} = \bar{G}_{\text{LNA}}\vec{n}_3. \tag{4.27}$$

The new equation system constituting of the respective nodal equations are:

$$\begin{aligned}
\vec{\text{n}}_1 &= \bar{S}_{\text{A}}\vec{\text{n}}_2, \\
\vec{\text{n}}_2 &= \bar{S}_{21,\text{DMN}}\vec{\text{n}}_4 + \bar{S}_{22,\text{DMN}}\vec{\text{n}}_1, \\
\vec{\text{n}}_3 &= \bar{I}\vec{\nu}_{\text{LNA}} + \bar{S}_{12,\text{DMN}} + \bar{S}_{11,\text{DMN}}\vec{\text{n}}_4, \\
\vec{\text{n}}_4 &= \bar{I}\vec{\mu}_{\text{LNA}}.
\end{aligned} \tag{4.28}$$

Manipulating (4.28) and solving for the $\vec{\text{n}}_3$,

$$\vec{\text{n}}_3 = (\bar{S}_{11,\text{DMN}} + \underbrace{\bar{S}_{12,\text{DMN}}(\bar{I} - \bar{S}_{\text{A}}\bar{S}_{22,\text{DMN}})^{-1}}_{\bar{G}_{\text{DMN}}}\bar{S}_{\text{A}}\bar{S}_{21,\text{DMN}})\bar{I}\vec{\mu}_{\text{LNA}} - \bar{I}\vec{\nu}_{\text{LNA}}. \tag{4.29}$$

The system scattering matrix $\bar{S}_{\text{sys}}$ at the input of the DMN with antenna attached is defined as:

$$\bar{S}_{\text{sys}} = \bar{S}_{11,\text{DMN}} + \bar{G}_{\text{DMN}}\bar{S}_{\text{A}}\bar{S}_{21,\text{DMN}}, \tag{4.30}$$

This equation is valid for any passive antenna array connected in cascade with another similar rank multi-port network. Further, using equation (4.26) and (4.30) the covariance matrix becomes:

$$\text{Var}\{\vec{b}_{\text{N, LNA}}\} = \bar{G}_{\text{LNA}}(\bar{T}_{v,\text{LNA}} - \bar{S}_{\text{sys}}\bar{T}_{\mu v,\text{LNA}} - \bar{T}_{\mu v,\text{LNA}}\bar{S}_{\text{sys}}^{\text{H}} + \bar{S}_{\text{sys}}\bar{T}_{\mu,\text{LNA}}\bar{S}_{\text{sys}}^{\text{H}})\bar{G}_{\text{LNA}}^{\text{H}}. \tag{4.31}$$

Here, the noise temperature matrices for the source waves are given by:

$$\text{Var}\left\{\begin{pmatrix}\vec{\nu}_{\text{LNA}} \\ \vec{\mu}_{\text{LNA}})\end{pmatrix}\right\} = kB\begin{pmatrix}\bar{T}_{v,\text{LNA}} & \bar{T}_{v\mu,\text{LNA}} \\ \bar{T}_{\mu v,\text{LNA}} & \bar{T}_{\mu,\text{LNA}}\end{pmatrix}. \tag{4.32}$$

Table 4.1: Measured noise parameters of the low-noise amplifiers developed during this work. These parameters are recorded with a chip mounted on the printed-circuit board.

amplifiers	**noise parameters**		
	$F_{\min}$ (dB)	R_{n} (Ω)	Z_{opt} (Ω)
ALM1912	1.66	8.2	28+j10
IMMS	1.7	6	26+j0.3

Since the LNA is an active device, it is not possible to obtain the covariance matrix for the respective noise source waves with only the help of the scattering parameters. However, these can be determined, in addition to the scattering parameters of the devices, with the three noise parameters noise resistance, R_{n}, optimal impedance, Z_{opt}, and the minimum noise figure, $NF_{\min}$ [12]. These noise parameters for different amplifiers have been measured using Maury noise parameter equipment [147]. The noise parameters measured for two different amplifiers employed during this work are displayed in Table 4.1. Furthermore, it is assumed that the noise generated by one LNA is uncorrelated to all other amplifiers. Therefore, the input-referred noise correlation matrices in equation simplify to $\bar{T}_{v,\text{LNA}} = T_{v,\text{LNA}}\bar{I}$, $\bar{T}_{\mu,\text{LNA}} = T_{\mu,\text{LNA}}\bar{I}$, and $\bar{T}_{v\mu,\text{LNA}} = \bar{T}^{\text{H}}_{v\mu,\text{LNA}} = T_{v\mu,\text{LNA}}\bar{I}$, in which $T_{v,\text{LNA}}$, $T_{\mu,\text{LNA}}$, and $T_{v\mu,\text{LNA}}$ are calculated from the measured noise parameters $NF_{\min}$, R_{n}, and Z_{opt} according to Appendix A.3.

4.4 Equivalent carrier-to-interference-plus-noise ratio

The equivalent CINR for a given direction of arrival at the input of the first-stage amplifier for a GNSS array receiver is given as:

$$\chi_o^{\text{int}}(\theta,\phi) = \frac{C(\theta,\phi)}{\sum_i C_{\text{int}}(\theta_i,\phi_i) + N_o}. \tag{4.33}$$

The equivalent available carrier power, $C(\theta,\phi)$, with DMN is found by solving the covariance matrix of the forward traveling wave at the input of the first-stage LNA, $\vec{b}_{\text{c}}$. Calculating the equation system at the respective nodes:

$$\begin{aligned}
\vec{\text{n}}_1 &= \vec{b}_{\text{A}} + \bar{S}_{\text{A}}\vec{\text{n}}_2,\\
\vec{\text{n}}_2 &= \bar{S}_{22,\text{DMN}}n_1 + \bar{S}_{21,\text{DMN}}\vec{\text{n}}_4,\\
\vec{\text{n}}_3 &= \bar{S}_{11,\text{DMN}}n_4 + \bar{S}_{12,\text{DMN}}\vec{\text{n}}_1,\\
\vec{\text{n}}_4 &= 0.
\end{aligned} \tag{4.34}$$

where

$$\vec{b}_{\mathrm{c}} = \bar{G}_{\mathrm{LNA}}\vec{\mathrm{n}}_3. \tag{4.35}$$

Using (4.35), and solving for n_3 by manipulating (4.34) to obtain

$$\vec{b}_{\mathrm{c}} = \bar{G}_{\mathrm{LNA}}\bar{G}_{\mathrm{DMN}}\vec{b}_{\mathrm{A}}. \tag{4.36}$$

This leads to the received signal covariance matrix

$$\bar{C}(\theta,\phi) = \mathrm{Var}\{\vec{b}_{\mathrm{c}}\} = \bar{G}_{\mathrm{LNA}}\bar{G}_{\mathrm{DMN}}\mathrm{Var}\{\vec{b}_{\mathrm{A}}\}\bar{G}^{\mathrm{H}}_{\mathrm{DMN}}\bar{G}^{\mathrm{H}}_{\mathrm{LNA}}. \tag{4.37}$$

Here, the covariance matrix of the antenna array received at the output of the antenna array ports is described by extending the previous definition given in (2.13) for the multi-element antenna as:

$$\mathrm{Var}\{\vec{b}_{\mathrm{A}}\} = C_{\mathrm{sat}}\vec{F}(\theta,\phi)\vec{F}^{\mathrm{H}}(\theta,\phi) \tag{4.38}$$

It is of more interest to find the scalar or the equivalent carrier power at the input of the LNA stage. This can be obtained using the beamforming weights $\vec{w}$ which transform the $\bar{C}(\theta,\phi)$ accordingly,

$$C(\theta,\phi) = P_{\mathrm{sat}}\vec{w}^{\mathrm{H}}\bar{C}(\theta,\phi)\vec{w}. \tag{4.39}$$

The noise spectral density can be obtained using the system noise temperature covariance matrix $\bar{T}_{\mathrm{sys}}$ derived in the previous section, and the beamforming weights in the direction of the desired satellite with interference suppression constraints. This can be written as follows:

$$N_{\mathrm{o}} = k\vec{w}^{\mathrm{H}}\bar{T}_{\mathrm{sys}}\vec{w}. \tag{4.40}$$

Now, the equivalent available interference power can be defined in a way similar to the received signal power. Moreover, it is assumed that interferers are narrow-band and uncorrelated. Therefore, for an arbitrarily polarised interferer

$$C_{\mathrm{int}}(\theta_i,\phi_i) = P_{\mathrm{int}}\vec{w}^{H}\left([\vec{F}_\theta \quad \vec{F}_\phi]\vec{p}\right)\vec{w}. \tag{4.41}$$

The vector for the polarisation of the interference is given by $\vec{p} = [\cos\alpha \quad \sin\alpha\cdot e^{j\beta}]^{\mathrm{T}}$, which in the case of the circular polarised interferer is

$$\vec{p}_{\mathrm{circ}} = \frac{1}{\sqrt{2}}[1 \quad \pm j]^{\mathrm{T}} \tag{4.42}$$

and for the linear polarised interferer is given by

$$\vec{p}_{\mathrm{lin}} = \frac{1}{\sqrt{2}}[\cos\alpha \quad \sin\alpha]^{\mathrm{T}}. \tag{4.43}$$

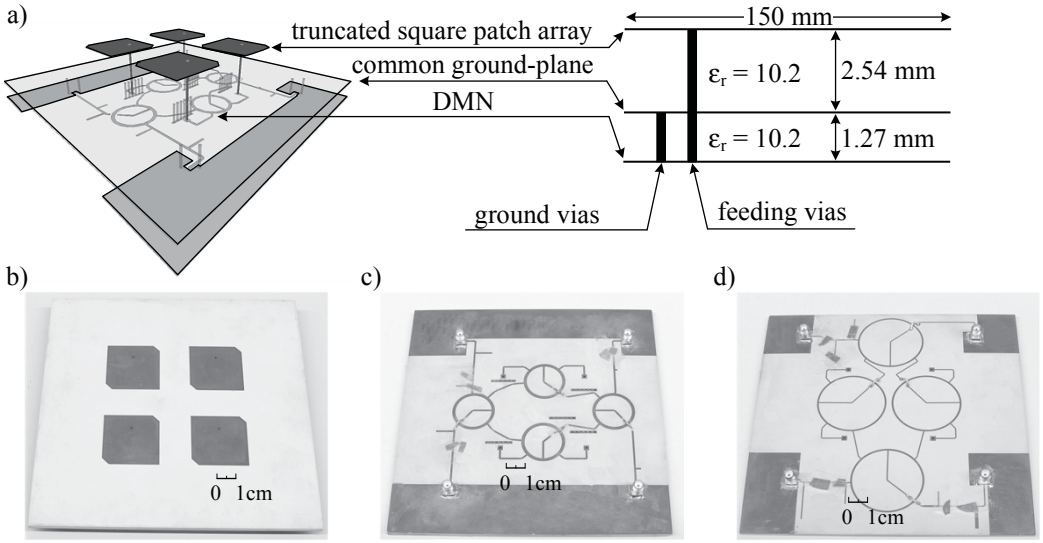

Figure 4.6: Customised four-element GNSS truncated square patch antenna array designed using commercially available substrates. (a) Exploded sketch with integrated DMN, (b) top view of the fabricated antenna version "A", "B", and "C", (c) bottom view of antenna version "B", and (d) bottom view of the antenna version "C".

4.5 Design, implementation, and evaluation of compact GNSS antenna arrays

Before investigating the equivalent CINR performance of the compact GNSS antenna array, different four-element square-shaped GNSS antenna arrays having $d = \lambda/4$ with and without DMN have been designed. These customised designs, with compact inter-element separation, are optimised such that the antenna properties are in accordance with the requirements for the RHCP reception in the GNSS, while utilising the eigenvectors. Here, the even mode is responsible for maximum radiation in the zenith directions, therefore the antenna array elements are individually optimised to achieve the minimum axial ratio in this direction, which according to Table. 2.3 is 3 dB for a bandwidth of 2 MHz.

4.5.1 Four-element $\lambda/4$ GNSS antenna arrays with integrated decoupling and matching networks

The different four-element compact GNSS antenna arrays incorporate variations of the individual elements and the DMN designs. These variations designs can be summarised as follows:

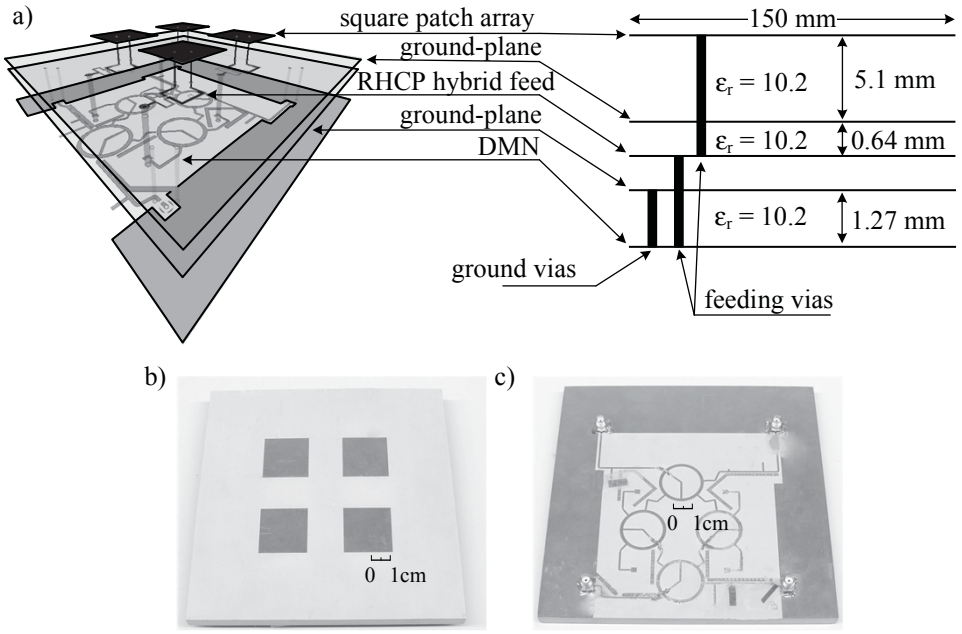

Figure 4.7: Customised four-element GNSS square patch antenna array version "D" with hybrid feed for conversion into circular polarisation, designed using commercially available substrates. (a) Exploded sketch with integrated DMN, (b) top view, and (c) bottom view of the fabricated antenna array.

1. Antenna "A": This consists of four truncated square patches to excite RHCP on the substrate with dielectric permittivity of $\epsilon_r = 10.2$ and a loss tangent of $\tan\delta = 0.0021$, i.e. RO3010 [148]. The thickness of the substrate is 2.54 mm. This antenna does not include DMN, and represents the antenna portion only in Fig. 4.6a and b.

2. Antenna "B": The antenna is similar to Antenna "A". However, this antenna is integrated with DMN, based on the design shown in Fig. 4.2. This constitutes four reduced length $180^{\text{o}}-$hybrid couplers, as the total circumference of the hybrid is a single waveguide wavelength, λ_{g} [79], and is designed over a substrate with a thickness of 1.27 mm and permittivity of $\epsilon_r = 10.2$. The complete sketch and fabricated antenna is shown in Fig. 4.6b and c, respectively.

3. Antenna "C": The antenna array design is also similar to Antenna "A". However, the integrated DMN is designed over a thin substrate with a reduced dielectric permittivity of $\epsilon_r = 3.55$, dielectric loss tangent is $\tan\delta = 0.0027$, and a thickness of 0.25 mm, i.e. RO4003 [148]. The bottom view of the fabricated antenna array are shown in Fig. 4.6d.

4. Antenna "D": The antenna array is based on dual-feed, linearly polarised, square

patches where RHCP is achieved by a separate feeding network consisting of four quadrature couplers, which provide the quadrature phase shift between the two feedings. The antenna substrate thickness is increased to $5.1\ \mathrm{mm}$ to enhance and attain the required bandwidth and radiation efficiency in the case of GNSS. All substrate layers have values for $\epsilon_r = 10.2$ and $\tan\delta = 0.0023$ according to the data-sheets of the substrate material provider. The design of the DMN is similar to Antenna "B". The complete antenna array design sketch and the fabricated top and bottom views of the antenna arrays are shown in Fig. 4.7a, b and c, respectively.

Antenna "A": This is a conventional four-element compact GNSS antenna array without DMN, which has similar efficiencies for the individual elements. The pattern shape of the individual antenna elements are uniform in the upper-hemisphere, with no nulls. The matching, or S_{ii}, is better than $-10\ \mathrm{dB}$ in the operating L1/E1 frequency band for all elements, whereas the maximum coupling between the adjacent and non-adjacent elements, or S_{ij}, is $-7\ \mathrm{dB}$. The measured radiation efficiency of each element is approximately 33% which is slightly lower than the simulation estimate of 37%, and may be attributed to the tolerances in $\tan\delta$ and metal conductivity values taken into account in the simulations. The measured RHCP realised gain radiation patterns, $F^i_{\text{RHCP}}(\theta,\phi)$, are shown for the antenna elements in Fig. 4.8a. The recorded maximum RHCP realised gains are 2.4, 3.4, 2.5 and $3.8\ \mathrm{dBi}$ for the respective antenna elements. The cross-polarisation, or measured LHCP realised gain radiation patterns, $F^i_{\text{LHCP}}(\theta,\phi)$ are displayed in Fig. 4.8b. These possess higher-order modes and are contributed mainly by the ground currents[16]. The maximum LHCP realised gains are -4, -2.1, -4, and $-1.8\ \mathrm{dBi}$ for the antenna elements.

Furthermore, the eigenanalysis by computing the covariance matrix, $\bar{R}$, using (3.12), is performed on the measured embedded patterns $\bar{F}_i(\theta,\phi)$. The efficiencies associated with the even, odd-1, odd-2 and π modes, are 64%, 38%, 26%, and 10%, respectively. As expected for the symmetric antenna array, the eigenmode absolute amplitudes and phases to decouple the antenna array are in close agreement to the modes of the $180^{\text{o}}-$hybrid couplers depicted in Fig. 4.2.

Antenna "B": The antenna array design is similar to Antenna "A". However, the DMN is integrated at the back of the antenna array. The DMN is responsible for the excitation of the eigenmodes which eventually decouple and match the resulting ports. The permittivity of the DMN substrate is $\epsilon_r = 10.2$, which offers miniaturisation, but the impedance matching bandwidth is reduced. This is compensated for by increasing the thickness of the substrate to $1.27\ \mathrm{mm}$. The matching coefficient for all modes is better than $-12\ \mathrm{dB}$ with a minimum bandwidth of $4\ \mathrm{MHz}$, $\bar{S}_{ii} \leq -10\ \mathrm{dB}$ criterion, which is sufficient to fulfil the GNSS requirements. The maximum decoupling coefficient is $-11\ \mathrm{dB}$. This is not perfect decoupling, and is associated with the ohmic losses of the network and the dominant surface waves due to the combination of higher permittivity and thicker substrate. The measured total eigenefficiencies at the output of the DMN for the

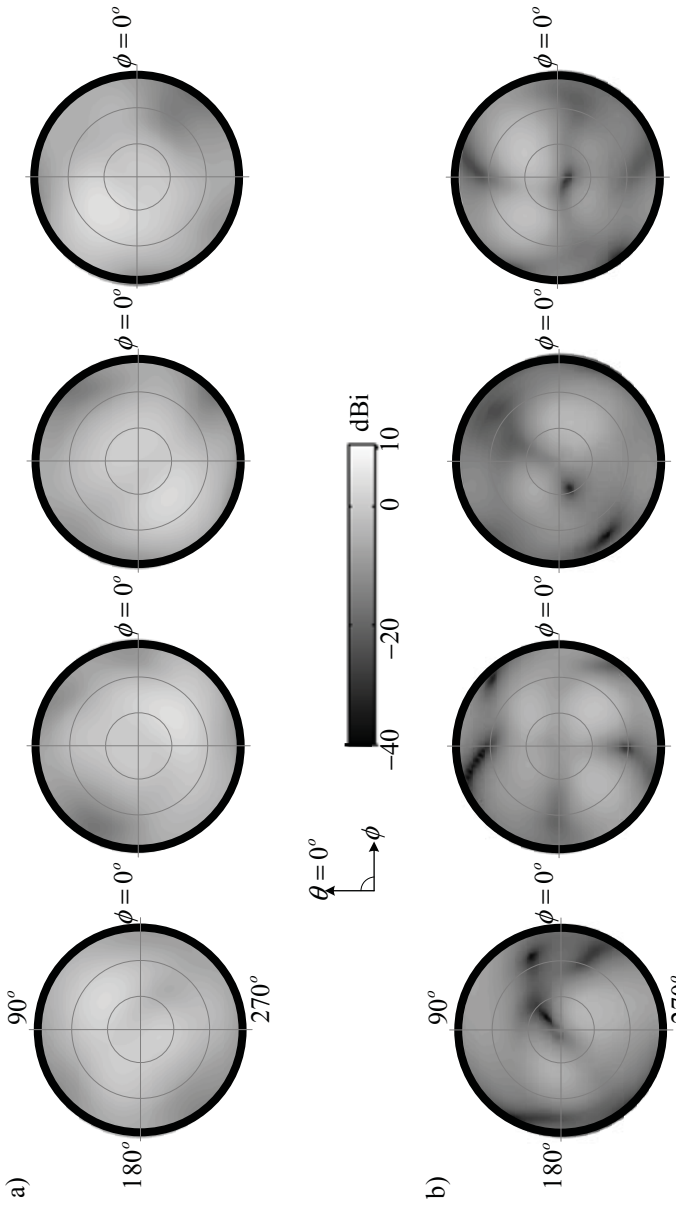

Figure 4.8: Measured embedded realised gain, (a) RHCP and (b) LHCP far-field patterns in the upper-hemisphere for each element, respectively, of the fabricated antenna "A".

even, odd-1, odd-2, and π modes are 63%, 56%, 38%, and 25%, respectively, at the centre frequency of L1/E1. The minimum eigenefficiency is considerably improved compared to Antenna "A", which is without DMN.

The measured RHCP realised gain radiation patterns for the modes are shown in Fig. 4.9a. Here, the recorded maximum RHCP realised gains are 6, 4.2, 2.4, and 0.2 dBi for the even, odd-1, odd-2, and π modes, respectively. The measured LHCP realised gain radiation patterns are shown in Fig. 4.9b. In this case, the maximum realised gains are -5.9, -1, -3, -0.2 dBi.

The truncated square patches are known to possess a narrow axial ratio bandwidth but it is sufficient to fulfil the criterion for the L1/E1 C/A-code signal, which is ± 1.023 MHz. However, this narrow bandwidth property offers little manufacturing tolerance, which may be unattractive for mass-production. Secondly, it is noteworthy that the axial ratio over the complete upper hemisphere is not uniform, and is drastically increased close to the horizon, which may be improved by the dual-feed linear polarised patch antenna array, such a type is described later in this section. Furthermore, the π mode LHCP maximum gain is equal to the RHCP, which is undesired for robustness, and will be examined using the equivalent CINR analysis.

Antenna "C": In order to decrease the mutual coupling more than -15 dB, a low permittivity and thin DMN substrate is employed for the DMN design. The thin DMN substrate with low dielectric permittivity minimises the generation of surface waves, and thus mutual coupling. However, there are certain disadvantages for this choice of substrate, including a larger size and narrower bandwidths. The measured matching coefficient for all modes is better than -12 dB for the minimum bandwidth for the π mode 4 MHz, for a $\bar{S}_{ii} \leq -10$ dB criterion. However, the maximum coupling coefficient is decreased significantly to -17 dB.

The measured RHCP realised gain radiation patterns are shown in Fig. 4.10a. The maximum RHCP realised gains for the respective modes are 5.8, 3.4, 2.6, -2.5 dBi. It may also be noted that for eigenmode antenna arrays as well, these maximum gain values do not correspond to the same directions. Therefore, in a fixed direction, the deviation among the gain values is larger.

The measured LHCP realised gain radiation patterns are displayed in Fig. 4.10b. The maximum LHCP realised gains for the even, odd-1, odd-2, and π modes are -7.2, -4, -4.5, and -2.9 dBi, respectively. The measured axial ratio in the main-lobe (zenith) direction is also below 3 dB. The measured eigenefficiencies at the output of the DMN for the even, odd-1, odd-2, and π modes are 63%, 46%, 35%, and 20%, respectively. In comparison to Antenna "B", the minimum eigenefficiency is decreased, which can be attributed to the choice of the dielectric substrate properties, but is still acceptable for the considered threshold in this study.

Antenna "D": This antenna design consists of a dual-feed linear polarised square patch antenna with a separate quadrature coupler feeding network to generate the RHCP

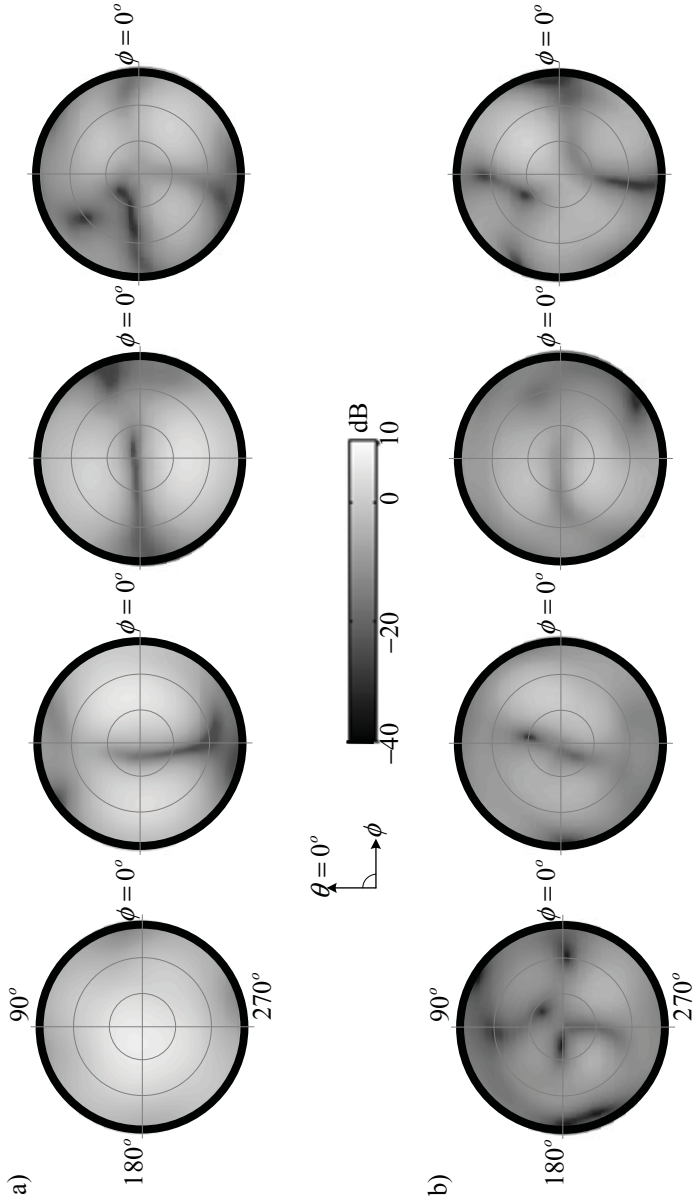

Figure 4.9: Measured eigemode realised gain, (a) RHCP and (b) LHCP patterns in the upper-hemisphere for even, odd-1, odd-2, π mode, respectively, of the fabricated antenna "B".

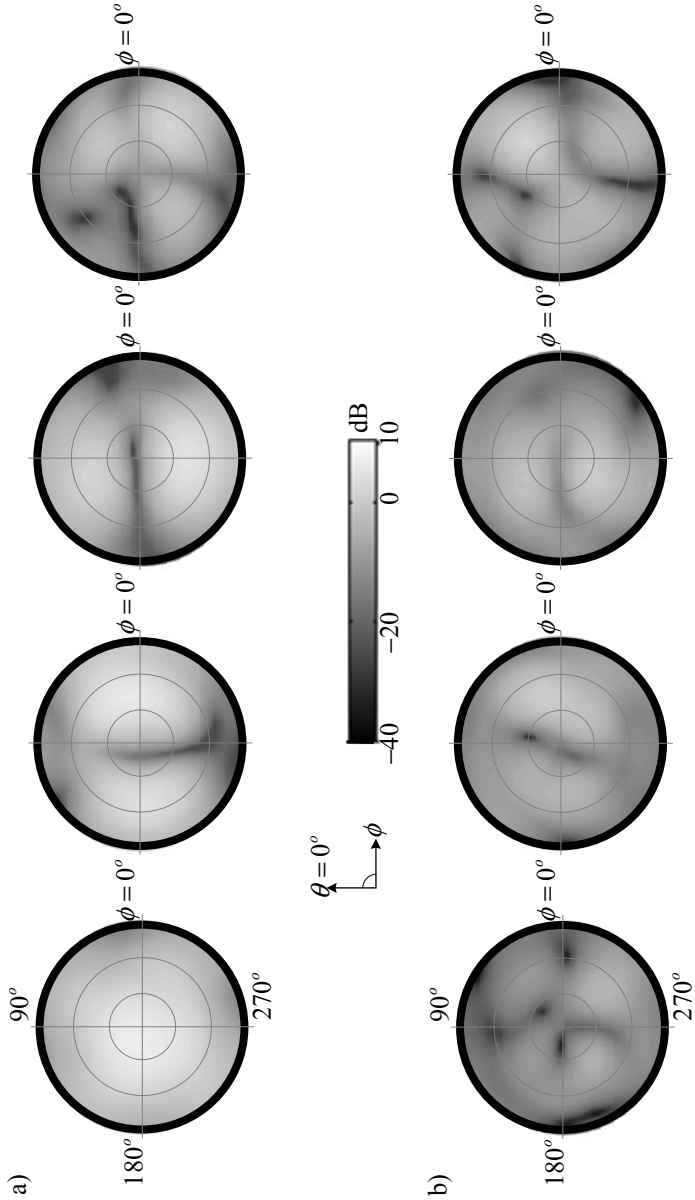

Figure 4.10: Measured eigemode realised gain, (a) RHCP and (b) LHCP patterns in the upper-hemisphere for even, odd-1, odd-2, π mode, respectively, of the fabricated antenna "C".

Table 4.2: Summarised measured radiation efficiencies of the different antenna versions. In the case of antenna "A" these are the embedded element efficiencies. Last row of the table indicates the maximum measured coupling between any two elements or modes of the antenna array.

mode	**antenna version**			
	A (w/o DMN)	**B**	**C**	**D**
even	64	63	63	49
odd-1	38	56	46	30
odd-2	26	38	35	10
π	10	25	20	7
max. coupling (dB)	-7	-11	-17	-14

from each element. This offers wide axial ratio bandwidth for the main-lobe direction, which provides greater manufacturing and material properties tolerances. Furthermore, the antenna substrate thickness is increased by twice that of Antenna "A", which provides wider impedance-matching and realised gain bandwidths across the operating band, which result in better manufacturing tolerances.

The integrated DMN design is similar to the Antenna "B" as shown in Fig. 4.7c. The measured matching coefficients are less than -15 dB, with maximum coupling coefficient of -14 dB. The measured -10 dB matching bandwidth is improved to 10 MHz in the π mode.

However, the measured modal eigenefficiencies differ greatly from the simulation. The measured modal efficiencies are 49%, 30%, 10%, and 7% whereas in the simulation they are 75%, 62%, 57%, and 35%. The high insertion loss is found to be linked to the employed gold-plating, which includes Nickel as a carrier layer. This was examined by a separate construction of Antenna "B" using conventional copper and gold-plating. Unfortunately, another version of Antenna "D" was not possible during this work. Nonetheless, this fabricated design is still functional, but with slightly degraded performance when compared to the above mentioned antennas, therefore it is unfair to consider it for further comparison analyses.

Table 4.3: Summarised maximum RHCP and LHCP realised gain values, in dBi, of the different four-element antenna designs.

	antenna version							
	A (w/o DMN)		**B**		**C**		**D**	
mode	RHCP	LHCP	RHCP	LHCP	RHCP	LHCP	RHCP	LHCP
even	2.4	-4	6	-5.9	5.8	-7.2	3.9	-6.8
odd-1	3.4	-2.1	4.2	-1	3.4	-4	3.4	-3.3
odd-2	2.5	-4	2.4	-3	2.5	-4.5	-2.5	-10
π	3.8	-1.8	0.2	-0.2	-2.5	-2.9	-7.2	-6.6

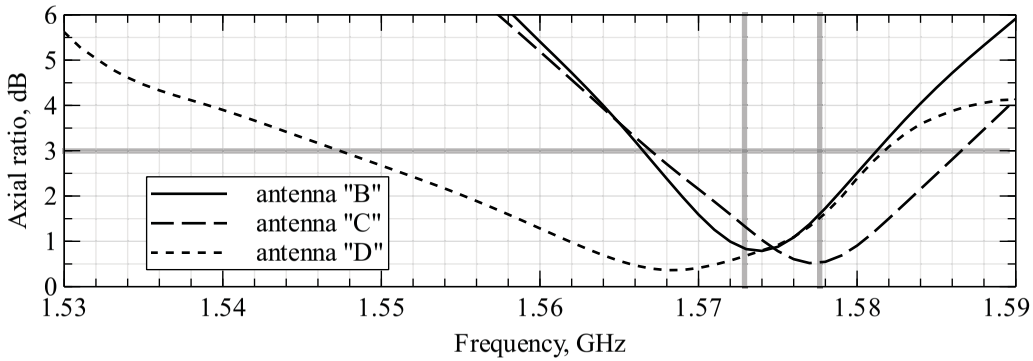

Figure 4.11: Measured axial ratio in the main-lobe direction of even mode vs. frequency for the different manufactured antenna versions with integrated DMN, the highlighted thick vertical grey lines indicate L1/E1 band, and highlighted horizontal grey lines represent the minimum axial ratio threshold in dB.

The axial ratios in the main-lobe directions for the even modes of the compact antenna array with DMN are shown in Fig. 4.11. The truncated square patch-based antenna array depicts narrow-band behaviour due to the single feed design. However, as mentioned earlier, it is sufficient for public navigation signals. The axial ratio for the dual-feed antenna array design "D" is de-tuned from the centre frequency, but due its broadband characteristics it achieved less than $3\ \mathrm{dB}$ for the desired band. In addition, in this design, the axial ratio in other directions (in the upper hemisphere) is better than the truncated square patch antenna arrays.

The summarised maximum realised gains in RHCP and LHCP at the centre frequency of the L1/E1 band, i.e. $f_o = 1575.42\ \mathrm{MHz}$ are shown in Table 4.3.

4.5.2 Co-polarised interference scenarios

The robustness performance of the compact antenna array receiver is analysed using the equivalent CINR model derived in (4.33). For simplification purposes, the non-linear effects of the FE components are not considered. Furthermore, the assumption is made that noise contribution from FE components other than the LNA are negligible, and thus they are ignored. Now, with a priori knowledge of the j interferer directions, the optimal weight coefficient in the deterministic case for desired satellite direction can be given as:

$$\vec{w}_d = \vec{F}_d^{\mathrm{H}}(\theta_d, \phi_d)\bar{O}_{\perp}^{\mathrm{int}}. \tag{4.44}$$

Here, $\bar{O}_{\perp}^{\mathrm{int}}$ represents the projection to the interference-free subspace and is found using (3.31), where the steering vectors are defined by the interferers' directions. There are also several other methods for estimating the beamforming weighting coefficients in the presence of interferences, such as the minimum variance distortionless response (MVDR), which provides additional constraints for interference attenuation with a certain trade-off for antenna array gain [17, Section 6.2.1]. In the context of this work the discussion will be limited to the aforementioned beamformer. The maximum possible interferers with one degree-of-freedom fixed for satellite direction are three, for four-element antenna array.

One interferer: A single RHCP interferer, with the same polarisation as the desired satellite, and JSR of $40\ \mathrm{dB}$ impinging from fixed direction $(\theta, \phi) = (15^{\mathrm{o}}, 90^{\mathrm{o}})$. The equivalent CINR using the weighting coefficients in (4.44) is computed for every satellite direction, with $C_{\mathrm{sat}} = -157$ dBW, in the upper hemisphere, and an elevation angle, θ, from $0^{\mathrm{o}} - 180^{\mathrm{o}}$, and azimuth angle, ϕ, from $0^{\mathrm{o}} - 360^{\mathrm{o}}$. For clarification, $\theta = 0^{\mathrm{o}}$ and $\theta = 180^{\mathrm{o}}$ correspond to the horizon. In Fig. 4.12a, the computed equivalent CINR in the azimuth directions with fixed elevation directions, $\theta = 15^{\mathrm{o}}$, of different antenna versions with and without DMN described in the previous section is shown. In Fig. 4.12b the equivalent CINR in elevation directions with fixed azimuth, $\phi = 90^{\mathrm{o}}$, for the respective compact antenna array is shown.

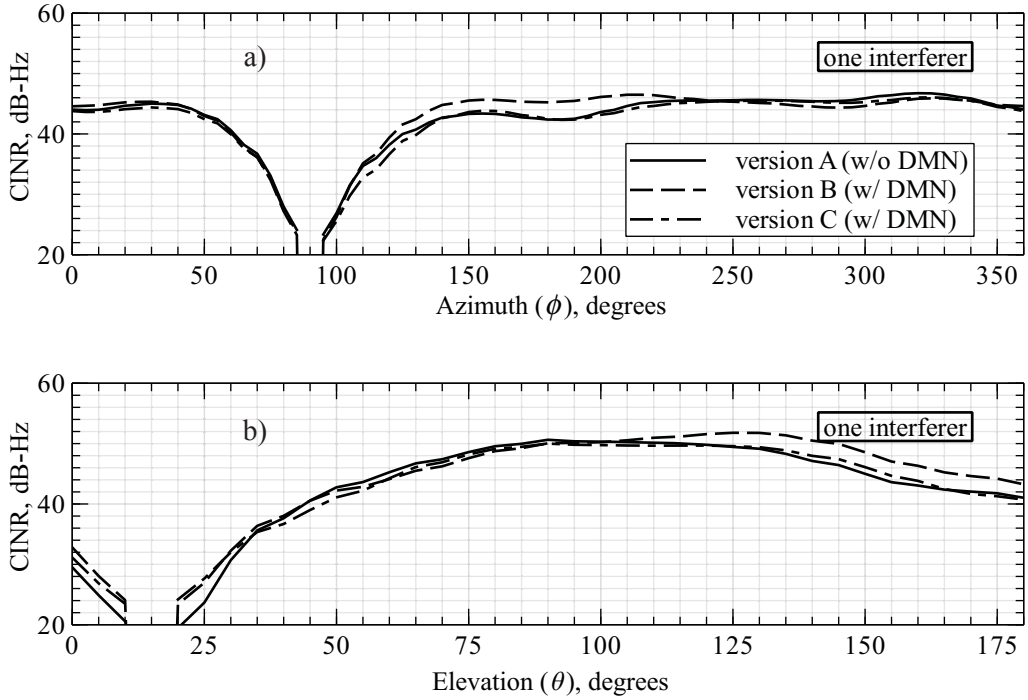

Figure 4.12: The calculated equivalent CINR for one RHCP interferer case with JSR of 40 dB impinging from fixed direction $(\theta, \phi) = (15^{\text{o}}, 90^{\text{o}})$, (a) in azimuth with elevation $\theta = 15^{\text{o}}$, and (b) in elevation with azimuth $\phi = 90^{\text{o}}$. Here, $\theta = 90^{\text{o}}$ refers to the zenith directions. The angular resolution of the far-field measurements is 5^{o}.

The equivalent CINR for Antenna "B" is 1–2 dB better than the other antennas in low elevation directions, which has best efficiency of all, but is not perfect decoupled. However, in certain azimuth directions without DMN Antenna "A" is $0.2 - 0.5$ dB better than the antenna arrays with DMN. In general, the equivalent CINR is similar in the upper hemisphere direction with or without DMN. However, the advantage of the DMN is marginally evident at low elevations. Therefore, it may be concluded that in the single interferer scenario, the benefit of DMN is not prominent, except at low elevations. This outcome is similar to the results obtained in our work [157].

Two interferers: At first, two RHCP interferers, with a JSR of 40 dB, each for fixed azimuth impinging directions $(\theta_1, \phi_1) = (15^{\text{o}}, 90^{\text{o}})$ and $(\theta_2, \phi_2) = (15^{\text{o}}, 180^{\text{o}})$ are investigated. The computed equivalent CINR for the desired satellite directions in the azimuthal directions with fixed elevation angle $\theta = 15^{\text{o}}$ is plotted in Fig. 4.13a. In azimuth directions close to the two interferers' directions, the equivalent CINR dropped by at least 2 dB compared to the single interferer case. This is related to the decrease in the antenna gain with the use of the higher-order modes observed in the previous sub-section.

Next, the interferer directions are distributed in elevations of $(\theta_1, \phi_1) = (15^{\text{o}}, 90^{\text{o}})$ and

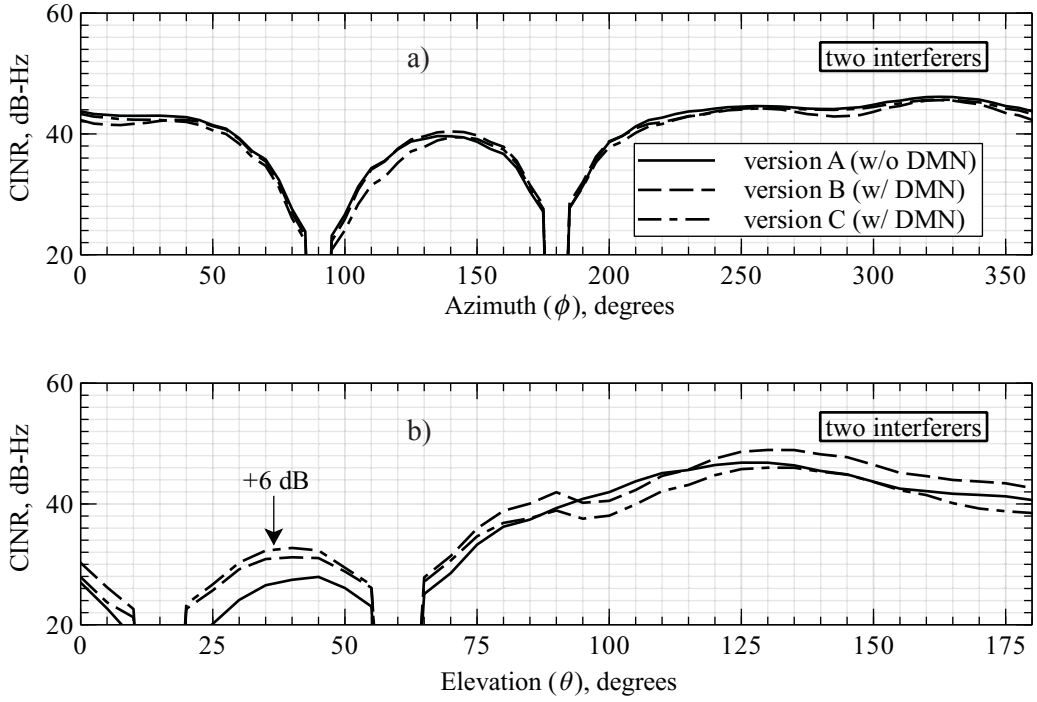

Figure 4.13: The calculated equivalent CINR for two RHCP interferer cases with JSR of 40 dB each. The impinging directions (a) $(\theta_1, \phi_1) = (15^{\text{o}}, 90^{\text{o}})$ and $(\theta_2, \phi_2) = (15^{\text{o}}, 180^{\text{o}})$ while the plot represents azimuth directions with fixed elevation $\theta = 15^{\text{o}}$, (b) $(\theta_1, \phi_1) = (15^{\text{o}}, 90^{\text{o}})$ and $(\theta_2, \phi_2) = (60^{\text{o}}, 90^{\text{o}})$, which is plotted for all elevation directions with fixed azimuth $\phi = 90^{\text{o}}$. Here, $\theta = 90^{\text{o}}$ refers to the zenith directions. The angular resolution of the far-field measurements is 5^{o}.

$(\theta_2, \phi_2) = (60^{\text{o}}, 90^{\text{o}})$, and the corresponding equivalent CINR with constant azimuth direction $\phi = 90^{\text{o}}$ for different antenna arrays is shown in Fig. 4.13b. The CINR is improved significantly by 3 dB for Antenna "B" close to the interferer elevation directions. However, without DMN provides better or equal CINR in other directions. In cases where the interferers are distributed in elevation and the desired source is impinging from a low elevation, DMN is a preferable choice for the compact antenna arrays. Note, the absolute CINR gain may differ for different types, inter-element separation and geometry of the antenna arrays. This is also affected by characteristics such as ohmic losses of the DMN.

Three interferers: This is the worst-case for the four elements compact antenna array, as it requires all degrees-of-freedom of the antenna array. This may sometimes become a limiting factor for the selection of antenna array configurations, if the equivalent CINR drops below the detectable threshold of the receiver. Therefore, it is necessary to analyse

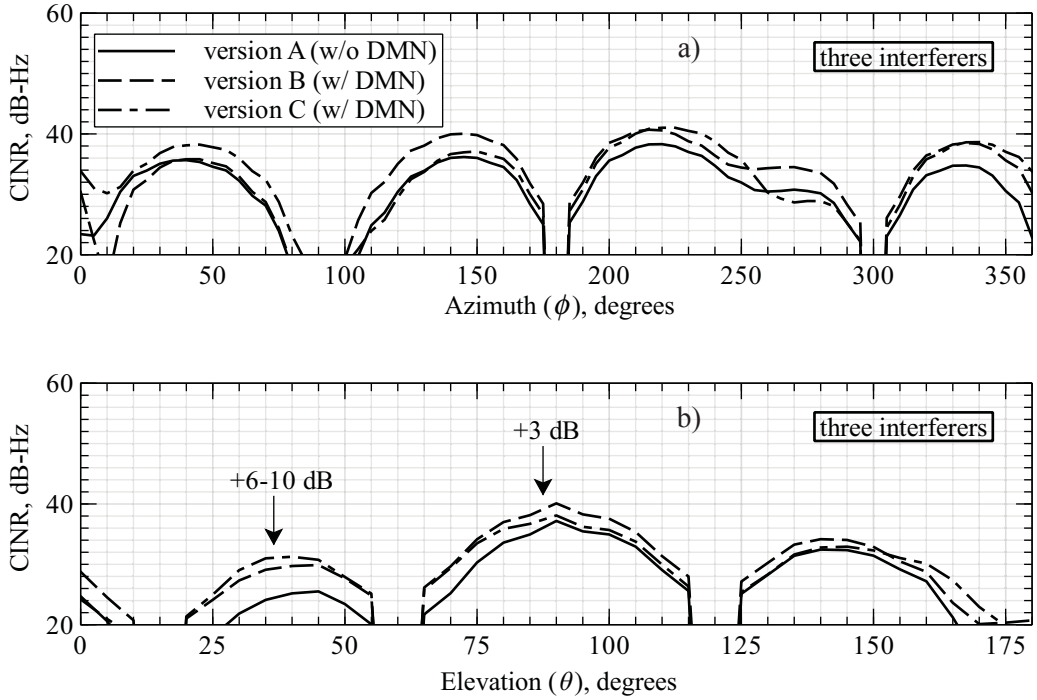

Figure 4.14: The calculated equivalent CINR for three RHCP interferer cases with JSR of 40 dB each. The impinging directions (a) $(\theta_1, \phi_1) = (15^{\text{o}}, 90^{\text{o}})$, $(\theta_2, \phi_2) = (15^{\text{o}}, 180^{\text{o}})$, $(\theta_3, \phi_3) = (15^{\text{o}}, 300^{\text{o}})$ while the plot represents azimuth directions with fixed elevation $\theta = 15^{\text{o}}$, (b) $(\theta_1, \phi_1) = (15^{\text{o}}, 90^{\text{o}})$, $(\theta_2, \phi_2) = (60^{\text{o}}, 90^{\text{o}})$, $(\theta_3, \phi_3) = (60^{\text{o}}, 180^{\text{o}})$, which is plotted for all elevation directions with fixed azimuth $\phi = 90^{\text{o}}$. Here, $\theta = 90^{\text{o}}$ refer to the zenith directions. The angular resolution of the far-field measurements is 5^{o}.

the equivalent CINR, while also considering the losses of the DMN. Therefore, introducing three RHCP interferers in the different azimuth directions with fixed elevation direction, at $(\theta_1, \phi_1) = (15^{\text{o}}, 90^{\text{o}})$, $(\theta_2, \phi_2) = (15^{\text{o}}, 180^{\text{o}})$, and $(\theta_3, \phi_3) = (15^{\text{o}}, 300^{\text{o}})$, reduces the CINR for all the antennas considerably by $5 - 10$ dB which confirms the fact that mutual coupling degrades the radiative performance of the antennas severely, as observed in the minimum eigenvalue analysis in the previous chapter. But the use of DMN restores the antenna CINR by at least 3 dB in all directions, which signifies its benefit.

In the case of three RHCP interferers distributed in elevation directions with fixed azimuths of $(\theta_1, \phi_1) = (15^{\text{o}}, 90^{\text{o}})$, $(\theta_2, \phi_2) = (60^{\text{o}}, 90^{\text{o}})$, and $(\theta_3, \phi_3) = (60^{\text{o}}, 180^{\text{o}})$, antennas with DMN (i.e. "B" and "C") deliver better performance, in particular Antenna "B". Overall, the antenna array performance with DMN is better up to a maximum of 10 dB in certain directions. Basically, this advantage is linked to the matching gain provided by the

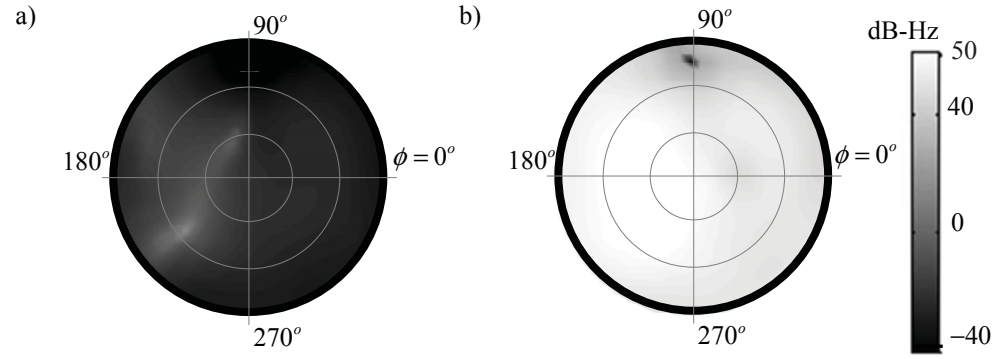

Figure 4.15: The calculated equivalent CINR for one LP interferer applying (a) single and (b) multiple degrees-of-freedom interference cancellation constraints.

DMN which appears dominant on its ohmic losses for all directions of the three interferers. Based on these results, it can be generalised that for robust navigation receivers it is *necessary* to deploy DMN for compact antenna arrays.

Non-linear characteristics of the analogue FE: So far we ignored the non-linear characteristics of the analogue FE, especially the gain compression. However, if the received input power exceeds a threshold due to high-power interferences, the amplifying gain of the analogue FE is compressed. As a result of the compression of either one of the output amplifiers of the analogue receiver circuit or the analogue-to-digital converters (ADC), the satellite signals are severely distorted or even blocked. This effect leads to a reduced equivalent CINR and an increased acquisition error.

In the case of single strong RHCP interferer and antenna "A" considered previously, it is observed that the received power is almost equal for all antenna elements. The analogue FE is prevented from saturation only for some directions where the interferer suppression is approximately $10\ \mathrm{dB}$. The reason is that the mutual coupling between the antenna elements cannot be eradicated using digital beamforming techniques. However, the received interference power with DMN, i.e. antenna "B", antenna "C", and antenna "D", is suppressed by approximately $15\ \mathrm{dB}$ in most directions for at least one of the receiver channels. The desired satellite signals coming from this direction are, therefore, not blocked, i.e. they are fully available for signal processing. This is because the DMN not only decouples the antenna elements, but also provides orthogonal patterns with nulls before the input of the analogue FE. This helps in suppressing the strong interferer before the input of the analogue FE and avoids its saturation, which provides additional benefit of the decoupling and matching network concerning the robustness of the receiver.

4.5.3 Arbitrary polarised interference scenarios

In the previous scenarios, only the co-polarised interferers were considered. These do not truly represent real-life scenarios, because in urban or non-line-of-sight scenarios, interferers become elliptically polarised. On the other hand, it is easier to form a linear polarised (LP) interferer than a circular polarised one. In addition, in the previous chapter it was shown that the cross-polarisation, or LHCP, becomes comparable to RHCP, in particular for the highest order mode of the compact antenna arrays.

Therefore, with a single LHCP or LP interferer and null-constraint in the RHCP direction, the CINR drops well below 0 dB, as shown in Fig. 4.15a. In the case of the LHCP interferer, it can be nullified using a single LHCP degree-of-freedom. However, with the LP interferer, it is not possible to nullify it with a single circular polarised degree-of-freedom, as it is received in both co- and cross- circularly polarised antennas, if their levels are comparable. But, if an additional LHCP null-constraint in the previously considered single LP interferer situation is used, which is fixing one of the remaining two degrees-of-freedom, for the suppression in cross-polarisation, with the RHCP and LHCP constraints nulling the same interference direction, then it can be mitigated. With this configuration, a similar CINR performance in all azimuth directions as compared to a single RHCP interferer with RHCP null-constraint is achieved. The calculated CINR for the complete upper hemisphere in the case of a LP interferer, fixed at $\theta = 15^{\text{o}}$, $\phi_i = 75^{\text{o}}$ is shown in Fig. 4.15b. For the four-element circularly polarised compact antenna array, this approach of interference cancellation will ensure nulling of, at maximum, one arbitrarily polarised interferer and either one RHCP or one LHCP interferer [158].

4.6 Low-cost compact GNSS antenna array

Until now, customised approaches of compact antenna arrays, using commercially available substrates, have been developed. These demand careful designing, optimising of the individual radiators, and even expensive manufacturing, to achieve the desired axial ratio and matching bandwidths, which may limit their economic mass-production on an industrial scale. In contrast, commercial off-the-shelf (COTS) antenna elements are cheap and readily available. These antennas have already been applied to conventional half-wavelength antenna arrays for improving navigation accuracy along with interference mitigation [89].

The developed compact antenna array consists of four radiating elements with an inter-element separation of a quarter of a free-space wavelength. The individual antenna elements, COTS GPS ceramic patch antennas (discussed in the previous chapter), are mounted with separated substrates on a common ground-plane, as shown in Fig. 4.16a. The overall size of the antenna array with a ground-plane is 100 mm $\times$ 100 mm, about

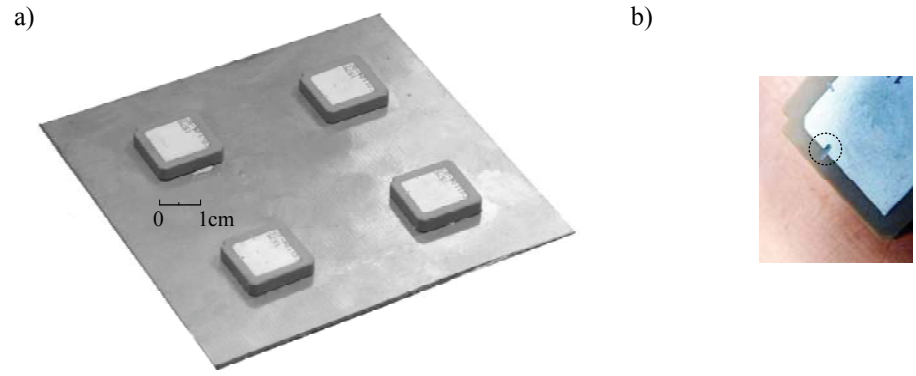

Figure 4.16: (a) Four-element square ceramic patch antenna array on a reduced ground-plane $10\ \mathrm{cm} \times 10\ \mathrm{cm}$ with inter-element separation of $d = \lambda/4$ and (b) slits applied to tune the individual antenna elements for axial ratio.

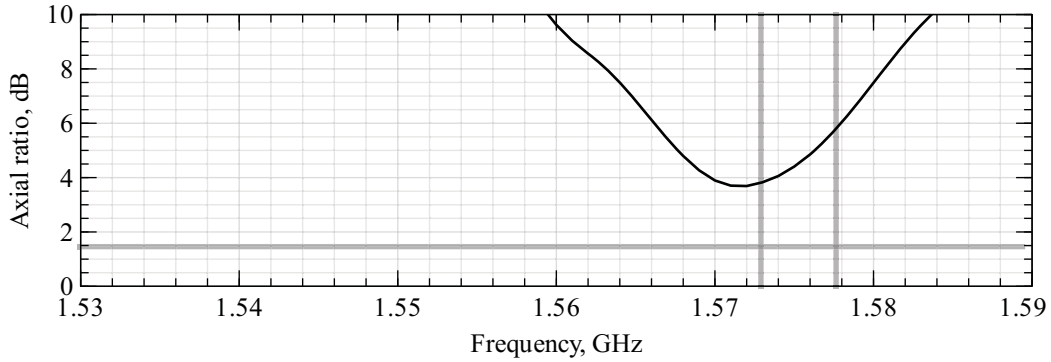

Figure 4.17: Measured axial ratio in the main-lobe directions for the antenna shown in Fig. 4.16a.

$\lambda/2$, which is considerably smaller than the dimensions of the antenna arrays described previously. The RHCP realised gain in main-lobe direction, is approximately $5\ \mathrm{dBi}$, and the maximum LHCP realised gain in the same direction is $-4.5\ \mathrm{dBi}$. The axial ratio versus frequency shown in Fig. 4.17, clearly reveals that the value remains above $3\ \mathrm{dB}$ over the entire signal bandwidth in the main-lobe direction which needs to be addressed in order to employ these arrays in navigation applications. This shortcoming may be removed by re-tuning the antenna elements, and is normally done by inserting slits on the edges of the patch, as highlighted in the inset of Fig. 4.16b. This modification for the even mode, while maintaining the precise manual etching of the individual radiators, is not easily realisable because of the narrowband axial ratio characteristics associated with these types of truncated patch antennas (cf. discussion in Section 4.5.1).

The significant level of cross-polarisation will cause the reception of unwanted multipath signals which undermine the robustness of the receiver. In order to minimise the

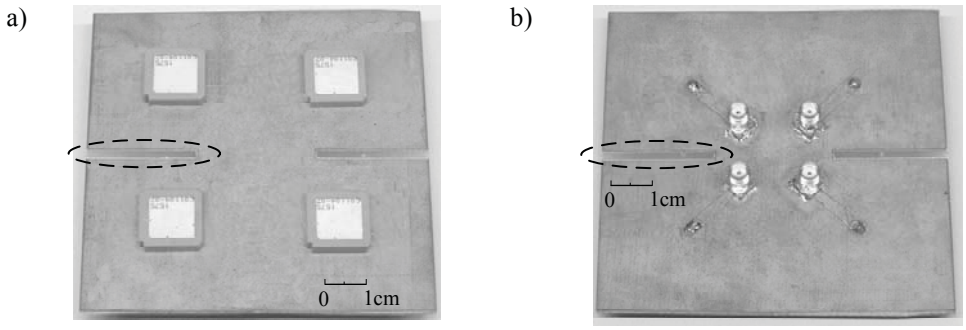

Figure 4.18: (a) Four-element square-shaped ceramic patch antenna array on a reduced ground-plane $10\ \mathrm{cm} \times 10\ \mathrm{cm}$ with inter-element separation of $d = \lambda/4$, (b) introduced slits, highlighted with dotted ellipse, in the ground-plane to tune the axial ratio.

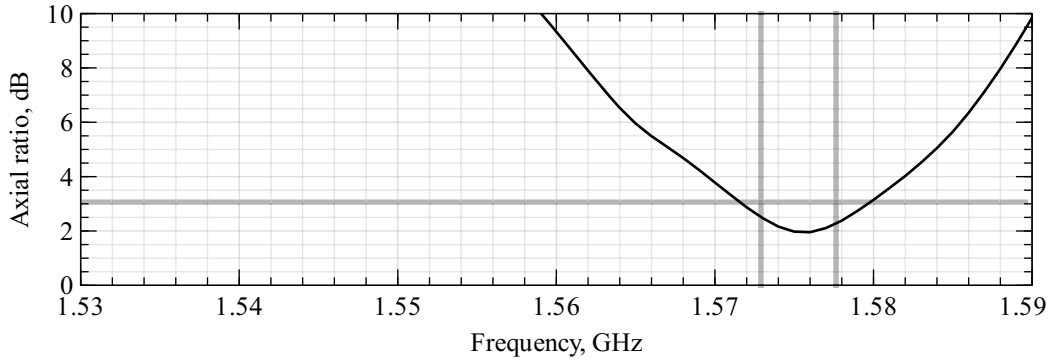

Figure 4.19: Measured axial ratio in the main-lobe directions for the antenna with ground-plane slits shown in Fig. 4.18.

axial ratio in the main-lobe direction, additional slits in the ground-plane highlighted in the inset of Fig. 4.18 are introduced. These slits decouple the higher-order modes which are responsible for cross-polarisation radiation, and suppress their radiation in the case of even mode excitation. The co-polarisation radiation is also affected, and the realised gain is reduced by $1\ \mathrm{dB}$, but this is still acceptable. The axial ratio versus frequency for the modified antenna is shown in Fig. 4.19, which in the operating band drops below $3\ \mathrm{dB}$ in the frequency range of interest, and fulfils the requirements for the navigation antennas.

4.6.1 Miniaturisation of decoupling and matching network

As discussed earlier, for a four-element antenna array, four hybrid couplers are required to excite the respective eigenmodes (cf. Fig. 4.6b and c). However, the size of the single miniaturised hybrid coupler is $0.32\lambda_g$ which is approximately $20\ \mathrm{mm}$ in diameter at the

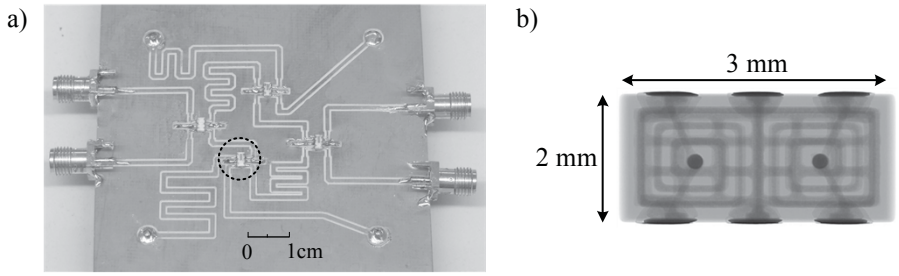

Figure 4.20: (a) The fabricated design of the DMN of the antenna array shown in Fig. 4.18. (b) X-ray view of the applied quadrature coupler.

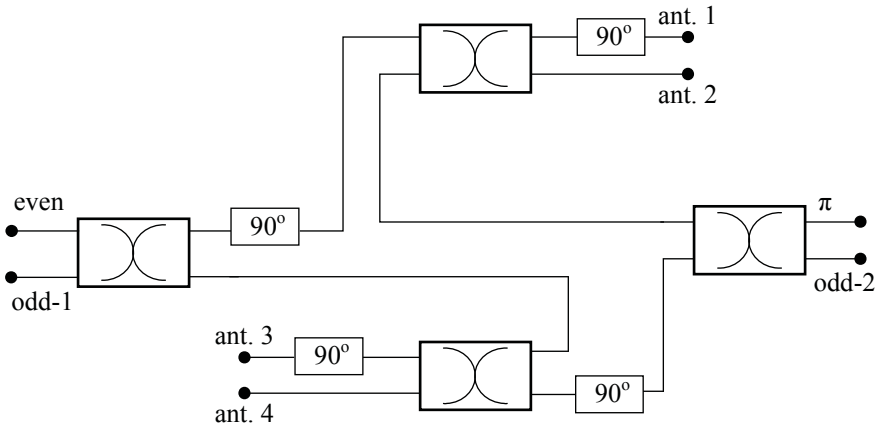

Figure 4.21: The block diagram of the decoupling network using OTS quadrature couplers for the four-element antenna array.

L1/E1 frequencies, while using a substrate with $\epsilon_r = 10.2$. Here, the waveguide wavelength is defined as $\lambda_g = \lambda_o/\sqrt{\epsilon_r}$. This results in a large size of the complete DMN and does not offer an attractive solution, neither for miniaturisation nor for mass production.

Therefore, a complete DMN using four COTS $90^{\text{o}}-$directional couplers on the low-cost FR-4 epoxy substrate with $\epsilon_r = 4.4$ and a thickness of 1.58 mm is fabricated, as shown in Fig. 4.20. The block diagram shown in Fig. 4.21, describes the circuit of the network, which includes 90^{o} delay lines to transform these quadrature couplers into $180^{\text{o}}-$hybrid couplers. As apparent from the figure, the use of COTS components offers a compact size and eases industrial-scale assembly. The overall size of the decoupling network only is reduced by *half* of the previous designs in Section $4.5.1$. Furthermore, overall size miniaturisation is also possible by high permittivity carrier substrate for the miniaturisation of the quadrature microstrip delay lines, which are a limiting factor for the overall size in this approach.

Earlier, the equivalent CINR was introduced as the crucial parameter for navigation receiver performance. Therefore, instead of describing the mutual coupling coefficients

Table 4.4: The analytically computed equivalent CINR values, in dB-Hz, for the COTS four-element antenna array with and without DMN in the fixed desired calculation of $\theta = 87.5^{\mathrm{o}}$ and $\phi = 108^{\mathrm{o}}$. The RHCP interferer directions are fixed in elevation directions, i.e., 15^{o}, and are distributed in azimuth directions.

number of interferers	interferer impinging directions	antenna configurations	
		without DMN	with DMN
zero (without)	-	56.3	56.2
one	$\theta = 15^{\mathrm{o}}$, $\phi = 0^{\mathrm{o}}$	50.5	51.7
two	$\theta = 15^{\mathrm{o}}$, $\phi = 0^{\mathrm{o}}$, and 180^{o}	45.4	46.5
three	$\theta = 15^{\mathrm{o}}$, $\phi = 0^{\mathrm{o}}$, 90^{o} and 180^{o}	41.75	45.86

of the antenna array with and without DMN, the CINR is calculated for the measured antenna patterns. The calculated equivalent CINR with and without interference scenarios are recorded in Table. 4.4. With no interference, the CINR in the desired direction is 56.3 dB-Hz without DMN and slits, which is 0.1 dB higher than with DMN and slits in the antenna array. Therefore, there is no advantage of DMN or the slits in the no interferer scenario. As the even mode of the antenna array matching is not affected by the mutual coupling, the DMN gives no benefit; rather it introduces insertion loss which undermines the performance of the antenna array.

In the case of one and two RHCP interferers, the CINR of the antenna array with DMN is 1 dB better than without DMN, which is in agreement with the previous conclusions. There is marginal improvement with DMN for the equivalent CINR in a minimum number of interferers. However, in the case of maximum interferers, i.e. three, the CINR with DMN is improved by 4 dB in the desired satellite direction. This validates the importance of DMN for robust compact navigation antenna arrays in interference-limited scenarios in particular.

4.7 Summary

In this chapter, the challenges of the decoupling and matching techniques and their implementations are described. In order to achieve the matching of the compact antenna arrays for all direction of arrivals, it is necessary to primarily perform the decoupling. Several decoupling techniques along with their limitations are discussed. The broadband decoupling, based on hybrid couplers network, is possible which allows larger tolerances for manufacturing. However, eigenmode matching techniques suffers from narrow bandwidth

characteristics, especially for the higher-order modes. The maximum achievable bandwidth is observed to be limited due to the inter-element separation of the antenna arrays.

The integration of the DMN with the compact planar antenna array in multi-layered substrate approach is successfully designed and fabricated. As far as the DMN is concerned, it is helpful to increase the minimum eigenvalue of the antenna by at least 50% as compared to the similar antenna array without decoupling and matching. However, for other eigenvalues the benefit is not significant. Therefore, it becomes necessary to find how does this improvement in efficiencies of eigenmodes translate into the navigation receiver's CNR performance, while including insertion losses of the DMN.

In order to evaluate the effect of ohmic losses and mutual coupling on navigation performance, the diversity receiver model incorporating equivalent CINR has been derived based on the measured correlated noise matrices of the antenna array. The absolute performance is dependent on the beamforming weights and the corresponding algorithm characteristics.

To investigate the equivalent CINR performance, several customised GNSS compact antenna array designs with integrated DMN are presented. In regards to the robustness, decoupling and matching network has no advantage or disadvantage in the case of no interference. However, the significance of the DMN seems to be noticeable in the presence of interference, because of the utilisation of the higher-order modes for beamforming. Moreover, the benefit of the DMN is more prominent for the maximum interferer scenario, which is three for the four-element antenna array. The equivalent CINR is improved by at least $3\ \mathrm{dB}$ in all directions, and extends to $10\ \mathrm{dB}$ in low-elevation directions.

Finally, an optimal miniaturised L1/E1 band RHCP compact antenna array, with integrated miniaturised DMN, using cheap commercial off-the-shelf high permittivity ceramic patch antennas and discrete quadrature directional couplers, is presented. This provides the possibility of mass-production with the constraint of low-cost.

Chapter 5

Practical Implementation of Adaptive Compact Navigation Receiver

An implementation of a complete navigation receiver, including the analogue FE, digital receiver, and baseband processing is essential to verify the equivalent CINR model derived in previous chapters. This also provides a platform from which to evaluate the performance of the compact GNSS antenna array in realistic scenarios with and without DMN. To the best of the author's knowledge, this insight is not yet available in the literature.

One approach of implementing the multi-channel analogue FE may involve existing GNSS single-channel analogue FEs. However, these are not compatible with interference signals because of their small dynamic range and high-gain amplification. If used, they will cause the FEs to be saturated and operate in the non-linear region for a very low-power interference or jammer signal. Therefore, different customised multi-channel FEs are developed and explained in this chapter while keeping the specifications of interferences in mind. The maximum JSR considered in this work is $40\ \mathrm{dB}$: beyond this, the analogue FE will saturate the input of the analogue-to-digital converters (ADCs). Secondly, the use of eigenmode antenna arrays in which radiation patterns are non-uniform and dissimilar, add more uncertainty in terms of applying conventional beamforming and interference suppression algorithms in the digital receiver. The consequence of the eigenmode antenna arrays on these adaptive algorithms is relevant in these implementations. Therefore, conventional adaptive nulling algorithms with CNR performance are investigated using the developed demonstrator.

The beginning of this chapter presents the overview of the demonstrator components. This follows a description of the algorithms in the baseband and the adaptive null-steering. Finally, the results of the demonstrator for indoor and outdoor experiments under the influence of the interference are revealed.

5.1 Overview of the compact multi-element GNSS demonstrators

The GNSS demonstrator can be divided into four main components:

1. Antenna array;
2. Analogue FE;
3. Digital receiver;
4. Baseband signal processing.

Antenna array: The antenna array block consists of the compact antenna array with miniaturisation of the inter-element separation to $d = \lambda/4$ along with the integrated DMN. These designs have been thoroughly discussed earlier (see Chapter 4). Furthermore, for the functionality of the complete demonstrator and signal processing algorithms, like beamforming and DOA, a calibration network is necessary and is integrated into this block as well, after the DMN. The purpose and description of this calibration network is described later (see Section 5.4).

Analogue FE: In the navigation receivers, the analogue FE is responsible for the amplification of the RF signal delivered or captured by the antenna and the down-conversion to the IF signal. The main blocks for the single-channel case have already been discussed in Chapter 1. There are several state-of-the-art single-channel FEs available off-the-shelf that are suitable for navigation signal reception. However, these are not suitable for use as robust navigation receivers. Basically, the high-gain amplification along with smaller $1\ \mathrm{dB}$ compression of the amplifiers causes their non-linearity in the presence of high-power in-band interferers. Moreover, the multi-channel FE demands the synchronisation of the local oscillator (LO), which is impossible to achieve in these FEs because of the lack of access to the internal LO stage. On the other hand, a multi-channel analogue FE that meets the specifications for robust GNSS applications is not yet commercially available. Therefore, the customised multi-channel FE design becomes crucial for the development of the GNSS demonstrator.

Digital receiver: The digital receiver block consists of the data acquisition, covariance matrix estimator, and signal conditioning stages. The data acquisition mainly consists of the ADCs with a common reference clock for sampling. As in this work, only C/A-code signals of the L1/E1 band are considered for the demonstrator; therefore, a minimum bandwidth of $\pm 1.023\ \mathrm{MHz}$ around the central frequency $f_o = 1575.42\ \mathrm{MHz}$ is required from this block, such that the sampling rate remains twice the signal bandwidth, to recover the complete signal. Next, the digitised data are used to estimate the received covariance

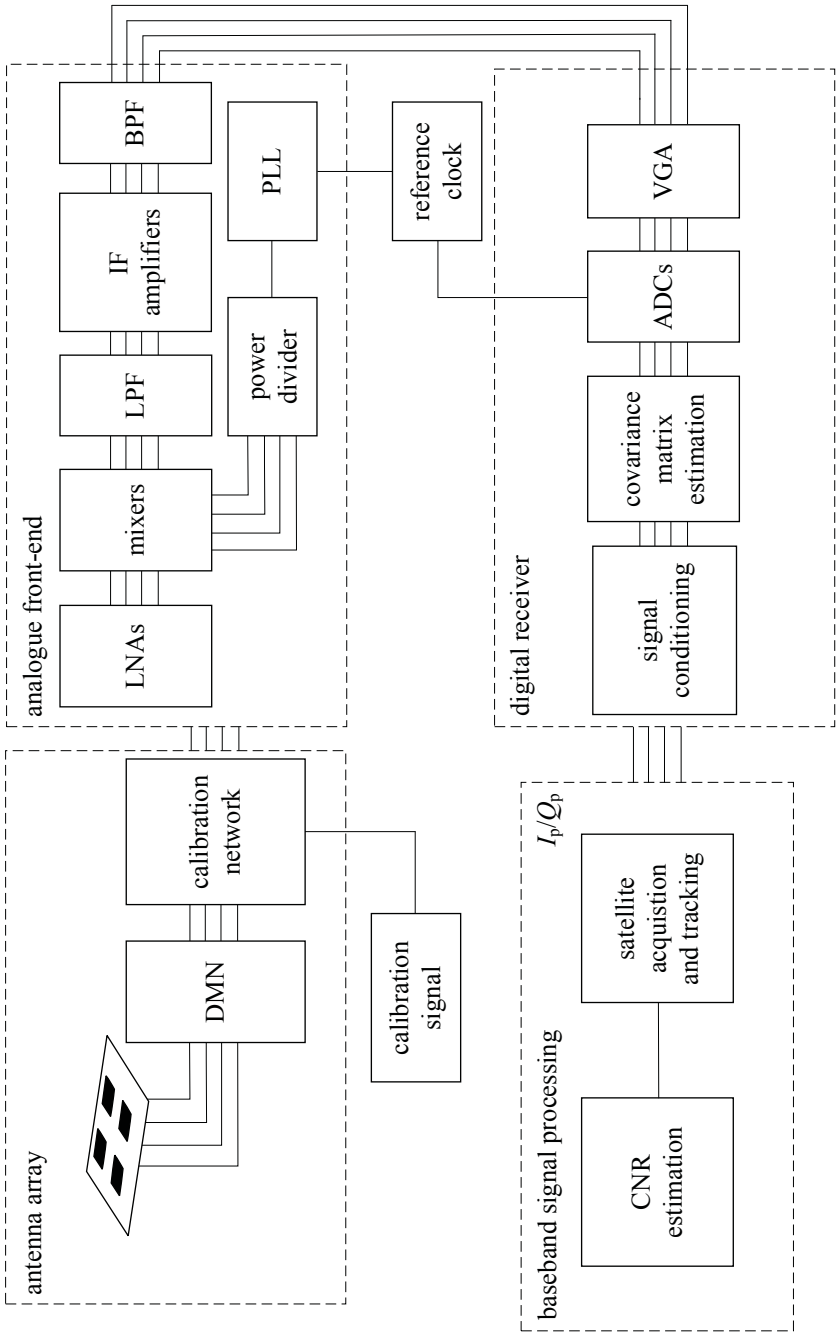

Figure 5.1: Block diagram of the compact GNSS antenna array receiver demonstrator.

matrix, $\bar{R}_y$, for the received signal matrix, $\bar{Y}$, which has dimension of $N \times M$, where M are the total number of recorded samples. This is given by

$$\bar{R}_y = \frac{1}{M}\bar{Y}\bar{Y}^{\mathrm{H}} \tag{5.1}$$

The accuracy of $\bar{R}_y$ is directly proportional to the N number of samples considered. The next step of signal conditioning may include the spatial filtering of the received signal from the unwanted signals, such as interference or jammer signals mainly in-band.

Baseband signal processing: The received signal is digitally down-converted to the baseband, which involves the removal of the carrier signal, by multiplication of the received signal with the in-phase (I_{p}) and the quadrature-phase (Q_{p}) replicas of the carrier sinusoidal signal. These baseband signals are then searched to acquire the transmitted satellite code signals. The acquired satellites, with SNR above the set threshold, are passed on to the tracking algorithm to lock the given satellite code and carrier in order to retrieve the transmitted navigation signals. Therefore, each $20\ \mathrm{ms}$ of tracked signal retrieves one complete navigation bit. These tracked navigation bits are then decoded to ascertain the satellite time and position information along with the vital CNR information.

The complete block diagram of the compact GNSS antenna array receiver demonstrator is shown in Fig. 5.1.

5.2 Multi-channel analogue front-end architecture

The parameters of the multi-channel analogue FE receiver architecture that govern its performance include the maximum allowed input signal power level, amplification gain, out-of-band suppression levels, noise figure, and dynamic range of the ADCs in the digital receiver. Considering the C/A-code, the received carrier power is below the thermal noise power level; therefore, the maximum allowed input signal detection level defines the maximum acceptable jammer power, which is $40\ \mathrm{dB}$. Both the amplification gain and the dynamic range, collectively, are defined by the minimum input detection power level of the analogue FE. This should also consider the maximum jammer power level to remain in the dynamic range of the ADC, which will otherwise be saturated.

There are two different types of low-IF analogue FEs implemented in this work. The first part constitutes off-the-shelf discrete integrated circuit (IC) printed-circuit board (PCBs). The second is a customised design and fabrication of a four-channel IC chip for L1/E1 band frequencies.

5.2.1 Analogue front-end based on discrete components

The analogue FE constitutes the following building blocks: LNAs, mixers, low-pass filters (LPFs), IF amplifiers, band-pass filters (BPFs), PLL, and a power divider as shown in

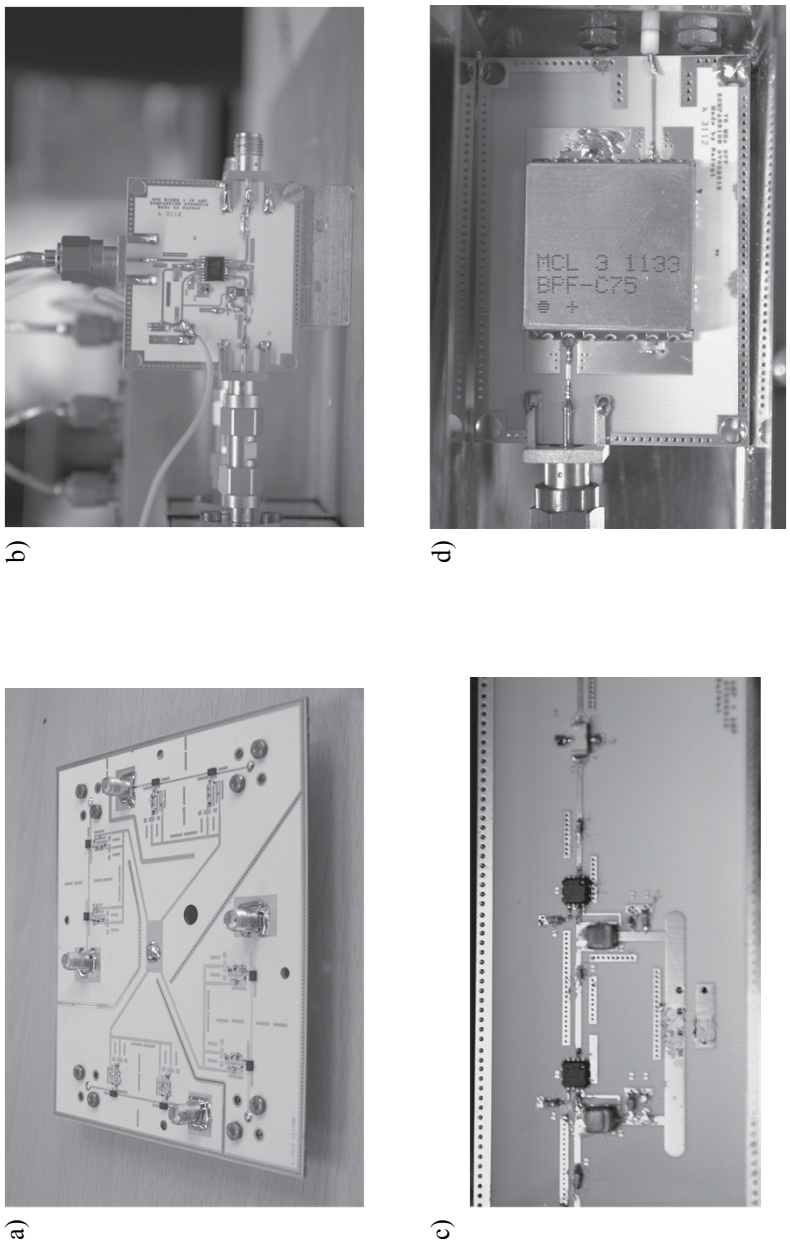

Figure 5.2: (a) Four-channel LNA PCB with integrated narrow band L1/E1 pre-selection filtering. (b) Single mixer PCB with integrated matching circuit and LPF. (c) IF amplifier PCB for single channel. (d) Narrow (BPF) for IF signal.

Fig. 5.1. The PCB designs for the individual ICs are optimised for better RF shielding, minimal cross-talk (coupling among the channels) and noise figures.

LNA: The first four-channel low-noise high-gain amplification stage is designed as a separate PCB mounted directly after the DMN outputs as shown in Fig. 5.2a. Moreover, to minimise the overall noise figure of the complete receiver, this is directly connected at the output of the DMN (after the calibration network, if employed). It consists of four independent channels, each providing high-gain amplification up to 36–38 dB. This is achieved using two LNAs from Avago Technologies ALM-1912 [149] in cascade configuration. In addition, each LNA is preceded by a bulk acoustic wave (BAW) filter, which delivers superior out-of-band rejection performance with steeper curves compared to surface acoustic wave (SAW) filters, for which the minimum is 40 dB. The measured NF for each channel is approximately 1.7 dB. The measured output 1 dB compression point is -30 dBm. Note that, because the fabrication and soldering tolerances result in ± 2 dB and ± 0.2 dB variation in the amplifications and the noise figure values, respectively, of the individual channels, careful calibration is required.

Mixer: An active mixer PCB with a high output 1 dB compression point is designed for down-conversion into the IF, which is chosen to be 74.8 MHz (see Fig. 5.2b). An LPF with a cut-off frequency of 95 MHz, LFCN-95+ from Minicircuits [150], is placed directly after the output of the mixer to reject image and high-frequency spurious signals. The minimum input power for the LO is 5–10 dBm. This PCB also includes a pre- and post-amplifier stage for the LO input and IF output, respectively. The mixer is a HMC421QS16 chip from Hittite [151]. The independent four-mixer PCBs are well separated from each other to avoid cross-talk, particularly for the LO signal, which is in the vicinity of the incoming L1/E1 signal (i.e. 1500.62 MHz). Furthermore, in order to maintain the phase coherence between the mixer LO inputs, a 0^{o}-phase output four-way splitter is used to divide the amplified PLL output (4 dBm) while keeping the output powers above the required threshold.

IF amplifier and band-pass filter: After the down-conversion, the IF signal is fed to the IF gain block with a high output 1 dB compression point of 20 dBm and 40 dB amplification gain. This is based on the Analog Devices ADL5531 ICs [152]. A narrow band-pass filter BPF-C75+ with 8 MHz bandwidth from Minicircuits [150] is necessary to reduce the out-of-band noise. The two separate PCBs are shown in Fig. 5.2c and d.

Phase-locked-loop synthesiser: The ADF4351 PLL frequency synthesiser PCB from Analog Devices [152] with an integrated voltage-controlled oscillator (VCO) consists of a programmable Universal Serial Bus interface controller for tuning the output frequency. The reference clock can be provided from the external signal generator or the internal fixed 25 MHz temperature-controlled oscillator (TXCO), which is robust against temperature changes. The output of the PLL is tuned to 1500.62 MHz with maximum output power from the PLL of only 4 dBm, which decreases to approximately -3 dBm with power divider and is below the recommended input power level for the LO input of the mixers.

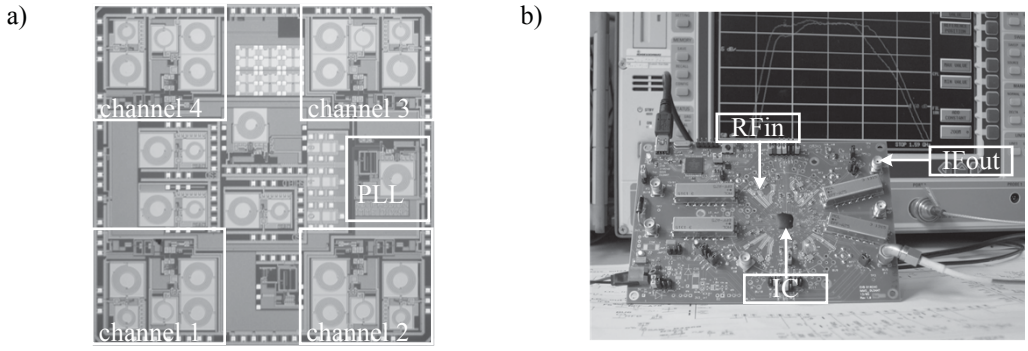

Figure 5.3: (a) Chip photograph of the FE IC. The enlarged area contains the active FE components, highlighted as channels and PLL. Other structures are for characterisation purposes only. Die size: $5\ \mathrm{mm} \times 5\ \mathrm{mm}$. (b) The four-channel FE IC evaluation board with IC under black top in the center of the board. The RF inputs, indicated as RFin, are mounted on the back side, and four IF outputs, indicated as IFout on the left and right corners of the PCB. Board size: $14\ \mathrm{cm} \times 9\ \mathrm{cm}$.

Therefore, an external broadband amplifier is applied at the output of the PLL to achieve the output power levels of $10\ \mathrm{dBm}$, which is the required minimum input power level for the mixers.

5.2.2 Integrated analogue front-end circuit

This work has been a contribution from partners at the Institute for Microelektronic und Mechatronic System (IMMS) [153]. The main part of the integrated multi-channel FE is implemented in a commercial $180\ \mathrm{nm}$ silicon CMOS process. An external SAW filter for pre-selection of the RF band is fabricated on the evaluation board. Furthermore, in order to reduce the out-of-band noise before sampling, an external IF filter is employed with a narrow band defined according to the signal bandwidth requirements. A detailed description of the IC and the evaluation board can be found in [159].

A micro-photograph of the manufactured FE IC is shown in Fig. 5.3a. The four individual signal paths are placed symmetrically in the corners of the IC in order to reduce coupling through the inductors or the substrate of the chip. The five on-chip inductors shown in Fig. 5.3a are clearly visible in the layout. The PLL, including the inductor of the voltage-controlled oscillator, is located on the centre right-hand side of the IC. The chip size is $5\ \mathrm{mm} \times 5\ \mathrm{mm}$. The RF and IF signal pads are shielded by ground pads in order to reduce the coupling between the bond wires.

The FE IC characterised on wafer level and populated within an evaluation board is shown in Fig. 5.3b. The board itself consists of a $0.25\ \mathrm{mm}$ thick RO4003 substrate with $\epsilon_r = 3.55$ from Rogers cooperation laminated on a $1.54\ \mathrm{mm}$ thick FR4 carrier substrate with $\epsilon_r = 4.4$. Off-chip matching of the LNA is realised with transmission lines and

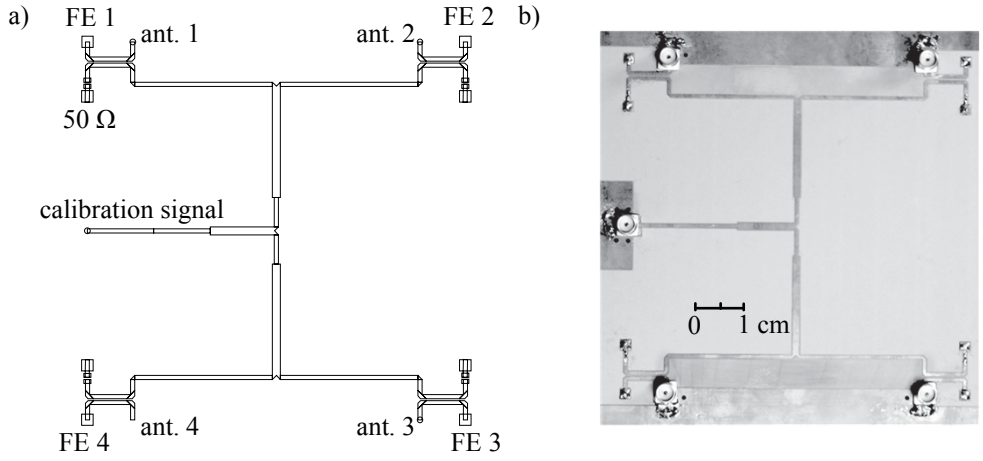

Figure 5.4: (a) Sketch of the calibration network, it constitutes a four-way power divider and four directional couplers. (b) The fabricated calibration network.

capacitors instead of discrete lumped components in order to minimise the losses of the matching circuit.

5.3 Calibration of the analogue front-end

Even though the analogue FE is operated using a coherent LO, the anomalies in the signal path lengths due to the design and fabrication may vary the relative phase and amplitudes of the signal among the channels. This may lead to inaccuracies in the DOA, beamforming, and position estimation for the navigation receiver. Therefore, it is necessary to calibrate the analogue FE with the accurate operation of the signal processing algorithms in digital and baseband domains.

A rudimentary technique for calibration involves the offline measurement of the relative phase and amplitude between the channels of the analogue FE. The term *offline* indicates the lack of the antenna array and digital receiver. These measured fixed values can be stored in the digital domain for compensation in the calculation of its algorithms. This can be termed an *offline calibration* method. However, if the inter-connecting cables or connectors either inside the analogue FE or between the ADC and the analogue FE are changed, then the measured calibration coefficients become invalid. Another drawback of such a calibration approach is that the temperature or heating effects are ignored, which may change the measured coefficients because of the environmental conditions and the operational time span of the receiver.

On the other hand, an *online* calibration is performed with the antenna array, analogue FE, and digital receiver connected and is more robust to hardware or temperature changes

within the system. One such technique employed in multi-antenna receivers is the calculation of relative calibration coefficients using a reference source or transmitter signal present in the environment. In the case of the GNSS signals, this is normally employed using the satellite available in the zenith. However, the probability of finding the satellite in the zenith permanently at a fixed Earth location is very low. Therefore, a satellite close to the zenith is normally considered for this purpose, which induces a bias in the signal processing estimation algorithms and is undesirable. Additionally, this method requires a priori knowledge of the satellite constellation, which makes it an impractical approach. Moreover, for the compact antenna array with mode patterns that are orthogonal in nature, it is not possible to acquire the satellite coming from zenith directions independently by every channel simultaneously.

In [120], a robust online calibration method is proposed that involves the injection of an artificially generated up-converted satellite reference signal in the digital receiver at the input of the analogue FE through a dedicated passive *calibration network*. In this work, this calibration network is implemented in the analogue FE. However, it is inserted after the DMN rather than the compact antenna array in order to avoid mismatching and coupling malefactors. The network design is based on microstrip line technology on a commercially available Rogers RO3010 substrate of thickness $1.27\ \mathrm{mm}$ and $\epsilon_r = 10.2$ with $\tan\delta = 0.0023$. The network comprises four directional couplers and a four-way power divider. The layout of the calibration network is shown in Fig. 5.4a, and the fabricated one is shown in Fig. 5.4b. The measured scattering parameters of the calibration network show an insertion loss of $0.2\ \mathrm{dB}$ between the antenna outputs and the FE inputs, a coupling factor of $-22\ \mathrm{dB}$ between the calibration signal and the FE inputs, directivity of $26\ \mathrm{dB}$, and an isolation of $48\ \mathrm{dB}$ between the antenna and the calibration signal within the operating band of L1/E1.

5.4 Data acquisition

The data acquisition block includes the ADCs and the interface to the personal computer. This is designed using low-cost digital video broadcast for terrestrial (DVB-T) dongles based on the RTL2832 chipset [154]. This platform provides an output of $I_\mathrm{p}/Q_\mathrm{p}$ 8-bit samples (each) with a maximum sampling rate of $2.56\ \mathrm{MSps}$. This provides a dynamic range of approximately $45\ \mathrm{dB}$ for a maximum input power of $10\ \mathrm{dBm}$. These dongles possess an on-board low-quality reference clock oscillator with high phase noise and without any option for an external reference clock input. However, in the case of multi-channel ADCs, it is necessary to synchronise the sampling clock. This synchronisation is achieved by manually disassembling the in-built oscillator and replacing it with an external connector that is fed with a shared high-precision clock source. The setup with the modified circuitry for the four dongles is displayed in Fig. 5.5

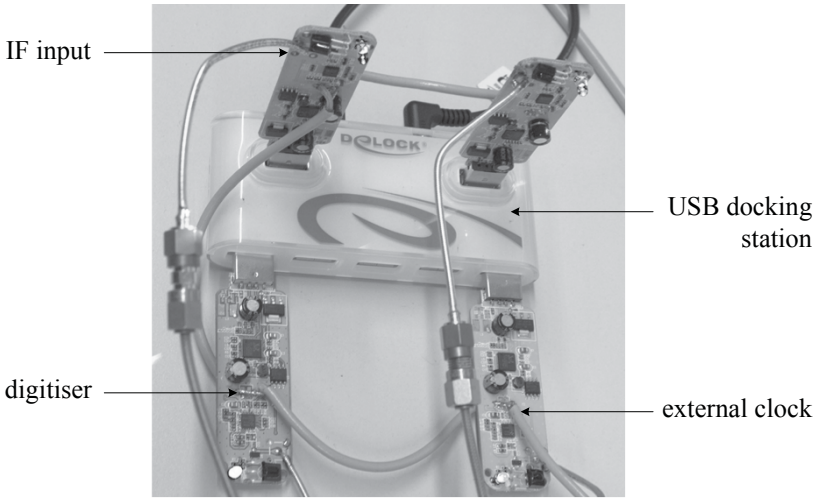

Figure 5.5: Four-channel data acquisition unit based on the broadband DVB-T dongles with 8-bit raw I_{p} an Q_{p} samples at a maximum sampling rate of 2.56 MSps.

The ADC sample outputs are transferred to the PC using a USB connection. The high-speed USB 2.0 interface delivers the captured data to the PC at a maximum rate of 30 MSps. The received digitised data is then stored using MATLAB. This provides flexibility and ease of implementation for the complex interference cancellation and navigation baseband signal processing algorithms.

During this study, another high-end data acquisition platform using a four channel ADC with 14-bit resolution and a sampling rate of 125 MSps integrated with a field-programmable gate array (FPGA) has also been implemented for the GNSS compact antenna arrays. This work is a contribution from the master's thesis work of Elamir [93]. This study is limited in terms of recording long datasets due to their huge size; therefore, that platform is not suitable for accurate CNR estimation and is not discussed here.

The complete integrated antenna array, DMN, calibration network, and LNA stage is shown in Fig. 5.6. It is attached to an assembly for mounting on the tripod and the measurement vehicle. The RF outputs of the LNAs are connected through coaxial cables to the analogue FE inputs shown in Fig. 5.7 for conversion into the IF.

5.5 Baseband signal processing

The baseband signal processing is performed in MATLAB because of its flexibility. It comprises three main blocks; acquisition, tracking, and CNR estimation. In the case of the eigenbeamformer the beamforming is performed post-correlation—that is, at the output of the tracking algorithms.

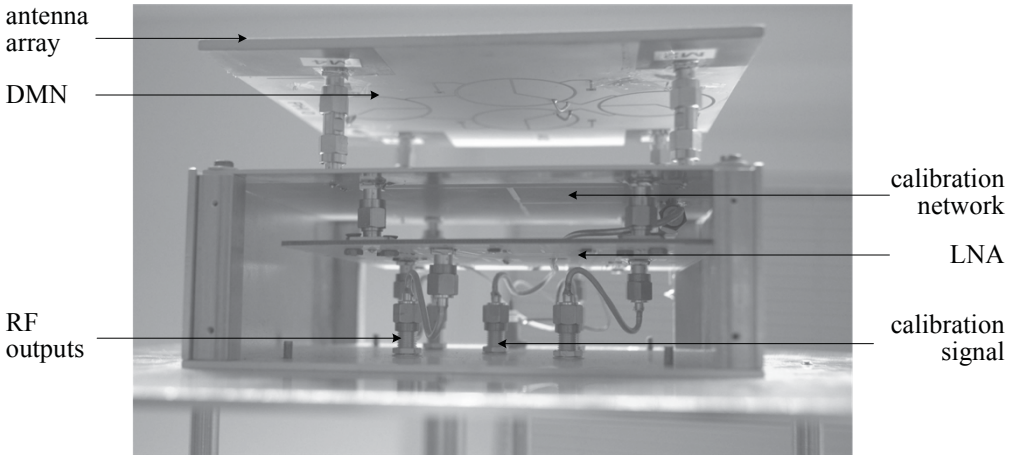

Figure 5.6: The integrated antenna array, DMN, calibration network, and the LNA PCBs. This assembly is directly mounted on the tripod for static testings and on the measurement vehicle rooftop for dynamic testings.

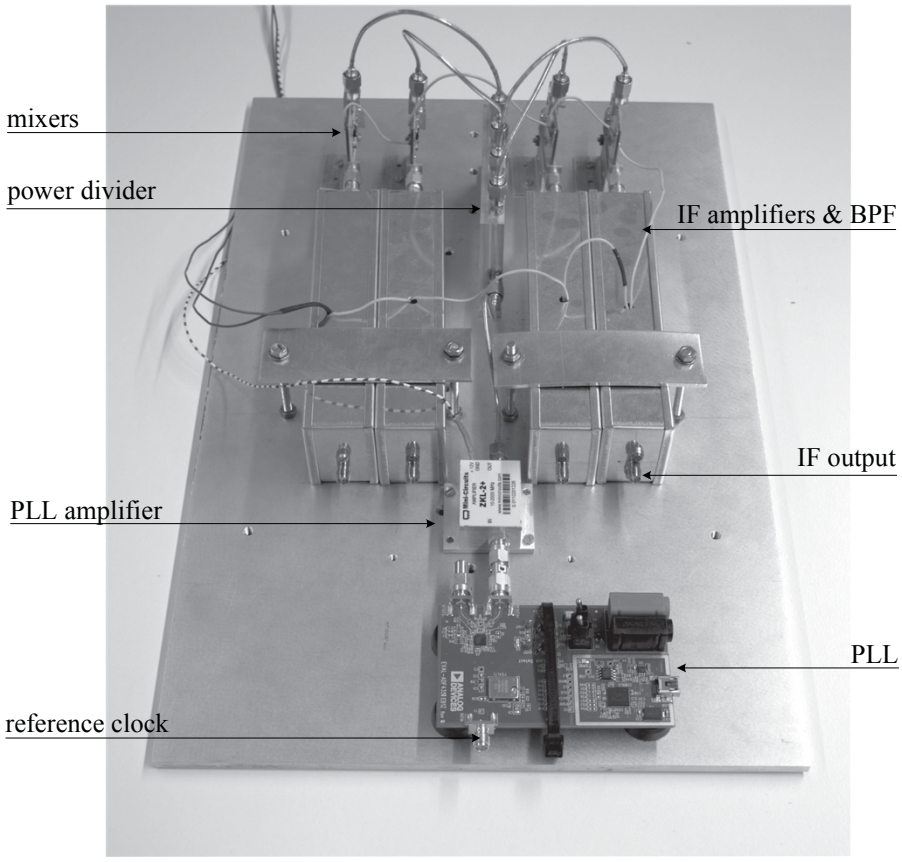

Figure 5.7: The designed and implemented four-channel FE, including PLL, mixer, IF amplifiers, and BPFs.

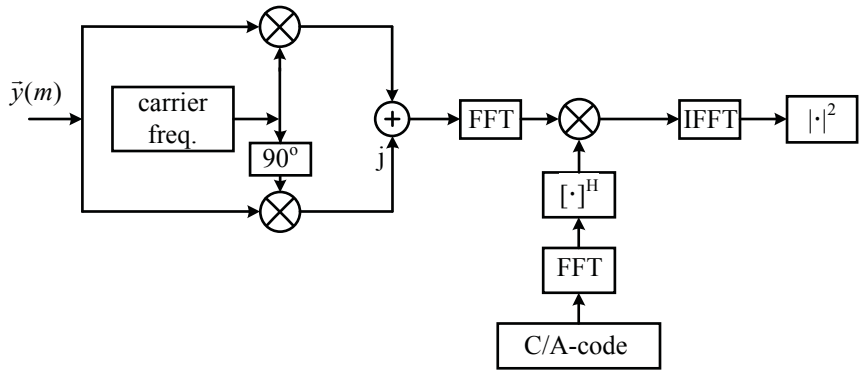

Figure 5.8: The acquisition algorithm block diagram implemented in the baseband processing.

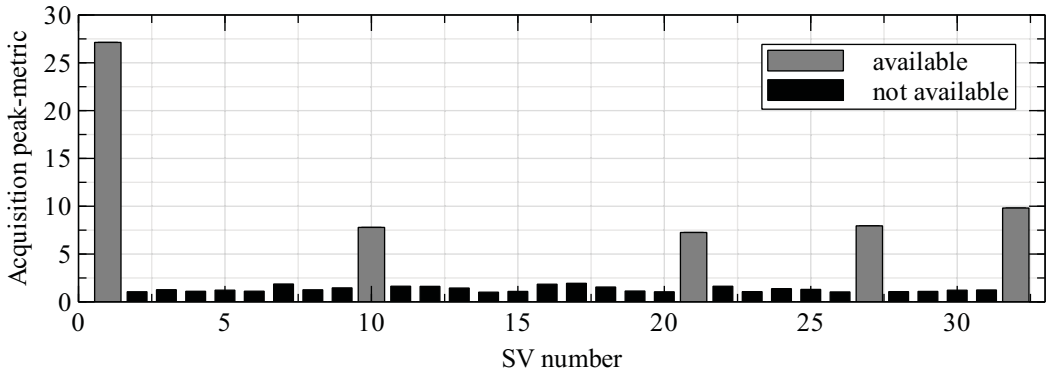

Figure 5.9: The output of the acquisition algorithm is the acquisition metric for the acquired GPS satellites. The grey bar indicates the availability of the satellite.

5.5.1 Acquisition

This is a typical parallel code phase search algorithm for C/A-code [4]. This is chosen as it is more efficient than the other serial code phase search approach discussed in the beginning. Also advantage in the frequency domain computation is calculating the peak metric for all code phase delays simultaneously. Only the carrier frequency spectrum is searched to find the maximum value. Here, the minimum data required for acquisition is 1 ms which is the time duration of a C/A-code transmitted from the satellite at L1/E1 band.

The signal flow diagram of the acquisition algorithm is shown in the Fig. 5.8. The received signal $\vec{y}(M)$, minimum one millisecond data, is multiplied by carrier frequency replicas to obtain the I_{p} and Q_{p} samples. In order to compensate the carrier frequency errors due to the PLL and ADC noise, it is swept over the frequency bandwidth of ± 20 kHz centred at the operating IF frequency of 74.8 MHz. The fast-fourier transform (FFT) is

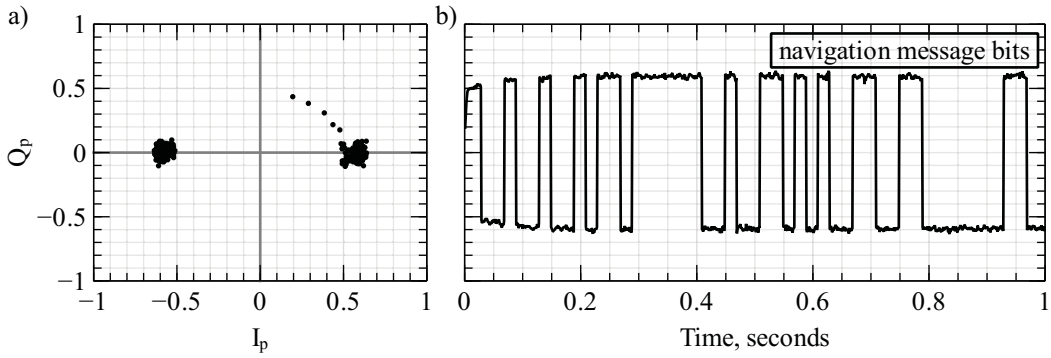

Figure 5.10: (a) The demodulated in-phase and quadrature navigation bits. (b) The retrieved navigation message over the time interval of one second.

taken for the complex signal and then multiplied by the FFT of the PRN code of the satellite after taking its Hermitian, $|\cdot|^{\mathrm{H}}$. This process is repeated for all possible satellite codes. It may be reduced by specifying only the number of satellites that are available at the time of tests and recordings.

The output of the acquisition delivers the peak metric values obtained for each satellite, which—by applying a threshold—can be categorised into the available and unavailable satellites as shown in Fig. 5.9. Here, the acquisition peak metric is set to 2.5. The information on the code phase delay and the carrier frequency shift is transferred to the tracking algorithms for tracking the acquired satellite signals.

5.5.2 Tracking

The tracking algorithm incorporates two tracking loops—one for the code delay and the second for the carrier frequency phase, called DLL and PLL, respectively, (see C.1). This is the conventional way of implementing the tracking as opposed to the more advanced Kalman filter based tracking algorithms, in which the navigation process dynamically controls the tracking loops in an optimal manner. The detailed description of the loop can be found in [4, Section 9.2.3]

The navigation message retrieved for satellite vehicle 21 is shown in Fig. 5.10. The I_{p} and Q_{p} deviation from its mean value in the amplitude is an indication of the noise present in the demodulated signal. The navigation message has a signal bit duration of $20\ \mathrm{ms}$. The navigation message sub-frame requires a minimum of $30\ \mathrm{s}$ of the data to determine the position and time estimates. These navigation bits are transferred to the CNR estimation algorithm described in the next section.

5.5.3 Estimation of carrier-to-noise ratio

The CNR estimation is generally applied after the tracking correlation, because it provides a closer estimate to the actual effective CNR [94]. The validity of the estimation assumes that the interference has already been suppressed or nullified. Normally, the pre-correlation CNR estimations are not reliable or stable because of their higher dependence on the analogue FE bandwidth compared to the signal spectrum[4]. There are two well-known estimators for the CNR as described in [80]. The first estimator is called the variance summing method, and the second is the power ratio method (PRM). In this work, the PRM method is implemented and will be described here only in its basic terms for the purpose of understanding. For further details about these estimators and their performance parameters, the reader is referred to [81]. In the PRM method, the CNR is given by:

$$\chi_{\text{o}} = 10\text{log}\left(\frac{1}{t_{\text{coh}}}\frac{\kappa - 1}{M - \kappa}\right), \qquad \text{dB-Hz}. \tag{5.2}$$

Here, t_{coh} is defined as the coherent integration time used in the correlators, which in this case is 1 ms. M represents the number of considered correlator outputs for CNR estimation. This can be a maximum value of 20 in order to avoid the navigation message transition bit. Therefore, in the implementation $M \in [1, 2, 4, 5, 10, 20]$ is taken to be 20 because of its higher accuracy in estimating the lower CNR values [80]. This means that a single CNR estimate for a given satellite vehicle is obtained after every 20 ms. In the above-mentioned (5.2), κ is defined as the averages of the calculated noise power P_{noise} and is given as:

$$\begin{aligned} \kappa &= \frac{1}{l}\sum_{k=1}^{l} P_{\text{noise}}(k), \\ \text{where} \qquad P_{\text{noise}}(k) &= \frac{P_{\text{NB}}(k)}{P_{\text{WB}}(k)}. \end{aligned} \tag{5.3}$$

The noise power is the ratio of the narrow-band noise power, P_{NB}, to the wide-band noise power, P_{WB}. These noise powers are calculated over M correlator samples. The narrow-band noise power has a bandwidth of $1/Mt_{\text{coh}}$, which in the case of $M = 20$ is 50 Hz, compared to the wide-band value of $1/t_{\text{coh}}$, which is 1 kHz. Both the narrow-band and the wide-band noise powers are calculated using L number of I_{p} and Q_{p} samples of the correlators and are described as:

$$
\begin{aligned}
P_{\mathrm{NB}}(k) &= \left(\sum_{(k-1)M+1}^{kM} I_{\mathrm{p}}(k) \right)^2 + \left(\sum_{(k-1)M+1}^{kM} Q_{\mathrm{p}}(k) \right)^2 , \\
P_{\mathrm{WB}}(k) &= \sum_{(k-1)M+1}^{kM} \left(I_{\mathrm{p}}^2(k) + Q_{\mathrm{p}}^2(k) \right) , \\
&\text{where} \qquad k \in [1, 2, ..., L/M].
\end{aligned}
\tag{5.4}
$$

For example, for 20 s of data, the total number of I_{p} an Q_{p} samples are $L = 20$ k with an accumulation time of 1 ms. Therefore, the maximum possible noise power values, k, can be $L/M = 1$ k samples, while considering $M = 20$. Therefore, without averaging $l = 1$, the possible CNR estimate values from 20 s of data will also be 1 k samples. Accordingly, with averaging or $l > 1$, the accuracy of the CNR estimator will increase, but the total number of output samples will decrease.

5.6 Adaptive null-steering or interference suppression

The weak GNSS signal power, which is below the thermal noise power level, makes it vulnerable against deliberate or inadvertent interference. Therefore, the multi-antenna system provides the possibility of suppressing these unwanted signals using the sophisticated algorithms of null-steering in signal processing. In the case of compact antenna arrays with integrated DMN, the new degrees-of-freedom or the eigenmodes are not identical as with the conventional multiple-antenna array because of the non-uniform radiation pattern shapes and efficiencies. Therefore, it is interesting to investigate the performance and properties of the conventional adaptive null-steering concepts for eigenmode antenna arrays in which the direction of the satellite and the interferers is unknown.

5.6.1 Power minimisation

The most popular and the simplest null-steering algorithm involves the minimisation of the mean square difference value between the reference antenna output and the auxiliary beamformer output. This leads to the optimal weighting vector function given in [121, Equation 7], which involves the inversion of the receiver covariance matrix $\bar{R}_y$,

$$
\vec{w} = \frac{\bar{R}_y{}^{-1}\vec{a}}{\vec{a}^{\mathrm{T}}\bar{R}_y\vec{a}} \tag{5.5}
$$

$$
\text{subject to:} \qquad \vec{w}^{\mathrm{H}}\vec{a} = 1, \tag{5.6}
$$

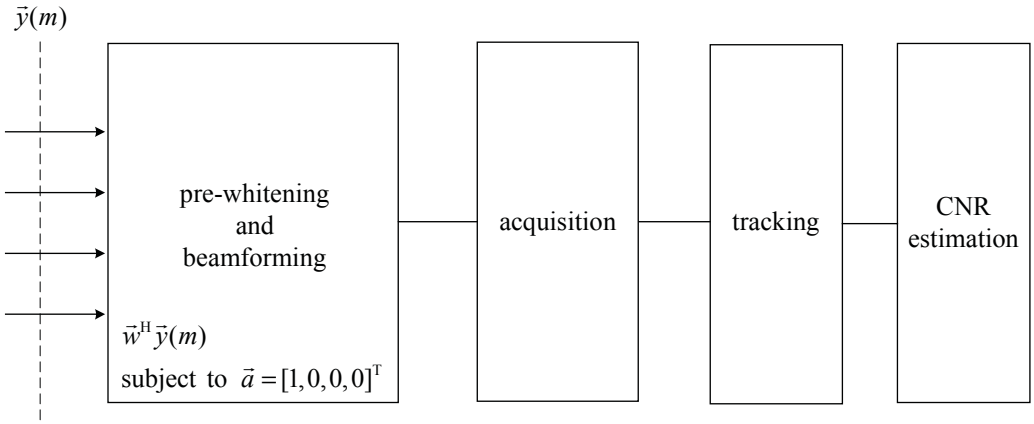

Figure 5.11: Adaptive baseband signal processing algorithm block diagrams, using power minimisation as the interference cancellation technique.

where $\vec{a}$ is the $N \times 1$ column vector, $\vec{a} = [1, 0, ..0]^{\mathrm{T}}$. The implementation block diagram of this algorithm in the digital receiver is illustrated in Fig. 5.11. Before analysing the performance of different antenna array configurations in the receiver, the measured antenna array RHCP patterns with and without DMN are considered to study the influence of interference cancellation on the effective antenna realised gain and pattern shapes. Therefore, with the assumption of the signal, interference and noise being uncorrelated, the received spatial covariance matrix $\bar{R}$ can be also expressed as the sum of interferers covariance matrix $\bar{R_{\mathrm{int}}}$, the receiver noise covariance matrix and the GNSS signal covariance matrix, which is

$$\bar{R} = \vec{F}^{H}(\theta_k, \phi_k)\bar{P}_i^{\mathrm{int}}\vec{F}(\theta_k, \phi_k) + \bar{R}_{\mathrm{nn}} + \vec{F}^{H}(\theta_s, \phi_s)\bar{P}_s^{\mathrm{sat}}\vec{F}(\theta_s, \phi_s). \tag{5.7}$$

Here, $\bar{P}_k^{\mathrm{int}}$ is a $k \times k$ diagonal matrix containing the power of the respective k^{th} interferer sources. Similarly, $\bar{P}_s^{\mathrm{sat}}$ is the diagonal matrix containing the power of the respective satellite signals, And the noise covariance matrix can be computed using the noise temperature covariance matrix derived in the last chapter for compact antenna arrays integrated with DMN, $\bar{R}_{\mathrm{nn}} = k_o B \bar{T}_{\mathrm{sys}}$. Therefore, the effective antenna patterns are analytically computed, for those without DMN (Antenna "A") and with DMN (Antenna "B") antenna arrays, using (5.7) and (5.5) in the case of a single fixed RHCP interferer impinging from direction $\theta = 5^{\mathrm{o}}$ and $\phi = 0^{\mathrm{o}}$. These are plotted in Fig. 5.12a and b, respectively. The antenna array with DMN has at least 2 dB better effective or equivalent realised gain in the directions other than the interferer because of the higher gain of the reference element, which is even mode in this case. Moreover, without DMN, the effective antenna pattern is distorted, because additional nulls in the directions other than the interferer directions appear, which are not intended. Thereby, simple nulling algorithms may take the advantage of the eigen-

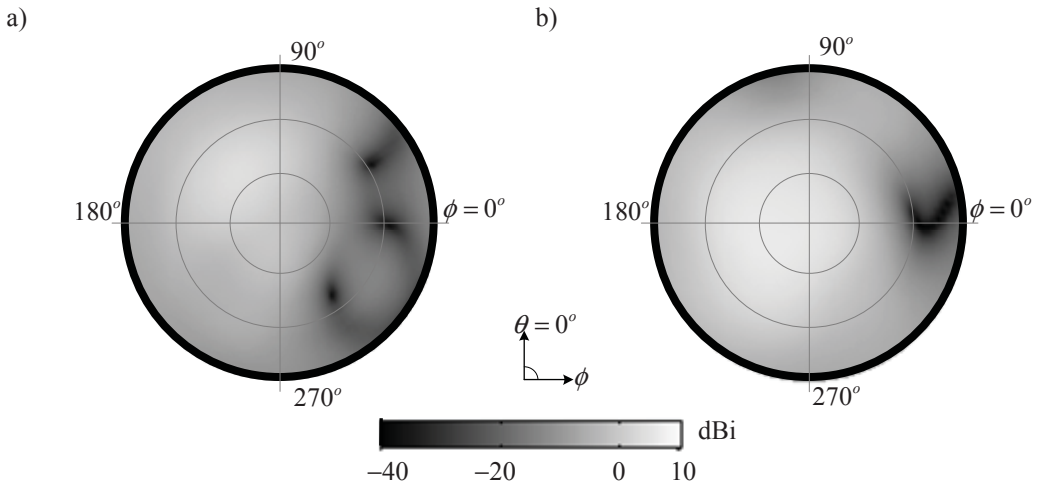

Figure 5.12: The equivalent gain pattern of the antenna for the computed weights using a power minimisation algorithm in fixed one interferer scenario: (a) without DMN and (b) with DMN antenna arrays.

mode antenna array, but it will interesting to analyse the equivalent CNR performance of the complete receiver in realistic scenarios, which will be performed in the coming section.

5.6.2 Eigenbeamformer

Generally, the inversion of the covariance matrix is difficult to implement in the hardware owing to its complexity and greater resource requirements. Therefore, a simplified approach using the eigen decomposition of the received covariance matrix for GNSS receivers has been recently proposed in [122]. This is performed in two stages: at the pre-correlation, the interference is removed; and then at post-correlation, the beamforming in the direction of the satellite is performed.

In the first step, the received covariance matrix is decomposed into the eigenvectors and eigenvalues, which can be given similar to (3.12).

$$\bar{R}_y = \bar{Q}_y \bar{\Lambda} \bar{Q}_y^H. \tag{5.8}$$

Here, the number of eigenvalues λ_i above a certain threshold value indicates the presence of the interference signal. Therefore, the eigenvectors associated with these eigenvalues indicate the interference subspaces that need to be suppressed or eliminated. This is achieved by projection of the received data into the interference-free subspace, which is given by the projection matrix $\bar{O}_{\perp}^{\mathrm{V}}$ (3.31):

$$\bar{O}_{\perp}^{\mathrm{V}} = (\bar{I}_N - \bar{V}(\bar{V}^{\mathrm{H}}\bar{V})^{-1})\bar{V}^{\mathrm{H}}. \tag{5.9}$$

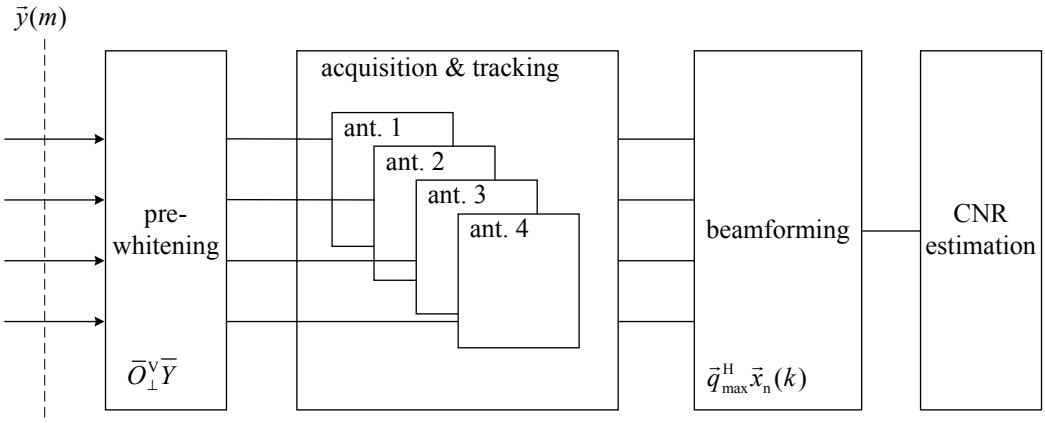

Figure 5.13: Adaptive baseband signal processing algorithm block diagrams, employing eigen-beamforming as the interference cancellation and beamforming technique.

where $\bar{V} = [\vec{q}_1, ..., \vec{q}_i]$, with $\vec{q}_i$ being the column vector and i indicating the number of eigenvectors to be considered—in other words, the number of interferers to be suppressed. For the four-element antenna array with one degree-of-freedom fixed for the satellite direction, maximum $i = 3$. $\bar{I}_N$ is the identity matrix of size $N \times N$. The interference-free received signal is then obtained by:

$$\bar{Y}_{\mathrm{w}} = \bar{O}_{\perp}^{\mathrm{V}}\bar{Y}. \tag{5.10}$$

Now, as shown in Fig. 5.13, $\bar{Y}_{\mathrm{w}}$ is processed for each row (antenna element) independently by the acquisition and tracking block of the baseband signal processing to retrieve the navigation message bits for each millisecond of C/A-codes $\vec{x}_{\mathrm{n}}(k)$, where new set of reduced samples $k \in \{1, 2, \cdots K\}$. The beamforming can be applied using the associated eigenvector of new covariance matrix (5.1) of the tracked navigation message with highest eigenvalue. This leads to the transformation of the navigation message as follows:

$$\vec{x}_{\mathrm{w}}(k) = \vec{q}_{\max}^{\mathrm{H}}\vec{x}_{\mathrm{n}}(k). \tag{5.11}$$

The post-correlation beamforming is necessary to improve the CNR of the antenna array from wanted satellite signal direction. The signal flow block diagram of the eigen-beamforming technique implemented in the digital receiver is shown in Fig. 5.13.

5.7 Experimental verification of the adaptive compact navigation receiver

In order to verify the results and performance of the demonstrator, two tests and measurement campaigns have been performed. One was inside the lab with a controlled en-

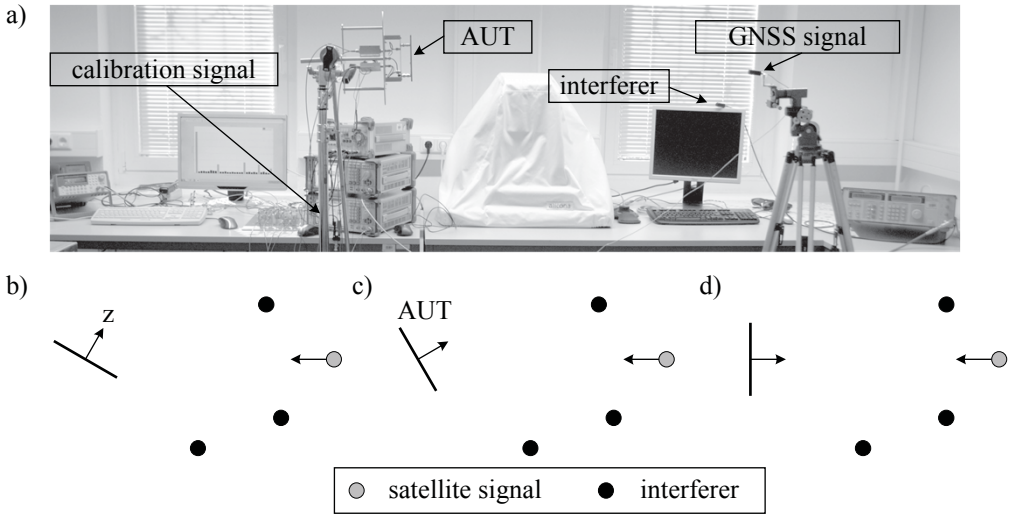

Figure 5.14: (a) Indoor setup for the satellite acquisition in the presence of the RHCP continuous wave interferers. The satellite directions are (b) low-elevation ($\theta = 30^{\text{o}}$) (c) medium-elevation ($\theta = 60^{\text{o}}$) and (d) high-elevation ($\theta = 90^{\text{o}}$). The interference directions for all the position of the AUT are fixed.

vironment for the artificial satellite transmission using the available GNSS signal generator SMBV100A from Rhode & Schwarz [155] along with sinusoidal interferers. The indoor setup is limited due to resources and the structural unavailability to transmit multiple satellites from several locations to test the antenna performance realistically. However, it provides the advantage of transmitting the interferer at any bandwidth, amplitude, and modulation. In the end, a measurement campaign is performed at a specific outdoor location, which is discussed in the later part of this section.

5.7.1 Indoor testing

The indoor test setup is shown in Fig. 5.14a. The antenna array with DMN, calibration network and LNAs is mounted on the tripod. The GNSS signal generator is tuned to transmit the single satellite signal with SV number 21. The interferer signal generator output is connected to the quadrafilar antenna with very low axial ratio for RHCP radiations in the upper-hemisphere. Similarly, the RHCP interferers, using the quadrafilar antenna, are setup connected to a sinusoidal signal generator tuned to frequency 1575.42 MHz. The received combined JSR in each case—i.e. one, two and three interferers—is adjusted to 30 dB. This choice of this JSR is motivated by the low dynamic range, 45 dB, of the medium-resolution ADC converters.

These investigations involve the configuration of different elevation angles of antenna arrays—which are shown in Fig. 5.14b, c, and d—while keeping the positions of the in-

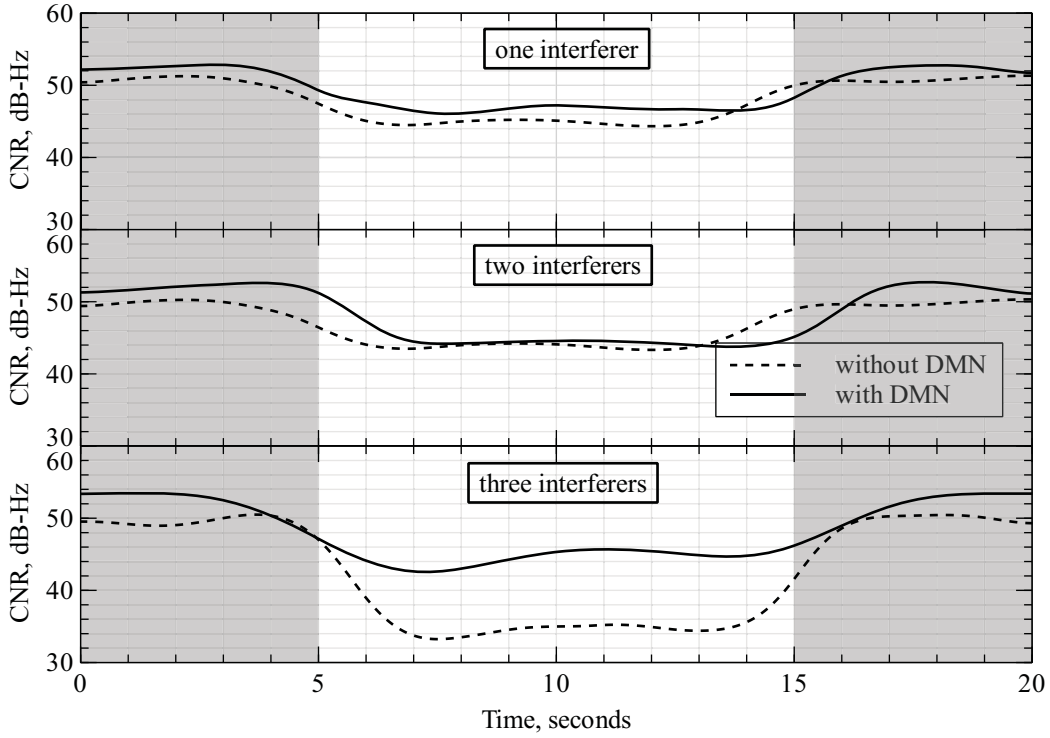

Figure 5.15: The recorded equivalent CNR for *low-elevation* satellite directions in the presence of one, two, and three interferers with and without DMN antenna arrays using power minimisation algorithms. Note: The shaded region indicates the time when the interference is switched OFF.

terferers and satellite fixed. For each configuration with and without DMN $I_{\mathrm{p}}/Q_{\mathrm{p}}$ data 8-bit resolution data samples at $2.2\ \mathrm{MSps}$ for $20\ \mathrm{s}$ are recorded on the hard drive for post-processing. Each time the interference is switched on after approximately $5\ \mathrm{s}$ of the recording for a duration of $10\ \mathrm{s}$ and then switched off for the next $5\ \mathrm{s}$. Further, the raw data is processed by applying the two previously described adaptive null-steering schemes to evaluate the equivalent CNR.

Power minimisation: The equivalent CNR for the antenna array with and without DMN in the case of one, two, and three interferers for the *power minimisation* scheme, with antenna elevation angle set to 30^{o} relative to the impinging satellite direction, is displayed in Fig. 5.15. Without interference—i.e. for the first $5\ \mathrm{s}$—it can be observed that the case with the DMN antenna array has 1–$2\ \mathrm{dB}$ better CNR. This is because of the fact that the reference antenna is a single element without the DMN antenna array, compared to with DMN in which it is taken as the even mode or the combined four antenna elements.

In the case of one interferer, the CNR drops for both with and without DMN, and the performance of the antenna array without DMN is slightly better. Similarly, with

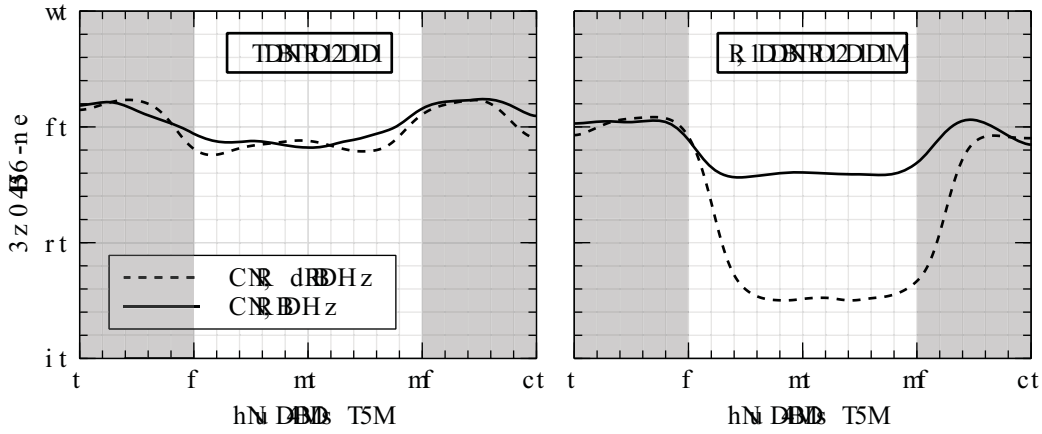

Figure 5.16: The recorded equivalent CNR for *medium-elevation* satellite directions in the presence of one and three interferers with and without DMN antenna arrays using power minimisation algorithms. Note: The shaded region indicates the time when the interference is switched OFF.

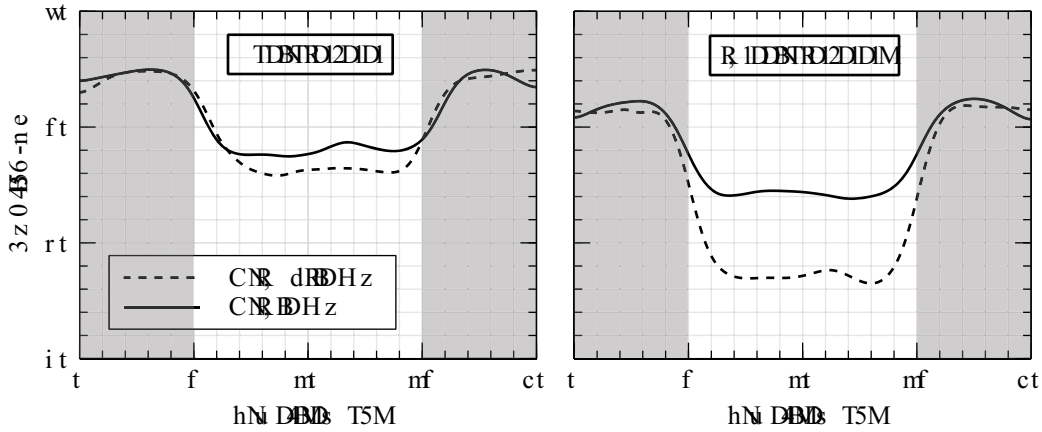

Figure 5.17: The recorded equivalent CNR for *high-elevation* satellite directions in the presence of one and three interferers with and without DMN antenna arrays using power minimisation algorithms. Note: The shaded region indicates the time when the interference is switched OFF.

two interferer, the CNR difference with and without DMN is marginal, and it appears that there is no advantage of applying DMN here as well. However, with three interferers switched on, the CNR with the DMN antenna array is considerably improved. A minimum difference of 10 dB is recorded here.

In the next step, the antenna array is moved to the elevation angle of approximately 60^{o}, which is classified as *medium elevation*, with respect to the satellite antenna, as shown in Fig. 5.14c. With interference, the CNR estimates are slightly improved by 1 dB in

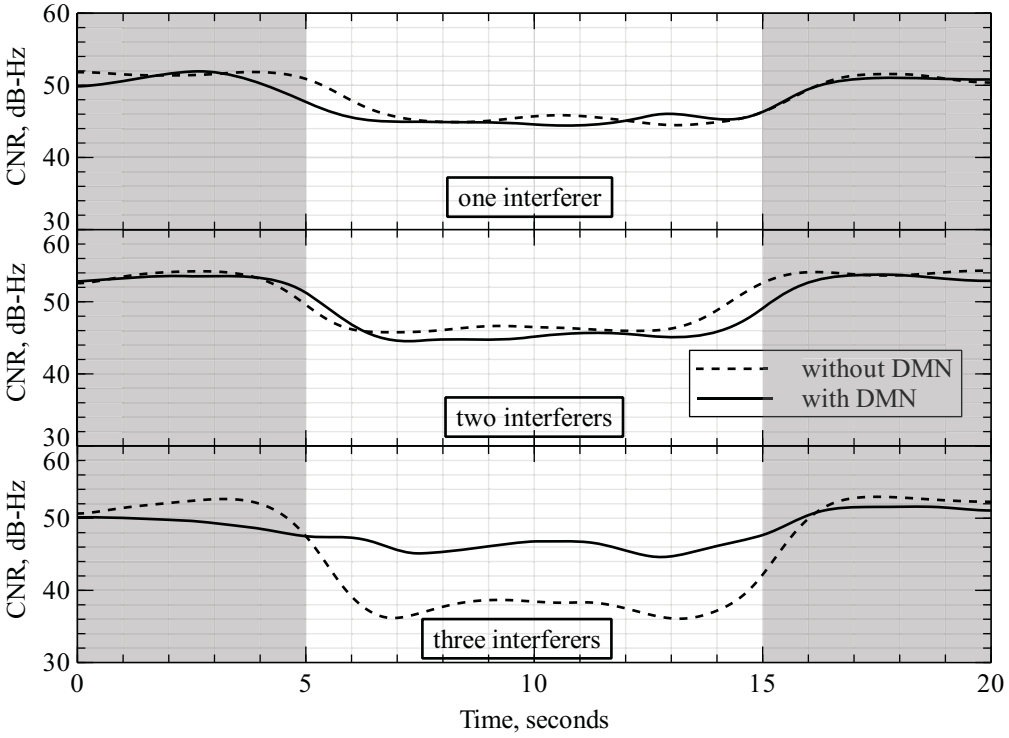

Figure 5.18: The recorded equivalent CNR for *low-elevation* satellite directions in the presence of one, two, and three interferers with and without DMN antenna arrays using eigenbeamforming algorithms. Note: The shaded region indicates the time when the interference is switched OFF.

comparison to the lower elevation scenario. With and without DMN, the performances of the CNR are similar to the case with one interferer. However, with three interferers, the CNR is again 10 dB greater than with DMN, which is also observed at the low elevation.

The antenna array is moved to the elevation angle of approximately 90^{o}, classified as *high elevation*. With one interferer, the CNR values are again comparable, and there is no advantage with DMN, as shown in Fig. 5.17. Similar to previous scenarios, the antenna array with DMN provides improved and robust CNR for the three-interferer case, which is 6 dB better than without DMN.

Eigenbeamforming: As discussed earlier, that power minimisation algorithm performance depends on the the choice of the reference antenna with which DMN provides better gain. Moreover, it is doesn't exploit the adaptive beamforming in the direction of the desired satellite, and each intereferer arrives from the far-field at discrete angles. Therefore, a complete and efficient eigenbeamforming algorithm based on pre-whitening and the adaptive beamforming described previously is also tested with the constructed demonstrator.

In Fig. 5.18 the CNR with and without DMN at the low-elevation configuration for

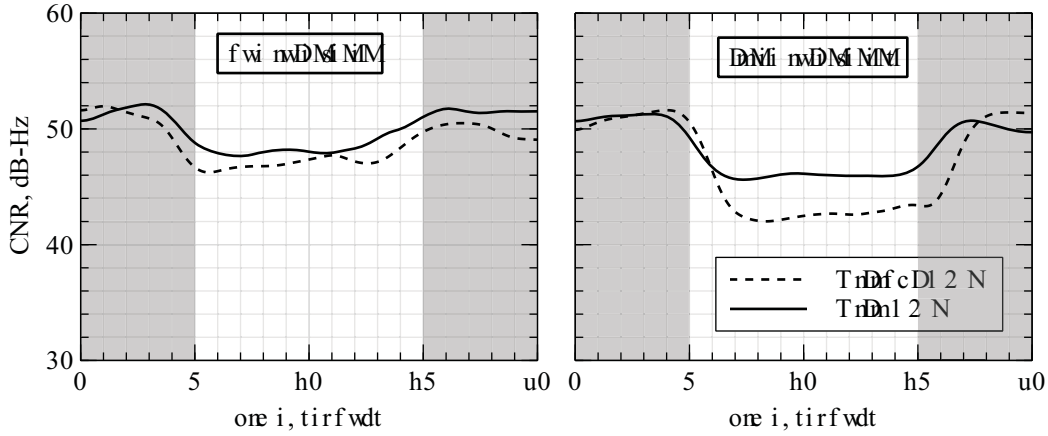

Figure 5.19: The recorded equivalent CNR for *medium-elevation* satellite directions in the presence of one and three interferers with and without DMN antenna arrays using eigenbeamforming algorithms. Note: The shaded region indicates the time when the interference is switched OFF.

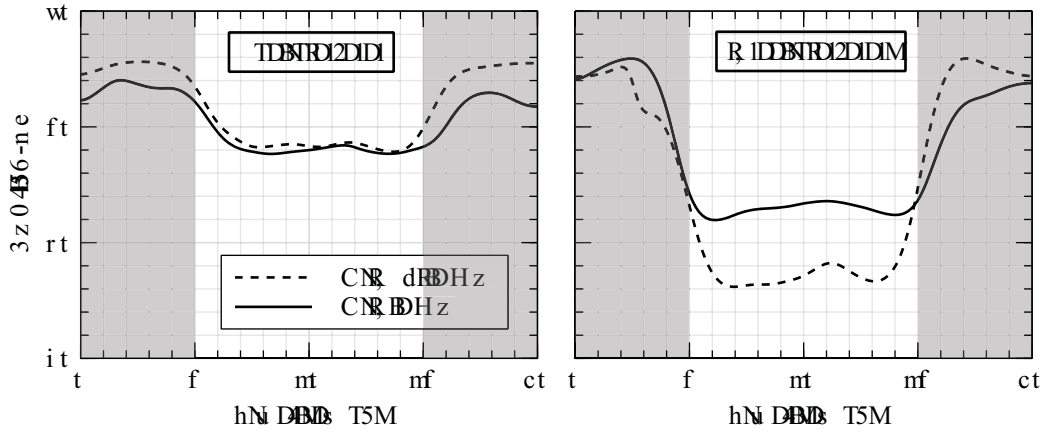

Figure 5.20: The recorded equivalent CNR for *high-elevation* satellite directions in the presence of one and three interferers with and without DMN antenna arrays using eigenbeamforming algorithms. Note: The shaded region indicates the time when the interference is switched OFF.

one, two, and three interferers are shown. In the interferer-free scenario—i.e. for the first 5 s, it can be observed that this time without DMN, CNR on the average is comparable to DMN because of the use of maximum degrees-of-freedom in the beamforming. This signifies the advantage of utilising beamforming for the improved CNR as well. However, similar to the results in the power minimisation algorithm, with one and two interferers, the CNR with DMN is equivalent to that without DMN; and in case of three interferers, the CNR with DMN has at least 10 dB superior performance.

Fig. 5.19 shows the CNR for the medium-elevation configuration. With one interferer

Figure 5.21: An outdoor test-setup against interference of the built demonstrator at the Galileo Test Range (GATE) in Berchtesgaden, Germany.

the performance of the CNR is equivalent with or without DMN. However, with three interferers without DMN, CNR is again $10\ \mathrm{dB}$ worse than that with DMN.

At the end of the indoor testing, the CNR obtained for the high-elevation configuration is shown in Fig. 5.20. The recorded CNR values show similar behaviour to the previous cases: with DMN, the performance gain is dominant for the maximum interferer case—i.e. three. The margin is at least $6\ \mathrm{dB}$ in this case.

5.7.2 Outdoor testing

The GNSS signals are easily available to acquire and track on Earth with a condition of visibility into the open sky. However, transmitting interference signals outdoors in the vicinity of the navigation signals operating bandwidth is prohibited, particularly within the European Union. This requires a special permission or license for a given location. Within Germany, these locations are classified as Galileo Test- und Entwicklungsumgebungen (GATEs) facilities, which include GATE, SeaGate, aviationGate, automotiveGATE, and railGATE, each of which targets various public transportation systems as their names suggest. These facilities are equipped with four artificial Galileo satellite signals transmitted from the top of the nearby mountains, which provide additional possibilities of testing the receiver with Galileo signals. However, these facilities are expensive for testing and measurement developing systems and have limited availability. During this work, only testing at GATE in Berechtesgaden has been possible for a period of one week only. The testing location is a rural area with no infrastructure around, therefore no multipaths are generated. Furthermore, these investigations focus on the maximum JSR and the position estimations with compact antenna arrays.

In these tests, a high-end digital receiver and baseband signal processing hardware unit is provided by project partners in Rheinisch-Westfälische Technische Hochschule (RWTH) Aachen and Deutschen Zentrum für Luft- und Raumfahrt (DLR) Oberpfaffenhofen [160]. This is a customised device designed and optimised for robust GNSS signal

reception in presence of the interferers and jammers. This provides simultaneous acquisition and tracking of the GPS and Galileo satellites. However, the maximum number of satellite tracking channels is limited to six, but is sufficient to determine the vital PVT information. This platform also delivers the DOA estimations for the satellites compared to their actual positions (see Appendix C.2). The complete setup of the demonstrator mounted on the measurement vehicle and interference is shown in Fig. 5.21, whereas the static tripod setup is shown in Appendix C.3. For further implementation details about the compact navigation receiver and the related algorithms, the reader is referred to the conference contribution [161, Section IV].

Initially, the experimental setup with fixed FE and different antennas configurations is analysed. The configuration includes a conventional half free-space wavelength antenna array from the Galileo antenna and receiver demonstrator for SoL applications (GALANT) [99], Antenna "A", Antenna "B" and Antenna "D". In Table 5.1, maximum recorded CNR values for high-elevation satellites without interference are presented. The conventional antenna array has $3\ \mathrm{dB}$ higher CNR than the compact antenna array. This is a trade-off for miniaturisation of the antenna array by half of the effective aperture area. In addition, there is no advantage from using the DMN in this scenario that is without interference and with the satellite impinging from high elevation, which was also observed during the indoor testing as well. Antenna "D" provides better cross-polarisation; however, the low gain gives lower CNR.

The Table 5.2 presents a summary of the maximum CW interferer suppression or JSR achieved by the receiver with different antennas connected. Similar to the case without interference, the single interferer maximum JSR is the same with and without DMN. The three interferer case with DMN is $10\ \mathrm{dB}$ more robust than without DMN. This verifies the result obtained in the CNR analysis, where the CNR difference for one interferer with and without DMN is negligible, whereas with three interferers the CNR is at least $3-4\ \mathrm{dB}$ better with DMN. The maximum performance gain depends on the interference impinging directions and the desired satellite's direction. Furthermore, The last row is the performance of the receiver without applying beamforming in the satellite direction and interference cancellation in the digital domain. The JSR is $20\ \mathrm{dB}$ lower than with digital algorithms. Therefore, robustness of the receiver relies on the use of sophisticated beamforming and interference cancellation algorithms.

Dynamic tests: In GATE, the dynamic tests are performed in the presence of a PPD jammer, which is installed inside a car at a fixed position. The compact antenna array receiver plus commercially available single element receivers are installed on the moving vehicle. The vehicle starts at position A and travels to and from position B, as shown in Fig. 5.22. The jammer is fixed at location X. The reference position of the vehicle is recorded using the inertial measurement unit (IMU).

The latitude position component, which is measured by the different receivers and the IMU are shown in Fig. 5.22. During both the forward and return journeys, the commercial

Table 5.1: Maximum recorded CNR (dB-Hz), for close to zenith satellites, using the demonstrator having with FE for the compact antenna array with and witout DMN in comparison to conventional half free-space wavelength antenna array.

	conventional antenna array $\lambda/2$	**compact antenna array** $\lambda/4$		
		antenna A (w/o DMN)	antenna B (w/ DMN)	antenna D (w/ DMN)
CNR (dB-Hz)	54	51	51	48

Table 5.2: Maximum allowed JSR (dB) to keep the CINR above 38 dB-Hz measured at GATE; all interferers transmit CW signal.

	measured JSR (dB)	
antenna type	1 CW interferer	3 CW interferers
antenna A (w/o DMN)	68	23
antenna B (w/ DMN)	68	33
antenna B w/o beamforming	48	-

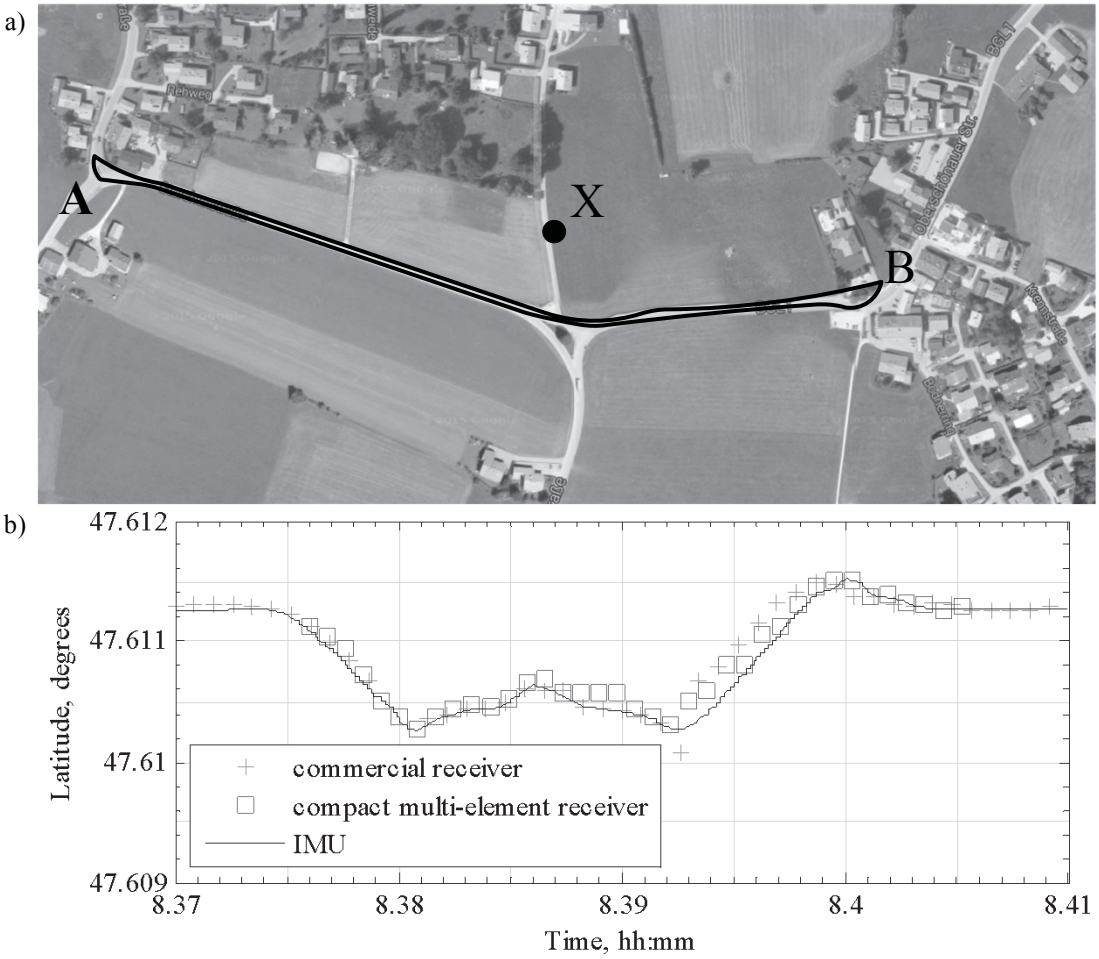

Figure 5.22: (a) The dynamic test setup with compact antenna array along with commercial receivers mounted on the vehicle. (b) The recorded positioning latitude component between route A and B.

receivers suffered from several outages and loss of position, while the compact antenna array receiver tracked continuously with small variance. During the turn at point B, the compact receiver lost the position. However, this is not due to the jammer, but probably due to shadowing. As mentioned before, the compact receiver has only six tracking channels, while the other receivers possess more, i.e. if three satellites are lost by shadowing, the compact receiver loses the position, while the others can still provide a position. Because of the limited time, analysis of the compact receiver with and without DMN has not been possible during this measurement campaign. However, these tests clearly demonstrate the necessity of multi-antenna systems for robust navigation and accurate position information. In addition, the principle of the compact antenna array receiver has been verified.

Further tests may involve more interferers along with multipath scenarios for robustness investigations of the navigation receiver.

5.8 Summary

This chapter presents the overview of the developed GNSS compact antenna array receiver. The receiver chain components are similar to the conventional single-channel GNSS receiver. However, the specifications are different, which include lower gain with a higher dynamic range in the ADCs, which define the maximum JSR. The overall saturation of the FE must be adjusted with the maximum allowed jammer input power. For the digital receiver to operate correctly, it is important that the analogue FE remain in the linear region, which is below the 1 dB output compression point for the intended unwanted jammer signals. Another salient feature of the customised receiver development provides the coherent LO for all channels, which is crucial for the digital beamforming and direction-of-arrival algorithms.

The results of the indoor and outdoor tests are presented. With the outdoor tests, the satellite signals are available, but it is impossible to transmit the interference signals without a license, which is allowed only at specific locations. The indoor setup allows for any type of interference signal; however, satellite signals are not available and are emulated using GNSS signal generators. The indoor measurements verify similar behaviour of the compact antenna array for the equivalent CNR, which is provided by the analytical results of the diversity receiver model presented in the last chapter. With DMN, the CNR for the three-interferer case provides an advantage of 6–10 dB.

The outdoor tests show similar characteristics of the DMN performance as observed earlier and also include the dynamic measurements with the moving receiver. These measurements provide the first insight into the performance of the compact GNSS antenna array, which provides the position, velocity, and time estimate. The estimated CNR shows that there is no advantage or disadvantage to employing DMN in the case of minimum or no interference scenarios. Furthermore, the measured maximum CNR for the compact antenna array with $d = \lambda/4$ as compared to the conventional $d = \lambda/2$ is 3 dB which is a trade-off for miniaturisation and cannot be recovered with DMN. However, the necessity of DMN is only prominent in the maximum interferer case, which is three for a four-element antenna array.

Chapter 6

Conclusions

The novel concept of *compact planar antenna arrays* in GNSS *receivers* has been successfully applied and verified in this work. This provides an attractive solution for the miniaturization of modern robust GNSS receivers. Furthermore, this enables the penetration and mass production of the multi-element antennas in the existing highly competitive GNSS market.

The choice of the number of elements determines the maximum number of unwanted signals to be suppressed. But, for a fixed aperture size this results in reduced inter-element separation with an increasing number of elements. This introduces*mutual coupling*, and degrades the radiative or reception performance of the array such that the *diversity* degrees-of-freedom become inefficient or useless. Consequently, in a small aperture size a four-element array may have similar diversity performance as compared to a three-element array. Therefore, it is necessary to devise corresponding figures-of-merit including mutual coupling effects. In this work, the eigenvector and associated eigenvalues of the measured antenna covariance matrix serve as the basic parameters in design optimization and selection of the coupled antenna array. This reveals that the *minimum eigenvalue* dominates the diversity performance, and therefore, needs to be maximized in the design process. The minimum eigenvalue is inversely proportional to the number of elements and the inter-element separation. Therefore, a choice of four elements with $d = \lambda/4$ provides better diversity degrees-of-freedom as compared to a six element array with $d = \lambda/5$. However, with an equal number of elements in compact configuration an optimized planar geometrical arrangement can produce an optimum minimum eigenvalue. In the aforementioned four-element array it is square shape whereas in the six element it is the hexagonal geometry which gives the maximum eigenvalues. Similarly, the direction finding capability of the compact array can be estimated with the help of the Cramer-Rao lower bound. The effect of geometrical arrangement of the array on the lower bound is severe. Even though the square shaped geometry for a four element array provides better minimum eigenvalue as compared to the y-shaped geometry yet it provides minimum mean Cramer-Rao lower

bound in the upper hemisphere. Therefore, the design process is a trade-off between robustness and better direction finding ability of the array.

The integration of the decoupling and matching network is also presented which allows further miniaturization for the robust design. The impedance matching of the compact antenna array for diversity degrees-of-freedom necessities the decoupling incipiently. This can be achieved by several techniques from the antenna level to the network based approach. It is also possible to achieve a *broadband decoupling*, e.g. hybrid coupler based, which allows larger manufacturing tolerances. As far as matching is concerned, it does become simpler after decoupling, however, the fractional bandwidth decreases with the higher-order modes. The matching is bounded by the compactness, in other words the electrical size of the antenna array, and its characteristic is typically narrow-band. Moreover, the practical implementations give rise to ohmic losses within this network which may or may not compromise its benefit. Therefore, an equivalent carrier-to-interference-plus-noise ratio including the effects of the antenna array, decoupling and matching network, low-noise amplifier and the beamformer has been derived. This yields valuable insights into the performance of the compact arrays with and without decoupling and matching network in the navigation scenarios before integration with the digital receiver. For the four element array $d = \lambda/4$ the equivalent carrier-to-interference-plus-noise ratio with the decoupling and matching network is at least $3\ \mathrm{dB}$ in all directions for the highest-order mode which is the three-interferer scenario. On the other hand, without interferer there is no benefit of employing the decoupling and matching network, while at the same time there is no disadvantage as well. Therefore, it can be concluded that the decoupling and matching is *necessary* for the compact antenna array especially when operating in the *interference limited* scenario.

The impact of polarization impurity in the compact antenna arrays has also been studied. The presence of mutual coupling also degrades the polarization properties of the antenna. In case of the even mode excitation or reception, the individual antenna elements can be geometrically altered, to minimize the cross-polarization levels. The individual antenna element designs also effect the polarization purity of the even mode. However, the cross-polarization levels of the higher order modes are comparable to the co-polarization levels. Furthermore, with the introduction of a decoupling and matching network performance is not improved or changed. In the case of the arbitrarily polarized interferer for the circular polarized compact antenna array the degrees-of-freedom to null the interferer are doubled. This reduces the maximum number of nulling degrees-of-freedom with one fixed for the desired satellite direction. A remedy to this adverse effect can be the application of dual-polarized antenna elements for greater robustness.

In the end, the complete GNSS receiver demonstrator design is presented. The robust receiver specification demands a customized multi-channel analogue front-end design along with an adaptation of the digital algorithms to cope with the non-uniform antenna gain patterns. The indoor and the outdoor measurement campaigns verify and validate

the results obtained analytically. The jammer-to-signal ratio obtained for the fabricated four-element compact antenna array is equal with and without decoupling and matching network in instance of the single interferer scenario whereas for three interferers it is improved by 10 dB compared with the former case. Basically, with the reduction of the antenna array size by half the carrier-to-noise ratio of the received satellites from the high-elevation angles is reduced by half which is sufficient to acquire and track them without the requirement of integration. The decoupling and matching networks mainly effect the reception performance of the antenna array in the interference scenarios particularly the maximum interferer case. Hence, in this case the improved robustness for the localisation capability of the navigation receive is the decisive argument to deploy the decoupling and matching network in the compact antenna arrays.

Appendix A

Multi-port junctions, exchangeable powers, and noise parameters

A.1 Multi-port junctions

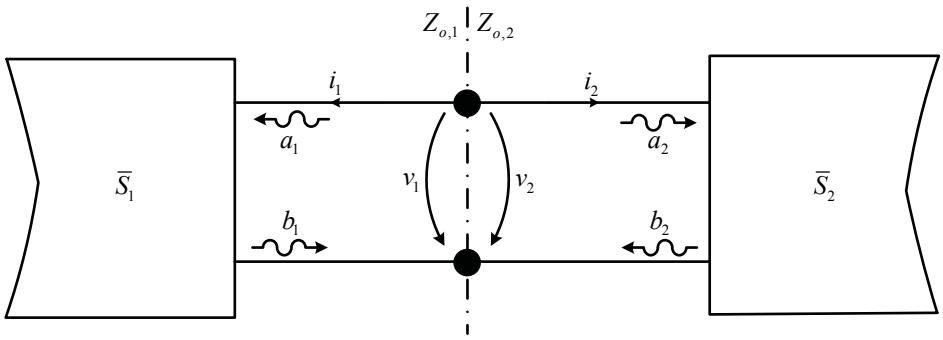

Figure A.1: Representation of the interface between two multi-port interface in terms of the power waves.

The condition to combine the scattering parameters of the multi-port network cascaded are discussed in this appendix. Consider the representation of the two networks connected with each other as shown in Fig. A.1 . The power waves in relation to the voltage and current are expressed as follows [82]

$$\begin{aligned} a_n &= \frac{v_n + Z_{\mathrm{o},n} i_n}{2\sqrt{\Re\{Z_{\mathrm{o},n}\}}}, \\ b_n &= \frac{v_n - Z^*_{\mathrm{o},n} i_n}{2\sqrt{\Re\{Z_{\mathrm{o},n}\}}}. \end{aligned} \tag{A.1}$$

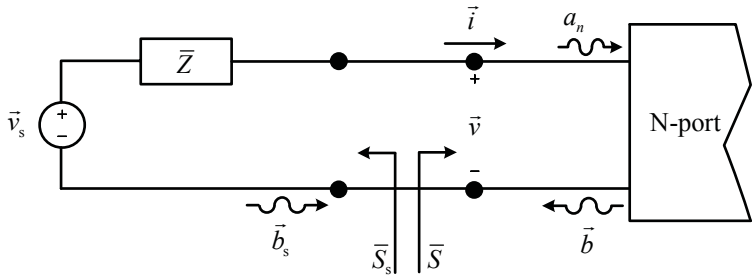

Figure A.2: N-port network reflection coefficients at n^{th} port connected to multichannel source.

From the graphical representation, the boundary conditions at the junction are

$$v_1 = v_2, \qquad \text{and } \; i_1 = -i_2. \tag{A.2}$$

This, in the wave domain, translates in the bound condition for the power waves, i.e. $b_1 = a_2$ and $b_2 = a_1$. Lets express these terms in accordance with (A.1) and using the boundary conditions defined above

$$b_1 = \frac{v_1 + Z^*_{\mathrm{o},1} i_1}{2\sqrt{\Re\{Z_{\mathrm{o},1}\}}}; \;\; a_2 = \frac{v_1 + Z_{\mathrm{o},2} i_1}{2\sqrt{\Re\{Z_{\mathrm{o},2}\}}}. \tag{A.3}$$

In order to hold equality of the power waves condition, it is necessary that the normalising reference impedance are complex conjugate of each other, which leads to $Z_{\mathrm{o},2} = Z^*_{\mathrm{o},1}$. Therefore, it is necessary for combining the scattering parameters for two different network, that the normalising reference impedance is conjugate of each other. In this thesis, the normalisation impedance is a real quantity, i.e. $Z_{\mathrm{o},n} = 50\Omega s$.

A.2 Expression for exchangeable power by incident power wave

Consider the N-port network connected to sources with conjugate matched normalised reference impedances as shown in Fig. A.2. Now, the power delivered to the network is defined by the power waves as

$$P_{\mathrm{N}} = \vec{a}^{\mathrm{H}}\vec{a} - \vec{b}^{\mathrm{H}}\vec{b} = \vec{a}^{\mathrm{H}}(\bar{I} - \bar{S}^{\mathrm{H}}\bar{S})\vec{a}. \tag{A.4}$$

The incident power from the source can be expressed in terms of the forward travelling wave $\vec{a}$ in the following manner

$$\vec{a} = \vec{b}_{\mathrm{s}} + \vec{b}\bar{S}_{\mathrm{s}}, \tag{A.5}$$

and using the fact that $\vec{b} = \bar{S}\vec{a}$ leads to

$$\vec{a} = \vec{b}_{\mathrm{s}}(\bar{I} - \bar{S}_{\mathrm{s}}\bar{S})^{-1}. \tag{A.6}$$

Therefore, the power flowing into the connected network is converted into

$$P_{\mathrm{N}} = \vec{b}_{\mathrm{s}}^{\mathrm{H}} \left(\frac{(\bar{I} - \bar{S}^{\mathrm{H}}\bar{S})}{(\bar{I} - \bar{S}_{\mathrm{s}}\bar{S})(\bar{I} - \bar{S}^{\mathrm{H}}\bar{S}_{\mathrm{s}}^{\mathrm{H}})} \right) \vec{b}_{\mathrm{s}} \tag{A.7}$$

And under the conjugate matching condition, i.e. $\bar{S} = \bar{S}_{\mathrm{s}}^{\mathrm{H}}$, the variance of the source wave in relation to exchangeable power is defined by

$$\mathrm{Var}\{\vec{b}_{\mathrm{s}}\} = P_{\mathrm{N}}(\bar{I} - \bar{S}_{\mathrm{s}}\bar{S}_{\mathrm{s}}^{\mathrm{H}}). \tag{A.8}$$

This is in agreement with the outcome of [95, Equation 2.247] (see also [83]).

A.3 Noise parameters

In order to characterise the noise properties of amplifiers several noise parameters have been developed. Rothe and Dahlke introduced these parameters based on the noise voltages and currents [84]. These are still the most extensive used type of noise parameters. There are almost an infinite number of ways to define these set of parameters. In this work, we are interested in finding the temperature noise parameters using the minimum noise figure NF_{min}, optimum reflection coefficient Γ_{opt} and the noise resistance R_{n}, which are measured through measurements. This transformation to the set of noise temperature parameters is given as follows:

$$Y_{\mathrm{opt}} = \frac{(1 - \Gamma_{\mathrm{opt}})}{(\Gamma_{\mathrm{opt}} Z_o + Z_o)}, \tag{A.9}$$

$$T_v = \frac{T_{\mathrm{amb}}}{Z_o}(R_{\mathrm{n}}(1 + |Z_o Y_{\mathrm{opt}}|^2) + Z_o(NF_{\mathrm{min}} - 1) - 2R_{\mathrm{n}}(Z_o \mathbb{R}\{Y_{\mathrm{opt}}\})), \tag{A.10}$$

$$T_\mu = \frac{T_{\mathrm{amb}}}{Z_o}(R_{\mathrm{n}}(1 + Z_o^2|Y_{\mathrm{opt}}|^2) - Z_o(NF_{\mathrm{min}} - 1) + 2R_{\mathrm{n}}(Z_o \mathbb{R}\{Y_{\mathrm{opt}}\})), \tag{A.11}$$

$$T_{v\mu} = \frac{T_{\mathrm{amb}}}{Z_o}(R_{\mathrm{n}}(1 - |Y_{\mathrm{opt}}|^2 Z_o^2) + 2\mathrm{j}T_{\mathrm{amb}} R_{\mathrm{n}} \mathbb{I}\{Y_{\mathrm{opt}}\}). \tag{A.12}$$

Appendix B

Printed quadrafilar helix GPS antenna using folded inverted-F antenna

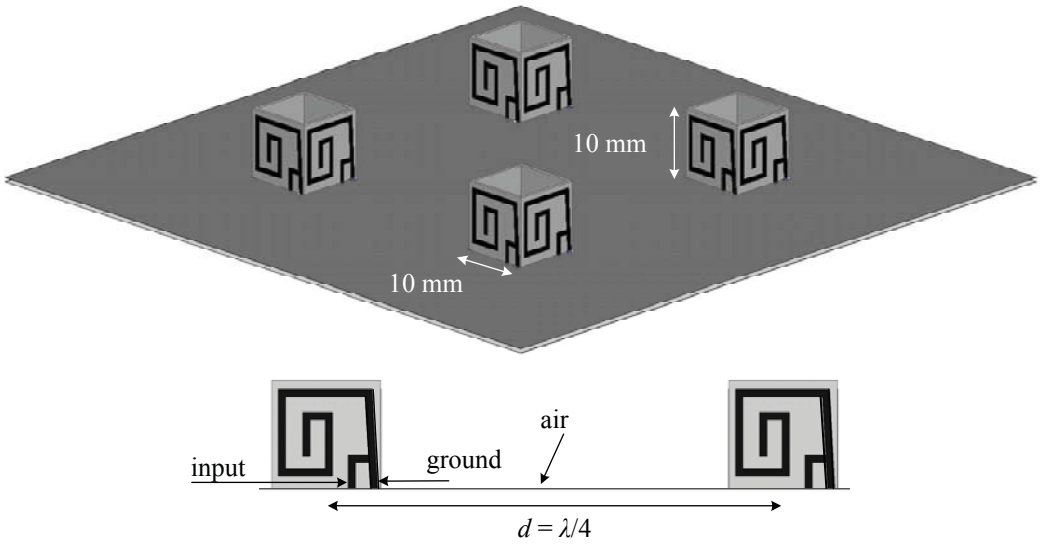

Figure B.1: (top) The simulated four-element QHA array (diametric view) using the inverted-F antenna elements. Overall size of the ground plane is 10 cm $\times$ 10 cm. (bottom) Side view of the antenna array.

In order to reduce the height of the QHA antenna to achieve planarity, printed quadrafilar helix GPS antennas are an attractive solution. In addition, by using the inverted-F antenna broad impedance matching bandwidth can be achieved. This is suitable in order to cope with the evolving GNSS multiple band signals. The reported single element of such a QHA implementation delivers 50% bandwidth at the L1-band [123]. On the other hand, these antennas offer broad beamwidth with very low cross-polarisation levels, which

provides additional robustness in the acquiring low-elevation satellites. A four-element antenna array using the commercially available RO4003, $\epsilon_r = 3.55$ and height of $10\ \mathrm{mm}$ is designed and simulated in this work, it is shown in Fig. B.1.

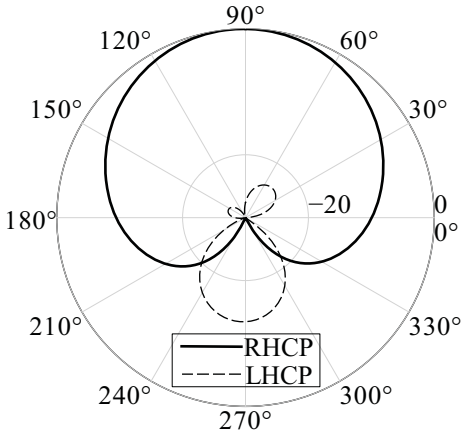

Figure B.2: The simulated normalised realised gain elevation cut with fixed azimuth ($\phi = 0^{\mathrm{o}}$), in dBi, for the even mode of the QHA array. The normalisation is with respect to the maximum RHCP gain.

The realised gain elevation cut for the fixed azimuth, i.e. $\phi = 0^o$ for the RHCP and LHCP are shown in Fig. B.2, in the case of even mode excitations. The RHCP pattern resembles cardiac shape and has higher gain at low-elevation as compared to conventional patch antenna. Also, the LHCP levels over the complete hemisphere are below $-20\ \mathrm{dB}$, which does excellent multipath rejection.

Appendix C

GNSS antenna array demonstrator

C.1 Tracking algorithm flow diagram

The signal flow of the tracking algorithm employed in the baseband signal processing block is sketched in the Fig. C.1. This includes a Costas loop based implementation of PLL to track the carrier wave signal and a code tracking loop, DLL, to keep the code aligned. The code tracking is performed on both I and Q in similar way.

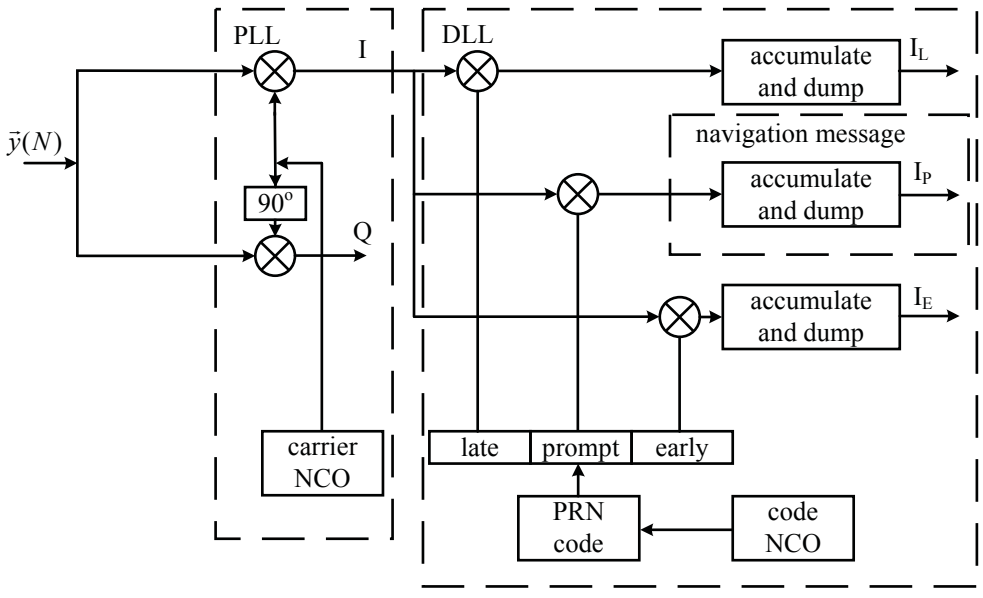

Figure C.1: Tracking algorithm signal flow diagram.

C.2 GNSS graphical user interface

The graphical user interface (GUI) displays the crucial navigation parameters like PVT, and CNR estimations. The pre-correlation and post-correlation beam patterns indicate the presence of interferences and satellites as shown in Fig. C.3. The DoA for acquired satellites using the compact antenna array with DMN are shown in Fig. C.4. The difference between these measurements aid in estimating the attitude of the receiver and also the spoofing satellites.

C.3 GNSS demonstrator – static setup

A complete GNSS demonstrator in the project framework of KOMPASSION shown in Fig. C.2, was developed which comprises the compact antenna array, a miniaturized multi-channel analog front end, and a digital receiver. The digital receiver comprises high-speed correlation blocks implemented on the FPGA. The beamforming and the DoA estimation is performed at the dedicated PC.

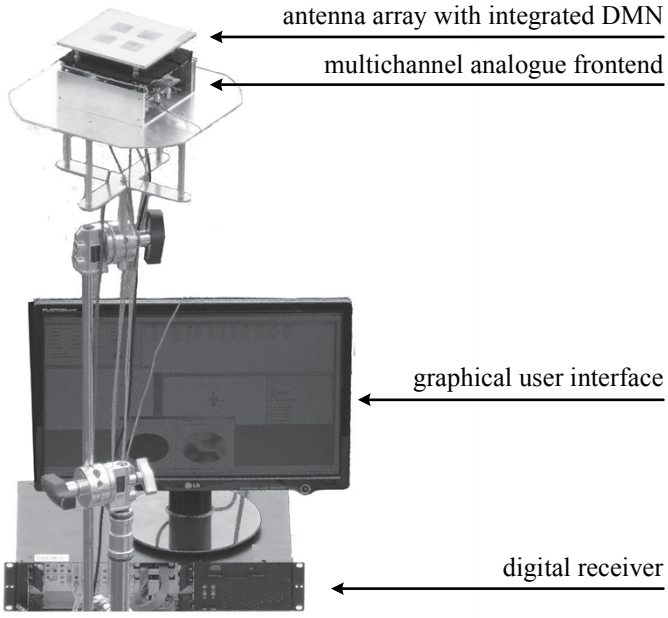

Figure C.2: The L-band allocation of frequency spectrum for the operating carrier frequencies and bandwidths of various GNSS signals.

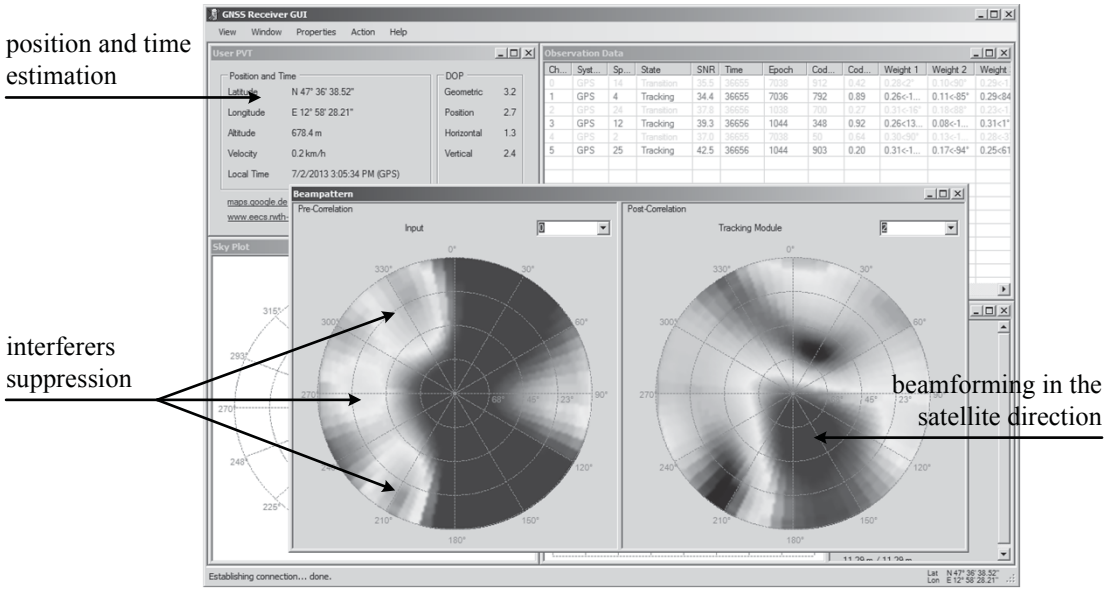

Figure C.3: The graphical user interface of the demonstrator.

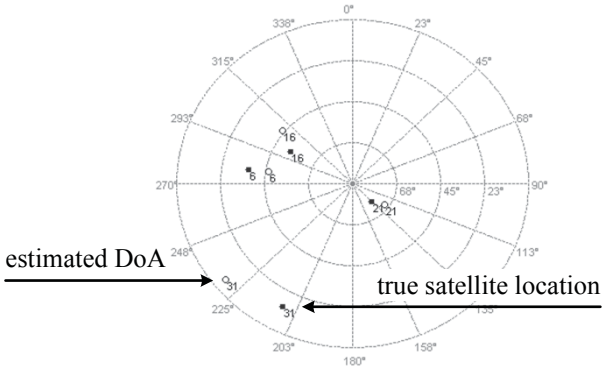

Figure C.4: The true satellite positions retrieved from the navigation messages along with the estimated DoA of these satellites.

Bibliography

Books

[1] B. R. Rao, *GPS - GNSS Antennas*. Artech House, 2013.

[2] R. Waterhouse, *Microstrip Patch Antennas: A Designers Guide*. Springer Science & Business Media, 2003.

[3] C. A. Balanis, *Antenna Theory: Analysis and Design*. John Wiley & Sons, 2012.

[4] E. Kaplan and C. Hegarty, *Understanding GPS: Principles and Applications*. Artech House, 2005.

[5] B. Hoffman-Wellenhof, H. Lichtenegger, and E. Wasle, *GNSS-Global Navigation Satellite Systems*. 2008, pp. 309–430.

[6] J. B.-Y. Tsui, *Fundamentals of Global Positioning System Receivers*. Wiley-Interscience, 2000.

[7] J. M. Samper, J. M. Lagunilla, and R. B. Perez, *GPS and Galileo: Dual RF Front-End Receiver and Design, Fabrication, & Test*. McGraw Hill Professional, 2008.

[8] W. L. Stutzman, *Polarization in Electromagnetic Systems*. Artech House, 1993.

[9] S. Drabowitch, A. Papiernik, H. Griffiths, J. Encinas, and B. L. Smith, *Modern Antennas*. Springer Science & Business Media, 2010.

[10] D. M. Pozar, *Microwave Engineering*. John Wiley & Sons, 2009.

[11] R. A. Horn and C. R. Johnson, *Matrix Analysis*. Cambridge Univ. Press, 2012.

[12] J. Engberg and T. Larsen, *Noise Theory of Linear and Nonlinear Circuits*. Wiley Chichester, 1995.

[13] J. G. Prokais, *Digital Communications*. McGraw Hill, New York, 2001.

[14] A. Paulraj, R. Nabar, and D. Gore, *Introduction to Space-Time Wireless Communications*. Cambridge Univ. Press, 2003.

[15] M. Abramowitz, I. A. Stegun, *et al.*, *Handbook of Mathematical Functions*. 1966, vol. 55, p. 62.

[16] K. F. Lee and K. M. Luk, *Microstrip Patch Antennas*. World Scientific, 2011, vol. 1.

[17] H. L. Van Trees, *Detection, Estimation, and Modulation Theory, Optimum Array Processing*. John Wiley & Sons, 2004.

Journal papers

[18] H. Kuusniemi, E. Airos, M. Z. H. Bhuiyan, and T. Króger, "GNSS jammers: How vulnerable are consumer grade satellite navigation receivers?" *European Journal of Navigation*, vol. 10, no. 2, pp. 14–21, 2012.

[19] K. D. McDonald *et al.*, "The modernization of GPS: Plans, new capabilities and the future relationship to Galileo," *Positioning*, vol. 1, no. 03, 2002.

[20] M. Petovello and P. Groves, "Multipath vs. NLOS signals," *Inside GNSS: GNSS Solutions*, Dec. 2013.

[21] S. Pullen and G. Gao, "GNSS jamming in the name of privacy, potential threat to GPS aviation," *Inside GNSS*, pp. 34–43, 2012.

[22] A. Hornbostel, A. Konovaltsev, H. Denks, and F. Antreich, "Simulation of multi-element antenna systems for navigation applications," *IEEE Systems Journal*, vol. 2, no. 1, pp. 7–19, 2008.

[23] H. T. Hui, "A new definition of mutual impedance for application in dipole receiving antenna arrays," *IEEE Antennas and Wireless Propagation Letters*, vol. 3, no. 1, pp. 364–367, 2004.

[24] A. Ludwig, "Mutual coupling, gain and directivity of an array of two identical antennas," *IEEE Transactions on Antennas and Propagation*, vol. 24, no. 6, pp. 837–841, 1976.

[25] I. J. Gupta and A. A. Ksienski, "Effect of mutual coupling on the performance of adaptive arrays," *IEEE Transactions on Antennas and Propagation*, vol. 31, no. 5, pp. 785–791, 1983.

[26] S. Stein, "On cross coupling in multiple-beam antennas," *IEEE Transactions on Antennas and Propagation*, vol. 10, pp. 548–557, Sep. 1962.

[27] R. G. Vaughan and J. B. Andersen, "Antenna diversity in mobile communications," *IEEE Transactions on Vehicular Technology*, vol. 36, no. 4, pp. 149–172, 1987.

[28] J. Weber, C. Volmer, K. Blau, R. Stephan, and M. A. Hein, "Miniaturized antenna arrays using decoupling networks with realistic elements," *IEEE Transactions on Microwave Theory and Techniques*, vol. 54, no. 6, pp. 2733–2740, 2006.

[29] J. C. Coetzee and Y. Yu, "Port decoupling for small arrays by means of an eigenmode feed network," *IEEE Transactions on Antennas and Propagation*, vol. 56, no. 6, pp. 1587–1593, 2008.

[30] J. W. Wallace and M. A. Jensen, "Mutual coupling in MIMO wireless systems: A rigorous network theory analysis," *IEEE Transactions on Wireless Communications*, vol. 3, no. 4, pp. 1317–1325, 2004.

[31] ——, "Termination-dependent diversity performance of coupled antennas: Network theory analysis," *IEEE Transactions on Antennas and Propagation*, vol. 52, no. 1, pp. 98–105, 2004.

[32] K. F. Warnick and M. A. Jensen, "Optimal noise matching for mutually coupled arrays," *IEEE Transactions on Antennas and Propagation*, vol. 55, no. 6, pp. 1726–1731, 2007.

[33] K. F. Warnick and M. A. Jensen, "Effects of mutual coupling on interference mitigation with a focal plane array," *IEEE Transactions on Antennas and Propagation*, vol. 53, no. 8, pp. 2490–2498, 2005.

[34] P. W. Bradford, J. Spilker, and P. Enge, "Global positioning system: Theory and applications," *The American Institute of Aeronautics and Astronautics (AIAA), Washington DC*, vol. 109, 1996.

[35] B. Górres, J. Campbell, M. Becker, and M. Siemes, "Absolute calibration of GPS antennas: Laboratory results and comparison with field and robot techniques," *GPS solutions*, vol. 10, no. 2, pp. 136–145, 2006.

[36] R. S. Conker, M. B. El-Arini, C. J. Hegarty, and T. Hsiao, "Modeling the effects of ionospheric scintillation on GPS/Satellite-based augmentation system availability," *Radio Science*, vol. 38, no. 1, pp. 1–1, 2003.

[37] N. Bergeot, C. Bruyninx, P. Defraigne, S. Pireaux, J. Legrand, E. Pottiaux, and Q. Baire, "Impact of the Halloween 2003 ionospheric storm on kinematic GPS positioning in Europe," *GPS solutions*, vol. 15, no. 2, pp. 171–180, 2011.

[38] M. V. Heckler, M. Cuntz, A. Konovaltsev, L. A. Greda, A. Dreher, and M. Meurer, "Development of robust safety-of-life navigation receivers," *IEEE Transactions on Microwave Theory and Techniques*, vol. 59, no. 4, pp. 998–1005, 2011.

[39] D. W. Browne, M. Manteghi, M. P. Fitz, and Y. Rahmat-Samii, "Experiments with compact antenna arrays for MIMO radio communications," *IEEE Transactions on Antennas and Propagation*, vol. 54, no. 11, pp. 3239–3250, 2006.

[40] C. Chiau, X. Chen, and C. Parini, "A compact four-element diversity-antenna array for PDA terminals in a MIMO system," *Microwave and Optical Technology Letters*, vol. 44, no. 5, pp. 408–412, 2005.

[41] S. C. Ko and R. D. Murch, "Compact integrated diversity antenna for wireless communications," *IEEE Transactions on Antennas and Propagation*, vol. 49, no. 6, pp. 954–960, 2001.

[42] B. Lindmark and L. Garcia-Garcia, "Compact antenna array for MIMO applications at 1800 and 2450 MHz," *Microwave and Optical Technology Letters*, vol. 48, no. 10, pp. 2034–2037, 2006.

[43] C. Volmer, J. Weber, R. Stephan, K. Blau, and M. A. Hein, "An eigen-analysis of compact antenna arrays and its application to port decoupling," *IEEE Transactions on Antennas and Propagation*, vol. 56, no. 2, pp. 360–370, 2008.

[44] S. H. Chae, S.-k. Oh, and S.-O. Park, "Analysis of mutual coupling, correlations, and TARC in WiBro MIMO array antenna," *IEEE Antennas and Wireless Propagation Letters*, vol. 6, pp. 122–125, 2007.

[45] S.-C. Chen, Y.-S. Wang, and S.-J. Chung, "A decoupling technique for increasing the port isolation between two strongly coupled antennas," *IEEE Transactions on Antennas and Propagation*, vol. 56, no. 12, pp. 3650–3658, 2008.

[46] A. Diallo, C. Luxey, P. Le Thuc, R. Staraj, and G. Kossiavas, "Study and reduction of the mutual coupling between two mobile phone PIFAs operating in the DCS1800 and UMTS bands," *IEEE Transactions on Antennas and Propagation*, vol. 54, no. 11, pp. 3063–3074, 2006.

[47] F. Boccardi, B. Clerckx, A. Ghosh, E. Hardouin, G. Jongren, K. Kusume, E. Onggosanusi, and Y. Tang, "Multiple-antenna techniques in LTE-advanced," *IEEE Communications Magazine*, vol. 50, no. 3, pp. 114–121, 2012.

[48] F. Rusek, D. Persson, B. K. Lau, E. G. Larsson, T. L. Marzetta, O. Edfors, and F. Tufvesson, "Scaling up MIMO: Opportunities and challenges with very large arrays," *IEEE Signal Processing Magazine*, vol. 30, no. 1, pp. 40–60, 2013.

[49] E. Gilbert and S. Morgan, "Optimum design of directive antenna arrays subject to random variations," *Bell System Technical Journal*, vol. 34, no. 3, pp. 637–663, 1955.

[50] H. T. Hui, "A practical approach to compensate for the mutual coupling effect in an adaptive dipole array," *IEEE Transactions on Antennas and Propagation*, vol. 52, no. 5, pp. 1262–1269, 2004.

[51] ——, "Improved compensation for the mutual coupling effect in a dipole array for direction finding," *IEEE Transactions on Antennas and Propagation*, vol. 51, no. 9, pp. 2498–2503, 2003.

[52] J. James and G. Wilson, "Microstrip antennas and arrays. part 1: Fundamental action and limitations," *IEE Journal on Microwaves, Optics and Acoustics*, vol. 1, no. 5, pp. 165–174, 1977.

[53] D. Jackson, J. Williams, A. K. Bhattacharyya, R. L. Smith, S. J. Buchheit, and S. Long, "Microstrip patch designs that do not excite surface waves," *IEEE Transactions on Antennas and Propagation*, vol. 41, no. 8, pp. 1026–1037, 1993.

[54] G. Kristensson, P. Waller, and A. Derneryd, "Radiation efficiency and surface waves for patch antennas on inhomogeneous substrates," *IEE Proceedings-Microwaves, Antennas and Propagation*, vol. 150, no. 6, pp. 477–483, 2003.

[55] W. K. Kahn, "Element efficiency: A unifying concept for array antennas," *IEEE Antennas and Propagation Magazine*, vol. 49, no. 4, pp. 48–56, 2007.

[56] J. N. Pierce and S. Stein, "Multiple diversity with nonindependent fading," *Proceedings of the IRE*, vol. 48, no. 1, pp. 89–104, 1960.

[57] D. Brennan, "On the maximum signal-to-noise ratio realizable from several noisy signals," *Proceedings of the Institute of Radio Engineers*, vol. 43, no. 10, pp. 1530–1530, 1955.

[58] L. R. Kahn, "Ratio squarer," *Proceedings of the Institute of Radio Engineers*, vol. 42, no. 11, pp. 1704–1704, 1954.

[59] C. Volmer, J. Weber, R. Stephan, and M. A. Hein, "A descriptive model for analyzing the diversity performance of compact antenna arrays," *IEEE Transactions on Antennas and Propagation*, vol. 57, no. 2, pp. 395–405, 2009.

[60] O. Norklit, P. D. Teal, and R. G. Vaughan, "Measurement and evaluation of multi-antenna handsets in indoor mobile communication," *IEEE Transactions on Antennas and Propagation*, vol. 49, no. 3, pp. 429–437, 2001.

[61] J. Tranquilla, J. Carr, and H. M. Al-Rizzo, "Analysis of a choke ring groundplane for multipath control in global positioning system (GPS) applications," *IEEE Transactions on Antennas and Propagation*, vol. 42, no. 7, pp. 905–911, 1994.

[62] P. Stoica and N. Arye, "Music, maximum likelihood, and Cramer-Rao bound," *IEEE Transactions on Acoustics, Speech and Signal Processing*, vol. 37, no. 5, pp. 720–741, 1989.

[63] P. Stoica and A. Nehorai, "Music, maximum likelihood, and Cramer-Rao bound: Further results and comparisons," *IEEE Transactions on Acoustics, Speech and Signal Processing*, vol. 38, no. 12, pp. 2140–2150, 1990.

[64] A. J. Weiss and B. Friedlander, "On the Cramer-Rao bound for direction finding of correlated signals," *IEEE Transactions on Signal Processing*, vol. 41, no. 1, p. 495, 1993.

[65] C.-Y. Chiu, C.-H. Cheng, R. D. Murch, and C. R. Rowell, "Reduction of mutual coupling between closely-packed antenna elements," *IEEE Transactions on Antennas and Propagation*, vol. 55, no. 6, pp. 1732–1738, 2007.

[66] D. Guha, S. Biswas, and Y. M. Antar, "Defected ground structure for microstrip antennas," *Microstrip and Printed Antennas: New Trends, Techniques and Applications*, 2010.

[67] T. Kokkinos, E. Liakou, and A. Feresidis, "Decoupling antenna elements of PIFA arrays on handheld devices," *Electronics Letters*, vol. 44, no. 25, pp. 1442–1444, 2008.

[68] S.-W. Su, C.-T. Lee, and F.-S. Chang, "Printed MIMO-antenna system using neutralization-line technique for wireless USB-dongle applications," *IEEE Transactions on Antennas and Propagation*, vol. 60, no. 2, pp. 456–463, 2012.

[69] M. L. Morris and M. A. Jensen, "Network model for MIMO systems with coupled antennas and noisy amplifiers," *IEEE Transactions on Antennas and Propagation*, vol. 53, no. 1, pp. 545–552, 2005.

[70] Y. Lv, X. Zhao, H. Liu, and X. Shen, "A novel compact HIS-EBG structure and its application in reduction of printed antenna mutual coupling," *Journal of Electronics (China)*, vol. 28, no. 2, pp. 161–168, 2011.

[71] Y. E. Erdemli, K. Sertel, R. Gilbert, D. E. Wright, J. L. Volakis, *et al.*, "Frequency-selective surfaces to enhance performance of broad-band reconfigurable arrays," *IEEE Transactions on Antennas and Propagation*, vol. 50, no. 12, pp. 1716–1724, 2002.

[72] H.-X. Xu, G.-M. Wang, and K. Lu, "Microstrip rat-race couplers," *IEEE Microw. Magazine*, vol. 12, no. 4, pp. 117–129, 2011.

[73] K. W. Eccleston and S. H. Ong, "Compact planar microstripline branch-line and rat-race couplers," *IEEE Transactions on Microwave Theory and Techniques*, vol. 51, no. 10, pp. 2119–2125, 2003.

[74] R. M. Fano, "Theoretical limitations on the broadband matching of arbitrary impedances," *Journal of the Franklin Institute*, vol. 249, no. 1, pp. 57–83, 1950.

[75] M. Gustafsson and S. Nordebo, "Bandwidth, Q factor, and resonance models of antennas," *Progress In Electromagnetics Research*, vol. 62, pp. 1–20, 2006.

[76] L. J. Chu, "Physical limitations of omni-directional antennas," *Journal of applied physics*, vol. 19, no. 12, pp. 1163–1175, 1948.

[77] R. Collin and S. Rothschild, "Evaluation of antenna Q," *IEEE Transactions on Antennas and Propagation*, vol. 12, no. 1, pp. 23–27, 1964.

[78] D. E. Riegle and P. Lin, "Matrix signal flow graphs and an optimum topological method for evaluating their gains," *IEEE Transactions on Circuit Theory*, vol. 19, no. 5, pp. 427–435, 1972.

[79] M. K. Mandal and S. Sanyal, "Reduced-length rat-race couplers," *IEEE Transactions on Microwave Theory and Techniques*, vol. 55, no. 12, pp. 2593–2598, 2007.

[80] M. S. Sharawi, D. M. Akos, and D. N. Aloi, "GPS CNO estimation in the presence of interference and limited quantization levels," *IEEE Transactions on Aerospace and Electronic Systems*, vol. 43, no. 1, pp. 227–238, 2007.

[81] A. . Van Dierendonck, "GPS receivers," *Global Positioning System: Theory and Applications*, vol. 1, pp. 329–407, 1996.

[82] K. Kurokawa, "Power waves and the scattering matrix," *IEEE Transactions on Microwave Theory and Techniques*, vol. 13, no. 2, pp. 194–202, 1965.

[83] S. W. Wedge and D. B. Rutledge, "Noise waves and passive linear multiports," *IEEE Microwave and guided wave letters*, vol. 1, no. 5, pp. 117–119, 1991.

[84] H. Rothe and W. Dahlke, "Theory of noisy four poles," *Proceedings of the IRE*, vol. 44, no. 6, pp. 811–818, 1956.

[85] R. Bauernfeind, T. Kraus, A. S. Ayaz, D. Dötterböck, and B. Eissfeller, "Analysis, detection and mitigation of in-Car GNSS jammer interference in intelligent transport systems," 2013.

[86] P. K. Enge, "The global positioning system: Signals, measurements, and performance," *International Journal of Wireless Information Networks*, vol. 1, no. 2, pp. 83–105, 1994.

[87] J. Rife, S. Khanafseh, S. Pullen, D. De Lorenzo, U.-S. Kim, M. Koenig, T.-Y. Chiou, B. Kempny, and B. Pervan, "Navigation, interference suppression, and fault monitoring in the sea-based joint precision approach and landing system," *Proceedings of the IEEE*, vol. 96, no. 12, pp. 1958–1975, 2008.

Theses

[88] G. Seco Granados *et al.*, "Antenna arrays for multipath and interference mitigation in gnss receivers," PhD thesis, 2000.

[89] D. S. De Lorenzo, "Navigation accuracy and interference rejection for GPS adaptive antenna arrays," PhD thesis, Stanford University, 2007.

[90] C. Volmer, "Compact antenna arrays in mobile communications: A quantitative analysis of radiator coupling," PhD thesis, Ilmenau, Techn. Univ., Diss., 2009, 2010.

[91] A. T. Balaei, "Detection, characterization and mitigation of interference in receivers for global navigation satellite systems," PhD thesis, 2007.

[92] S. Backén, "Towards dynamic array processing for GNSS software receivers," PhD thesis, Luleå University of Technology, 2007.

[93] M. Elamir, "Beamforming and direction-of-arrival estimation algorithms for compact antenna arrays for robust satellite navigation," Master thesis, Ilmenau, Techn. Univ., 2013.

[94] M. M. Sayre, "Development of a block processing carrier to noise ratio estimator for the global positioning system," PhD thesis, Ohio University, 2003.

[95] H. Bosma, "On the theory of linear noisy systems," PhD thesis, Technische Hogeschool Eindhoven, 1967.

Conference proceedings

[96] R. Benton, M. Nijjar, C. Woo, A. Podell, G. Horvath, E. Wilson, and S. Mitchell, "GaAs MMICs for an integrated GPS front-end," in *IEEE 14th Annual Gallium Arsenide Integrated Circuit (GaAs IC) Symposium*, 1997, pp. 123–126.

[97] D. Borio, C. O Driscoll, and J. Fortuny, "GNSS jammers: Effects and countermeasures," in *6th ESA Workshop on Satellite Navigation Technologies and European Workshop on GNSS Signals and Signal Processing, (NAVITEC)*, 2012, pp. 1–7.

[98] H. Kuusniemi, "Effects of GNSS jammers and potential mitigation approaches," in *United Nations/Latvia Workshop on the Applications of GNSS*, 2012.

[99] M. Cuntz, A. Konovaltsev, A. Hornbostel, E. Schittler Neves, and A. Dreher, "GALANT–Galileo antenna and receiver demonstrator for safety-critical applications," in *Proceedings of the 10th European Conference on Wireless Technology, Munich Germany*, 2007, p. 59.

[100] M. Heckler, M. Cuntz, A. Konovaltsev, L. Greda, A. Dreher, and M. Meurer, "Development of robust safety-of-life navigation receivers at the German Aerospace Center (DLR)," in *IEEE MTT-S International Microwave Symposium Digest (MTT)*, 2010, pp. 85–88.

[101] G. Kappen, C. Haettich, and M. Meurer, "Towards a robust multi-antenna mass market GNSS receiver," in *IEEE/ION Position Location and Navigation Symposium (PLANS)*, IEEE, 2012, pp. 291–300.

[102] H. J. Chaloupka and X. Wang, "Novel approach for diversity and MIMO antennas at small mobile platforms," in *15th IEEE International Symposium on Personal, Indoor and Mobile Radio Communications (PIMRC)*, vol. 1, 2004, pp. 637–642.

[103] H. J. Chaloupka, X. Wang, and J. Coetzee, "Performance enhancement of smart antennas with reduced element spacing," in *IEEE Wireless Communications and Networking Conference (WCNC)*, vol. 1, 2003, pp. 425–430.

[104] W. Kunysz, "Antenna phase center effects and measurements in GNSS ranging applications," in *14th IEEE International Symposium on Antenna Technology and Applied Electromagnetics & the American Electromagnetics Conference (ANTEM-AMEREM)*, 2010, pp. 1–4.

[105] V. Pathak, S. Thornwall, M. Krier, S. Rowson, G. Poilasne, and L. Desclos, "Mobile handset system performance comparison of a linearly polarized GPS internal antenna with a circularly polarized antenna," in *IEEE International Symposium of Antennas and Propagation Society, Columbus, USA*, vol. 3, 2003, pp. 666–669.

[106] J. W. Betz, "Effect of narrowband interference on GPS code tracking accuracy," in *Proceedings of the National Technical Meeting of The Institute of Navigation*, 2000, pp. 16–27.

[107] J. T. Ross, J. L. Leva, and S. Yoder, "Effect of partial-band interference on receiver estimation of C/N0: Measurements," in *Proceedings of the National Technical Meeting of The Institute of Navigation*, 2001, pp. 829–838.

[108] R. H. Mitch, R. C. Dougherty, M. L. Psiaki, S. P. Powell, B. W. Hanlon, J. A. Bhatti, and T. E. Humphreys, "Signal characteristics of civil GPS jammers," 2011, pp. 20–23.

[109] T. Kraus, R. Bauernfeind, and B. Eissfeller, "Survey of in-car jammers-analysis and modeling of the RF signals and IF samples (suitable for active signal cancelation)," in *Proceedings of the 24th International Technical Meeting of The Satellite Division of the Institute of Navigation (ION-GNSS)*, 2001, pp. 430–435.

[110] A. Brown and D. Morley, "Test results of a 7-element small controlled reception pattern antenna," in *Proceedings of ION GPS*, 2001, pp. 1–8.

[111] A. Brown and R. Silva, "A GPS digital phased array antenna and receiver," in *IEEE International Conference on Phased Array Systems and Technology*, 2000, pp. 153–156.

[112] D. Reynolds, A. Brown, and A. Reynolds, "Miniaturized gps antenna array technology and predicted anti-jam performance," in *Proceedings of the 12 th International Technical meeting of the Satellite Division of the Institute of Navigation, GPS-99, Nashville*, 1999, pp. 777–785.

[113] A. Brown, N. Gerein, L. Savage, *et al.*, "Multipath characterization using digital phased arrays," in *ION 57th Annual Meeting, Albuquerque, NM*, 2001.

[114] A. K. Brown and B. Mathews, "GPS multipath mitigation using a three dimensional phased array," in *Proceedings of ION GNSS*, 2005, pp. 659–666.

[115] Q. Li and A. P. Feresidis, "Reduction of mutual coupling between compact MIMO antennas arrays," in *IEEE Loughborough Antennas and Propagation Conference (LAPC)*, 2010, pp. 277–280.

[116] D. Pozar, M. Bailey, and M. Despande, "Calculated self and mutual impedance of rectangular microstrip antennas," in *IEEE International Symposium of Antennas and Propagation Society*, vol. 20, 1982, pp. 62–65.

[117] D. Schulz and R. S. Thomae, "Cramer-Rao lower bounds for polarimetric 2D direction of arrival estimation," in *Proceedings of 19th International ITG-VDE Workshop on Smart Antennas (WSA)*, 2015, pp. 1–8.

[118] M. Ivrlač and J. Nossek, "On the diversity performance of compact antenna arrays," in *DBC Signal Processing Antennas Proc. of the 30th URSI General Assembly and Scientific Symposium*, 2011.

[119] B. K. Lau and J. B. Andersen, "Unleashing multiple antenna systems in compact terminal devices," in *IEEE International Workshop on Antenna Technology (IWAT)*, 2009, pp. 1–4.

[120] A. Konovaltsev, M. Cuntz, L. Greda, M. V. Heckler, M. Meurer, *et al.*, "Antenna and RF front end calibration in a GNSS array receiver," in *IEEE International Microwave Workshop Series on RF Front-ends for Software Defined and Cognitive Radio Solutions (IMWS)*, 2010, pp. 1–4.

[121] M. D. Zoltowski and A. S. Gecan, "Advanced adaptive null steering concepts for GPS," in *IEEE Military Communications Conference (MILCOM)*, vol. 3, 1995, pp. 1214–1218.

[122] M. Sgammini, F. Antreich, L. Kurz, M. Meurer, and T. G. Noll, "Blind adaptive beamformer based on orthogonal projections for GNSS," in *Proceedings of ION-GNSS*, 2012.

[123] W.-I. Son, W.-G. Lim, M.-Q. Lee, S.-B. Min, and J.-W. Yu, "Printed square quadrifilar helix antenna (QHA) for GPS receiver," in *38th European Microwave Conference (EuMC)*, IEEE, 2008, pp. 1292–1295.

[124] S. Dossche, S. Blanch, and J. Romeu, "Decorrelation of a closely spaced four element antenna array," in *IEEE International Symposium of Antennas and Propagation Society*, vol. 1, 2005, pp. 803–806.

[125] F. Römer and M. Haardt, "Deterministic Cramer-Rao bounds for strict sense non-circular sources," in *Proc. ITG/IEEE Workshop on Smart Antennas (WSA)*, 2007.

[126] J. W. Wallace and M. A. Jensen, "Impact of antenna coupling on diversity performance: Complete network theory analysis," in *IEEE International Conference on Communications*, vol. 2, 2004, pp. 947–951.

[127] D. Williams, S. Clark, J. Cook, P. Corcoran, and S. Spaulding, "Four-element adaptive array evaluation for united states navy airborne applications," in *Proceedings of the 13th International Technical Meeting of the Satellite Division of The Institute of Navigation*, 2000, pp. 2523–2532.

Miscellaneous

[128] European GNSS Space Agency, *GSA's GNSS market report*, 2015. [Online]. Available: `www.esa.int/OurActivities/Navigation/Thefuture-Galileo/WhatisGalileo`.

[129] u-blox, *Concurrent multi-GNSS receiver single-chips (UBX-M8030)*. [Online]. Available: `www.u-blox.com/en/gps-chips/stand-alone-gps-chips/ubx-m8030-ctktka`.

[130] GSA - European GNSS Agency, *GNSS market report*, Mar. 2015.

[131] Russian Institute of Space Device Engineering, *Glonass inteface control document*, 2008. [Online]. Available: `www.unavco.org/help/glossary/docs/ICDGLONASS5.1(2008)en.pdf`.

[132] Global Positioning System Directorate, *Navstar GPS space segment/navigation user segment interfaces*, Sep. 2013.

[133] ——, *Navstar GPS space segment/navigation user segment L1C interfaces*, Sep. 2013.

[134] ——, *Navstar GPS space segment/navigation user segment L5 interfaces*, Sep. 2013.

[135] Federal Aviation Administration, *Global positioning system (GPS) standard positioning service (SPS) performance analysis report*, Jul. 2014. [Online]. Available: www.nstb.tc.faa.gov/reports/PAN860714.pdf.

[136] MediaTek, *Multi-GNSS receiver-MT333*. [Online]. Available: www.mediatek.com/en/products/connectivity/gps/mt3333/.

[137] Trimble, *Buffalo GNSS receiver*. [Online]. Available: www.trimble.com/embeddedsystems.

[138] Furuno Electronics, *Concurrent multi-GNSS receiver chip*. [Online]. Available: www.furuno.com/en/products/gnss-chip/ePV7010B.

[139] ST Microelectronics, *Fully integrated GPS/Galileo/Glonass/Beidou2/QZSS receiver with embedded RF and in-package flash*. [Online]. Available: www.st.com/web/catalog/sense-power/FM1934/CL1942/SC612/PF260027.

[140] IEEE-STD-145-1993, *IEEE standard definition of terms for antennas.* Mar. 1993.

[141] A.-M. Dinius, *GPS antenna multipath rejection performance*, 1995.

[142] ANSYS, Inc., *ANSYS HFSS*. [Online]. Available: www.ansys.com.

[143] ANTCOM Corporation, *GPS, GNSS, SBAS, CRPA antennas*. [Online]. Available: www.antcom.com/.

[144] K. Sander, *GeoHelix P2 antennas*. [Online]. Available: www.sander-electronic.de.

[145] Coilcraft Inc., *RF chip inductors*. [Online]. Available: www.coilcraft.com.

[146] Murata Inc., *Capacitors and inductors*. [Online]. Available: www.murata.com.

[147] Maury Microwave, *Noise figure / noise parameter measurements*. [Online]. Available: www.maurymw.com.

[148] bibinitperiod Corp., *Advanced Connectivity Solutions*. [Online]. Available: www.rogerscorp.com.

[149] Avago Technologies, *Infotainment GPS - low-noise amplifiers*. [Online]. Available: www.avagotech.com.

[150] Minicircuits, *RF and microwave products*. [Online]. Available: www.minicircuits.com.

[151] Hittite Microwave Corp., *Microwave products*. [Online]. Available: www.hittite.com.

[152] Analog Devices, *RF and Microwave products*. [Online]. Available: www.analog.com.

[153] Institute fúr Mikroelektronik- und Mechatronik-Systyme, *IMMS GmbH*. [Online]. Available: www.imms.de.

[154] OsmocomSDR, *DVB-T dongles for software defined radios*. [Online]. Available: www.sdr.osmocom.org/trac/wiki/rtl-sdr.

[155] Rohde & Schwarz, *Test and measurement equipment*. [Online]. Available: www.rohde-schwarz.com.

[156] The Global Positioning System, 2015. [Online]. Available: www.gps.gov/systems/gps/.

Own Publications

[157] S. Irteza, E. Schafer, C. Volmer, M. Sgammini, R. Stephan, E. Hennig, and M. A. Hein, "Noise characterization of a multi-channel receiver using a small antenna array with full diversity for robust satellite navigation," in *IEEE International Conference on Wireless Information Technology and Systems (ICWITS)*, 2012, pp. 1–4.

[158] S. Irteza, E. Schafer, M. Sgammini, R. Stephan, and M. A. Hein, "Impact of polarization impurity on compact antenna array receiver for satellite navigation systems," in *IEEE European Microwave Conference (EuMC)*, 2013, pp. 346–349.

[159] E. Schafer, S. Irteza, A. Jager, B. Bieske, A. Richter, M. A. Khan, M. Sathyamurthy, S. Kerkmann, A. Rolapp, E. Hennig, *et al.*, "A four-channel GNSS front-end IC for a compact interference-and jamming-robust multi-antenna Galileo/GPS receiver," in *IEEE 7th ESA Workshop on Satellite Navigation Technologies and European Workshop on GNSS Signals and Signal Processing (NAVITEC)*, 2014, pp. 1–6.

[160] A. Dreher, N. Basta, S. Irteza, S. Caizzone, G. Kappen, M. Sgammini, M. Meurer, R. Stephan, E. Hein M. A. Schafer, M. A. Khan, A. Richter, B. Bieske, L. Kurtz, and T. G. Noll, "Compact adaptive multi-antenna navigation receiver," *Proceedings of the 25th International Technical Meeting of The Satellite Division of the Institute of Navigation (ION-GNSS)*, pp. 917–925, Sep. 2012.

[161] N. Basta, A. Dreher, S. Caizzone, M. Sgammini, F. Antreich, G. Kappen, S. Irteza, R. Stephan, M. A. Hein, E. Schäfer, *et al.*, "System concept of a compact multi-antenna gnss receiver," in *7th German Microwave Conference (GeMiC), Ilmenau, Germany*, 2012.

[162] N. Basta, S. Irteza, E. Schafer, and L. Kurtz, "System concept for a compact multi-antenna GNSS receiver," in *COSTA-VISTA Workshop, Istanbul, Turkey*, 2012.

[163] A. Hornbostel, N. Basta, M. Sgammini, L. Kurz, S. Irteza, and A. Dreher, "Experimental results of interferer suppression with a compact antenna array," in *European Navigation Conference (ENC)*, 2013.

[164] M. Ibraheam, S. Irteza, S. Caizzone, A. Dreher, R. Stephan, and M. A. Hein, "Compact dual-band dual-polarized antenna array for robust satellite navigation receivers," in *9th European Conference on Antennas and Propagation (EuCAP)*, 2015.

[165] M. Ibraheam, S. Irteza, and M. A. Hein, "Enhancing the radiation efficiency of compact antenna arrays using spatial tilting," in *IEEE 8th European Conference on Antennas and Propagation (EuCAP)*, 2014, pp. 2357–2361.

[166] M. Ibraheam, A. Krauss, S. Irteza, and M. A. Hein, "Reduction of mutual coupling in compact antenna arrays using element tilting," in *VDE/ITG German Microwave Conference (GeMiC), Aachen, Germany*, 2014, pp. 1–4.

[167] S. Irteza, M. Ibraheam, T. Harz, Y. Bulbin, R. Stephan, and M. A. Hein, "Compact satellite navigation antenna array using off-the-shelf ceramic patch antennas," in *IEEE 9th European Conference on Antennas and Propagation (EuCAP)*, 2015.

[168] S. Irteza, N. Murtaza, S. Caizzone, R. Stephan, and M. A. Hein, "Compact planar L-band antenna arrays with optimal diversity performance," in *IEEE-APS Topical Conference on Antennas and Propagation in Wireless Communications (APWC)*, 2011, pp. 512–515.

[169] S. Irteza, E. Schäfer, R. Stephan, A. Hornbostel, and M. A. Hein, "Compact antenna array receiver for robust satellite navigation systems," *International Journal of Microwave and Wireless Technologies*, pp. 1–11, 2014.

[170] S. Irteza, E. Schafer, M. Ibraheam, B. Bieske, R. Stephan, and M. Hein, "Beamforming in compact antenna arrays for robust satellite navigation," in *IEEE-APS Topical Conference on Antennas and Propagation in Wireless Communications (APWC)*, 2014, pp. 528–531.

[171] S. Irteza, E. Schafer, M. Sgammini, R. Stephan, and M. Hein, "Four-element compact planar antenna array for robust satellite navigation systems," in *IEEE 7th European Conference on Antennas and Propagation (EuCAP)*, IEEE, 2013, pp. 21–25.

[172] S. Irteza, R. Stephan, A. Dreher, L. Kurz, M. Meurer, T. Harz, Y. Bulbin, and M. A. Hein, "Satellitennavigationsempfänger für sichere intelligente transportsysteme," in *Positionierung und Navigation für Intelligente Transportsysteme, POSNAV, Germany*, 2014.

[173] S. Irteza, R. Stephan, and M. A. Hein, "Kompassion: Kompakte adaptive terminalantenne zur störungsfreien satellitennavigation," Technische Informationsbibliothek u. Universitätsbibliothek, Hannover, Schlussbericht, 2014.

Notations and Abbreviations

$\{.\}^{\mathrm{H}}$ Hermitian transpose.

$\{.\}^{\mathrm{T}}$ transpose operation.

$\{.\}^{*}$ complex conjugate element-wise operation without transpose.

$\bar{\{.\}}$ matrix.

$\vec{\{.\}}$ vector.

$\Re\{.\}$,$\Im\{.\}$ real and imaginary parts of a complex variable.

$\{|.|\}$ absolute value.

$\{.\}_i$ i^{th} element of the vector $\vec{\{.\}}$.

$\vec{\{.\}}(i)$ i^{th} column vector of the matrix $\bar{\{.\}}$.

$\log$ base-10 logarithm.

$\mathrm{tr}\bar{\{.\}}$ trace of a matrix.

$\det\bar{\{.\}}$ determinant of a matrix.

$\bar{\{.\}}^{-1}$ inverse of a matrix.

$\mathrm{Var}\{.\}$ variance of a random variable.

$\mathrm{Var}\vec{\{.\}}$ covariance of a vector.

a,b signal power waves travelling in the inwards (a) and outwards (b) directions.

$F_i(\theta,\phi)$ embedded realised amplitude far-field pattern of port i.

$\bar{R}$ covariance matrix of the antenna array.

$\bar{I}$ the identity matrix unless otherwise stated.

N number of antenna elements.

P power.

$\bar{Q}$ unitary matrix of eigenvectors or eigenmodes of $\bar{R}$.

I_{p},Q_{p} in-phase and quadrature-phase.

$\bar{S}$ scattering parameters matrix.

T,$\bar{T}$ equivalent noise temperature and the temperature covariance matrix.

$\vec{w}$ vector of the beamforming weights for a multi-element receiver.

Z_{o} characteristic impedance of a transmission line.

Γ reflection coefficient of a single-port.

χ_{o} carrier-to-noise density ratio.

γ signal-to-noise ratio.

N_{o} noise spectral density.

θ elevation angle in degrees.

ϕ azimuth angle in degrees.

λ free-space wavelength.

f_o operating frequency.

ν,μ noise power waves travelling in the inwards (ν) and outwards (μ) directions.

$\bar{R}_{acc}$ accepted covariance matrix of the antenna array calculated using scattering matrix.

$\bar{R}_{rad}$,$\bar{R}$ radiated or received covariance matrix of the antenna array calculated using antenna array embedded patterns.

$\bar{R}_y$ covariance matrix of the antenna array calculated using recorded streams of raw data.

D_n Pseudo-range from n^{th} satellite.

x_{n} navigation message.

x_{c} C/A-code.

x_{m} BPSK modulated satellite signal.

GNSS Global Navigation Satellite Systems.

DMN Decoupling and Matching Networks.

SNR Signal-to-Noise Ratio.

CNR Carrier-to-Noise Ratio.

CINR Carrier-to-Interference-plus-Noise Ratio.

SoL Safety-of-Life.

PVT Position Velocity and Time.

GPS Global Positioning System.

GLONASS Global Orbiting Navigation Satellite System.

PRN Pseudo Random Number.

CDMA Code Division Multiple Access.

FDMA Frequency Division Multiple Access.

NRZ Non-Return to Zero.

C/A Coarse Acquisition Codes.

RNSS Radio Navigation Satellite Systems.

P Precision Codes.

FE Front-End.

RF Radio Frequency.

IF Intermediate Frequency.

RHCP Right-Hand Circularly Polarised.

DLL Code Tracking Loop.

PLL Phase Locked Loop.

CMOS Complementary Metal Oxide Semiconductor.

URE User Range Error.

GDOP Geometric Dilution of Position.

SV Satellite Vehicle.

LNA Low-Noise Amplifier.

NF Noise Figure.

LHCP Left-Hand Circular Polarised.

XPD Cross-Polarisation Discrimination.

IEEE Institute of Electrical and Electronics Engineers.

QHA Quadrafilar Helix Antenna.

FRPA Fixed-Radiation Pattern Antenna.

CRPA Controlled-Radiation Pattern Antenna.

GSM Global System for Mobile.

BPSK Binary Phase Shift Keying.

JSR Jammer-to-Signal Ratio.

CW Continuous Wave (Sinusoidal Signal).

PPD Personal Privacy Device.

DOA Direction-of-Arrival.

MIMO Multi-input Multi-output.

LTE Long-Term Evolution.

DGS Defected Ground Structures.

EBG Electromagnetic Band-Gap.

LP Linearly Polarised.

CRLB Cramer-Rao lower bound.

COTS Commercial Off-the-Shelf.

LO Local Oscillator.

ADC Analogue-to-Digital Converter.

BPF Band-Pass Filter.

LPF Low-Pass Filter.

PCB Printed-Circuit Board.

IC Integrated Circuit.

m units in metres.

cm centimetres.

nm nanometres.

dB decibels.

dBW decibels Watts.

dBm decibels milliWatts.

s seconds.

ms milliseconds.

$\mathrm{dB\text{-}Hz}$ decibels-Hertz.

dBi decibels with respect to isotropic antenna.

kHz kiloHertz or 1000 hertz.

MHz megaHertz or 1000 kilohertz.